Role of charge-density fluctuations and many-particle Coulomb correlations in the mechanism of high-temperature superconductivity of cuprate metal-oxide compounds

É. A. Pashitskiĭ* and V. I. Pentegov

Institute of Physics, National Academy of Sciences of Ukraine, pr. Nauki 46, 03022 Kiev, Ukraine
(Submitted July 31, 2000; revised October 2, 2000)
Fiz. Nizk. Temp. **27**, 140–152 (February 2001)

The charge-fluctuation (plasmon) mechanism of *d*-wave Cooper pairing in high-T_c superconductors (HTSCs) is considered. This mechanism arises from the interaction of current carriers with collective low-frequency electron-density excitations. It is shown that for layered crystals of cuprate metal-oxide compounds the existence of a one-electron spectrum of anisotropic extended saddles (flat bands) with an anomalously high density of states can give rise to damped long-wavelength charge-density fluctuations that lead to suppression of the static screened Coulomb repulsion in the region of small momentum transfers. As a result, an effective attraction between electrons arises in the *d*-wave Cooper channel; this attraction is substantially enhanced by many-particle Coulomb correlations of the local-field-effects type, described by a Coulomb vertex Γ_c. It leads to Cooper pairing with $d_{x^2-y^2}$ symmetry of the superconducting order parameter and can make for rather high maximum values of the critical temperature, $T_c \sim 100$ K, at the optimum doping level for cuprate metal-oxide compounds. Taking the anisotropy of the electron–phonon interaction into account makes it possible to describe the weak oxygen isotope effect in HTSC compounds. [DOI: 10.1063/1.1353700]

1. INTRODUCTION

One of the most characteristic features of high-T_c superconductors (HTSCs) based on layered cuprate metal-oxide compounds (MOCs) with hole-type conductivity is the $d_{x^2-y^2}$ symmetry of the superconducting order parameter, which has been observed directly in a number of phase-sensitive experiments, e.g., from the shift in the magnetic-field dependence of the Josephson currents in systems of the SQUID type with Josephson contacts on mutually perpendicular faces of layered cuprate MOC crystals[1–4] and from the spontaneous generation of half-integer magnetic flux quanta in HTSC rings with an odd number of weak links.[5–7] An indication of *d*-wave symmetry of the superconducting gap in HTSC crystals has also been obtained in angle-resolved photoelectron spectroscopy (ARPES) experiments,[8,9] where a strong anisotropy of the superconducting gap was observed in the layer plane ab, with deep minima (zeroes) along the diagonals of the two-dimensional (2D) Brillouin zone.

The possibility of *d*-wave symmetry of the superconducting order parameter in HTSCs was first discussed in Refs. 10 and 11 in the the framework of the site representation of the Hubbard model and then in a series of papers[12–17] in a model of an almost antiferromagnetic quasi-2D Fermi liquid with strong spin correlations. According to these models, $d_{x^2-y^2}$ symmetry of the superconducting gap is realized in HTSCs on account of the effective anisotropy of the electron–electron attraction arising either in real space, as in the Hubbard model with repulsion at one site and attraction at neighboring sites of the 2D square lattice,[10] or in momentum space, due to the fact that the electron–electron repulsion induced by spin-density fluctuations (magnons) has sharp peaks at the corners of the Brillouin zone.[15]

However, in addition to the exchange (spin-fluctuation) channel of electron–electron interaction there is also a direct Coulomb (charge-fluctuation) channel, which was not taken into account in Refs. 10–17. We note that attempts have been made[18,19] to treat the spin and Coulomb channels simultaneously in the Hubbard site approximation, which corresponds to taking into account the local repulsion of electrons at one site but does not take into account the long-range character of the Coulomb interaction.

On the other hand, in Refs. 20–23 it was shown in the random phase approximation (RPA) that the extended saddles observed in the quasi-2D band spectrum of cuprate MOCs in the ARPES experiments[24–28] and which lead to strong anisotropy of the effective mass and group velocity of quasiparticles near the Fermi surface can give rise to a long-wavelength, low-frequency (LF) branch of strongly damped electron-density excitations having an acoustical dispersion relation ($\omega_q \propto q$ as $q \to 0$), analogous to acoustic plasmons[29] in many-band metals with a multiply connected anisotropic Fermi surface and in many-valley degenerate semiconductors and semimetals.[30–33]

The small-angle inelastic scattering of electrons on these LF collective fluctuations of the charge density leads to weakening of the screened Coulomb repulsion in the region of small momentum transfers $\mathbf{q}$.[22] In combination with the strong anisotropy of the one-electron spectrum in the basal plane ab due to the extended saddles, the minimum of the electron–electron repulsion at small q (like the repulsion peaks at the corners of the Brillouin zone[15–17]) corresponds to an effective attraction in the *d*-wave Cooper channel and makes for $d_{x^2-y^2}$ symmetry of the order parameter.[20–23]

In this paper we use empirical data on the band structure

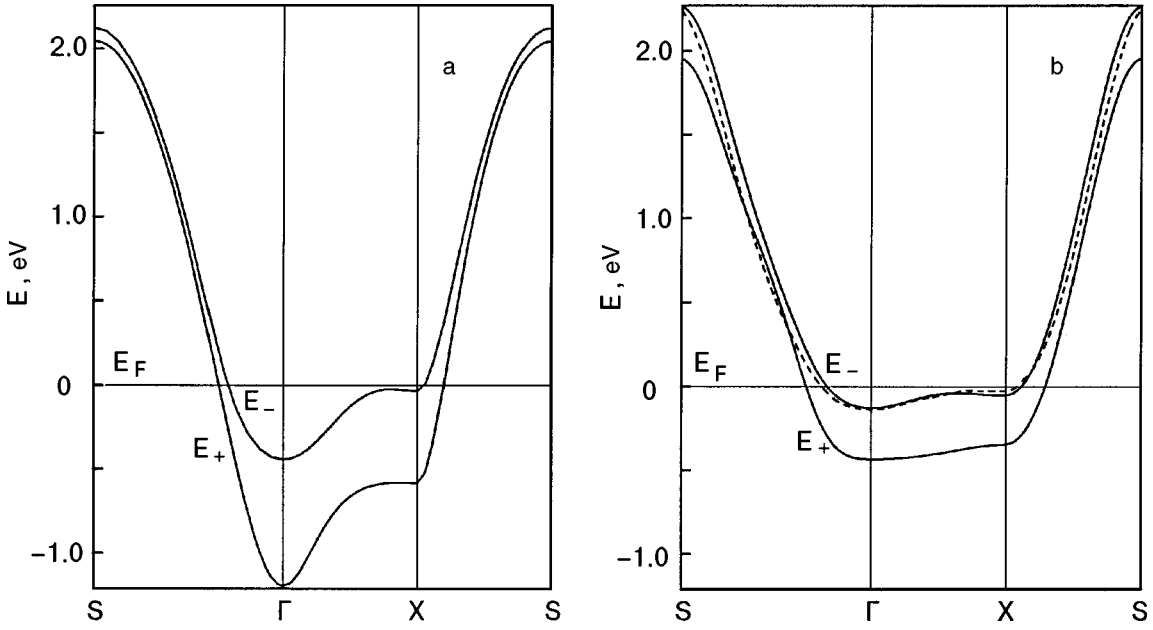

FIG. 1. Dispersion relations for the bonding $E_+(k_x,k_y)$ and antibonding $E_-(k_x,k_y)$ branches (solid curves) of the band spectrum of the Y-123 crystal along the principal symmetry directions of the Brillouin zone; obtained by calculation in Ref. 34 (a) and proposed in Ref. 28 on the basis of experimental data (b). The dashed curve shows the spectrum $E_-(k_x,k_y)$ renormalized on account of the electron–electron interaction.

of cuprate MOC layered crystals to carry out a self-consistent numerical calculation of the electronic polarizability, the self-energy of the electrons, and the screened Coulomb interaction with allowance for many-particle Coulomb correlations, which are described by a Coulomb vertex part Γ_c. It is shown that such many-particle local-field effects lead to substantial enhancement of the electron–electron interaction considered in Refs. 20–23, which arises in the *d*-wave Cooper channel on account of the suppression of the Coulomb repulsion at small momenta by long-wavelength fluctuations of the charge density. By numerical solution of the integral equation for an anisotropic superconducting order parameter with $d_{x^2-y^2}$ symmetry in the strong-coupling approximation, we evaluate the dimensionless electron–plasmon interaction constant and the critical temperature T_c for transition to the superconducting state for various positions of the Fermi level relative to the bottom of the saddles in the quasi-2D band spectrum of the electrons in the CuO_2 cuprate layers. It is shown that the effective attraction due to suppression of the Coulomb repulsion by the retarded electron–plasmon interaction can make for rather high maximum values $T_c \geqslant 100$ K at the optimum doping level in cuprate MOCs. By taking the anisotropy of the electron–phonon interaction into account, one can describe the weak oxygen isotope effect in HTSC compounds.

2. LOW-FREQUENCY CHARGE-DENSITY FLUCTUATIONS IN LAYERED CRYSTALS WITH AN ANISOTROPIC QUASI-2D ELECTRONIC SPECTRUM

We shall show in the random phase approximation that a sufficiently strong anisotropy of the quasi-2D electronic spectrum of layered crystals in the layer plane *ab* can give rise to damping of a LF branch of long-wavelength collective electron-density excitations with an acoustic dispersion relation $\omega_q \propto q$ as $q \to 0$, which is analogous to the branch of acoustic plasmons in metals with a multiply connected Fermi surface.[29–33]

Let us consider two different types of anisotropic electron spectra with extended saddles (Fig. 1). The first version (Fig. 1a) corresponds to the theoretical band spectrum calculated in Ref. 34 for 2D CuO_2 cuprate layers in the crystal $YBa_2Cu_3O_7$ (Y-123). As the second version (Fig. 1b) we choose the empirical band spectrum of the Y-123 crystal proposed in Ref. 28, based on the data of the ARPES experiments. The upper (antibonding) $E_-(\mathbf{k})$ and lower (bonding) $E_+(\mathbf{k})$ branches of this spectrum in the second case are described by the expressions

$$\begin{aligned} E_-(k_x,k_y) = {} & 0.4368 - 0.54695(\cos k_x + \cos k_y) \\ & + 0.5612 \cos k_x \cos k_y - 0.0388 \\ & \times (\cos 2k_x + \cos 2k_y) + 0.0674 \cos 2k_x \cos 2k_y \\ & - 0.05205(\cos k_x \cos 2k_y + \cos 2k_x \cos k_y), \end{aligned} \tag{1a}$$

$$\begin{aligned} E_+(k_x,k_y) = {} & 0.1756 - 0.56295(\cos k_x + \cos k_y) \\ & + 0.554 \cos k_x \cos k_y - 0.0887 \\ & \times (\cos 2k_x + \cos 2k_y) + 0.1286 \cos 2k_x \cos 2k_y \\ & - 0.03505(\cos k_x \cos 2k_y + \cos 2k_x \cos k_y). \end{aligned} \tag{1b}$$

Figure 2 shows the results of our numerical calculations of the real and imaginary parts of the longitudinal electronic permittivity of a layered crystal with a quasi-2D band spectrum,

$$\varepsilon_e(\mathbf{q},\omega) = \varepsilon_\infty + V_c(\mathbf{q})\Pi_e(\mathbf{q}_\parallel,\omega). \tag{2}$$

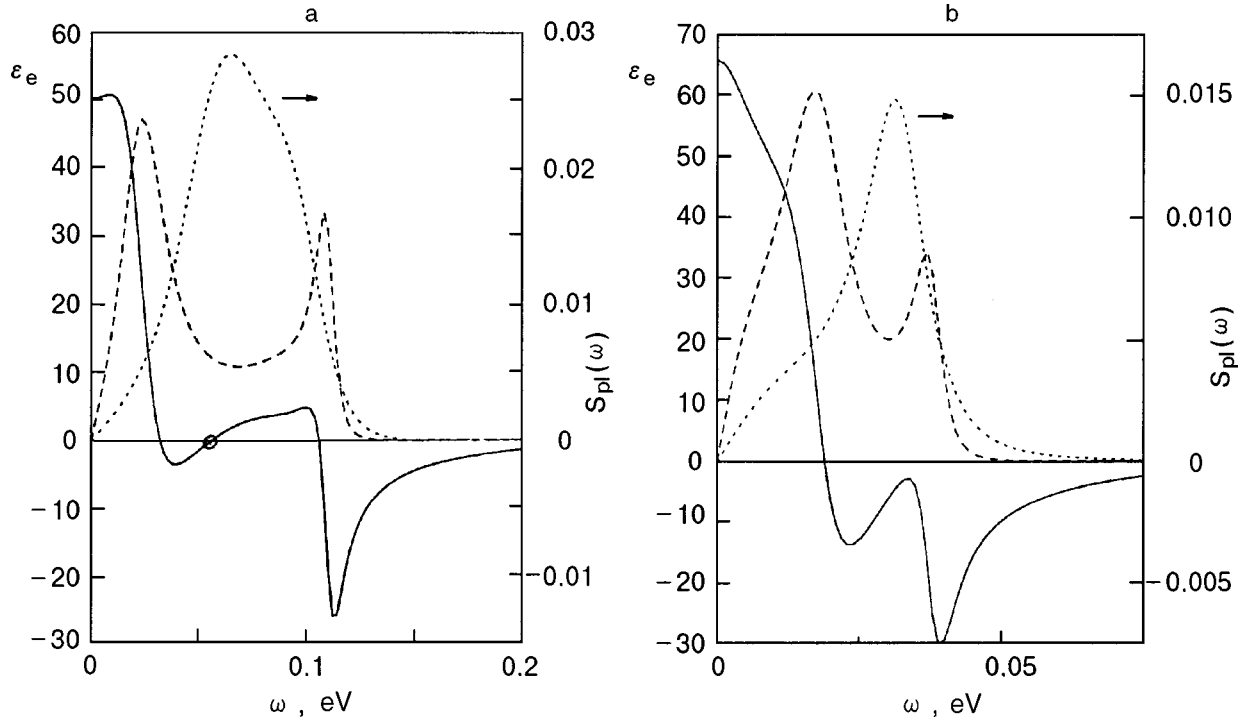

FIG. 2. Frequency dependence of the real (solid curve) and imaginary (dashed curve) parts of the electronic permittivity and also the spectral function of the charge-density fluctuations (dotted curve) calculated in the RPA for $q_x = q_y = \pi/16a$ and $q_z = 0$ on the basis of the theoretical (a) (Fig. 1a) and empirical (b) (Fig. 1b) spectra. The circle indicates the position of the weakly damped branch of acoustic plasmons.

Here ε_∞, the high-frequency dielectric constant of the crystal, is mainly determined by the electronic polarizability, which is due to interband transitions, in particular between the branches $E_+(\mathbf{k})$ and $E_-(\mathbf{k})$; $\Pi_e(\mathbf{q}_\parallel, \omega)$ is the polarization operator for the electrons in the conduction band and is a function of the longitudinal (in the plane of the layers) momentum $\mathbf{q}_\parallel$; $V_c(\mathbf{q})$ is the matrix element of the unscreened Coulomb repulsion of the electrons, which in a crystal with one conducting layer per unit cell is given by

$$V_c(\mathbf{q}) = \frac{2\pi e^2}{q_\parallel} \frac{\sinh q_\parallel c}{\cosh q_\parallel c - \cos q_z c}, \tag{3}$$

where c and q_z are the lattice constant and the momentum along the axis $\mathbf{c} \| \mathbf{z}$.

According to Ref. 35, the presence of two or three layers in the unit cell of a layered crystal will substantially complicate the expression for the Coulomb matrix elements and the electronic permittivity. However, in view of the specific ''stack'' structure of cuprate MOC crystals, where the distance between the CuO_2 conducting layers within a stack is much less than the distance between the stacks of two or three identical two-dimensional CuO_2 layers, we can to good accuracy use expression (3) under the condition that the doubled or tripled value of the one-band polarization operator is used in (2).

Figure 2a shows the frequency dependence of $\mathrm{Re}\,\varepsilon_e(\mathbf{q}, \omega)$ and $\mathrm{Im}\,\varepsilon_e(\mathbf{q}, \omega)$ calculated in the RPA on the basis of the one-electron spectrum corresponding to the dispersion of the upper (antibonding) branch of the theoretical band spectrum shown in Fig. 1a, and Fig. 2b shows the corresponding frequency dependence for the empirical spectrum shown in Fig. 1b.

We see that in the first case (Fig. 2a) the function $\mathrm{Re}\,\varepsilon_e(\mathbf{q}, \omega)$ has three zeros in the long-wavelength region, one of them lying at the minimum of $\mathrm{Im}\,\varepsilon_e(\mathbf{q}, \omega)$ and determining the frequency of weakly damped acoustic plasmons, while in the second case (Fig. 2b) there is only one zero of $\mathrm{Re}\,\varepsilon_e(\mathbf{q}, \omega)$, which lies near the maximum of $\mathrm{Im}\,\varepsilon_e(\mathbf{q}, \omega)$ and corresponds to strongly damped (overdamped) collective LF excitations of the electron density.

Nevertheless, the frequency dependence of the spectral function of the charge-density fluctuations (plasmons) shown in Figs. 2a and 2b,

$$S_{\mathrm{pl}}(\mathbf{q}, \omega) = -\frac{1}{\pi} \mathrm{Im}\, \varepsilon_e^{-1}(\mathbf{q}, \omega) \tag{4}$$

is in both cases characterized by the presence of a maximum in the region of the minimum of $\mathrm{Im}\,\varepsilon_e(\mathbf{q}, \omega)$, where this minimum is due to the antiphase collective oscillations of electrons on parts of the anisotropic Fermi surface with substantially different effective masses and Fermi velocities.

By virtue of the Kramers–Kronig relation for the inverse permittivity[36,37] the features of the spectral function (4) should be reflected in the behavior of the retarded screened Coulomb interaction:

$$\tilde{V}_c(\mathbf{q}, \omega) \equiv \frac{V_c(\mathbf{q})}{\varepsilon_e(\mathbf{q}, \omega)} = V_c(\mathbf{q}) \left[1 + \int_{-\infty}^{\infty} \frac{d\omega' S_{\mathrm{pl}}(\mathbf{q}, \omega')}{\omega - \omega' + i\eta} \right]. \tag{5}$$

We note that the second (integral) term in (5) can be regarded as the spectral representation of the plasmon Green's function.

As we shall see below, the existence of a LF maximum in the frequency dependence of $S_{\rm pl}(\mathbf{q},\omega)$ in the long-wavelength region $q \ll \pi/a$ (where a is the lattice constant in the plane of the layers) leads to suppression of the static Coulomb repulsion

$$\tilde{V}_c(\mathbf{q},0)=\frac{V_c(\mathbf{q})}{\varepsilon_e(\mathbf{q},0)}=V_c(\mathbf{q})\left[1-2\int_0^\infty \frac{d\omega'}{\omega'}S_{\rm pl}(\mathbf{q},\omega')\right] \tag{6}$$

at small $\mathbf{q}$, which corresponds to d-wave symmetry of the Cooper pairing of the current carriers.

3. SCREENED COULOMB INTERACTION WITH ALLOWANCE FOR MANY-PARTICLE CORRELATIONS IN THE LAYERED CRYSTALS OF CUPRATE METAL OXIDES

For describing the effects of screening of the Coulomb interaction, we shall start from the expression for the renormalized electron polarization operator $\tilde{\Pi}_e(\mathbf{q}_\parallel,\omega)$ at $T\neq 0$ in the Matsubara representation:

$$\tilde{\Pi}_e(\mathbf{q}_\parallel,\nu_n)=-\frac{2T}{a^2N^2}\sum_{\omega_n}\sum_{\mathbf{k}_\parallel} G(\mathbf{k}_\parallel,\omega_n)G(\mathbf{k}_\parallel+\mathbf{q}_\parallel,\omega_n+\nu_n) \times\Gamma_c(\mathbf{k}_\parallel,\omega_n;\mathbf{k}_\parallel+\mathbf{q}_\parallel,\omega_n+\nu_n), \tag{7}$$

where $\nu_n=2n\pi T$ and $\omega_n=(2n+1)\pi T$ are the discrete boson and fermion frequencies ($n=0,1,2,\ldots$), N^2 is the number of discrete values of the momentum within the first Brillouin zone, Γ_c is the Coulomb vertex part describing the many-particle local-field effects (see below), and $G(\mathbf{k}_\parallel,\omega_n)$ is the one-electron Green's function:

$$G(\mathbf{k}_\parallel,\omega_n)=\frac{1}{i\omega_n-E(\mathbf{k})+\mu-\Sigma_c(\mathbf{k}_\parallel,\omega_n)}. \tag{8}$$

Here μ is the chemical potential, which is related to the electron density n_e as

$$n_e=\frac{2T}{a^2N^2}\sum_{\mathbf{k}_\parallel}\sum_{\omega_n>0}\mathrm{Re}\,G(\mathbf{k}_\parallel,\omega_n)+\frac{1}{2}; \tag{9}$$

$$\Sigma_c(\mathbf{k}_\parallel,\omega)=-\frac{T}{a^2N^2}\sum_{\omega_n'}\sum_{\mathbf{k}_\parallel'}\tilde{V}_c(\mathbf{k}_\parallel-\mathbf{k}_\parallel',\omega_n-\omega_n') \times G(\mathbf{k}_\parallel',\omega_n')\Gamma_c(\mathbf{k}_\parallel,\omega_n;\mathbf{k}_\parallel',\omega_n') \tag{10}$$

is the Coulomb part of the self-energy of the electrons,

$$\tilde{V}_c(\mathbf{q}_\parallel,\nu_n)=\left\langle\frac{V_c(\mathbf{q})}{\varepsilon_\infty+V_c(\mathbf{q})\tilde{\Pi}_e(\mathbf{q}_\parallel,\nu_n)}\right\rangle_\perp \tag{11}$$

is the matrix element of the screened Coulomb interaction in the layered crystal, averaged over the transverse momentum q_z.

We note that expression (3) for $V_c(\mathbf{q})$ corresponds to the long-wavelength approximation, when $qa\ll 1$ (for $a\ll c$). In order to carry out calculations over the whole volume of the Brillouin zone, it is necessary, strictly speaking, to use the Bloch electronic functions, so that for $q\approx\pi/a$ the Coulomb matrix element (11) should depend not only on the momentum transfer $\mathbf{q}=\mathbf{k}-\mathbf{k}'$ but also on the electron momenta $\mathbf{k}$ and $\mathbf{k}'$. However, it can be shown that the corrections to (3) due to the periodic Bloch factors are comparatively small for $q<\pi/a$.

To calculate the Coulomb vertex Γ_c we use the Nambu approximation:[38,39]

$$\Gamma_c(\mathbf{k}_\parallel,\omega_n;\mathbf{q}_\parallel,\nu_m)=\frac{1}{2}[Z_c(\mathbf{k}_\parallel+\mathbf{q}_\parallel,\omega_n+\nu_m)+Z_c(\mathbf{k}_\parallel,\omega_n)], \tag{12}$$

which satisfies the Ward identities[40] at $q\to 0$ for a charged Fermi liquid. Here Z_c is the Coulomb renormalization factor of the electron spectrum with allowance for retardation effects in the electron–plasmon interaction:

$$Z_c(\mathbf{k}_\parallel,\omega_n)=1-\frac{\mathrm{Im}\,\Sigma_c(\mathbf{k}_\parallel,\omega_n)}{\omega_n}. \tag{13}$$

The system of equations (7)–(13) was solved by an iterative method using a fast Fourier decomposition on a lattice containing $N\times N$ points in a 2D Brillouin zone ($N=64$) and up to 2048 points on the imaginary frequency axis, with a subsequent analytical continuation to the real-ω axis with the use of multipoint Padé approximants.

As the initial spectrum $E(\mathbf{k}_\parallel)$ in (8) we chose the upper branch $E_-(\mathbf{k}_\parallel)$ of the empirical spectrum (1), the saddles of which lie near the Fermi level (Fig. 1b). The existence of a second branch, $E_+(\mathbf{k}_\parallel)$ in this spectrum and the associated virtual interband electronic transitions were taken into account by introducing a parameter $\varepsilon_\infty>1$ in expression (2). According to the data of optical experiments,[41] the quantity ε_∞ in cuprate MOC crystals is anisotropic, and in the long-wavelength limit lies in the interval $\varepsilon_\infty\approx 4$–$8$. However, the value of ε_∞ should decrease with increasing momentum on account of spatial dispersion effects. Therefore, for the effective value of ε_∞ to use in the calculations below we chose the minimum value $\varepsilon_\infty=4$. It should be noted that the renormalized one-electron spectrum $\tilde{E}_-(\mathbf{k}_\parallel)$ shown by the dashed curve in Fig. 1b differs relatively little from the initial spectrum, and so the use of the latter as the ''bare'' dispersion relation is justified.

Figure 3 shows the results of the numerical calculations of the momentum dependence of the static polarization operator, obtained using spectrum (1b) in the framework of a self-consistent solution of the system of equations (7)–(13) under the condition that the Fermi level lies near the bottom of the saddles (solid curve) and obtained in the RPA for this same spectrum (dashed curve), and also that for a simple band with the spectrum $E(\mathbf{k}_\parallel)=E_0(\cos k_x a+\cos k_y a)$ (dotted curve). We see that in the first two cases there are pronounced maxima of the static polarization operator in the region of low momentum transfers $\mathbf{q}_\parallel$, whereas in the last case there is a broad maximum at the Γ point of the Brillouin zone.

Figure 4 shows the momentum dependence of the matrix element of the static screened Coulomb repulsion (11) for the empirical spectrum (1b) in the self-consistent approach (solid curve) and in the RPA (dashed curve), and the corresponding dependence for a simple band (dotted curve). We see that a substantial weakening of the Coulomb repulsion occurs in the region of small $q_\parallel$ (in comparison with the case of a wide 2D band). This effect is a consequence of the Kramers–

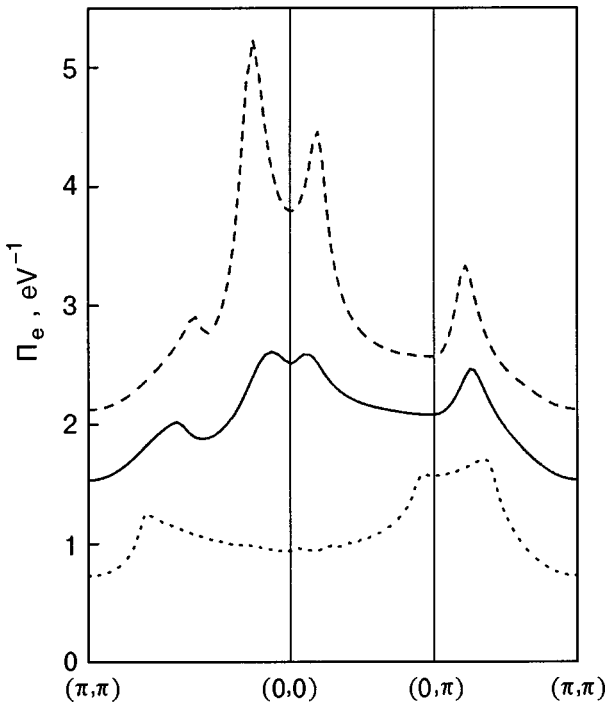

FIG. 3. Momentum dependence of the static polarization operator along the principal symmetry directions of the Brillouin zone; calculated in the RPA (dashed curve) and with allowance for many-particle Coulomb correlations (solid curve) on the basis of the empirical spectrum (1b) for $\varepsilon_\infty=4$ and at the optimum hole concentration, which corresponds to coincidence of the Fermi level with the position of a Van Hove singularity in the renormalized spectrum. The dashed curve shows the polarization operator calculated in the RPA for a simple 2D band 2 eV wide at the same hole concentration.

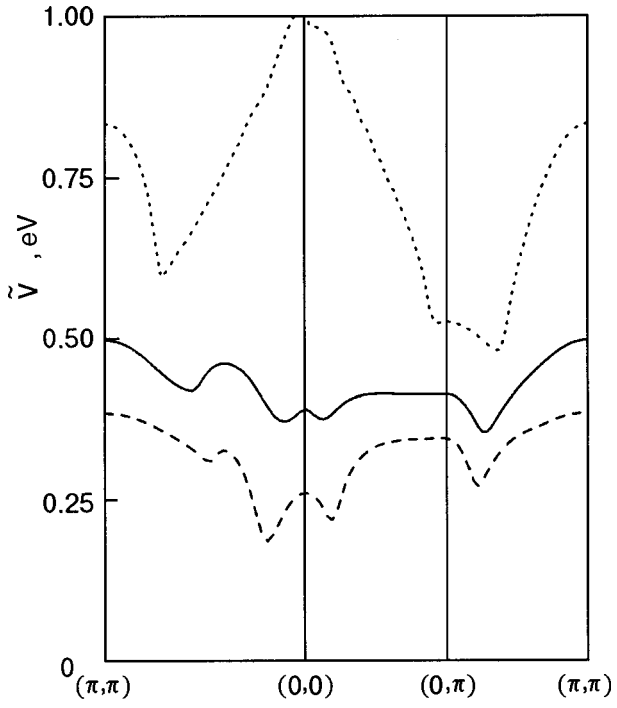

FIG. 4. Momentum dependence of the q_z-averaged matrix element of the static screened Coulomb repulsion along the principal symmetry directions of the Brillouin zone; calculated in the RPA (dashed curve) and with allowance for many-particle Coulomb correlations (solid curve) on the basis of the empirical spectrum (1b), and also in the RPA for a simple 2D band (dotted curve) for the same parameters as in Fig. 3.

Kronig relation (6) and is due to the retarded electron–plasmon interaction of the current carriers with collective electron-density excitations that exist in the long-wavelength region on account of the anisotropy of the band spectrum due to the extended saddles and which are manifested in the form a low-frequency peak in the spectral function of the charge-density fluctuations (Fig. 2).

We shall show below that the suppression of the Coulomb repulsion at small momentum transfers in combination with the strong anisotropy of the band spectrum and the electronic density of states leads to an effective attraction between electrons in the *d*-wave Cooper channel which is substantially enhanced on account of many-particle Coulomb correlations.

4. EQUATION FOR AN ANISOTROPIC SUPERCONDUCTING GAP AND THE MECHANISM OF *d*-WAVE COOPER PAIRING

Let us start from the standard theory of superconductivity, including the electron–phonon and electron–plasmon interactions and the Coulomb repulsion in the strong-coupling approximation.[42] In what follows we shall take into account only the normal Γ_c and anomalous $\tilde{\Gamma}_c$ Coulomb vertices, assuming for simplicity that the normal phonon vertex $\Gamma_{\rm ph}\approx 1$.

In this approximation the linearized (for $T\to T_c$) equation for the anomalous self-energy part Σ_2 at the Fermi surface with allowance for the Kramers–Kronig relation (5) takes the form

$$\Sigma_2(\mathbf{k}_\parallel,0)=-\int\frac{d^2k'_\parallel}{(2\pi)^2}\int_{-\infty}^{\infty}\frac{d\omega}{2\pi}\,\mathrm{Im}\times\left\{\frac{\Sigma_2(\mathbf{k}'_\parallel,\omega)}{\omega^2Z^2(\mathbf{k}'_\parallel,\omega)-\xi^2(\mathbf{k}'_\parallel)+i\eta}\right\}\times\left[\int_0^\infty d\Omega\left\{[\langle g^2_{\rm ph}(\mathbf{k},\mathbf{k}')\rangle_\perp S_{\rm ph}(\Omega)+\langle V_c(\mathbf{k}-\mathbf{k}')S_{\rm pl}(\mathbf{k}-\mathbf{k}',\Omega)\rangle_\perp\Gamma_c^2(\mathbf{k}'_\parallel,\omega;\mathbf{k}_\parallel-\mathbf{k}'_\parallel,\Omega)]\left(\frac{\tanh(\omega/2T_c)+\coth(\Omega/2T_c)}{\Omega+\omega-i\eta}+\frac{\tanh(\omega/2T_c)-\coth(\Omega/2T_c)}{\Omega-\omega+i\eta}\right)-\langle V_c(\mathbf{k}-\mathbf{k}')\rangle_\perp\Gamma_c^2(\mathbf{k}'_\parallel,\omega;\mathbf{k}_\parallel-\mathbf{k}'_\parallel,\Omega)\tanh\frac{\omega}{2T_c}\right\}\right]. \tag{14}$$

Here Z is the total renormalization factor with allowance for the electron–phonon and electron–plasmon interactions, $\xi(\mathbf{k}_\parallel)$ is the electron energy measured from the Fermi level, the angle brackets $\langle\ldots\rangle_\perp$ denote averaging over q_z, and the square of the normal Coulomb vertex Γ_c arises because on the right-hand side of (14) the contribution of the anomalous Coulomb vertex $\tilde{\Gamma}_c$ is taken into account to first order in Σ_2 (see Ref. 43).

Since the Fermi energy in cuprate MOCs is low ($E\approx 0.2$–0.3 eV), the width of the electron–electron repulsion region due to the electron–phonon and electron–plasmon in-

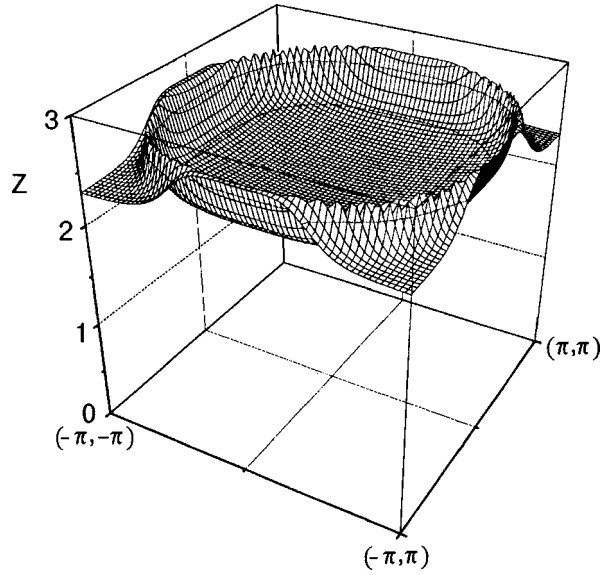

FIG. 5. Momentum dependence of the Coulomb renormalization factor $Z_c(\mathbf{k}_\parallel)$ in the static approximation within the first Brillouin zone, calculated with allowance for many-particle Coulomb correlations on the basis of the empirical spectrum (1b) for the same parameters as in Figs. 3 and 4. The maximum values of the function $Z_c(\mathbf{k}_\parallel)$ are reached at $\mathbf{k}_\parallel=\mathbf{k}_F$.

teractions is comparable to E_F, so that the frequency dependence of Σ_2, Z, and Γ_c in the integrand in (14) can be neglected. On the other hand, as numerical calculations have shown, in the static approximation ($\omega=0$) the momentum dependence of $Z(\mathbf{k}_\parallel,0)$ and $\Gamma_c(\mathbf{k}_\parallel 0;\mathbf{q}_\parallel,0)$ is comparatively weak.

Figure 5 shows the momentum dependence of the Coulomb part of the renormalization factor $Z_c(\mathbf{k}_\parallel,0)$ in the first Brillouin zone, and Fig. 6a shows the result of a calculation in the Nambu approximation (12) for the dependence of $\Gamma_c(\mathbf{k}_\parallel,0;\mathbf{q}_\parallel,0)$ on $\mathbf{q}_\parallel$ for $k_x=k_y$ and $k=k_F$. The numerical calculations of Z_c and Γ_c were done for the same position of the Fermi level as for the calculations of Π_e and $\tilde{V}_c$ in Figs. 3 and 4.

For comparison, Fig. 6b shows the analogous dependence for the quantity $1+\Gamma_c^{(1)}$, where $\Gamma_c^{(1)}$ is the first correction to the Coulomb vertex function in renormalized perturbation theory:

$$\Gamma_c^{(1)}=(\mathbf{k}_\parallel,\omega_n;\mathbf{q}_\parallel,\nu_m)$$
$$=\frac{T}{a^2N^2}\sum_{\omega_n'}\sum_{\mathbf{k}_\parallel'}\tilde{V}_c(\mathbf{k}_\parallel-\mathbf{k}_\parallel',\omega_n-\omega_n')$$
$$\times G(\mathbf{k}_\parallel'+\mathbf{q}_\parallel,\omega_n'+\nu_m)G(\mathbf{k}_\parallel',\omega_n'). \qquad (15)$$

We see that both approaches — the Nambu approximation (12) and taking the first correction (15) into account — lead to similar momentum dependence of $\Gamma_c(\mathbf{k}_\parallel,0;\mathbf{q}_\parallel,0)$ with almost the same mean values $\overline{\Gamma}_c$, possibly indicating a rather rapid convergence of the diagram series for Γ_c.

As follows from Figs. 5 and 6, the amplitudes of the variation of Z_c and Γ_c do not exceed 10%. Therefore, we can to good accuracy replace Z_c and Γ_c in Eq. (14) by their mean values $\overline{Z}_c$ and $\overline{\Gamma}_c$. The mean value $\overline{Z}$ in this case can be written in the form

$$\overline{Z}=1+\overline{\lambda}_{\rm ph}+\overline{\lambda}_{\rm pl}. \qquad (16)$$

Here $\overline{\lambda}_{\rm ph}$ and $\overline{\lambda}_{\rm pl}$ are the averaged dimensionless coupling constants in the isotropic s channel:

$$\overline{\lambda}_{\rm ph(pl)}$$
$$=\frac{\int\frac{d^2k_\parallel}{(2\pi)^2}\delta(\tilde{\xi}(\mathbf{k}_\parallel))\int\frac{d^2k_\parallel'}{(2\pi)^2}\delta(\tilde{\xi}(\mathbf{k}_\parallel'))W_{\rm ph(pl)}(\mathbf{k}_\parallel,\mathbf{k}_\parallel')}{\int\frac{d^2k_\parallel}{(2\pi)^2}\delta(\tilde{\xi}(\mathbf{k}_\parallel))}, \qquad (17)$$

where $W_{\rm ph}$ and $W_{\rm pl}$ are the anisotropic matrix elements of the electron–phonon and electron–plasmon interactions,

$$W_{\rm ph}(\mathbf{k}_\parallel,\mathbf{k}_\parallel')=2\int_0^\infty\frac{d\Omega}{\Omega}\langle g_{\rm ph}^2(\mathbf{k}_\parallel,\mathbf{k}_\parallel')\rangle_\perp S_{\rm ph}(\Omega); \qquad (18)$$

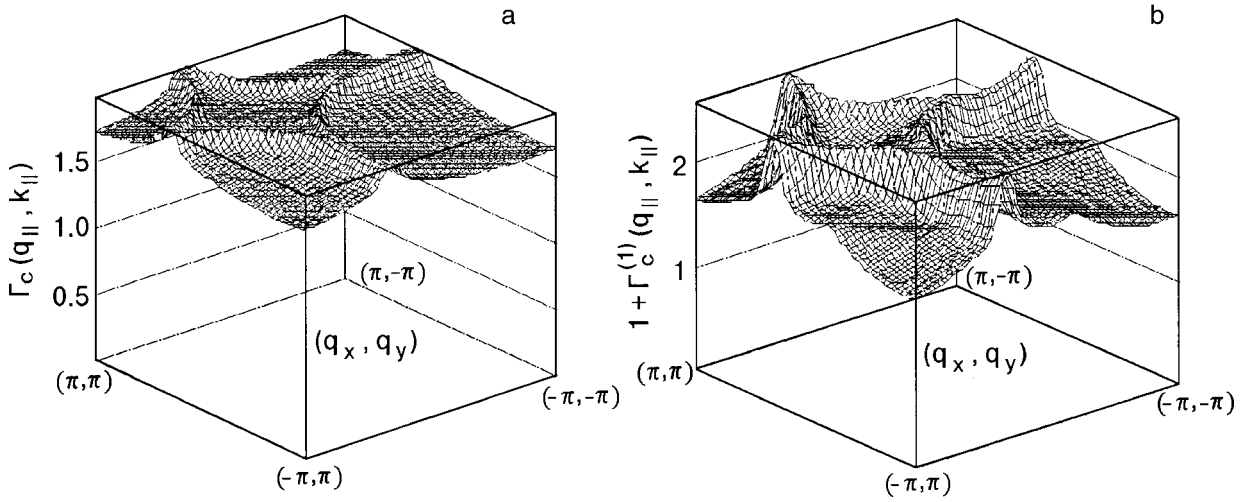

FIG. 6. Dependence of the Coulomb vertex function $\Gamma_c(\mathbf{k}_\parallel,\mathbf{q}_\parallel)$ on $\mathbf{q}$ for $k_x=k_y$, $k=k_F$ in the static approximation in the framework of the Nambu approach (12) (a) and with allowance for the first correction $\Gamma_c^{(1)}(\mathbf{k}_\parallel,\mathbf{q}_\parallel)$ (b).

$$W_{\rm pl}(\mathbf{k}_\parallel,\mathbf{k}'_\parallel)=2\int_0^\infty\frac{d\omega}{\omega}\langle V_c(\mathbf{k}_\parallel-\mathbf{k}'_\parallel)S_{\rm ph}(\mathbf{k}_\parallel-\mathbf{k}'_\parallel,\omega)\rangle_\perp\overline{\Gamma}_c^2, \tag{19}$$

and $\tilde{\xi}(\mathbf{k}_\parallel)=\xi(\mathbf{k}_\parallel)/\overline{Z}$ is the renormalized electron energy.

On the other hand, by virtue of relation (12) we can set

$$\overline{\Gamma}_c=\overline{Z}_c\equiv(1+\overline{\lambda}_{\rm pl}). \tag{20}$$

The calculations that were done give the value $\overline{\Gamma}_c=\overline{Z}_c\approx 2.3$, which corresponds to an averaged electron–plasmon interaction constant $\overline{\lambda}_{\rm pl}\approx 1.3$.

If it is assumed that the main contribution to the integral over Ω in (14) comes from the phonon and plasmon modes in the spectral functions $S_{\rm ph}(\Omega)$ and $S_{\rm pl}(\mathbf{q},\Omega)$ with frequencies $\Omega\gg T_c$, then the quantity $\omega\sim T_c$ in the denominators $(\Omega\pm\omega\mp i\eta)$ can be neglected in comparison with Ω. As a result, on doing the integration over ω in (14), bypassing the pole at the point $\omega=\tilde{\xi}(\mathbf{k}'_\parallel)$, and then changing from integration over $\mathbf{k}'_\parallel$ to integration over $\tilde{\xi}$ and over the azimuthal angle φ' between $\mathbf{k}'_\parallel$ on the Fermi surface and the direction of one of the crystallographic axes (a or b) in the plane of the layers, with the help of the static Kramers–Kronig relation (6) we arrive at an equation for the anisotropic gap at the Fermi surface as a function of the angle φ between $\mathbf{k}_\parallel$ and the a (or b) axis:

$$\begin{aligned}\overline{Z}\Delta(\varphi)=\frac{1}{2}\int_0^{2\pi}\frac{d\varphi'}{2\pi}\Delta(\varphi')\int_{-\tilde{E}_F}^{\tilde{E}_F}\frac{d\tilde{\xi}}{\tilde{\xi}}\nu(\varphi',\tilde{\xi})\\ \times[W_{\rm ph}(\varphi,\varphi')\theta(\tilde{\omega}_{\rm ph}-|\tilde{\xi}|)\\ -\tilde{V}_c(\varphi,\varphi')\overline{\Gamma}_c^2]\tanh\frac{\tilde{\xi}}{2T_c},\end{aligned} \tag{21}$$

where $\Delta(\varphi)\equiv\Delta(\mathbf{k}_F(\varphi))\equiv\Sigma_2(\mathbf{k}_F(\varphi),0)/\overline{Z}$ is the renormalized superconducting gap, $\nu(\varphi',\tilde{\xi})$ is the angle- and energy-dependent electronic density of states, $\tilde{E}_F$ and $\tilde{\omega}_{\rm ph}$ are the renormalized values of the Fermi energy and the limiting frequency of the phonon spectrum, $\theta(x)$ is the Heaviside step (theta) function, and $\tilde{V}_c(\varphi,\varphi')$ is the q_z-averaged matrix element (11) of the static Coulomb repulsion at the Fermi surface:

$$\tilde{V}_c(\varphi,\varphi')\equiv\tilde{V}_c(|\mathbf{k}_F(\varphi)-\mathbf{k}_F(\varphi')|)=\left\langle\frac{V_c(|\mathbf{k}_F(\varphi)-\mathbf{k}_F(\varphi')|;q_z)}{\varepsilon_\infty+V_c(|\mathbf{k}_F(\varphi)-\mathbf{k}_F(\varphi')|;q_z)\tilde{\Pi}_e(|\mathbf{k}_F(\varphi)-\mathbf{k}_F(\varphi')|,0)}\right\rangle_\perp. \tag{22}$$

Thus the character of the anisotropy of the electron–electron Coulomb interaction is largely determined by the momentum dependence of the static polarization operator, which for $T\neq 0$ is given by the expression

$$\begin{aligned}\tilde{\Pi}_e(\mathbf{q}_\parallel,0)=2\int\frac{d^2k_\parallel}{(2\pi)^2}\frac{f_F(\xi(\mathbf{k}_\parallel-\mathbf{q}_\parallel))-f_F(\xi(\mathbf{k}_\parallel))}{\xi(\mathbf{k}_\parallel)-\xi(\mathbf{k}_\parallel-\mathbf{q}_\parallel)}\\ \times\frac{\Gamma_c(\mathbf{k}_\parallel,\xi(\mathbf{k}_\parallel);\mathbf{k}_\parallel-\mathbf{q}_\parallel,\xi(\mathbf{k}_\parallel))}{Z(\mathbf{k}_\parallel,\xi(\mathbf{k}_\parallel))Z(\mathbf{k}_\parallel-\mathbf{q}_\parallel,\xi(\mathbf{k}_\parallel))}.\end{aligned} \tag{23}$$

We call attention to the circumstance that the integrand in (23) contains a function of two variables,

$$F(\xi(\mathbf{k}_\parallel),\xi(\mathbf{k}_\parallel-\mathbf{q}_\parallel))=\frac{f_F(\xi(\mathbf{k}_\parallel-\mathbf{q}_\parallel))-f_F(\xi(\mathbf{k}_\parallel))}{\xi(\mathbf{k}_\parallel)-\xi(\mathbf{k}_\parallel-\mathbf{q}_\parallel)}, \tag{24}$$

which has a sharp maximum at $\xi(\mathbf{k}_\parallel)=\xi(\mathbf{k}_\parallel-\mathbf{q}_\parallel)=0$, where it has the value $F(0,0)=1/4T$ (Fig. 7). Therefore, at sufficiently low values of T the functions Γ_c and Z, which are comparatively smooth with respect to $\xi(\mathbf{k}_\parallel)$, can to good accuracy be taken out from under the integral sign at the point $\xi(\mathbf{k}_\parallel)=0$ and for $\mathbf{k}_\parallel=(\mathbf{k}_\parallel-\mathbf{q}_\parallel)=\mathbf{k}_F$. When the relatively weak momentum dependence of the static functions Γ_c and Z (see Figs. 5 and 6) is also taken into account, expression (23) can be written approximately in the form

$$\tilde{\Pi}_e(\mathbf{q}_\parallel,0)\cong\Pi_e(\mathbf{q}_\parallel,0)\overline{\Gamma}_c/\overline{Z}^2, \tag{25}$$

where $\Pi_e(\mathbf{q}_\parallel,0)$ is the static polarization operator calculated in the RPA (see Fig. 3).

We note that because of the anomalously high density of states in the region of the extended saddles, the value of the static polarization operator may be so large that the condition $V_c(\mathbf{q})\tilde{\Pi}_e(\mathbf{q}_\parallel,0)\gg\varepsilon_\infty$ holds in the entire volume of the Brillouin zone, so that we can to good accuracy set

$$\tilde{V}_c(\mathbf{q}_\parallel)\approx 1/\tilde{\Pi}_e(\mathbf{q}_\parallel,0)\approx\overline{Z}^2/\Pi_e(\mathbf{q}_\parallel,0)\overline{\Gamma}_c. \tag{26}$$

It follows that in Eq. (21), in addition to the weakening of the electron–phonon interaction on account of the renormalization of $\overline{Z}^{-1}$, in this case the Coulomb interaction is enhanced on account of the multiplicative factor $\overline{Z\Gamma}_c$.

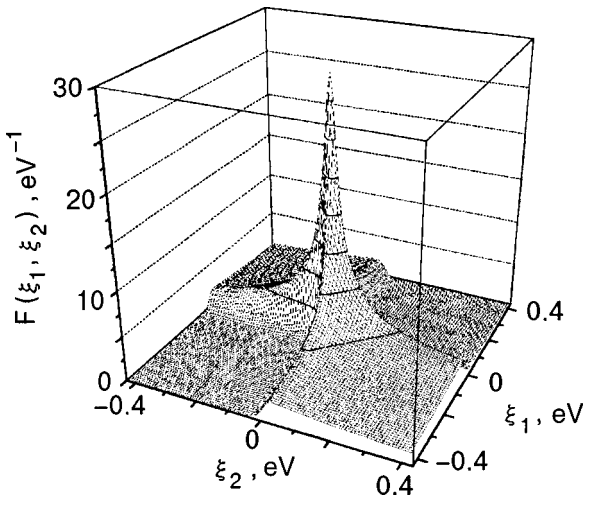

FIG. 7. Plot of the function $F(\xi_1,\xi_2)$ (see Eq. (24)) in the integrand for the static polarization operator (23) versus ξ_1 and ξ_2 at $T=100$ K.

5. CRITICAL TEMPERATURE AND ISOTOPE EFFECT

The critical temperature of the superconducting transition is determined by the eigenvalues of the linearized integral equation for the gap (26), which can be written

$$\Delta(\varphi)=\int_0^{2\pi}\frac{d\varphi}{2\pi}K(T_c;\varphi,\varphi')\Delta(\varphi'), \tag{27}$$

where

$$K(T_c,\varphi,\varphi')=\frac{1}{2\bar{Z}}\int_{-\tilde{E}_F}^{\tilde{E}_F}\frac{d\tilde{\xi}}{\tilde{\xi}}\tanh\frac{\tilde{\xi}}{2T_c}\,\nu(\varphi',\tilde{\xi})\times[W_{\rm ph}(\varphi,\varphi')\,\theta(\tilde{\omega}_{\rm ph}-|\tilde{\xi}|)-\tilde{V}_c(\varphi,\varphi')\bar{\Gamma}_c^2]. \tag{28}$$

Neglecting the energy dependence of the density of states, we write the anisotropic kernel of (28) in the form

$$K(T_c,\varphi,\varphi')=\frac{1}{\bar{Z}}\left[\Lambda_{\rm ph}(\varphi,\varphi')\ln\frac{2\gamma\tilde{\omega}_{\rm ph}}{\pi T_c}+\Lambda_c(\varphi,\varphi')\ln\frac{2\gamma\tilde{E}_F}{\pi T_c}\right], \tag{29}$$

where

$$\Lambda_{\rm ph}(\varphi,\varphi')=\nu(\varphi',0)W_{\rm ph}(\varphi,\varphi');\qquad \Gamma_c(\varphi,\varphi')=-\nu(\varphi',0)\tilde{V}_c(\varphi,\varphi')\bar{\Gamma}_c^2; \tag{30}$$

and γ is the Euler constant ($\gamma\approx1.78$).

Following Ref. 17, we shall solve equation (27) by expanding the kernel $K(T_c,\varphi,\varphi')$ and the gap $\Delta(\varphi)$ in Fourier series in φ and φ'. In this case we shall for simplicity approximate the anisotropic density of states in (30) by an expression that reflects the C_{4v} symmetry of the electronic spectrum in the plane of the 2D layers:

$$\nu(\varphi,0)=\frac{\nu_1}{2}(1+\cos4\varphi)+\frac{\nu_2}{2}(1-\cos4\varphi),\quad \nu_1>\nu_2. \tag{31}$$

We note that the values of the parameters ν_1 and ν_2 depend on the position of the Fermi level relative to the bottom of the saddles.

Since the explicit form of the matrix element of the electron–phonon interaction is unknown, let us first calculate T_c without taking into account the phonon term in (29). In that case a numerical solution shows that the maximum critical temperature is reached for a gap that transforms according to the irreducible representation B_1 of the group C_{4v}:

$$\Delta(\varphi)=\sum_{n=1}^{\infty}a_{4n-2}\cos(4n-2)\varphi. \tag{32}$$

This corresponds to $d_{x^2-y^2}$-wave symmetry of the superconducting order parameter, while the dimensionless electron–plasmon interaction constant in the d-wave channel, $\lambda_{\rm pl}^d$, is determined by the maximum positive eigenvalue of the anisotropic Coulomb kernel $\Lambda_c(\varphi,\varphi')$.

Figure 8 shows the dependence of the constant $\lambda_{\rm pl}^d$ on the reduced concentration x of the doped current carriers (holes) for $\varepsilon_\infty=4$ and for two values of the averaged electron–phonon interaction constant $\bar{\lambda}_{\rm ph}$, which enters into the renormalization factor $\bar{Z}$ in (25) and, hence, into the Coulomb kernel $\Lambda_c(\varphi,\varphi')$. The maximum value of $\lambda_{\rm pl}^d$ is reached at $x=x_0$, which corresponds to coincidence of the Fermi level with a Van Hove singularity in the quasiparticle density of states.

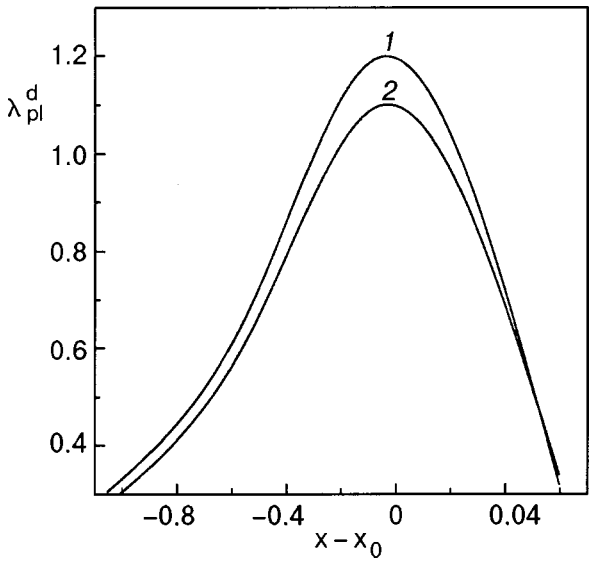

FIG. 8. Dimensionless electron–plasmon interaction constant in the d channel, $\lambda_{\rm pl}^d$, as a function of x for $\bar{\lambda}_{\rm ph}=0.5$ (*1*) and 0.8 (*2*), with $\varepsilon_\infty=4$ and $\bar{\lambda}_{\rm pl}=1.3$.

To estimate the contribution of the anisotropy electron–phonon interaction component responsible for the $d_{x^2-y^2}$ symmetry of the gap, we introduce a constant $\lambda_{\rm ph}^d$, the value of which ($\lambda_{\rm ph}^d=0.2$–0.3) is chosen in accordance with the electron–phonon interaction model considered in Ref. 44.

In this approximation the critical temperature for the transition to a superconducting state with d-wave symmetry of the gap is given, with allowance for (29), by the expression

$$T_c\approx E_F^{\lambda_{\rm pl}^d/\lambda_d}\tilde{\omega}_{\rm ph}^{\lambda_{\rm ph}^d/\lambda_d}\exp\left(-\frac{1+\bar{\lambda}_{\rm pl}+\bar{\lambda}_{\rm ph}}{\lambda_d}\right),\qquad \lambda_d=\lambda_{\rm ph}^d+\lambda_{\rm pl}^d. \tag{33}$$

Figure 9 shows the curves of T_c versus x for various values of the electron–phonon interaction constants for $\varepsilon_\infty=4$; the curves are in qualitative agreement with the experimental data for cuprate MOCs. It follows from the results that a weak isotropic electron–phonon interaction with $\bar{\lambda}_{\rm ph}\leqslant0.5$ has practically no effect on the maximum value of T_c, whereas for values of $\bar{\lambda}_{\rm ph}$ comparable to $\bar{\lambda}_{\rm pl}$ there occurs an appreciable suppression of T_c in the d-wave Cooper channel owing to strong-coupling effects, which determine the value of the renormalization factor $(1+\bar{\lambda}_{\rm pl}+\bar{\lambda}_{\rm ph})$ in (33).

Finally, Figure 10 shows the curves of the isotope-effect exponent $\alpha\equiv(1/2)\partial\ln T_c/\partial\ln\tilde{\omega}_{\rm ph}=(1/2)\lambda_{\rm ph}^d/(\lambda_{\rm pl}^d+\lambda_{\rm ph}^d)$ as a function of x for $\varepsilon_\infty=4$ for the same nonzero values of the electron–phonon interaction constant as in Fig. 9. These curves demonstrate the tendency for α to decrease with increasing T_c, a finding which is also in agreement with the

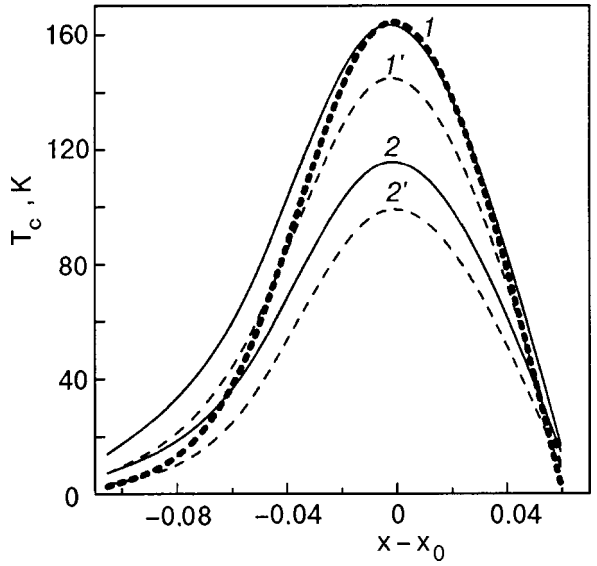

FIG. 9. Curves of T_c versus x for various values of the electron–phonon interaction constant, with $\varepsilon_\infty = 4$ and $\bar{\lambda}_{pl} = 1.3$. Curves *1* and *1′* correspond to $\bar{\lambda}_{ph} = 0.5$ for $\lambda^d_{ph} = 0.3$ and 0.2, and curves *2* and *2′* to $\bar{\lambda}_{ph} = 0.8$ for $\lambda^d_{ph} = 0.3$ and 0.2. The heavy dotted curve shows the dependence of T_c on x in the absence of electron–phonon interaction ($\bar{\lambda}_{ph} = \lambda^d_{ph} = 0$).

available experimental data on the change in T_c and α upon the substitution of the oxygen isotope ^{18}O for ^{16}O (Refs. 45 and 46).

6. CONCLUSION

To sum up, in this paper we have shown that because of the presence of extended saddles in the quasi-2D band spectrum of 2D cuprate layers in MOC crystals, damped (overdamped) long-wavelength electron-density oscillations with an acoustical dispersion relation appear in their collective electronic spectrum. The interaction of the current carriers with these excitations is manifested in the suppression of the screened Coulomb repulsion in the region of small momentum transfers and, as a result, in the appearance of an effective attraction between quasiparticles in the *d*-wave Cooper channel. We have also demonstrated that in the framework of the charge-fluctuation (plasmon) mechanism of HTSC considered here, it is necessary to take the Coulomb vertex functions into account for correct estimation of the superconducting transition temperature T_c. With the aid of a numerical solution of the integral equation for an anisotropic superconducting order parameter with $d_{x^2-y^2}$ symmetry in the strong-coupling approximation, we have shown that the many-particle Coulomb correlations of the local-field-effects type, which are described by Coulomb vertices Γ_c, lead to a substantial enhancement of the electron–electron attraction in the *d*-wave channel. At the optimum doping level for cuprate MOCs, when the Fermi level coincides with the position of a Van Hove singularity, the values of T_c can exceed 100 K, and, if the anisotropic electron–phonon interaction is also taken into account, one can describe the weak oxygen isotope effect in HTSC materials.

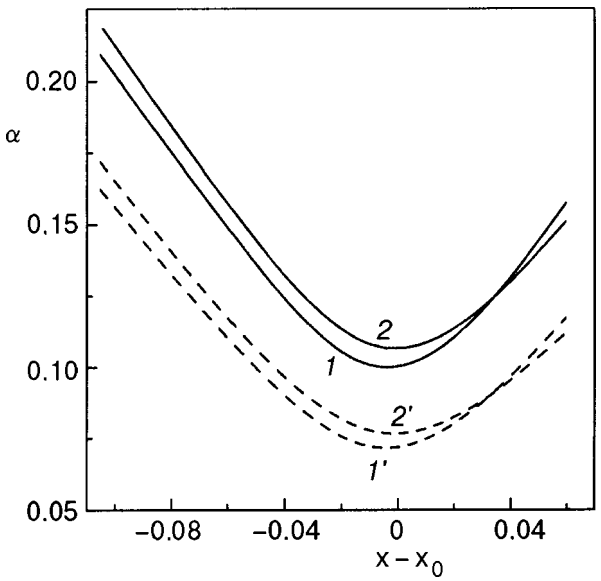

FIG. 10. Isotope-effect exponent α as a function of x for the parameters corresponding to curves *1*, *1′*, *2*, and *2′* in Fig. 9.

In closing we thank B. I. Al'tshuler, V. M. Loktev, and A. V. Semenov for helpful discussions.

*E-mail: pashitsk@iop.kiev.ua

[1] D. A. Wollman, D. J. Van Harlingen, W. C. Lee, D. M. Ginsberg, and A. J. Leggett, Phys. Rev. Lett. **71**, 2134 (1993).
[2] I. Iguchi and Z. Wan, Phys. Rev. B **49**, 12388 (1994).
[3] D. A. Browner and H. R. Ott, Phys. Rev. B **50**, 6530 (1994).
[4] D. A. Wollman, D. J. Van Harlingen, J. Giapintzakis, and D. M. Ginsberg, Phys. Rev. Lett. **74**, 797 (1995).
[5] S. S. Tsuei, J. R. Kirtley, C. C. Chi, Lock See Yu-Jahnes, A. Gupta, T. Shaw, J. Z. Sem, and M. B. Ketchen, Phys. Rev. Lett. **73**, 593 (1994).
[6] J. R. Kirtley, S. S. Tsuei, M. Rupp, J. Z. Sun, L. S. Yu.-Jahnes, A. Gupta, M. B. Ketchen, K. A. Moler, and M. Bhushan, Phys. Rev. Lett. **76**, 1336 (1996).
[7] C. C. Tsuei, J. R. Kirtley, Z. F. Ren *et al.*, Nature (London) **387**, 481 (1997).
[8] M. R. Norman, M. Randeria, H. Ding, J. C. Campuzano, and A. F. Bellman, Phys. Rev. B **52**, 15107 (1995).
[9] H. Ding, M. R. Norman, J. C. Campuzano, M. Randeria, A. F. Bellman, T. Yokoya, T. Takahashi, T. Mochiku, and K. Kadowaki, Phys. Rev. B **54**, R9678 (1996).
[10] D. J. Scalapino, E. Loh, and J. E. Hirsch, Phys. Rev. B **35**, 6694 (1987).
[11] N. E. Bickers, R. T. Scalettar, and D. J. Scalapino, Int. J. Mod. Phys. B **1**, 687 (1987).
[12] A. J. Millis, H. Monien, and D. Pines, Phys. Rev. B **42**, 167 (1990).
[13] T. Moriya, Y. Takahashi, and K. Ueda, J. Phys. Soc. Jpn. **59**, 1905 (1990).
[14] P. Monthoux, A. V. Balatsky, and D. Pines, Phys. Rev. B **46**, 14803 (1992).
[15] P. Monthoux and D. Pines, Phys. Rev. B **47**, 6069 (1993).
[16] P. Monthoux and D. J. Scalapino, Phys. Rev. Lett. **72**, 1874 (1999).
[17] D. Pines, J. Phys. **20**, 535 (1998).
[18] A. I. Liechtenstein, O. Gunnarsson, O. K. Andersen, and R. M. Martin, Phys. Rev. B **54**, 12505 (1996).
[19] C.-H. Pao and N. E. Bickers, Phys. Rev. Lett. **72**, 1870 (1994).
[20] E. A. Pashitskii, V. I. Pentegov, A. V. Semenov, and E. Abraham, Int. J. Mod. Phys. B **12**, 2946 (1998).
[21] A. V. Semenov, Int. J. Mod. Phys. B **12**, 3141 (1998); in *Symmetry and Pairing in Superconductors*, Vol. 63 of NATO Science Series, Kluwer Academic Publishers (1999), p. 101.
[22] E. A. Pashitskii, V. I. Pentegov, and A. V. Semenov, in *Symmetry and Pairing in Superconductors*, Vol. 63 of NATO Science Series, Kluwer Academic Publishers (1999), p. 121.
[23] É. A. Pashitskiĭ, V. I. Pentegov, A. V. Semenov, and É. Abrakham, JETP Lett. **69**, 753 (1999).
[24] D. S. Dessau, Z.-X. Shen, D. M. King, D. S. Marshall, L. W. Lombardo, P. H. Dickinson, A. G. Loeser, J. DiCarlo, C.-H. Park, A. Kapitulnik, and W. E. Spicer, Phys. Rev. Lett. **71**, 2781 (1993).

[25] A. A. Abrikosov, J. C. Campuzano, and V. Gofron, Physica C **214**, 73 (1993).
[26] D. M. King, Z.-X. Shen, and D. S. Dessau, Phys. Rev. Lett. **73**, 3298 (1994).
[27] K. Gofron, J. C. Campuzano, A. A. Abrikosov, M. Lindroos, A. Bansil, H. Ding, D. Koelling, and B. Dabrowski, Phys. Rev. Lett. **73**, 3302 (1994).
[28] M. C. Schabel, C.-H. Park, A. Matsuura *et al.*, Phys. Rev. B **57**, 6090 (1998).
[29] D. Pines, Can. J. Phys. **34**, 1379 (1956).
[30] D. Pines and J. R. Shrieffer, Phys. Rev. **124**, 1387 (1961).
[31] O. V. Konstantinov and V. I. Perel', Fiz. Tverd. Tela (Leningrad) **9**, 3061 (1967) [*sic*].
[32] É. A. Pashitskiĭ, Zh. Éksp. Teor. Fiz. **55**, 2387 (1968) [Sov. Phys. JETP **28**, 1267 (1969)].
[33] J. Ruvalds, Adv. Phys. **30**, 677 (1981).
[34] O. K. Andersen, O. Jensen, A. I. Liechtenstein, and I. I. Mazin, Phys. Rev. B **49**, 4145 (1994).
[35] A. Griffin and A. J. Pindor, Phys. Rev. B **39**, 11503 (1989).
[36] D. Pines and P. Nozières, *Theory of Quantum Liquids* [Benjamin, New York (1966); Mir, Moscow (1967)].
[37] V. L. Ginzburg and D. A. Kirzhnits (Eds.), *Problems of High-Temperature Superconductivity* [in Russian], Nauka, Moscow (1977).
[38] Y. Nambu, Phys. Rev. **117**, 648 (1960).
[39] Y. Takada, J. Phys. Chem. Solids **54**, 1779 (1993).
[40] J. M. Luttinger and J. C. Ward, Phys. Rev. **118**, 1417 (1960).
[41] T. Timusk, S. L. Herr, K. Kamaras, C. D. Porter, D. B. Tanner, D. A. Bonn, J. D. Garrett, C. V. Stager, J. E. Greedan, and M. Reedyk, Phys. Rev. B **38**, 6683 (1988).
[42] G. M. Éliashberg, Zh. Éksp. Teor. Fiz. **38**, 966 (1960) [Sov. Phys. JETP **11**, 696 (1960)]; **39**, 1437 (1960); **12**, 1000 (1961).
[43] O. Dolgov and E. G. Maksimov, Usp. Fiz. Nauk **138**, 95 (1982) [Sov. Phys. Usp. **25**, 688 (1982)]; O. V. Dolgov, D. A. Kirzhnits, and E. G. Maksimov, Rev. Mod. Phys. **53**, 81 (1981).
[44] A. Sherman, Phys. Rev. B **55**, 582 (1997).
[45] J. P. Franck, J. Jung, M. A.-K. Mohamed, S. Gygak, and G. I. Sproule, Phys. Rev. B **44**, 5317 (1991).
[46] H. J. Bornemann and D. E. Morris, Phys. Rev. B **44**, 5322 (1991).

Translated by Steve Torstveit

Equilibrium magnetic characteristics of high-T_c superconductors with allowance for the spatial distribution of the order parameter in the vortex cores. I. Equilibrium magnetization

L. G. Mamsurova,* K. S. Pigalskiy, and N. G. Trusevich

N. N. Semenov Institute of Chemical Physics, Russian Academy of Sciences, ul. Kosygina 4, 117977 Moscow, Russia

W. V. Pogosov

Moscow Institute of Physics and Technology, Institutskiĭ per. 7, 141700 Dolgoprudnyĭ, Moscow Region, Russia

(Submitted August 11, 2000)
Fiz. Nizk. Temp. **27**, 153–161 (February 2001)

An investigation is made into the accuracy of the theoretical description of the field dependence of the equilibrium magnetization $M(H)$ of type-II superconductors with Ginzburg–Landau parameters $\kappa \gg 1$ in various approximations for magnetic fields H much less than the upper critical field H_{c2}. It is found that taking the spatial distribution of the order parameter into account has a substantial effect on the behavior of the magnetization $M(H)$ even at the very lowest fields in the close vicinity of the lower critical field H_{c1}. The mechanisms through which and the degree to which the field dependence $M(H)$ is influenced by such factors as the self-energy of the vortex, the accuracy of description of the spatial distribution of the vortex field, the suppression of the order parameter due to the overlapping of the vortices, and the use of the principle of superposition of fields are investigated for fields in the interval $H_{c1} \leqslant H \ll H_{c2}$. In this field interval an analytical expression for $M(H)$ is obtained by direct evaluation of the lattice sums with allowance for the influence of the structure of the vortex cores. © *2001 American Institute of Physics.* [DOI: 10.1063/1.1353701]

INTRODUCTION

The problem of taking into account the effect of suppression of the order parameter in the vortex cores in calculating the equilibrium magnetization of type-II superconductors has been solved in various approximate approaches (see, e.g., Refs. 1–5). The most thorough discussion of this problem and of the question of the ''quantitative incorrectness'' of the widely used London approximation in the theory of superconductivity is found in Ref. 4.

Indeed, a simple analysis shows that there are several reasons for inaccuracy of the London approximation. The first of these stems from the impossibility of calculating the self-energy of a vortex in the framework of this approximation, particularly that which is due to the spatial variation of the order parameter (in the London approximation it is assumed that the modulus of the order parameter is constant outside the vortex cores, and the core itself is described by a two-dimensional δ function). The second cause of inaccuracy is the error in the calculation of the electromagnetic energy on account of the rather rough description of the spatial distribution of the field of an individual vortex (in the London model, in particular, the self-field of a flux line diverges on its axis). The third factor stems from the impossibility of taking into account the additional suppression of the order parameter due to overlapping of the vortices.

It is clear that in the case of high fields, when the density of vortices is large and their cores occupy an appreciable volume in comparison with the volume of the superconductor, the role of the factors listed above becomes important, and it is without a doubt necessary to use other models that take these circumstances into account. Foremost among these other models is the variational model of Hao, Clem *et al.*[3,4] (see also Ref. 6), which yielded a rather simple analytical expression for $M(H)$ that describes the experimental results well for almost all the known HTSC compounds over a wide range of magnetic fields, all the way up to the second critical field H_{c2} (Refs. 7–14).

It should be noted, however, that the problem set forth above has not been analyzed in detail in the region of small fields, just slightly above the first critical field H_{c1}. At the same time, in this field region, where the distance between vortices is still much larger than the size of the vortex cores, the statement made in Ref. 4 that the London approximation is quantitatively incorrect and that it is necessary to take into account the energy of the vortex cores in a calculation of the equilibrium magnetization is not so obvious. It is therefore of interest to ascertain the region of magnetic fields in which the influence of the structure of the vortex cores begins to have an appreciable effect on the behavior of the field dependence $M(H)$.

In this paper we do a systematic analysis of each of the factors mentioned above and assess the effect of taking them into account. This will make it possible to ascertain explicitly the mechanisms by which and the degree to which these factors influence the behavior of the equilibrium magnetization of type-II superconductors (for the case $\kappa \gg 1$) in the field region $H_{c1} \leqslant H \ll H_{c2}$.

We shall also show that the analytical expression for $M(H)$ obtained in Ref. 4 in the framework of a variational model gives a quantitatively inaccurate result in the low-field region. As compared to the London approximation or the approach of Ref. 4, we shall obtain (both numerically and analytically) a more accurate field dependence $M(H)$, taking into account the self-energy of the vortices and the influence of the structure of the vortex cores on the spatial distribution of the field of a vortex, i.e., the influence of those factors that are most important to take into account in the region of moderate fields.

CALCULATION AND ANALYSIS OF THE FIELD DEPENDENCE OF THE MAGNETIZATION, WITH THE SPATIAL DISTRIBUTION OF THE ORDER PARAMETER TAKEN INTO ACCOUNT TO VARYING DEGREES OF ACCURACY

In the field region $H \ll H_{c2}$ the distances between neighboring vortices in a regular lattice is much greater than the size of the vortex cores. For this reason the vortex state here can be represented as a system of individual interacting filaments. Here the self-energy of each filament, its field, and also the structure of the order parameter and its core are assumed to be the same as for an isolated filament (i.e., independent of the presence of other vortices).

As we know,[15] in this field region the Gibbs free energy of the vortex lattice (per unit volume) can be written in the form

$$G=\frac{B}{\Phi_0}\left(F_0+\sum_i F_{0i}\right)-\frac{BH}{4\pi}, \tag{1}$$

where F_0 is the self-energy of each filament, F_{0i} is the energy of interaction of the given filament with the others, B is the average magnetic induction of the sample, and Φ_0 is the magnetic flux quantum.

On the other hand, in the Ginzburg–Landau theory the energy of a vortex filament can be represented as a sum of the electromagnetic energy F_{em} and the energy $F_{\rm cor}$ due to the spatial variation of the order parameter. Using the second Ginzburg–Landau equation, we can write the electromagnetic energy of a unit length of vortex as

$$F_{em}=\frac{\Phi_0}{8\pi}b(0), \tag{2}$$

where $b(0)$ is the total local field at the center of the vortex. We shall assume that this field is a superposition of the field $b_0(0)$ produced by the filament itself and the field $b_0(|\mathbf{r}_i-\mathbf{r}_0|)$ produced by the vortices surrounding it, i.e.,

$$b(0)=b_0(0)+\sum_i b_0(|\mathbf{r}_i-\mathbf{r}_0|), \tag{3}$$

where $\mathbf{r}_i$ is the radius vector of the ith vortex in the plane of a transverse section, and the field $b_0(r)$ is the same as the field of an isolated flux line.

Thus the total self-energy of a vortex consists of the energy $F_{\rm cor}$ of its core and the electromagnetic self-energy F_{em}^0:

$$F_0=F_{\rm cor}+\frac{\Phi_0}{8\pi}b_0(0). \tag{4}$$

The interaction energy F_{0i} is of an electromagnetic nature:

$$F_{0i}=\frac{\Phi_0}{8\pi}b_0(|\mathbf{r}_i-\mathbf{r}_0|). \tag{5}$$

In accordance with Eqs. (4) and (5), we can rewrite expression (1) in the form

$$G=\frac{B}{\Phi_0}\left(F_{\rm cor}+\frac{\Phi_0}{8\pi}b_0(0)\right)+\frac{B}{8\pi}\sum_i b_0(|\mathbf{r}_i-\mathbf{r}_0|)-\frac{BH}{4\pi}. \tag{6}$$

From the condition of minimum Gibbs free energy ($dG/dB=0$) we find the magnetic field at which the vortex lattice is found in a thermodynamic equilibrium state:

$$H=\frac{4\pi}{\Phi_0}F_{\rm cor}+\frac{b_0(0)}{2}+\frac{1}{2}\frac{d}{dB}\left[B\sum_i b_0(|\mathbf{r}_i-\mathbf{r}_0|)\right]. \tag{7}$$

We note that the same condition of minimum G at $B\to 0$ gives the value of the first critical field:

$$H_{c1}=\frac{4\pi}{\Phi_0}F_{\rm cor}+\frac{b_0(0)}{2}. \tag{8}$$

Therefore, if we neglect the change in $F_{\rm cor}$ and $b_0(0)$ with increasing field in the range of fields considered, then

$$H=H_{c1}+\frac{1}{2}\frac{d}{dB}\left[B\sum_i b_0(|\mathbf{r}_i-\mathbf{r}_0|)\right]. \tag{9}$$

Hence for the magnetization $-4\pi M=H-B$ we obtain

$$-4\pi M=H_{c1}+\frac{1}{2}\frac{d}{dB}\left[B\sum_i b_0(|\mathbf{r}_i-\mathbf{r}_0|)\right]-B. \tag{10}$$

We see from formula (10) that in the field interval under study the quantitative accuracy of the functions $M(H)$ obtained depends largely on the accuracy of determination of the lower critical field H_{c1} and of the function $b_0(r)$ describing the local field of an isolated vortex. In other words, formula (10) for the magnetization can be a significantly more accurate quantitative result if, instead of the expressions for H_{c1} and $b_0(r)$ obtained in the London approximation, one uses more accurate values that can be calculated for them in the framework of other approaches, including numerical solution of the Ginzburg–Landau equations.

It is known[15] that in the London approximation

$$b_0(r)=\frac{\Phi_0}{2\pi\lambda^2}K_0\left(\frac{|\mathbf{r}-\mathbf{r}_0|}{\lambda}\right), \tag{11}$$

where K_0 is the zeroth-order Bessel function of imaginary argument, and λ is the London penetration depth of the magnetic field. In this model the field H_{c1} can be found only approximately, using the standard procedure of cutting off the vortex field (11) at $|\mathbf{r}-\mathbf{r}_0|=\xi$, where ξ is the coherence length:

$$H_{c1}=\frac{\Phi_0}{4\pi\lambda^2}K_0(1/\kappa). \tag{12}$$

Taking into account the spatial variation of the order parameter in the vortex cores gives the exact value of H_{c1}:

$$H_{c1}=\frac{\Phi_0}{4\pi\lambda^2}(\ln\kappa+C_1), \tag{13}$$

and gives for the field at the center of an isolated vortex

$$b_0(0)=\frac{\Phi_0}{2\pi\lambda^2}(\ln\kappa-C_0), \tag{14}$$

where C_1 and C_0 are constants.

At present the values of the constants C_1 and C_0 for $\kappa \gg 1$ can be regarded as reliably established: $C_1=0.496815$ and $C_0=0.282276$. These values were obtained in Ref. 16 by numerical solution of the system of Ginzburg–Landau differential equations and are in good agreement with the results obtained in Ref. 17.

For $\kappa=100$ and the given values of C_1 and C_0 we obtain the value of $4\pi M_{\rm cor}$ in a field $H=H_{c1}$: $-4\pi M_{\rm cor}=\kappa F_{\rm cor}/4\pi=(C_1+C_0)/2\kappa=0.038$. This value can then be used for comparison with the resultant magnetization. (Here and below we have switched to Ginzburg–Landau units, in which all lengths are measured in units of λ and fields are in units of $\sqrt{2}H_c$, where H_c is the thermodynamic critical field; then $\Phi_0=2\pi/\kappa$, $H_{c2}=\kappa$.)

The exact distribution of the field of an individual vortex $b_0(r)$ can be found by numerical solution of the system of Ginzburg–Landau equations. The results are presented in Fig. 1a. Also shown for comparison in this figure is the field distribution (11) obtained in the London approximation. We see that the main difference in the curves shown is observed near the center of the vortex and is a consequence of taking into account the distribution of the order parameter in this region (the behavior of the function $f(r)$ is given in Fig. 1b). It should be noted that the numerical values of $b_0(r)$ presented in Fig. 1a can be described quite well by the analytical expression

$$b_0(r)=\frac{f_\infty K_0(f_\infty(r^2+\xi_\nu^2)^{1/2})}{\kappa\xi_\nu K_1(f_\infty\xi_\nu)}, \tag{15}$$

which was obtained in Ref. 4 by a variational method from the second Ginzburg–Landau equation with the use of the following trial function for the modulus of the order parameter:

$$f=\frac{f_\infty r}{(r^2+\xi_\nu^2)^{1/2}}, \tag{16}$$

where ξ_ν and f_∞ are variational parameters representing the effective radius of the core and the order parameter far from the vortex core (for $\kappa\gg1$ in the field range under consideration here, they can be considered constant: $\xi_\nu=\xi_{\nu0}=\sqrt{2}/\kappa$, $f_\infty=1$). The behavior of the function (16) and of the field (15) is shown by the solid curves in Fig. 1; we see that they describe the exact numerical values very well. Therefore in the calculations of $M(H)$ below we shall use the analytical expression (15) for the description of $b_0(r)$.

Figure 2 shows the magnetization curves $M(H)$ for superconductors with $\kappa=100$, with the spatial distribution of the order parameter taken into account to varying degrees of accuracy. Let us first discuss the curves *1′*, *2′*, and *3′*, given by the data points in the figure. All of these curves correspond to numerical summation according to formula (10) for a triangular vortex lattice. Here curve *1′* (triangles) corresponds to the purely London approximation, i.e., $b_0(r)$ and H_{c1} are described by expressions (11) and (12). Curve *2′* (crosses) was obtained with the use of formulas (11) and (13) for the given characteristics. For curve *3′* (circles) expressions more accurate than those given by the London approximation are used for both $b_0(r)$ and H_{c1}, i.e., Eqs. (15) and (13), respectively.

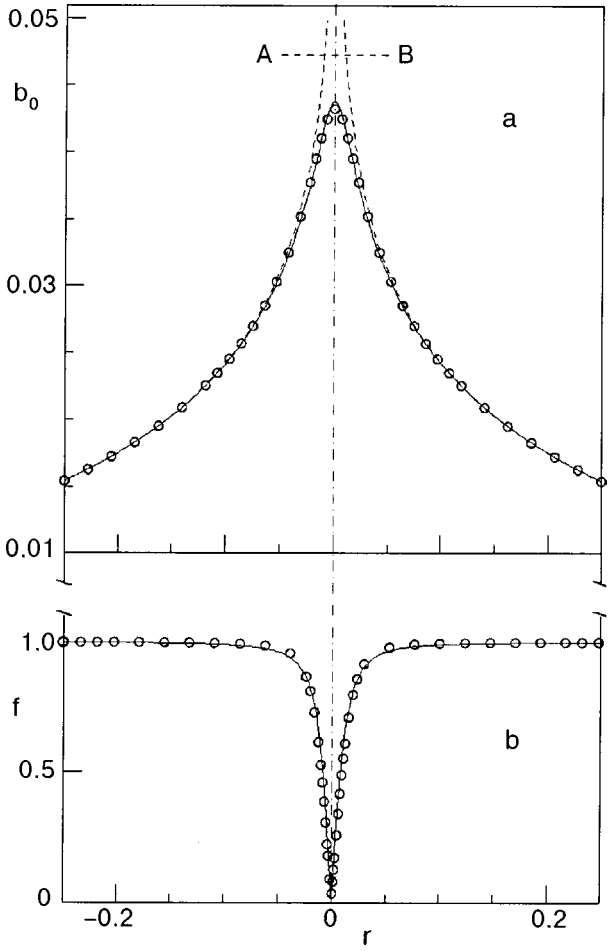

FIG. 1. Spatial distribution of the field of an individual vortex (a) and of the order parameter (b) (in Ginzburg–Landau dimensionless units). The data points represent a numerical solution of the system of Ginzburg–Landau equations. The continuous curves represent the corresponding analytical relations (15) and (16). The dashed curve is the field of an isolated vortex in the London approximation (11). The line *AB* corresponds to the cutoff of the function $K_0(r)$ at a distance $r=\xi$.

We see that curves *1′* and *2′* demonstrate the difference in the behavior of $M(H)$ due to the different form of the formulas for H_{c1}, while curves *2′* and *3′* reflect the influence of the form of the function $b_0(r)$ on the behavior of $M(H)$. For fields $H<0.005H_{c2}$, where the magnetization is mainly determined by the self-energy of the flux line, curves *2′* and *3′* are in good agreement (see the inset to Fig. 2), since the same value of H_{c1} (13) was used for them. From a comparison of curves *1′*, *2′*, and *3′* we see that taking the suppression of the order parameter in the vortex cores into account, which in this case is done by a simple replacement of formulas (11) and (12) by the more accurate expressions (15) and (13), has a substantial effect on the whole trend of the curve $M(H)$, starting from the lowest fields.

Figure 2 also shows continuous curves of $M(H)$, which

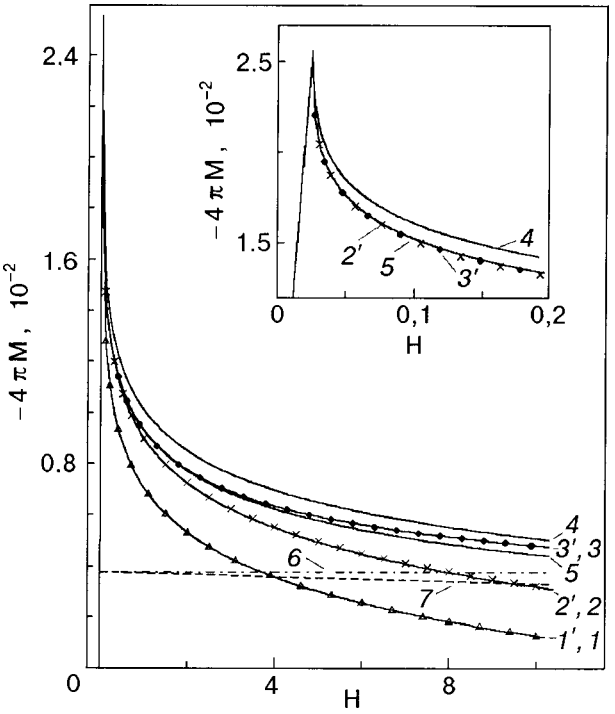

FIG. 2. Field dependence of the magnetization of a type-II superconductor with $\kappa=100$ (in Ginzburg–Landau dimensionless units). The data points show the results of a numerical calculation for a triangular vortex lattice according to formula (10) in which the following have been substituted for H_{c1} and $b_0(r)$: curve *1′* — Eqs. (12) and (11); curve *2′* — Eqs. (13) and (11); curve *3′* — Eqs. (13) and (15). The continuous curves represent the analytical relations: *1,2* — calculation according to the Fetter formula (17) together with (12) or (13), respectively; *3* — according to the formula obtained in Ref. 6; *4* — according to the formula obtained in Ref. 4; *5* — according to formula (22). Curves *6* (dot-and-dash) and *7* (dotted) give the function $-4\pi M_{\rm cor}(H)$ for the cases $F_{\rm cor}=$const and $F_{\rm cor}=F_{\rm cor}(H)$ (see Ref. 4), respectively. The inset shows $-4\pi M(H)$ in the immediate vicinity of H_{c1}.

correspond to the analytical results. For example, curves *1* and *2* were calculated from the known Fetter formula,[18] obtained in the London model:

$$-4\pi M=H_{c1}-\frac{\Phi_0}{8\pi\lambda^2}\times\left(\ln\frac{\lambda^2(H-H_{c1})}{\Phi_0}+\ln 4\pi+2-C-A_6\right), \tag{17}$$

where $C=0.5772\ldots$ is the Euler constant, A_6 is a numerical parameter (for a triangular lattice $A_6=0.07968\ldots$). As we see from Fig. 2, formula (17) gives a good description of the results of the numerical calculation (curves *1′* and *2′*), starting from fields $H>0.0015H_{c2}$, if expression (12) or (13), respectively, is used for H_{c1}. (At lower fields formula (17) is inapplicable, so that it was necessary to use the calculated curves *1′* and *2′* for further analysis in the field range directly adjacent to H_{c1}.)

It is of interest to compare the numerically calculated curve *3′* with the analytical dependence $M(H)$ given in Ref. 4. We note that the approach used in the present paper for calculating curve *3′* should give a result that differs only slightly from the result of the variational model used in Ref. 4.

Indeed, let us analyze the results of Ref. 4 in more detail. They imply, in particular, that the expression for the self-energy F_0 of each vortex (per unit length) under the condition $f_\infty=1$ can be written as

$$F_0=F_{\rm cor}+F_{em}^0=\frac{\pi\xi_\nu^2}{2+B\kappa\xi_\nu^2}+\frac{2\pi(1+B\kappa\xi_\nu^2)}{\kappa^2(2+B\kappa\xi_\nu^2)}+\frac{2\pi K_0(\xi_\nu)}{\kappa^2\xi_\nu K_1(\xi_\nu)}. \tag{18}$$

Substituting expression (18) into the general formula for the Gibbs free energy (1) and taking into account that in low fields the terms of the type $B\kappa\xi_\nu^2\ll 1$, we obtain for the magnetization

$$-4\pi M=\frac{\kappa\xi_\nu^2}{8}+\frac{1}{8\kappa}+\frac{K_0(\xi_\nu)}{2\kappa\xi_\nu K_1(\xi_\nu)}+\frac{\kappa}{8\pi}\frac{d}{dB}\left[B\sum_i b_0(|\mathbf{r}_i-\mathbf{r}_0|)\right]-B-\frac{B}{2\kappa^2}. \tag{19}$$

In the same variational model one obtains

$$H_{c1}=\frac{\kappa\xi_\nu^2}{8}+\frac{1}{8\kappa}+\frac{K_0(\xi_\nu)}{2\kappa\xi_\nu K_1(\xi_\nu)}. \tag{20}$$

It follows that

$$-4\pi M=H_{c1}+\frac{\kappa}{8\pi}\frac{d}{dB}\left[B\sum_i b_0(|\mathbf{r}_i-\mathbf{r}_0|)\right]-B-\frac{B}{2\kappa^2}. \tag{21}$$

The form of formula (21) is completely identical to that of (10) except for the last term [reflecting the field dependence of $F_{\rm cor}(B)$], which is very small anyway for large κ and small B. The values of H_{c1} calculated according to formulas (13) and (20) agree if one sets $C_1=0.52$ in (13). Thus, in view of the fact that the expression for $b_0(r)$ used by us is the same as that used in Ref. 4 and that the principle of superposition was used in the calculation of F_{em} both in Ref. 4 and here, one expects that the total expression for the magnetization obtained in Ref. 4 should give a result in the low-field range that is practically an exact match to the numerical data described by curve *3′* in Fig. 2. (We note that the function $M(H)$ in Ref. 4 is insensitive to the field dependence of ξ_ν and f_∞ up to $H\approx 0.6H_{c2}$; this, as we have said, allows us to set them equal to constants.) However, as we see from curve *4* in Fig. 2, which corresponds to the function $M(H)$ of Ref. 4 (let us call it the Hao–Clem curve) differs noticeably from curve *3′*, practically right from the lowest fields $H\approx H_{c1}$ (see the inset to Fig. 2). This fact is evidence of an error in the calculations of Ref. 4.

An analysis showed that in fact this error arose in Ref. 4 in the calculation of the electromagnetic energy, in going from a sum over the reciprocal vortex lattice to an integral. Our calculations carried out in the framework of the same variational model as in Ref. 4 but without using the aforementioned procedure, i.e., with a direct summation over the vortex lattice, yielded an analytical expression for $M(H)$ in

the field range $H_{c1} \leqslant H \ll H_{c2}$ which is somewhat different from the expression obtained in Ref. 4 and is more accurate:

$$-4\pi M = H_{c1} + \frac{1}{2\kappa\xi_\nu K_1(\xi_\nu)} \left\{ -\ln(1-\exp(-2\pi\xi_\nu/d)) + \frac{3\pi}{2d}\exp(-\xi_\nu) + \frac{\pi\exp(-d)}{1-\exp(-d)} \times \left(\frac{3}{d} - \frac{\xi_\nu}{2d} + \frac{1}{1-\exp(-d)} \right) + B\kappa\xi_\nu^2 \ln d + \frac{\pi\xi_\nu}{d} \frac{\exp(-2\pi\xi_\nu/d)}{1-\exp(-2\pi\xi_\nu/d)} \right\} - \frac{K_0(\xi_\nu)}{2\kappa\xi_\nu K_1(\xi_\nu)} - \frac{B}{2\kappa^2} - B, \quad (22)$$

where $d = \sqrt{2\pi/\kappa B}$ is the distance between vortices. A derivation of formula (22) is given in the Appendix.

The dependence $M(H)$ corresponding to formula (22) is shown by curve *5* in Fig. 2. As expected, in the low-field range curve *5* is in good agreement with the results of the numerical calculation (curve *3′*) (see also the inset in Fig. 2). The slight difference between the given curves in the field range $H > 4$ is due to the fact that curve *5* takes into account the change in energy of the vortex cores with increasing field in the form set forth in the variational method,[4] while curve *3′* does not take it into account. (For clarity the contribution to the magnetization from the field dependence of $F_{\rm cor}(H)$ is shown in Fig. 2 by curve *7*, in comparison with the straight line *6*, which corresponds to $-4\pi M_{\rm cor} = \text{const} = 0.038$.)

Thus, returning to the Hao–Clem curve and comparing it with the more accurate curve *5*, we can see that the inaccuracy in the calculation of F_{em} in Ref. 4 leads to an error of 8–14% in the values of $M(H)$ in the field region under study.

Let us conclude by briefly discussing the possible influence on the behavior of the $M(H)$ curve of the factor due to the change in the spatial distribution of the order parameter $f(r)$ as a result of overlapping of the vortices, which was not taken into account in the derivation of formula (22). This factor should affect the value of F_0 and also alter the spatial distribution of the field of a vortex. It is important to note that here it becomes incorrect to use the principle of superposition of fields in the form (3), i.e., in the form of a sum of the fields of isolated vortices.

A theoretical treatment taking into account (implicitly) all of the factors mentioned above was carried out in Refs. 1 and 6 in the framework of the variational method without the use of the principle of superposition, i.e., in a manner more self-consistent than in Ref. 4. Despite the use of different trial functions in the different papers, the resulting $M(H)$ curves obtained in Refs. 1 and 6 agree to a high degree of accuracy. Since the corresponding analytical expressions have a rather awkward form, we present the results directly in the form of the $M(H)$ curve (the solid curve *3*) in Fig. 2. We note that curve *3* is in good agreement with the results of a numerical solution of the Ginzburg–Landau equations for a regular vortex lattice by the method proposed in Ref. 2 (the difference is not more than 0.3% in the investigated field interval).

As we see in Fig. 2, this more accurate curve *3* is in fact slightly different from curve *5*, which was calculated with the use of the principle of superposition. However, it turns out that curve *3* is practically identical to the numerically calculated curve *3′* all the way to fields $H \approx 15$. Analysis showed that this agreement is to some degree accidental and happens because in the calculation of curve *3′* the neglect of the field dependence of $M_{\rm cor}$ is compensated by the error introduced by the use of the principle of superposition.

Thus a comparison of curves *3*, *3′*, and *5* shows that in the magnetic field region considered in this study, for which the distance between vortices is not less than $d \approx 8\xi$, the change in the order parameter due to the overlapping of the vortices is so small that it can be neglected in calculations of the equilibrium magnetization of superconductors.

CONCLUSIONS

A comparative analysis of the field dependence of the equilibrium magnetization $M(H)$ of type-II superconductors ($\kappa = 100$) has revealed a substantial difference in the behavior of the curves obtained with and without allowance for the spatial distribution of the order parameter; this difference starts at fields $H = H_{c1}$ and increases as the field is increased further.

An approach is proposed which eliminates the main source of inaccuracy of the London approximation and in the simplest way takes the structure of the vortex cores into account in the expression for $M(H)$. In this approach one still uses formula (10) for the magnetization $M(H)$ but now with H_{c1} and the spatial distribution of the vortex field $b(r)$ in that formula replaced by expressions obtained not in the London approximation but in other approaches that give a more accurate result. In particular, one can use the results of an exact numerical solution of the Ginzburg–Landau equation or of the variational method developed in Ref. 4.

Using expression (13) for H_{c1} with a constant $C_1 \approx 0.5$ correctly takes into account not only the energy of the vortex cores but also the value of the vortex field at the center, and using the analytical expression (15) obtained in Ref. 4 for $b(r)$ (which gives a good description of the results of the numerical solution of the Ginzburg–Landau equations) makes it possible to calculate the electromagnetic interaction energy of the vortices more adequately than in the London model. The additional changes in the order parameter in the vortex cores due to the influence of the fields of neighboring vortices is too small to have a noticeable effect on the behavior of the $M(H)$ curves in the field range under study ($H \leqslant 0.1H_{c2}$).

We have obtained an analytical expression for $M(H)$ in the magnetic field range $H_{c1} \leqslant H \ll 0.1H_{c2}$ by direct summation over the lattice of individual vortices with allowance for the spatial distribution of the order parameter. This analytical expression is in good agreement with the results of a numerical calculation by the method described above.

At the same time, the analysis done in the present paper has shown that the analytical value for $M(H)$ obtained in Ref. 4 in the framework of the Clem variational model (and which solves essentially the same problem of taking the structure of the vortex cores into account) gives a quantitatively incorrect result when used in the low-field region. The

reason for this lies in the error that arose in the calculations of Ref. 4 when the sum over the reciprocal vortex lattice was replaced by an integral.

This study was supported by the Russian Foundation for Basic Research (Project No. 00-03-32246 and, in part, by Project No. 00-02-18032).

APPENDIX

As we see from Eq. (10), to calculate the magnetization one needs to find the total magnetic field $b_f(0)$ produced on the axis of a given vortex by all the other vortices. For simplicity we consider a square vortex lattice; the result for the magnetization in this case will not differ appreciably from the result obtained for a hexagonal lattice.[18] Using (15), we obtain for $b_f(0)$

$$b_f(0)=\frac{1}{\kappa\xi_\nu K_1(\xi_\nu)}\sum_{m=-\infty}^{+\infty}\sum_{n=-\infty}^{+\infty}K_0\left(\sqrt{d^2(m^2+n^2)+\xi_\nu^2}\right)-\frac{K_0(\xi_\nu)}{\kappa\xi_\nu K_1(\xi_\nu)}, \tag{A1}$$

where $d=\sqrt{2\pi/kB}$ is the distance between neighboring vortices. Let us find the field b produced by an individual vortex row at an arbitrary point of the superconductor. We introduce a coordinate system with its center on the axis of one of the vortices, with the x axis perpendicular to the plane containing the vortex row, the y axis lying in this plane and orthogonal to the vortex, and the z axis directed along the vortex axes. In this case we obtain

$$b(x,y)=\frac{1}{\kappa\xi_\nu K_1(\xi_\nu)}\sum_{m=-\infty}^{\infty}K_0\left(\sqrt{(dm+y)^2+x^2+\xi_\nu^2}\right). \tag{A2}$$

In the sum in (A2) we do a Fourier transformation with respect to the coordinate y:

$$b(x,y)=\frac{f_\infty}{\kappa\xi_\nu K_1(f_\infty\xi_\nu)}\sum_{m=-\infty}^{\infty}\int dq\exp(-iq(y+dm))\times\int\frac{dy}{2\pi}\exp(iqy)K_0\left(f_\infty\sqrt{x^2+y^2+\xi_\nu^2}\right). \tag{A3}$$

Doing the integral over y and q on the right-hand side of this last expression with the use of the standard formulas for definite integrals of Bessel functions[19] and the relation

$$\sum_{m=-\infty}^{+\infty}\exp(-iqm)=2\pi\sum_{m=-\infty}^{+\infty}\delta(q-2\pi m)$$

we obtain

$$b(x,y)=\frac{1}{\kappa\xi_\nu K_1(\xi_\nu)}\frac{\pi}{d}\sum_{m=-\infty}^{+\infty}\left(1+\frac{4\pi^2m^2}{d^2}\right)^{-1/2}\times\exp\left(-\sqrt{x^2+\xi_\nu^2}\sqrt{1+(4\pi^2m^2)/d^2}\right)\cos\left(\frac{2\pi my}{d}\right). \tag{A4}$$

Using (A4) we obtain for $b_f(0)$

$$b_f(0)=\frac{\pi}{\kappa d\xi_\nu K_1(\xi_\nu)}\sum_{n=-\infty}^{\infty}\exp\left(-\sqrt{n^2d^2+\xi_\nu^2}\right)+\frac{2\pi}{\kappa d\xi_\nu K_1(\xi_\nu)}\sum_{m=1}^{\infty}\left(1+\frac{4\pi^2m^2}{d^2}\right)^{-1/2}\times\exp\left(-\xi_\nu\sqrt{1+(4\pi^2m^2)/d^2}\right)-\frac{K_0(\xi_\nu)}{2\kappa\xi_\nu K_1(\xi_\nu)}. \tag{A5}$$

Since the relation $\xi_\nu\ll d$ holds in the field region $H\ll H_{c2}$, we expand the first term on the left-hand side of (A5) in powers of ξ_ν/d, keeping the term proportional to ξ_ν^2/d^2. In the second term we take into account that $d^2\ll 4\pi^2$ for fields not too close to H_{c1}. Hence we find

$$b_f(0)=\frac{\pi}{\kappa d\xi_\nu K_1(\xi_\nu)}\left\{-\frac{d}{\pi}\ln\left(1-\exp\left(-\frac{2\pi\xi_\nu}{d}\right)\right)+\exp(-\xi_\nu)+\frac{2\exp(-d)}{1-\exp(-d)}+\frac{\xi_\nu^2}{d}\ln d\right\}-\frac{BK_0(\xi_\nu)}{\kappa\xi_\nu K_1(\xi_\nu)}. \tag{A6}$$

Equations (21) and (A6) yield Eq. (22) for $M(B)$. Here the dependence of the magnetic field on the induction is given by the relation $H(B)=B-4\pi M$. Thus we have obtained the function $M(H)$ implicitly.

*E-mail: mamsurova@chph.ras.ru

[1] H. Koppe and J. Willebrand, J. Low Temp. Phys. **2**, 499 (1970).
[2] E. H. Brandt, Phys. Rev. Lett. **78**, 2208 (1997).
[3] Z. Hao and J. R. Clem, Phys. Rev. Lett. **67**, 2371 (1991).
[4] Z. Hao, J. R. Clem, M. W. McElfresh, L. Civale, A. P. Malozemoff, and F. Holtzberg, Phys. Rev. B **43**, 2844 (1991).
[5] E. H. Brandt, Rep. Prog. Phys. **58**, 1465 (1995).
[6] W. V. Pogosov, A. L. Rakhmanov, and K. I. Kugel, Zh. Éksp. Teor. Fiz. **118**, 676 (2000) [JETP **91**, 588 (2000)].
[7] M.-S. Kim, M.-K. Bae, W. C. Lee, and S.-I. Lee, Phys. Rev. B **51**, 3261 (1995).
[8] M. Xu, J. Sok, J. E. Ostenson, D. K. Finnemore, and B. Dabrowski, Phys. Rev. B **53**, 15313 (1996).
[9] Y. C. Kim, J. R. Thompson, J. G. Ossandon, D. K. Christen, and M. Paranthaman, Phys. Rev. B **51**, 11767 (1995).
[10] P. Pugnat, G. Fillion, H. Noel, M. Ingold, and B. Barbara, Europhys. Lett. **29**, 425 (1995).
[11] D. N. Zheng, A. M. Campbell, and R. S. Liu, Phys. Rev. B **48**, 6519 (1993).
[12] J. Sok, M. Xu, W. Chen, B. J. Suh, J. Gohng, D. K. Finnemore, M. J. Kramer, L. A. Schwarzkopf, and B. Dabrowski, Phys. Rev. B **51**, 6035 (1995).
[13] M.-S. Kim, S.-I. Lee, S.-C. Yu, I. Kuzemskaya, E. S. Itskevich, and K. A. Lokshin, Phys. Rev. B **57**, 6121 (1998).
[14] A. A. Nugroho, I. M. Sutjahja, A. Rusydi, M. O. Tjia, A. A. Menovsky, F. R. de Boer, and J. J. M. Franse, Phys. Rev. B **60**, 15384 (1999).
[15] D. Saint-James, G. Sarma, and E. J. Thomas, *Type II Superconductivity* [Pergamon Press, Oxford (1969); Mir, Moscow (1970)].
[16] E. A. Shapoval, JETP Lett. **69**, 577 (1999).
[17] C.-R. Hu, Phys. Rev. B **6**, 1756 (1972).
[18] A. L. Fetter, Phys. Rev. **147**, 153 (1966).
[19] I. S. Gradshteyn and I. M. Ryzhik, *Table of Integrals, Series, and Products* [Academic Press, New York (1980); Nauka, Moscow (1963)].

Translated by Steve Torstveit

Equilibrium magnetic characteristics of high-T_c superconductors with allowance for the spatial distribution of the order parameter in the vortex cores. II. Vibrational contribution to the dynamic magnetic permeability

L. G. Mamsurova* and K. S. Pigalskiy

N. N. Semenov Institute of Chemical Physics, Russian Academy of Sciences, ul. Kosygina 4, 117977 Moscow, Russia

W. V. Pogosov

Moscow Institute of Physics and Technology, Institutskiĭ per. 7, 141700 Dolgoprudnyĭ, Moscow Region, Russia

(Submitted August 11, 2000)
Fiz. Nizk. Temp. **27**, 162–169 (February 2001)

The vibrational contribution $\mu_v(H)$ to the dynamic magnetic permeability μ'_{ac} is calculated with allowance for the spatial variation of the order parameter in the magnetic field region $H \ll H_{c2}$, where the properties of type-II superconductors are usually described in the London approximation. The features of the behavior of the analytical relations $\mu_v(H)$ are analyzed for the case when the vortices execute small oscillations about their equilibrium positions corresponding to the thermodynamic-equilibrium vortex lattice. It is shown that taking into account the suppression of the order parameter in the vortex cores leads to substantial differences in the behavior of $\mu_v(H)$ in comparison with the analogous dependence obtained in the London approximation. It is found that the main factor responsible for these differences is a change in shape of the effective potential well in which the vibrational motion of the subsurface vortices takes place.
[DOI: 10.1063/1.1353702]

INTRODUCTION

The vibrational contribution to the dynamic magnetic permeability reflects the oscillatory motion of the vortices about their equilibrium positions when the static magnetic field H is modulated by a weak alternating magnetic field (of low frequency ω and vanishingly small amplitude h). In the magnetic field $H(t)=H+h\sin(\omega t)$ this contribution is given by

$$\mu_v = \lim_{h\to 0}(\mu'_{ac}), \tag{1}$$

where

$$\mu'_{ac} = \frac{1}{2\pi h}\int_0^{2\pi/\omega} \cos(\omega t)\,\frac{dB}{dt}\,dt \tag{2}$$

is the real part of the complex magnetic permeability (i.e., the Fourier expansion coefficient of the periodically time-varying volume-averaged magnetic induction $B(t)$).

According to the definition (1), (2), a nonzero contribution to the dynamic magnetic permeability can arise for two reasons: if the number of vortices varies over the period $\tau=-2\pi/\omega$, or if the value of their magnetic flux varies. Accordingly, two different approaches for explaining the existence of the vibrational contribution μ_v are found in the literature, reflecting the two possibilities mentioned.

The first approach was proposed by Campbell.[1] In that approach the variation of the induction during modulation of the magnetic field occurs on account of a change in the number of vortices. Here the governing role is played by pinning. The vibrations of each vortex occur inside a potential well produced by the interaction of the vortex with a pinning center, and μ_v is largely determined by the steepness of this well, the so-called Labusch constant.[2]

Another type of vibrational contribution to μ'_{ac} was considered in our previous papers (see, e.g., Refs. 3–7). According to the ideas developed in those papers, the given contribution μ_v is due exclusively to the distortion of the field of the near-surface vortices (lying in a layer of thickness $\sim\lambda$, where λ is the London penetration depth of the magnetic field) on account of their interaction with the surface.

It is known[8] that for this reason the trapped magnetic flux of the vortices lying at a depth $\sim\lambda$ is less than the flux quantum Φ_0 and depends on the distance to the surface. During the vibrational motion of the vortices under the influence of an alternating field their position relative to the surface varies, leading to a nonzero value of μ_v according to formulas (1) and (2). As was shown in Ref. 4, for this mechanism to be realized it is necessary that the number of vortices not change over the period τ. One of the possible factors preventing the entry and exit of vortices from the sample is the presence of a surface barrier.

It is important to note that in contrast to the Campbell approach, the existence of the second type of vibrational contribution is indifferent to the presence or absence of pinning in the sample. Moreover, since the Meissner current density in a near-surface layer of thickness $\sim\lambda$ exceeds the critical current density, it can be assumed that the interaction of the vortices with the surface is decisive, and in comparison with it, the pinning can be neglected altogether. Thus the

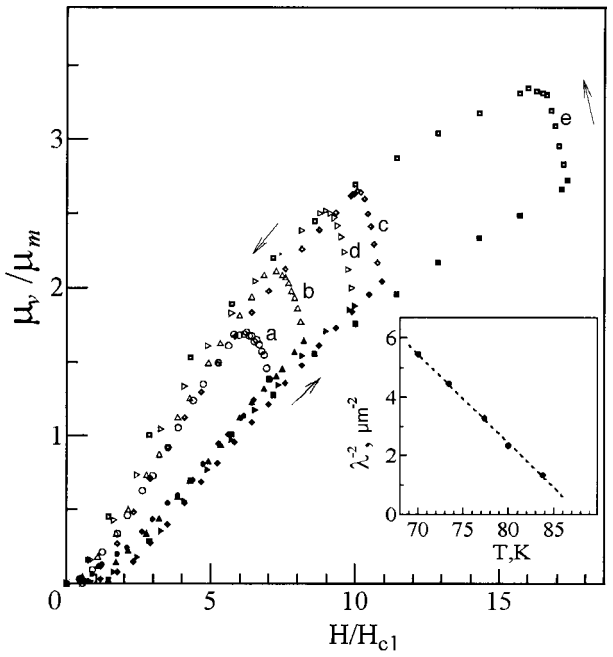

FIG. 1. Normalized experimental field dependence of the vibrational contribution μ_v to the dynamic magnetic permeability of a $YBa_2Cu_3O_x$ single crystal at different temperatures T [K]: 70 (a), 73.4 (b), 77.3 (c), 80 (d), 83.8 (e). The arrows indicate the directions of change of the magnetic field. The inset shows the London penetration depth corresponding to a normalization factor $\mu_m = 2\lambda/D$, where D is the thickness of the sample.

second approach is an alternative to the Campbell approach not only for the reason mentioned above but also because it assumes a different nature of the effective potential well in which the vibrational motion of the vortices takes place. Here this well is formed mainly by the interaction of the vortices with the surface and with each other, and not with pinning centers.

To ascertain which of the two approaches mentioned better reflects the dynamics of the near-surface vortices, it is necessary to do both experimental and theoretical studies of the vibrational contribution $\mu_v(H)$ to the dynamic magnetic permeability.

Our previous experimental studies[3–7] done mainly on YBaCuO single crystals and the results of other authors (see, e.g., Refs. 9 and 10) have shown that $\mu_v(H)$ exhibits hysteretic behavior in the magnetic field H (the $\mu_v(H)$ curve for increasing field is lower than for decreasing field). Here the field dependence of $\mu_v(H)$ corresponding to different temperatures exhibits scaling behavior, i.e., the curves are described by a universal dependence in reduced coordinates[6,7] (Fig. 1). This behavior, in our view, indicates a fundamental nature of this effect, unrelated to defects in the sample. Indeed, an attempt to explain the observed hysteresis of $\mu_v(H)$ by the presence of pinning near the surface proved unsuccessful, since it gave an irreversibility of the opposite sign from the experimental one.[5,6] Thus the only remaining possibility for explaining this effect is the existence of hysteresis of the magnetic induction $B(H)$ near the surface on account of the formation of a surface barrier.

By neglecting pinning processes one can treat the vibrational motion of near-surface vortices theoretically without using any unknown empirical parameters (such as the Labusch constant) and obtain an analytical expression relating the quantity $\mu_v(H)$ under study with the value of the average induction $B(H)$ in the surface layer of the sample. This problem was solved in the London approximation in Refs. 6 and 7.

A comparison of the calculated $\mu_v(H)$ curves obtained in Refs. 6 and 7 with the experimental curves yielded a rather important result. It was found that in real YBaCuO samples (both single-crystal and polycrystalline) the surface barrier is strongly suppressed in comparison with what would be expected for an ideal surface. The lower branch of the hysteresis of $\mu_v(H)$ is described well by the calculated curve corresponding to practically equilibrium values of the induction $B(H) = B_{eq}(H)$, while the presence of the surface barrier has a more substantial effect on the exit of the vortices from the superconductor.

In the present study we wanted to concentrate our attention specifically on the fact that the experimental curve of $\mu_v(H)$ measured under conditions of increasing magnetic field corresponds to the behavior of the equilibrium function $B_{eq}(H)$ even in low fields ($H > (2-3)H_{c1}$). And, as follows from the results given in part I of this paper, the theoretical curve of $B_{eq}(H)$ calculated with allowance for the spatial distribution of the order parameter in the vortex cores differs significantly from the corresponding curve obtained in the London approximation. Furthermore, since, as we have said, the quantity $\mu_v(H)$ itself is due to distortion of the field of the vortex near the surface, the use of a more accurate expression for the field of an individual vortex, taking into account the structure of its core, can lead to a substantial modification of the $\mu_v(H)$ curve obtained previously in the London approximation.

In this connection it is of interest to obtain a more accurate analytical relation for $\mu_v(H)$ (as compared to the London approximation), which would take into account the suppression of the order parameter in the vortex core. In this paper we obtain such a relation and analyze the behavior of $\mu_v(H)$ for different forms of the $B_{eq}(H)$ curves obtained in Part I of this paper.

THEORY

Let us consider a superconducting sample in the form of a massive slab of thickness $D \gg \lambda$ in an external static magnetic field H parallel to its surface. We introduce a coordinate system xyz, with the z axis along the field direction, the y axis parallel to the surface, and the x axis directed into the interior of the superconductor, perpendicular to its surface.

In accordance with the results of an analysis[4,8] one can assume to high accuracy that the vortex rows, starting with the second, are regularly spaced a distance d apart, i.e., $x_n = x_1 + (n-1)d$, where x_n is the distance from the center of the nth vortex row to the surface, and x_1 is that for the first row. The distance between adjacent vortices within a row is denoted as a. We shall consider the field region $H \ll H_{c2}$, in which the distances x_1, d, and a are much larger than the size of the vortex cores.

Let us briefly analyze the main aspects of the theoretical treatment[4,6,7] of the vibrational contribution to the dynamic magnetic permeability in the London approximation.

In calculating $\mu_v(H)$ we start from the analytical expression derived in Ref. 4:

$$\mu_v = \frac{2\Phi_0}{Da\lambda}\frac{\exp(-x_1/\lambda)}{1-\exp(-d/\lambda)}\left(\frac{\partial x_1}{\partial H}\right)_{B_v}, \tag{3}$$

where the differentiation is done at a constant number of vortices in the sample or, equivalently, at a constant magnetic induction B_v, which is given by

$$B_v = \Phi_0/da. \tag{4}$$

Formula (3) reflects the circumstance that μ_v is almost completely determined by the distance from the surface to the first vortex row and by the change in this distance during the modulation of the external magnetic field by the ac component.

The Gibbs energy G for the a vortex in the first row was calculated in Refs. 6 and 7 by summing the contributions over the lattice of the vortices and their images. From the condition that the Gibbs potential be a minimum for a vortex in the first row ($\partial G/\partial x_1 = 0$) an analytical expression is obtained for the equilibrium position of the first vortex row, $x_1(H)$:

$$x_1(H) = \frac{d}{2} + \cosh^{-1}\left(\frac{H}{\tilde{B}_v}\right), \tag{5}$$

where

$$\tilde{B}_v = B_v\frac{d}{2\lambda\sinh(d/2\lambda)}. \tag{6}$$

A calculation of the magnetic permeability according to formula (3) in the case of a small amplitude of the sinusoidal magnetic field reduces to the problem of small oscillations of the first vortex row about its equilibrium position:

$$x_1(t,H) = x_1(H) + \frac{\Phi_0 h\exp[-x_1(H)/\lambda]}{4\pi k\lambda}\sin(\omega t). \tag{7}$$

Here k is the elastic constant, which governs the steepness of the effective potential well in which the small harmonic oscillations of the vortices take place. On the assumption that k is determined mainly by the interaction of the vortices with one another and with the Meissner current and not by pinning, i.e., $k = \partial^2 G/\partial x_1^2$, it was found that

$$k = \frac{\Phi_0}{4\pi\lambda^2}\exp(-d/2\lambda)\frac{\tilde{B}_v(H^2-\tilde{B}_v^2)^{1/2}}{H+(H^2-\tilde{B}_v^2)^{1/2}} \tag{8}$$

and, finally, for μ_v

$$\mu_v = \frac{2\lambda}{D}\frac{\tilde{B}_v^2}{(H^2-\tilde{B}_v^2)^{1/2}[H+(H^2-\tilde{B}_v^2)^{1/2}]}. \tag{9}$$

Let us now turn to a more accurate treatment of the characteristic μ_v and take into account the suppression of the order parameter in the vortex cores. We shall determine how the equilibrium position of the first vortex row and the mobility of the vortex lattice changes upon a small change in the external magnetic field when this factor is taken into account. We write the Gibbs thermodynamic potential B for a vortex in the first row (per unit length of the vortex filament) as

$$G = F_0 + F_{em} - \frac{\Phi_0 H}{4\pi}, \tag{10}$$

where F_0 is the energy due to the change in the order parameter near the vortex core, and F_{em} is the electromagnetic energy of a vortex. Using the second Ginzburg–Landau equation, we can write this last equation in the form $F_{em} = \Phi_0 b(x_1,0)/8\pi$, where $b(x_1,0)$ is the total magnetic field at the center of a vortex of the first row.

In order to satisfy the boundary conditions (the field at the surface of the superconductor is equal to the external field) we use the method of images. Then the local magnetic field b at an arbitrary point of the superconductor can be written as the sum of the field b_v of all the vortices, the field b_i of their images, and the field b_m produced by the Meissner currents:

$$b = b_v + b_i + b_m, \tag{11}$$

where

$$b_v = \sum_m\sum_n b_0(x-x_n, y-y_m); \tag{12}$$

$$b_i = \sum_m\sum_n b_0(x+x_n, y-y_m); \tag{13}$$

$$b_m = H\exp(-x). \tag{14}$$

In expression (14) and below we use the Ginzburg–Landau system of units, in which all distances are normalized to λ and the magnetic fields to $\sqrt{2}H_c$ (H_c is the thermodynamic critical field), in which case $\Phi_0 = 2\pi/\kappa$.

To write the field b_0 of an isolated vortex as a function of the distance r from the center of the vortex, we use the expression obtained in Ref. 11 by the variational method:

$$b_0(r) = \frac{f_\infty K_0(f_\infty(r^2+\xi_v^2)^{1/2})}{\kappa\xi_v K_1(f_\infty\xi_v)}, \tag{15}$$

where the K_i are modified Bessel functions of order i, and ξ_v and f_∞ are variational parameters representing the effective size of the vortex core and the order parameter far from the vortex core. This function describes the results of a numerical solution of the Ginzburg–Landau equations to sufficient accuracy (see Part I of this paper). We note that, as follows from Ref. 11, the variational parameters vary slowly in fields $H < 0.6H_{c2}$, and one can set $f_\infty = 1$, $\xi_v = \sqrt{2}/\kappa$. As was mentioned in Part I of this paper, the use of expression (15) for the field of an isolated vortex makes it possible to avoid the troublesome divergence of the function K_0 at the center of the vortex which arises in the London approximation, and can give a more accurate description of the field of the vortex.

Representing the local magnetic field in the form (11)–(14), we find the equilibrium distance from the surface to the first vortex row in a field H by minimizing the Gibbs thermodynamic potential (10). Since the electromagnetic energy is the only term on the right-hand side of (10) that depends on x_1, we obtain an equation from which we can determine x_1:

$$\frac{\partial b(x_1,0)}{\partial x_1}=0. \tag{16}$$

Let us calculate $b_0(x_1,0)$ by a method analogous to that used in the Appendix to part I of this paper, performing the summation over vortex rows parallel to the surface, for a square vortex lattice ($d=a$). Calculates have shown that the results of μ_v in the investigated field interval are practically independent of the form of the lattice. Then for determining the equilibrium distance x_1 we obtain the equation

$$\frac{Bd}{2\xi_\nu K_1(\xi_\nu)}\left\{\frac{\exp(-d)+\exp(-2x_1)}{1-\exp(-d)}-\frac{\xi_\nu^2}{2}[g(x_1)+f(d)]\right\}$$
$$=H\exp(-x_1), \tag{17}$$

where we have introduced the notation

$$g(x_1)=\frac{1}{4x_1^2}+\frac{1}{(2x_1+d/2)d};\quad f(d)=\frac{5}{3d^2}.$$

In deriving Eq. (17) we took into account that the distance between vortices is much greater than the value of ξ_v in low fields and have kept only the first terms of the expansion in powers of ξ_v^2/d^2. The solution of equation (17) can be approximated by the following analytical formula:

$$x_1(H)=\frac{d}{2}+\cosh^{-1}\left(\frac{H}{\widetilde{B}_v}\right), \tag{18}$$

where we have introduced the notation

$$\widetilde{B}_v=\frac{B_v}{\xi_v K_1(\xi_v)}\left(1-\frac{d^2}{24}-\frac{5\xi_v^2}{6d}\right). \tag{19}$$

Expression (18) for x_1 differs from the analogous London expression (5) in the form of $\widetilde{B}_v$. In the limit $\xi_v\to 0$ formula (19) reduces to the expansion (6) in powers of d.

Considering small oscillations of the first vortex row about its equilibrium position in analogy with the treatment in Refs. 6 and 7 and substituting the resulting expression for $x_1(t,H)$ into Eq. (3), we obtain the final expression for $\mu_v(H)$. It turns out that it can be reduced to the form (9) with the sole difference that the quantity $\widetilde{B}_v$ will be described by formula (19) instead of (6), as in the London approximation.

We note that in the above analysis we used expression (3) for $\mu_v(x_1)$, which was derived in the London approximation. This expression is valid if the flux of a vortex near the surface is described by the well-known relation given in Ref. 8:

$$\Phi_v=\Phi_0[1-\exp(-x/\lambda)], \tag{20}$$

where x is the distance from the surface to the vortex. When the structure of the vortex cores is taken into account, expression (20) is no longer exact. However, if the distance x is greater than the size of the vortex cores, then the corrections to (20) will be negligible. Indeed, if expression (15) is used for the field of an isolated vortex and is substituted into the more general formula for the vortex flux which is valid in our approach:

$$\Phi_v=\Phi_0\left[1-2\int b_0(r)d^2r\right] \tag{21}$$

(where the integration is over the region outside the superconductor), then it is easy to show that $\Phi_v(x)$ remains of the form (20) to high accuracy. For $\kappa=100$ the correction to the term $\exp(-x/\lambda)$ is a quantity $\sim 10^{-4}$.

Thus we see that taking the spatial variation of the order parameter into account by using a more accurate expression for the field of an individual vortex than that obtained in the London approximation leads primarily to a change in the parameter $\widetilde{B}_v$. This changes both the equilibrium position $x_1(H)$ of the first vortex row and the mobility dx_1/dH of the vortex lattice, which both appear in the initial expression (3) for $\mu_v(x_1)$.

Analysis of the structure of the analytical relation (9) for $\mu_v(H)$ shows that the sensitivity of this characteristic to the model used is determined by the factor $(H^2-\widetilde{B}_v^2)^{1/2}$, which contains the difference of two quantities of nearly the same size. It is this term that reflects the contribution to $\mu_v(H)$ of the elastic constant k. It can therefore be assumed that the inclusion of the spatial distribution of the order parameter in an analysis of the dynamics of the near-surface vortices will have the most substantial effect on the shape of the effective potential well in which the vibrational motion takes place for the vortices near the surface.

By assuming a definite form of the function $B(H)$ in (9), one can obtain calculated curves of $\mu_v(H)$ for subsequent analysis and comparison with the experimental data.

DISCUSSION OF THE RESULTS. COMPARISON OF THE THEORY WITH EXPERIMENT

Let us discuss the features of the behavior of $\mu_v(H)$ for the case when the vortices execute small oscillations about their equilibrium positions corresponding to the thermodynamic equilibrium of the vortex lattice in an external field H, i.e., for the case $B(H)=B_{eq}(H)$. We shall use four versions of the $B_{eq}(H)$ curves, corresponding to the field dependence of the equilibrium magnetization given in Part I of this paper. These curves take into account the spatial distribution of the order parameter parameter to varying degrees of accuracy.

Figure 2 shows the $\mu_v(H)$ curves in reduced coordinates (μ_v is normalized to $2\lambda/D$, see (9), and H is normalized to $\sqrt{2}H_c$), calculated according to formula (9), in which $\widetilde{B}_v$ has the form (19) (curves *1* and *2*) or the form (6) (curves *3* and *4*).

Curve *1* gives the results of the most-accurate calculations of the vibrational contribution μ_v to the dynamic magnetic permeability, in which the electromagnetic energy F_{em} is calculated by direct summation over the vortex lattice, with expression (15), which takes the influence of the structure of the vortex cores into account, used for the field $b_0(r)$ of an individual vortex. For the function $B_{eq}(H)$ to be substituted into (19), we use the analytical expression (22) from Part I of this paper, which was derived under these same conditions.

Curve *2* in Fig. 2 corresponds to the function $B_{eq}(H)$ obtained by Hao, Clem *et al.*,[11] which also take the aforementioned factors into account. However, in contrast to our calculations, in Ref. 11 the calculation of the electromagnetic energy was simplified by changing the sum over the reciprocal vortex lattice to an integral.

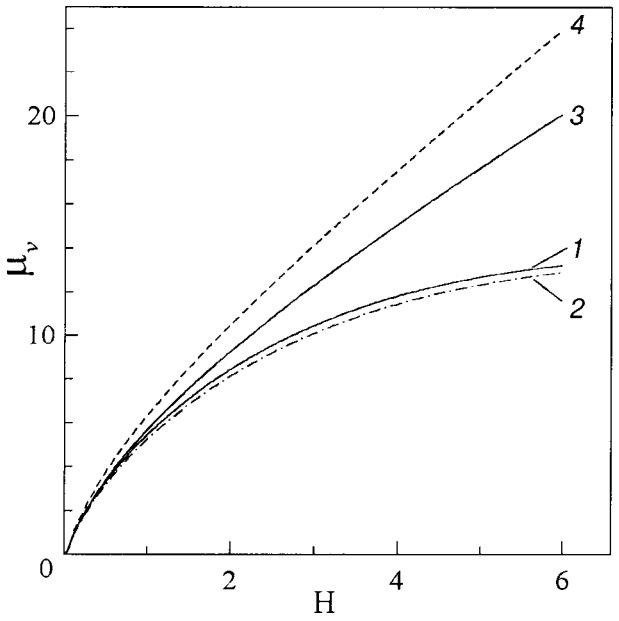

FIG. 2. Normalized theoretical field dependence of the vibrational contribution μ_v to the dynamic magnetic permeability for the case of a thermodynamic-equilibrium vortex lattice $B(H)=B_{eq}(H)$ for different values of $B_{eq}(H)$ and $\tilde{B}_v$: *1* — B_{eq} calculated according to formula (22) of Part I of this paper, $\tilde{B}_v$ calculated according to formula (19); *2* — B_{eq} obtained in Ref. 11, $\tilde{B}_v$ calculated according to formula (19); *3,4* — B_{eq} calculated according to the Fetter formula[12] with the exact and with an approximate value of H_{c1}, respectively, and $\tilde{B}_v$ calculated according to formula (6).

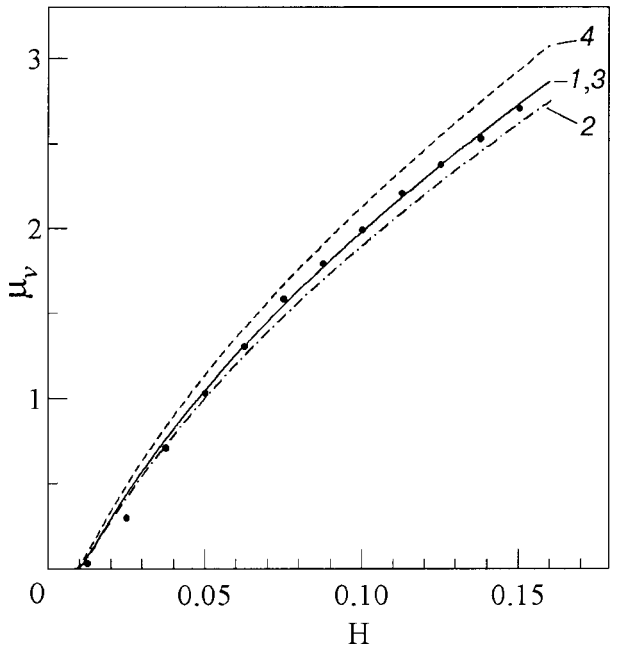

FIG. 3. Normalized field dependence of the vibrational contribution μ_v to the dynamic magnetic permeability for the initial region of magnetic fields. The points are experimental, the curves are calculated for different values of $B_{eq}(H)$ and $\tilde{B}_v$ (the numbers on the curves correspond to the numbers on the analogous curves in Fig. 2).

Curves *3* and *4* in Fig. 2 were calculated in the London approximation. Here the function $B_{eq}(H)$ obtained by Fetter[12] was used (see formula (17) of Part I), into which was substituted either the exact value of H_{c1}, including the energy of the vortex cores ($H_{c1}=(\ln\kappa+0.5)/2\kappa$ — curve *3*), or else the approximation adopted in the London model ($H_{c1}=K_0(1/\kappa)/2\kappa$ — curve *4*).

As we see in Fig. 2, the results of the more accurate calculations of $\mu_v(H)$ with allowance for the structure of the vortex cores are indeed different from the corresponding results obtained in the London approximation. It should be noted that the $\mu_v(H)$ curves *1* and *3*, like the magnetization curves (see Part I), completely coincide in the region of very low fields ($H\leqslant 0.01H_{c2}$). This means that in the given field region, taking the energy of the vortex cores into account by using the exact expression for H_{c1} turns out to be completely adequate for obtaining satisfactory results for $\mu_v(H)$ even in the London approximation. The difference between these curves at higher fields is due exclusively to the different degree of accuracy of the description of the field at the center of an individual vortex. The good agreement of curves *1* and *2* in Fig. 2 indicates that the computational simplification made in Ref. 11, which leads to appreciable ($\sim$10% or more) changes in $B_{eq}(H)$ (see Part I), has practically no effect on the behavior of $\mu_v(H)$.

Figure 3 shows the calculated curves of $\mu_v(H)$ in comparison with the experimental data measured under conditions of increasing magnetic field at $T=84$ K for a YBaCuO single crystal in the geometry $H\perp c$. The technique used to obtain the experimental curves of $\mu_v(H)$ is described in detail in Ref. 4. We see that the experimental data for $\mu_v(H)$ are in good agreement with the calculated curves *1* and *3* in regard to both their behavior and their absolute value. A criterion of good agreement is the numerical value of the single adjustable parameter — the London penetration depth of the magnetic field. The value obtained at $T=84$ K, viz., $\lambda=\sqrt{\lambda_{ab}\lambda_c}=0.85$ μm (which corresponds to $\lambda_{ab}=0.38$ μm), although somewhat different (by a factor of 1.4) from the known bulk values of λ for YBaCuO single crystals,[12] is in good agreement with the surface values.[13] An analogous result is obtained at other temperatures.

The difference in λ for the approximation of the experimental $\mu_v(H)$ data by the calculated curves *2* and *4* is $\sim$5% in the given field interval. However, the corresponding analysis for the higher field region, in which taking the structure of the vortex cores into account leads to a substantial change in the form of the $\mu_v(H)$ curve, made it possible to obtain more-reliable information about both the agreement of the theoretical treatment with the experimental data and about the values of λ in the near-surface layer. Such an analysis will be the subject of further investigations.

CONCLUSION

In this paper we have not addressed the question of why the experimental curves of $\mu_v(H)$ obtained in increasing magnetic field are described well by the theoretical curves obtained for the case of thermodynamic equilibrium of the vortex lattice: $B=B_{eq}(H)$. Possible reasons for the strong suppression of the surface barrier for the entry of vortices in real YBaCuO samples have already been discussed in our previous papers,[6,7] and this matter is still in need of additional investigation.

The results obtained in the present study demonstrate the degree to which the inaccuracy of the London approximation

affects the description of the field dependence of the vibrational contribution $\mu_v(H)$ to the dynamic magnetic permeability in the field region $H \ll H_{c2}$. We have shown that in the lowest fields ($H \leqslant 0.01 H_{c2}$), taking the energy of the vortex cores into account by using the exact expression for H_{c1} in the calculation of $B_{\mathrm{eq}}(H)$ turns out to be completely adequate for correction description of the equilibrium curves of $\mu_v(H)$ by the formulas obtained in the London approximation. In the range of higher fields, however, the accuracy of the description of the field of an individual vortex becomes important, and this field changes when the spatial variation of the order parameter near the vortex core is taken into account.

We have shown that the changes occurring when the spatial variation of the order parameter is taken into account most strongly affect the shape of the effective potential well in which the vibrational motions of the near-surface vortices take place under the influence of a weak ac magnetic field. As a result, the field dependence of the vibrational contribution to the dynamic magnetic permeability undergoes substantial changes.

This study was supported by the Russian Foundation for Basic Research (Project No. 00-03-32246 and, in part, Project No. 00-02-18032).

*E-mail: mamsurova@chph.ras.ru

[1] A. M. Campbell, J. Phys. C **2**, 1492 (1969).
[2] R. Labusch, Cryst. Lattice Defects **1**, 1 (1969).
[3] L. G. Mamsurova, K. S. Pigalskiy, V. P. Sakun, and L. G. Scherbakova, Physica C **200**, 175 (1992).
[4] L. G. Mamsurova, K. S. Pigalskiy, V. P. Sakun, and L. G. Shcherbakova, Fiz. Tverd. Tela (St. Petersburg) **37**, 2954 (1995) [Phys. Solid State **37**, 1630 (1995)].
[5] K. S. Pigalskiy and L. G. Mamsurova, Fiz. Tverd. Tela (St. Petersburg) **39**, 1943 (1997) [Phys. Solid State **39**, 1737 (1997)].
[6] K. I. Kugel, L. G. Mamsurova, K. S. Pigalskiy, and A. L. Rakhmanov, Physica C **300**, 270 (1998).
[7] K. I. Kugel, L. G. Mamsurova, K. S. Pigalskiy, and A. L. Rakhmanov, Fiz. Nizk. Temp. **24**, 823 (1998) [Low Temp. Phys. **24**, 617 (1998)].
[8] V. V. Shmidt and G. S. Mkrtchyan, Usp. Fiz. Nauk **112**, 459 (1974) [Sov. Phys. Usp. **17**, 170 (1975)].
[9] S. K. Hasanain, S. Shahzada, A. Mumtaz, and G. S. Bhatti, Physica C **269**, 149 (1996).
[10] M. Ciszek, J. Olejniczak, and A. J. Zaleski, Physica C **208**, 245 (1993).
[11] Z. Hao, J. R. Clem, M. W. McElfresh, L. Civale, A. P. Malozemoff, and F. Holtzberg, Phys. Rev. B **43**, 2844 (1991).
[12] A. L. Fetter, Phys. Rev. **147**, 153 (1966).
[13] J. Y. Lee, K. M. Paget, T. R. Lemberger, S. R. Fortyn, and X. Wu, Phys. Rev. B **50**, 3337 (1994).
[14] S. B. Qadri, M. S. Osofsky, V. M. Browring, and E. F. Skelton, Appl. Phys. Lett. **68**, 2729 (1996).

Translated by Steve Torstveit

LOW TEMPERATURE MAGNETISM

Features of the nonlinear dynamics of domain walls in ferrimagnets

V. S. Gerasimchuk* and A. A. Shitov

Donbass State Academy of Civil Engineering, ul. Derzhavina 2, 339023 Makeevka, Ukraine
(Submitted February 28, 2000; revised September 14, 2000)
Fiz. Nizk. Temp. **27**, 170–177 (February 2001)

The nonlinear motion of a 180° domain wall with two inequivalent sublattices in the field of a sound wave propagating orthogonally to the plane of the domain wall is investigated. The dependence of the drift velocity of the domain wall on the polarization and the parameters of the sound wave is found. An analysis of the long-wavelength and short-wavelength approximations is carried out. The conditions for drift of the stripe domain structure in ferrites are determined. © *2001 American Institute of Physics.* [DOI: 10.1063/1.1353703]

At present there is steady interest in the study of the dynamical properties of large-scale magnetic inhomogeneities (domain structures, domain walls, magnetic solitons, etc.) in magnetically ordered crystals. An important place in these studies is occupied by questions of the interaction of magnetic inhomogeneities with the elastic stress fields created by a sound wave.[1,2]

The magnetoelastic interaction, which couples the magnetic and elastic subsystems of a crystal, is responsible for the excitation of acoustic and domain oscillations,[2,3] sound generation, reradiation, and scattering by moving domain walls,[4–7] and, conversely, the vibrational and drift motion of domain walls in the field of an external sound wave.[1,8–10]

The experiments of Refs. 11–13, in which sound acted directly on domains and domain walls, detected linear oscillations and directed motion of 180° domain walls. It should be noted that while the experimental studies have been done mainly on iron garnets, practically all of the theoretical calculations have been done for one-sublattice ferromagnets (with the exceptions of Ref. 1, which considered an antiferromagnet near the inversion point of the sublattices, and Ref. 10, where the object of study was a two-sublattice weak ferromagnet).

In the present paper we investigate theoretically the influence of an arbitrarily polarized sound wave on a 180° domain wall in ferrites with two inequivalent magnetic sublattices.

MODEL AND EQUATIONS OF MOTION

Suppose that an arbitrarily polarized sound wave with an arbitrary value of the wave vector $\mathbf{k}$ is propagating in the direction perpendicular to a planar domain wall. We assume that the sound wave is specified as an external field, ignoring the back effect of the magnetic subsystem on the elastic subsystem.

The nonlinear macroscopic dynamics of a ferrite with two inequivalent sublattices in the field of a sound wave can be described on the basis of the Lagrangian density $L\{\mathbf{l}\}$, represented in terms of the unit antiferromagnetism vector $\mathbf{l}$ ($\mathbf{l}^2=1$):[14]

$$L\{\mathbf{1}\}=M_0^2\left\{\frac{\alpha}{2c^2}\dot{\mathbf{1}}^2-\frac{\alpha}{2}(\nabla\mathbf{1})^2-\frac{\beta_1}{2}l_x^2-\frac{\beta_2}{2}l_y^2-\gamma u_{ik}l_il_k+\frac{\nu}{gM_0}\frac{l_z\dot{l}_x-l_x\dot{l}_z}{1+l_y}\right\}, \tag{1}$$

where the dot over a variable denotes a time derivative, $M_0^2=1/2(\mathbf{M}_1^2+\mathbf{M}_2^2)$, M_0 is the modulus of the sublattice magnetization vectors, $c=(gM_0\sqrt{\alpha\delta})/2$ is the minimum spin-wave phase velocity, δ and α are the homogeneous and inhomogeneous exchange interaction constants, respectively, g is the gyromagnetic ratio, β_1 and β_2 ($\beta_2>\beta_1>0$) are the effective rhombic anisotropy constants, u_{ik} is the elastic strain tensor, γ is the magnetoelastic constant, and

$$\nu=\frac{|M_1-M_2|}{M_{1,2}} \tag{2}$$

is a parameter of the dynamical model of the ferrite.[14] The value of this parameter $\nu\gg(\beta/\delta)^{1/2}\sim10^{-2}$–$10^{-1}$ serves as a criterion of applicability of this model of the ferrite as an effective ferromagnet with a fixed modulus of the resultant magnetization vector $M_s=|\mathbf{M}_s|=|\mathbf{M}_1+\mathbf{M}_2+\ldots|$ ($\mathbf{M}_i$ are the sublattice magnetization vectors). This representation, which takes into account the strong exchange interaction between sublattices, is usually used in interpreting experiments on the dynamics of nonlinear excitations in ferrites. Near the compensation point of the ferrite, where the moduli of the sublattice magnetization vectors are only slightly different ($|M_1-M_2|\ll M_{1,2}$), the representation of the ferrite as an effective ferromagnet becomes inadequate. If the parameter ν is small ($\nu\to0$), then the dynamical properties of the ferrite are close to those of an antiferromagnet and considerably different from the properties of ferromagnetic crystals.[14]

Let us parametrize the vector $\mathbf{l}$ by the angle variables θ and φ as

$$l_z+il_x=\sin\theta\exp(i\varphi),\quad l_y=\cos\theta. \tag{3}$$

In terms of these variables we write the Lagrangian density of the ferrite (1) as

$$L(\theta,\varphi)=M_0^2\left\{\frac{\alpha}{2c^2}[(\dot\theta)^2+\sin^2\theta(\dot\varphi)^2]-\frac{\alpha}{2}[(\nabla\theta)^2+\sin^2\theta(\nabla\varphi)^2]-\frac{\beta_1}{2}\sin^2\theta\sin^2\varphi-\frac{\beta_2}{2}\cos^2\theta-\gamma[\sin 2\theta(u_{zy}\cos\varphi+u_{yx}\sin\varphi)+u_{yy}\cos^2\theta+\sin^2\theta(u_{zz}\cos^2\varphi+u_{xz}\sin 2\varphi+u_{xx}\sin^2\varphi)]+\frac{\nu}{gM_0}\dot\varphi(1-\cos\theta)\right\} \tag{4}$$

and the dynamic drag function of the domain wall as

$$F=\frac{\lambda M_0}{2g}\dot{\mathbf{l}}^2=\frac{\lambda M_0}{2g}(\dot\theta^2+\dot\varphi^2\sin^2\theta), \tag{5}$$

where λ is the Gilbert damping constant.

The equations of motion for the angle variables of the vector $\mathbf{l}$ with allowance for the relaxation terms have the form

$$\alpha\nabla[\sin^2\theta(\nabla\varphi)]-\frac{\alpha}{c^2}\frac{d}{dt}(\dot\varphi\sin^2\theta)-\beta_1\sin^2\theta\sin\varphi\cos\varphi+\gamma[\sin^2\theta(u_{zz}\sin 2\varphi-2u_{xz}\cos 2\varphi-u_{xx}\sin 2\varphi)+\sin 2\theta(u_{zy}\sin\varphi-u_{yz}\cos\varphi)]-\frac{\nu}{gM_0}\dot\theta\sin\theta=\frac{\lambda}{gM_0}\dot\varphi\sin^2\theta, \tag{6}$$

$$\alpha\left(\Delta\theta-\frac{1}{c^2}\ddot\theta\right)+\sin\theta\cos\theta\left[\alpha\left(\frac{1}{c^2}\dot\varphi^2-(\nabla\varphi)^2\right)-\beta_1\sin^2\varphi+\beta_2\right]-\gamma[\sin 2\theta(u_{zz}\cos^2\varphi+u_{xz}\sin 2\varphi+u_{xx}\sin^2\varphi-u_{yy})+2\cos 2\theta(u_{zy}\cos\varphi+u_{yx}\sin\varphi)]+\frac{\nu}{gM_0}\dot\varphi\sin\theta=\frac{\lambda}{gM_0}\dot\theta. \tag{7}$$

If $\beta_1,\beta_2>0$, then the antiferromagnetism vector $\mathbf{l}$ in the homogeneous ground state is parallel to the Z axis, and two types of 180° domain walls can exist. We assume that the stable domain wall is that in which the vector $\mathbf{l}$ is rotated in the plane of the domain wall XZ, while the distribution of the magnetization is homogeneous along the Y axis. Such a domain wall corresponds to $\beta_2>\beta_1>0$ and $\theta=\theta_0=\pi/2$ (Ref. 14), and the angle variable $\varphi=\varphi_0(y)$ satisfies the equation

$$\alpha\varphi_0''-\beta_1\sin\varphi_0\cos\varphi_0=0. \tag{8}$$

The solution of equation (8) describing a static 180° domain wall and satisfying the boundary conditions $\varphi_0(-\infty)=0$ and $\varphi_0(+\infty)=\pi$ has the form

$$\varphi_0'=\frac{1}{y_0}R\sin\varphi_0=\frac{1}{y_0}R\rho\cosh^{-1}\frac{y}{y_0},\qquad \cos\varphi_0(y)=-R\tanh\frac{y}{y_0}, \tag{9}$$

where $y_0=\sqrt{\alpha/\beta_1}$ is the thickness of the domain wall, $R=\pm1$ is the topological charge, and $\rho=\pm1$ is a parameter describing the direction of rotation of the vector $\mathbf{l}$ in the domain wall.

As we know, 180° domain walls separating domains with opposite directions of the magnetization in a stripe domain structure have opposite topological charges R. The rotation of the vector $\mathbf{l}$ in the domain walls from $-R$ to $+R$ (or vice versa) can occur either through the positive or through the negative direction of the Z axis, depending on the parameter ρ. Therefore, the neighboring domain walls in a stripe domain structure with rotation of the vector $\mathbf{l}$ in the XZ plane correspond to values $l_z(y=\pm\infty)=\mp R$ and to one of the two values $l_x(y=0)=\pm\rho$. In the presence of an external field and a certain matching of the signs of the topological charges R and parameters ρ in adjacent domain walls in a weak ferromagnet, translational motion of the stripe domain structure as a whole can occur.[10]

The solutions of the system of equations of motion (6),(7) will be sought using the formalism of the perturbation theory for solitons[10,15–17] with the introduction of a collective coordinate of the center of the domain wall, $Y(t)$. In this case the zero-order function $\varphi_0(\xi)$, $\xi=y-Y(t)$, describes the motion of the unperturbed domain wall and has a structure analogous to the static solution (9). The higher-order functions $\theta_n(\xi,t)$ and $\varphi_n(\xi,t)$ $(n=1,2,\ldots)$ describe the motion of the perturbed domain wall and the excitation of spin waves as a result of the interaction with a sound wave.

LINEAR OSCILLATIONS OF THE DOMAIN WALLS

Suppose a monochromatic sound wave is propagating in the direction perpendicular to the plane of the domain wall, $\mathbf{u}=\mathrm{Re}\{u_0\exp[i(k_yy-\omega t)]\}$. The equations of the first order of perturbation theory in powers of the amplitude of the sound wave comprise a system of equations for the functions $\theta_1(\xi,t)$ and $\varphi_1(\xi,t)$:

$$\left(\hat L+\sigma+\frac{1}{\omega_1^2}\frac{d^2}{dt^2}+\frac{\omega_r}{\omega_1^2}\frac{d}{dt}\right)\theta_1(\xi,t)-\frac{\omega_\nu}{\omega_1^2}\frac{d\varphi_1(\xi,t)}{dt}=-\frac{R}{y_0\omega_1^2}\omega_\nu V_1\sin\varphi_0+\frac{ik\gamma}{\beta_1}\exp\{i[k(Y+\xi)-\omega t]\}\times(u_{0x}\sin\varphi_0+u_{0z}\cos\varphi_0), \tag{10}$$

$$\left(\hat L+\frac{1}{\omega_1^2}\frac{d^2}{dt^2}+\frac{\omega_r}{\omega_1^2}\frac{d}{dt}\right)\varphi_1(\xi,t)+\frac{\omega_\nu}{\omega_1^2}\frac{d\theta_1(\xi,t)}{dt}=\frac{R}{y_0\omega_1^2}(\dot V_1+\omega_rV_1)\sin\varphi_0, \tag{11}$$

where $\omega_1=c/y_0=gM_0\sqrt{\beta_1\delta}/2$, $\omega_r=\lambda\delta gM_0/4$, $\omega_\nu=\nu\delta gM_0/4$ are the frequency characteristics of the ferrite, $k=k_y=\omega/s$ is the wave vector of the sound wave, ω and s are the frequency and velocity of the wave, and $\sigma=(\beta_2-\beta_1)/\beta_1$.

The Hermitian operator $\hat L=-y_0^2d^2/d\xi^2+1-2/[\cosh^2(\xi/y_0)]$ has a set of known Vinterov functions $f_0(\xi)$

and $f_p(\xi)$ and eigenvalues λ_0 and λ_p. We seek the solution of the system of first-order equations (10) and (11) in the form of an expansion in the complete set of eigenfunctions of the operator $\hat{L}$, with the result

$$\varphi_1(\xi,t)=\frac{\pi\gamma k^2 y_0}{2\beta_1}\mathrm{Re}\{B_1(\xi)\exp[i(kY-\omega t)]\}, \tag{12}$$

$$\theta_1(\xi,t)=\frac{\pi\gamma k^2 y_0}{2\beta_1}\mathrm{Re}\{B_2(\xi)\exp[i(kY-\omega t)]\}. \tag{13}$$

Here we have adopted the notation

$$B_1(\xi)=\frac{\nu\omega}{\omega_0}\left[-\frac{y_0}{\pi}[Ru_{0z}D_1(\xi)+i\rho u_{0x}D_2(\xi)]+b_1 f_k(\xi)\right], \tag{14}$$

$$B_2(\xi)=-\frac{y_0}{\pi}[\rho u_{0x}D_3(\xi)+iRu_{0z}D_4(\xi)] + b_2 f_k(\xi)+b_3 f_0(\xi),$$

$$D_1(\xi)=\sqrt{L}\int_{-\infty}^{\infty}dp f_p(\xi)\frac{\Omega(p,q)}{\sinh[\pi y_0(k-p)/2]},$$

$$D_2(\xi)=\sqrt{L}\int_{-\infty}^{\infty}dp f_p(\xi)\frac{\Omega(p,q)}{\cosh[\pi y_0(k-p)/2]},$$

$$D_3(\xi)=\sqrt{L}\int_{-\infty}^{\infty}dp f_p(\xi)\frac{\Omega(p,q)(\lambda_p-q)}{\cosh[\pi y_0(k-p)/2]},$$

$$D_4(\xi)=\sqrt{L}\int_{-\infty}^{\infty}dp f_p(\xi)\frac{\Omega(p,q)(\lambda_p-q)}{\sinh[\pi y_0(k-p)/2]},$$

$$b_1=\frac{2R\sqrt{L}u_{0z}\Omega(k,q)}{\pi k y_0},\quad b_2=-i(\lambda_k-q)b_1,$$

$$b_3=\frac{\sqrt{2y_0 q}}{(\sigma-q)q+kq_1}\left[\frac{Ru_{0z}}{\cosh(\pi k y_0/2)}+\frac{\rho i u_{0x}}{\sinh(\pi k y_0/2)}\right],$$

where $\Omega(n,q)=\{\sqrt{\lambda_n}[(\lambda_n-q)(\lambda_n-q+\sigma)-\kappa q_1]\}^{-1}$, with $\lambda_n=1+n^2y_0^2$ $(n=p,k)$, $q=q_1+iq_2$, $q_1=(\omega/\omega_1)^2$, and $q_2=(\omega\omega_r/\omega_1^2)$; $\kappa=\delta\nu^2/4\beta_1$, $\omega_0=\beta_1 g M_0$, and L is the length of the crystal.

It follows from the solutions (12) and (13) that a sound wave propagating in the direction perpendicular to the plane of rotation of the vector **l** in the domain wall will excite localized and nonlocalized spin waves. These excitations are brought about only by transverse acoustic oscillations.

From Eq. (11) under the condition of vanishing amplitude of the Goldstone mode[10] we obtain an equation for the determining the domain wall velocity

$$\dot{V}_1(t)+\left(\omega_r-\frac{i\omega\kappa}{\sigma-q}\right)V_1(t) = \frac{\pi\gamma(ky_0)^2\omega\omega_0\kappa}{2\nu\beta_1(\sigma-q)}\left[\frac{Ru_{0x}}{\sinh(\pi k y_0/2)}-\frac{i\rho u_{0z}}{\cosh(\pi k y_0/2)}\right] \times\exp[i(kY-\omega t)]. \tag{15}$$

The solution of equation (15) can be written as

$$V_1(t) = \frac{\pi\gamma(ky_0)^2\omega\omega_0\kappa}{2\nu\beta_1(\sigma-q)\{\omega_r-i\omega[1+\kappa/(\sigma-q)]\}} \times\left[\frac{Ru_{0x}}{\sinh(\pi k y_0/2)}-\frac{i\rho u_{0z}}{\cosh(\pi k y_0/2)}\right]\exp[i(kY-\omega t)]. \tag{16}$$

It follows from (16) that in the approximation linear in the amplitude of the sound wave, the domain wall velocity in the ferrite is $V_1(t)\sim\kappa\sim\nu$. Interestingly, in a weak ferromagnet in the linear approximation a transverse sound wave does not excite oscillations of the domain wall.[10]

The solution (16) can be used to find the domain wall displacement $y(t)$ over the period of the oscillations:

$$y(t)=\frac{\pi\gamma(ky_0)^2\omega_\nu}{2\beta_1[Q_1^2+Q_2^2]}\left[\left(\frac{Q_1Ru_{0x}}{\sinh(\pi k y_0/2)}+\frac{Q_2\rho u_{0z}}{\cosh(\pi k y_0/2)}\right)\times\sin(kY-\omega t)+\left[\left(\frac{Q_2Ru_{0x}}{\sinh(\pi k y_0/2)}-\frac{Q_1\rho u_{0z}}{\cosh(\pi k y_0/2)}\right)\times\cos(kY-\omega t)\right], \tag{17}$$

where $Q_1=\omega_r(\sigma-2q_1)$; $Q_2=\omega(\kappa+\sigma-q_1)-\omega_r q_2$. In particular, for yttrium iron garnet $Y_3Fe_5O_{12}$ the average values of the absolute magnitude of the displacement at a frequency $\omega\sim10^6$ s^{-1} for $\nu=10^{-2}$ and 10^{-3} are 10^{-7} and 10^{-8} cm, respectively. The values obtained for the absolute magnitude of the displacement are in good agreement with the results of Refs. 11 and 18.

NONLINEAR MOTION OF THE DOMAIN WALLS

Let us write the system of second-order equations for the functions $\theta_2(\xi,t)$ and $\varphi_2(\xi,t)$:

$$\hat{L}\varphi_2=-\frac{ik\gamma}{\beta_1}\exp[i(k(Y+\xi)-\omega t)]\theta_1(u_{0z}\sin\varphi_0 - u_{0x}\cos\varphi_0)-2R_{y_0}\theta_1\theta_1'\sin\varphi_0+\frac{1}{\omega_1^2}(\dot{V}_1+\omega_r V_1)\varphi_1' + \frac{R}{y_0\omega_1^2}(\dot{V}_2+\omega_r V_2)\sin\varphi_0+\varphi_1^2\sin 2\varphi_0 + \frac{\omega_\nu}{\omega_1^2}V_1\theta_1'-\frac{1}{\omega_1^2 y_0^2}V_1^2\sin\varphi_0\cos\varphi_0, \tag{18}$$

$$(\hat{L}+\sigma)\theta_2 = -\frac{ik\gamma}{\beta_1}\exp[i(k(Y+\xi)-\omega t)] \times[2\theta_1 u_{0y}+\varphi_1(u_{0z}\sin\varphi_0-u_{0x}\cos\varphi_0)] + \frac{1}{\omega_1^2}(\dot{V}_1+\omega_r V_1)\theta_1' + 2Ry_0\theta_1\varphi_1'\sin\varphi_0 + \theta_1\varphi_1\sin 2\varphi_0 - \frac{\omega_\nu}{\omega_1^2}\left(V_1\varphi_1' + \frac{R}{y_0}V_2\sin\varphi_0\right). \quad (19)$$

The solution, as for the system of first-order equations (10), (11), can be sought in the form of an expansion in eigenfunctions of the operator $\hat{L}$. However, we shall not give the complete solution of system (18), (19) here. Since we are interested only in determining the domain wall velocity in the second order of perturbation theory, $V_2(t)$, it is sufficient for our purposes to find the coefficient $d_0^{(2)}$ in the expansion

$$\varphi_2(\xi,t) = \mathrm{Re}\left\{\sum_p [d_p^{(2)}f_p(\xi)+d_0^{(2)}f_0(\xi)]\exp[i(ky-\omega t)]\right\} \quad (20)$$

and equate it to zero.[10] When solutions (12)–(14) are taken into account, the equation for $V_2(t)$ becomes

$$\dot{V}_2(t)+\omega_r V_2 = N + N_1\exp(2i\omega t)+N_2\exp(-2i\omega t), \quad (21)$$

where

$$N = R\rho\,\mathrm{Re}\left\{\int_{-\infty}^{\infty}\frac{d\xi}{\cosh\xi/y_0}\left[\frac{ik\gamma\omega_1^2}{4\beta_1}\exp[i(k(Y+\xi)-\omega t)] \times\theta_1^*(\xi,t)(u_{0z}\sin\varphi_0-u_{0x}\cos\varphi_0) - V_1\frac{\omega_\nu}{4}\theta_1^{*\prime}(\xi,t) - \frac{\omega_1^2}{2}\theta_1(\xi,t)\theta_1^*(\xi,t)\sin\varphi_0\cos\varphi_0 - \frac{1}{4}(\dot{V}_1+\omega_r V_1)\varphi_1^{*\prime}(\xi,t) - \frac{\omega_1^2}{2}\varphi_1(\xi,t)\varphi_1^*(\xi,t)\sin\varphi_0\cos\varphi_0\right]\right\}, \quad (22)$$

(the asterisk * denotes the complex conjugate).

The explicit form of the expressions for N_1 and N_2, which are similar to Eq. (22), will not be needed, since in the subsequent averaging of the solutions of equation (21) the terms containing N_1 and N_2 vanish.

Integrating (21) and averaging over the period of the oscillations, we obtain the solution for the drift velocity of a domain wall in the field of a sound wave:

$$V_{\mathrm{dr}} = \mu_{xx}(k)(ku_{0x})^2 + R\rho\mu_{xz}(k)(ku_{0x})(ku_{0z}) + \mu_{zz}(k)(ku_{0z})^2, \quad (23)$$

where $\mu_{ij}(k)$ is the nonlinear mobility of a domain wall in the field of an acoustic wave. Analysis of the rather awkward expressions for $\mu_{ij}(k)$ in the general case is difficult and not very informative. It is better to examine the characteristic limiting situations.

The most interesting of these from the standpoint of experiment is the long-wavelength approximation ($ky_0 \ll 1$), which corresponds to the frequency region $\omega = sk \ll 10^{10}\ \mathrm{s}^{-1}$. In this limit the expressions for the nonlinear mobility reduce to

$$\mu_{ij}(k) = \mu_0[A(k)+F(k)], \quad (24)$$

where $\mu_0 = \eta_0\delta(\gamma M_0)^2/4\beta_1$, and $\eta_0 = \pi y_0 g^2/4\omega_r$ is the characteristic nonlinear domain wall mobility in a ferrite in an alternating magnetic field.[17]

The structure of expression (24) reflects the circumstance that the nonlinear mobility in a ferrite is formed by terms that can be interpreted as an antiferromagnetic component $A(k)$ and a ferromagnetic component $F(k)$. The functions $A(k)$ and $F(k)$ depend importantly on the polarization of the sound wave, and for the corresponding mobilities from (23) are as follows: for μ_{xz}

$$A(k) = \frac{(ky_0)^2}{(\sigma+1)}\left[\frac{1}{2}+\frac{1}{\pi}+\frac{1}{3\pi(\sigma+1)}-\frac{\pi}{3\sigma}\right], \quad F(k) = -\frac{1}{2}\frac{q_1 q_3}{\sigma(\sigma+1)}, \quad (25)$$

for μ_{xx}

$$A(k) = \frac{2ky_0 q_2}{\sigma^2(\sigma+1)}, \quad F(k) = \frac{1ky_0 q_2 q_3}{22\sigma(\sigma+1)}, \quad (26)$$

and for μ_{zz}

$$A(k) = \frac{\pi k y_0 q_2}{2\sigma(\sigma+1)^2}, \quad F(k) = -\frac{\pi}{4}\frac{ky_0 q_2 q_3}{\sigma(\sigma+1)}, \quad (27)$$

where $q_3 = \omega_\nu^2/(\omega_r^2+\omega^2)$.

It follows from expressions (25)–(27) that the nonlinear domain wall mobility in a ferrite obeys $\mu_{ij}\sim\omega^2$, and the drift velocity obeys $V_{\mathrm{dr}}\sim k^4$, i.e., it is invariant with respect to the substitution $k\to -k$. Thus the direction of induced motion of the domain wall does not depend on the direction of propagation of the sound wave. Since $ky_0 \gg q_2$ and $q_1 \gg ky_0 q_2$, the greatest effect is due to the nonlinear mobility $\mu_{xz}(k)$.

In the neighborhood of the compensation point of the ferrite (in the formal limit $\nu = 0$) the results of this study should agree[1)] with the corresponding results of Ref. 10 if the Dzhyaloshinskiĭ interaction in the weak ferromagnet is neglected. It should also be noted that in a weak ferromagnet[10] the easy axis is the X axis, while in a ferrite it is the Z axis.

The character of the dependence of the drift velocity (23) on the topological charge R of the domain wall and the parameter ρ suggests that drift of the stripe domain structure formed by the 180° domain walls of the investigated structure (8), (9) can occur. Drift of the domain walls occurs if the sound wave is polarized along the X or Z axis. In this case V_{dr} is independent of R and ρ, and the domain wall motion is therefore independent of the direction of rotation of the vector **l** in the neighboring domain walls. The drift of a domain wall can also occur in the case when the sound wave is polarized in the XZ plane. For this, however, it is necessary to have a certain matching of the signs of the parameters R and ρ. The conditions for this matching are discussed in Ref. 10.

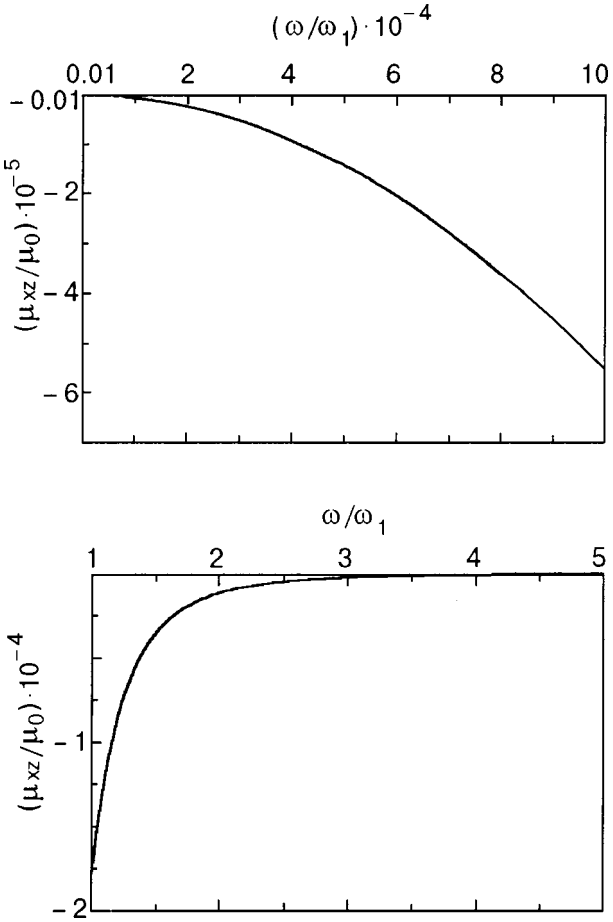

FIG. 1. Frequency dependence of the nonlinear mobility μ_{xz} in the iron garnet $Y_3Fe_5O_{12}$ in the long-wavelength (a) and short-wavelength (b) approximations.

It is convenient to represent the expression for the characteristic nonlinear domain wall mobility in the field of a sound wave as

$$\mu_0=\frac{\pi y_0 g(\gamma M_0)^2}{4\beta_1\lambda M_0^3}, \tag{28}$$

from which we see that in a specified sound field the maximum effect should be expected in magnets having a large magnetoelastic coupling constant and a low saturation magnetization. It is clear on physical grounds that the damping should be insignificant, and the domain wall thickness should be large. These requirements are best met by materials with antiferromagnetic and weak ferromagnetic types of magnetic ordering.

Let us make some numerical estimates. Using the typical parameters for a ferrite (e.g., $Y_3Fe_5O_{12}$; Ref. 19): $y_0 \approx 10^{-5}$ cm, $\beta_1 \approx 0.6$, $\sigma \sim 1$, $\lambda \sim 10^{-4}$, $M_0 = 140$ Oe, $\gamma M_0^2 \approx 3.5\times 10^6$ erg/cm^3, $g = 1.76\times 10^7$ (s·Oe)$^{-1}$, $\omega_1 \sim 10^{11}$ s^{-1}, and $\nu \approx 5\times 10^{-3}$, at a frequency $\omega \sim 10^8$ s^{-1} we obtain a value of the characteristic nonlinear mobility $\mu_0 \approx 10^{13}$ cm/s. For a sound velocity $s \sim 10^5$ cm/s and a maximum permissible value of the strain tensor $ku_0 \sim 10^{-5}$, the domain wall drift velocity reaches 0.8 cm/s. Estimates show that for the chosen value of ν the ferromagnetic component makes the larger contribution to the domain wall drift velocity. The frequency dependence of the nonlinear mobility $\mu_{xz}(k)$ in a ferrite is shown in Fig. 1a and agrees qualitatively with the corresponding frequency dependence for a weak ferromagnet.

In the short-wavelength approximation ($ky_0 \gg 1$), which corresponds to hypersonic frequencies $\omega \gg 10^{10}$ s^{-1}, the nonlinear mobilities of a ferrite fall off as ω^{-4}:

$$\frac{Mu_{xz}}{\mu_0}=-\left(\frac{1}{2}+\frac{4}{\pi}\right)\frac{1}{[(ky_0)^2-q_1]^2},$$
$$\frac{\mu_{xx}}{\mu_0}=-\frac{4}{3\pi}\frac{q_2}{ky_0[(ky_0)^2-q_1]^2}, \quad \mu_{zz}=2\mu_{xx}, \tag{29}$$

and the magnitude of the effect in this case is inversely proportional to the square of the frequency, in agreement with Ref. 20.

As in the long-wavelength approximation, the main contribution to the drift velocity comes from the off-diagonal mobility $\mu_{xz}(k)$. The frequency dependence of the nonlinear mobility $\mu_{xz}(k)$ in the short-wavelength approximation is shown in Fig. 1b.

The authors thank A. L. Sukstanskiĭ for a discussion of the results of this study.

*E-mail: vsg@donace.dn.ua

[1)]There is a misprint in the corresponding expressions for the nonlinear mobility in a weak ferromagnet in Ref. 10, and for that reason the expressions for the functions $A(k)$ differ from those given above.

[1] V. G. Bar'yakhtar and B. A. Ivanov, Fiz. Met. Metalloved. **39**, 478 (1975).
[2] A. A. Lugovoĭ, E. A. Turov, *Dynamical and Kinetic Properties of Magnets*, edited by S. V. Vonsovskiĭ and E. A. Turov [in Russian], Nauka, Moscow (1986).
[3] L. É. Gurevich and É. V. Liverts, Zh. Éksp. Teor. Fiz. **88**, 1257 (1985) [Sov. Phys. JETP **61**, 743 (1985)].
[4] G. M. Nedlin and R. Kh. Shapiro, Fiz. Tverd. Tela (Leningrad) **18**, 1696 (1976) [Sov. Phys. Solid State **18**, 985 (1976)].
[5] A. V. Mitin and V. A. Tarasov, Zh. Éksp. Teor. Fiz. **72**, 793 (1977) [Sov. Phys. JETP **45**, 414 (1977)].
[6] E. A. Turov and A. A. Lugovoĭ, Fiz. Met. Metalloved. **50**, 903 (1980).
[7] R. J. Yeh, H. E. Wigen, and H. Döotch, Solid State Commun. **44**, 1183 (1982).
[8] Yu. I. Gorobets and S. I. Denisov, Ukr. Fiz. Zh. **35**, 271 (1990).
[9] S. I. Denisov, Fiz. Tverd. Tela (Leningrad) **31**, 270 (1989) [Sov. Phys. Solid State **31**, 1992 (1989)].
[10] V. S. Gerasimchuk and A. L. Sukstanskiĭ, Zh. Éksp. Teor. Fiz. **106**, 1146 (1994) [JETP **79**, 622 (1994)].
[11] V. K. Vlasko-Vlasov and O. A. Tikhomirov, Fiz. Tverd. Tela (Leningrad) **32**, **1678**, (1990) [Sov. Phys. Solid State **32**, 978 (1990)].
[12] V. K. Vlasko-Vlasov and O. A. Tikhomirov, Fiz. Tverd. Tela (Leningrad) **33**, 3498 (1991) [Sov. Phys. Solid State **33**, 1964 (1991)].
[13] M. V. Chetkin, V. V. Lykov, A. A. Makovozova, and A. G. Belonogov, Fiz. Tverd. Tela (Leningrad) **33**, 307 (1991) [Sov. Phys. Solid State **33**, 177 (1991)].
[14] B. A. Ivanov and A. L. Sukstanskiĭ, Zh. Éksp. Teor. Fiz. **84**, 370 (1983) [Sov. Phys. JETP **57**, 214 (1983)].
[15] V. G. Bar'yakhtar, Yu. I. Gorobets, and S. I. Denisov, Zh. Éksp. Teor. Fiz. **98**, 1345 (1990) [Sov. Phys. JETP **71**, 751 (1990)].
[16] V. S. Gerasimchuk and A. L. Sukstanskiĭ, Zh. Éksp. Teor. Fiz. **103**, 151 (1993) [JETP **76**, 82 (1993)].
[17] V. S. Gerasimchuk and A. L. Sukstanskiĭ, J. Magn. Magn. Mater. **146**, 323 (1995).
[18] V. G. Bar'yakhtar, B. A. Ivanov, P. D. Kim, A. L. Sukstanskiĭ, and D. Ch. Khvan, JETP Lett. **37**, 41 (1983).
[19] S. Krupicka, *Physik der Ferrite und der Verwandten Magnetischen Oxide* [Academia, Prague (1973); Mir, Moscow (1976)].
[20] V. S. Gerasimchuk and Yu. I. Gorobets, Ukr. Fiz. Zh. **24**, 289 (1979).

Translated by Steve Torstveit

Anomalies of the magnon spectrum of a bounded antiferromagnet with a center of antisymmetry. II. Effects of the inhomogeneous exchange interaction

S. V. Tarasenko*

A. A. Galkin Physics and Technology Institute, National Academy of Sciences of Ukraine, ul. R. Lyuksemburg 72, 83114 Donetsk, Ukraine

(Submitted July 14, 2000)
Fiz. Nizk. Temp. **27**, 178–187 (February 2001)

By simultaneously taking into account the electric-dipole, magnetic-dipole, and inhomogeneous exchange interactions, it is shown that the spectrum of propagating bulk magnons in a thin-film tetragonal antiferromagnet with a center of antisymmetry can exhibit anomalies that do not exist in either the model of an infinite magnet or in thin films of centrosymmetric antiferromagnets. [DOI: 10.1063/1.1353704]

INTRODUCTION

It was shown in Ref. 1 that in an infinite antiferromagnet the presence of a center of antisymmetry can lead to the formation of a new class of nonexchange magnons — electrostatic spin waves. The physical mechanism responsible for the existence of this type of propagating spin excitations in an infinite magnetically ordered crystal is the indirect spin–spin exchange through the long-range electric-dipole field. As a result, in a tetragonal antiferromagnet with a center of antisymmetry, for a certain geometry of the problem it becomes possible to have simultaneous (with the same wave number $k_\perp$ and frequency ω) and independent propagation of nonexchange magnons of the magnetostatic and electrostatic types.

In addition, it follows from the results of Ref. 1 that in the general case the dispersion relation of an electrostatic spin wave depends substantially on the relationship between the Néel and Debye temperatures of the magnetically ordered crystal. In particular, for a low-temperature antiferromagnet ($T_N < T_D$), it is found that when the interaction of the spin subsystem of a real crystal and the lattice is taken into account in a consistent way for magnetic crystals of the type under discussion, then in addition to the dipole mechanism of spin–spin interaction there arises an indirect interaction of spins via the long-range field of quasistatic magnetoelastic deformations. Here it must be taken into account that in the spin-wave spectrum of antiferromagnets there are simultaneously an exchange weakening of magnetic dipole effects and an exchange enhancement of the effects of the linear magnon–phonon interaction. As a result, as was shown in Ref. 1, the dispersion curves of modes belonging to the spectrum of bulk nonexchange electric-dipole-active magnons propagating along a thin film of an antiferromagnet magnetoelectric can exhibit previously unknown anomalies for $k_\perp \neq 0$: 1) regions of the dispersion curve with $\partial\omega/\partial k_\perp = 0$; 2) points of degeneracy of the dispersion curves for modes with indices ν and ρ; 3) bunching points of the spectrum for $k_\perp = 0$ and $k_\perp \to \infty$.

However, the construction of a consistent theoretical model for the dynamics of a real magnetic crystal at temperatures below the magnetic ordering temperature is impossible without taking into account the nonlocal part of the Heisenberg exchange, whereas all the calculations in Ref. 1 were done without allowing for the effects of the inhomogeneous exchange interaction (for that purpose it was assumed in Eq. (3) and beyond in Ref. 1 that the condition $\alpha = 0$ holds, where α is the inhomogeneous exchange interaction constant).[1)]

Therefore, our goal in the present paper is to determine the necessary conditions under which the inhomogeneous exchange interaction will lead to the formation of previously uninvestigated anomalies in the spectrum of bulk spin-wave excitations of a thin film of a tetragonal antiferromagnet with a center of antisymmetry but which are absent in the model of an infinite crystal.

Following Ref. 1, in what follows we shall analyze the electric-dipole-active part of the magnon spectrum in the collinear phase ($\mathbf{l} \| 0z$) of a two-sublattice model of a tetragonal antiferromagnet (fourfold axis $0z$), limiting consideration the a spin-wave propagation geometry that admits the independent existence of nonexchange magnons of the magnetostatic and electrostatic types.

This paper consists of several sections. In Sec. 1, on the basis of a calculation that simultaneously takes into account the magnetic-dipole, electric-dipole, magnetoelastic, and inhomogeneous exchange interactions in a thin-film magnetoelectric antiferromagnet with a center of antisymmetry, we study the additional (in comparison with the zero-exchange approximation) anomalies that arise in the spin dynamics on account of the nonlocality of the Heisenberg mechanism of spin–spin interaction. Section 2 is devoted to an analysis of how the structure of the solutions obtained is related to the shape of the wave-vector surface of the corresponding type of normal spin-wave excitations of an infinite magnetoelectric. In Sec. 3 we present the results of a study of the main features that arise in the spectrum of bulk magnons as a result of the change in the electrodynamic boundary conditions on the surface of a thin-film magnetoelectric antiferromagnet. An analysis of the influence of the acoustic retardation effect on the overall structure of the spectrum of bulk normal oscillations of a thin magnetoelectric film is presented in Sec. 4. The main conclusions drawn from the results of this study are discussed in the Conclusion.

1. EFFECTS OF INHOMOGENEOUS EXCHANGE

As we have said, in an analysis of the dispersion relations (1.16) in Ref. 1, we neglected effects due to the inhomogeneous exchange interaction, for which purpose in Eqs. (1.18)–(1.21) we formally took the limit $\alpha\to 0$. It follows from (1.16) that in the case when $\alpha\neq 0$ ($\omega/c\to 0$, $\omega/c_{\rm ph}\to 0$) relations (1.18)–(1.21) can be written in the following forms:

for $T_N > T_D$ with $\mathbf{n}\| 0z$

$$\Omega_\nu^2(k_\perp)=[R+s^2(k_\perp^2+\kappa_\nu^2)]\left(1-\xi^2+\frac{\xi^2\varepsilon_\perp k_\perp^2}{\kappa_\nu^2\varepsilon+k_\perp^2(1+\varepsilon_\perp)}\right); \tag{1}$$

and with $\mathbf{n}\| 0x$

$$\Omega_\nu^2(k_\perp)=[R+s^2(k_\perp^2+\kappa_\nu^2)]\left(1-\xi^2+\frac{\xi^2\varepsilon_\perp \kappa_\nu^2}{k_\perp^2\varepsilon+\kappa_\nu^2(1+\varepsilon_{\perp-})}\right); \tag{2}$$

for $T_N < T_D$ with $\mathbf{n}\| 0z$

$$\Omega_\nu^2(k_\perp)=[R_\nu(k_\perp)+s^2(k_\perp^2+\kappa_\nu^2)]\times\left(1-\xi^2+\frac{\xi^2\varepsilon_\perp k_\perp^2}{\kappa_\nu^2\varepsilon+k_\perp^2(1+\varepsilon_\perp)}\right); \tag{3}$$

and with $\mathbf{n}\| 0x$

$$\Omega_\nu^2(k_\perp)=[R_\nu(k_\perp)+s^2(k_\perp^2+\kappa_\nu^2)]\times\left(1-\xi^2+\frac{\xi^2\varepsilon_\perp \kappa_\nu^2}{k_\perp^2\varepsilon+\kappa_\nu^2(1+\varepsilon_\perp)}\right). \tag{4}$$

A joint analysis of relations (1.18)–(1.21) and (1)–(4) shows that if the relation $\Omega_\nu(k_\perp)<\Omega_\rho(k_\perp)$ holds in the neighborhood of a bunching point (ω_A^* or ω_B^*) for modes with specified indices ν and ρ ($\nu<\rho$) in the zero-exchange limit (1.18)–(1.21), then, even for an infinitely small value of the inhomogeneous exchange interaction constant α, it becomes possible for the bunching point to vanish and for an additional crossing point of the dispersion curves to appear at $k_\perp\neq 0$ for the modes $\Omega_\nu(k_\perp)$ and $\Omega_\rho(k_\perp)$ given by relations (1)–(4). If this condition does not hold in the neighborhood of a given bunching point of the dispersion curves (1.18)–(1.21), then taking into account a nonzero value $\alpha\neq 0$ will lead only to a vanishing of the bunching point in (1)–(4).

It follows from a comparison of Eqs. (1), (2) and (1.18), (1.19) that in a high-temperature antiferromagnet with a center of antisymmetry, taking into account a nonzero value $\alpha\neq 0$ will substantial alter the structure of the spectrum of propagating bulk spin-wave excitations in comparison with (1.18), (1.19). In particular, for $\mathbf{n}\|\mathbf{l}$ it becomes possible for two crossing points $\Omega_\nu(k_{\nu\rho})=\Omega_\rho(k_{\nu\rho})$ of the dispersion curves of the modes with the specified indices ν and ρ to appear for $k_\perp\neq 0$. It follows from (1) that both of these crossover points in the spectrum of the electric-dipole-active exchange spin-wave excitations of a high-temperature antiferromagnet exist only when both the electric-dipole and the inhomogeneous exchange mechanisms of spin–spin interaction are taken into account (i.e., for $\hat{\gamma}\neq 0$ the constant $\alpha\neq 0$). If, on the contrary, $\mathbf{n}\perp\mathbf{l}\|\mathbf{k}_\perp$, then as follows from (2), simultaneously taking the electric-dipole and Heisenberg mechanisms of spin–spin exchange into account can lead to the formation of a minimum on the dispersion curve at $k_\perp\neq 0$ for a mode with index ν in the spectrum of dipole–exchange spin-wave excitations of a thin-film magnetoelectric with $T_N > T_D$.

For a film of a low-temperature antiferromagnet with a center of antisymmetry, analysis of relations (3) and (4) shows that even without the magnetoelectric interaction (formally this corresponds to taking the limit $\hat{\gamma}\to 0$), hybridization of the elastostatic and Heisenberg mechanisms of spin–spin interaction will lead to the following features in the bulk magnon spectrum in comparison with the zero-exchange ($\alpha\to 0$) limit (1.20), (1.21): 1) the presence of two crossover points of the dispersion curves of elastic–exchange spin-wave excitations with indices ν and ρ ($k_{\nu\rho}^{\pm}$); 2) the formation of two extrema of the dispersion curve $\Omega_\nu(k_\perp)$, one of which corresponds to a maximum, at $k_{*\nu}^-$, and the other to a minimum, at $k_{*\nu}^+$. In the zero-exchange limit $\alpha\to 0$ there is a limiting transition to the characteristic points of the spectra given by (1.20) and (1.21): $k_{*\nu}^-\to k_{*\nu}$, $k_{*\nu}^+\to\infty$, $k_{\nu\rho}^-\to 0$, $k_{\nu\rho}^+\to k_{\nu\rho}$.

Taking the electrostatic mechanism of nonlocal spin–spin interaction into account in addition to the elastostatic and Heisenberg mechanisms in turn leads to the appearance of additional anomalies in the spectrum of spin-wave excitations in comparison with the limiting case of purely elastic–exchange magnons studied above (i.e., for $\gamma\to 0$ the constant $\alpha\neq 0$). First, in those cases when in the zero-exchange limit (1.20), (1.21) the dispersion curve of a mode of bulk spin-wave oscillations in the neighborhood of the short-wavelength bunching point corresponds to a wave of the backward type ($\partial\Omega_\nu/\partial k_\perp<0$), taking the inhomogeneous exchange interaction into account will lead to the formation of a minimum on the corresponding dispersion curve. Second, it follows from (3) and (4) that for $\mathbf{n}\|\mathbf{l}$ or for $\mathbf{n}\perp\mathbf{k}_\perp$ the dispersion curves corresponding to modes of the magnon spectrum with indices ν and ρ can have no crossover point or can have two or four of them. In particular, for $\mathbf{n}\|\mathbf{l}$ in the case when the spectrum has four crossover points (k_1–k_4, with $k_i<k_j$ for $i<j$ $(i,j=1-4)$), it is easy to see that when the electrostatic mechanism of spin–spin interaction is neglected ($\hat{\gamma}\to 0$), one has $k_1\to 0$, $k_2\to k_{\nu\rho}^-$, $k_3\to k_{\nu\rho}^+$, and $k_4\to\infty$.

An analysis of relations (1)–(4) shows that for $\alpha\neq 0$ the number of crossover points of the spectrum for modes with indices ν and ρ is always even ($N_{\nu\rho}\leqslant 4$). With increasing $(\kappa_\nu^2-\kappa_\rho^2)$ and $\alpha\neq 0$ the value of $N_{\nu\rho}$ can change only by amounts that are multiples of two. In the final analysis, for large enough values of ν and ρ or a small enough thickness d of the magnetic film, the corresponding dispersion curve $\Omega_\nu(k_\perp)$ described by relations (1)–(4) will, for any value of the wave number $k_\perp$, be a wave of the forward type ($\partial\Omega_\nu/\partial k_\perp>0$) having neither inflection points ($\partial^2\Omega_\nu/\partial k_\perp^2=0$) nor crossover points ($N_{\nu\rho}=0$).

It is known from crystallography[2] that in an analysis of the conditions of reflection and refraction of a bulk normal oscillation at the boundary of a crystal, an important role is played by the shape of the refraction surface of that normal oscillation. Thus the local geometry of the surface of wave

vectors of the investigated bulk normal oscillations of an infinite crystal should also have a substantial effect on the structure of the spectrum of bulk normal oscillations of a crystal of finite size, since the spatial distribution of the amplitude of the bulk modes is the result of the interference of the normal modes incident on and reflected from the boundaries of the sample. For this reason in the next Section we shall analyze the influence of the electric-dipole, elastostatic, and inhomogeneous exchange interactions on the shape of the refraction surface of normal spin-wave modes in an infinite magnet and the relation of its local geometry to the aforementioned anomalies in the spectrum of bulk magnons in a thin magnetoelectric film of a high-temperature or low-temperature antiferromagnet.

2. CONNECTION WITH THE SHAPE OF THE REFRACTION SURFACE

Since the wave vector of the wave under study in relations (1.9) and (1)–(4) lies in the xz plane, in order to solve the stated problem it is necessary to study the shape of a section of the isofrequency surface ($\omega=\text{const}$) of the investigated electric-dipole-active spin wave in $\mathbf{k}$ space by a plane $k_x k_z$ (or, in other words, the shape of the curve of intersection of the isofrequency surface and the plane) with the aid of Eq. (1.9) under the condition $\omega/c\to 0$, $\omega/c_{\text{ph}}|\mathbf{k}|\to\infty$ for $T_N>T_D$ or $\omega/c\to 0$, $\omega/c_{\text{ph}}|\mathbf{k}|\to 0$ for $T_N<T_D$. The corresponding expression can be written in the form

$$s^2\mathbf{k}^2=\omega^2\left(1-\xi^2+\frac{\xi^2\varepsilon_\perp}{\varepsilon\tan^2\theta+(1+\varepsilon_\perp)}\right)^{-1}-\omega_0^2-\omega_{me}^2 \quad \text{for } T_N>T_D \tag{5}$$

and

$$s^2\mathbf{k}^2=\omega^2\left(1-\xi^2+\frac{\xi^2\varepsilon_\perp}{\varepsilon\tan^2\theta+(1+\varepsilon_\perp)}\right)^{-1}-\omega_0^2-\omega_{me}^2\left(1-\frac{c_{44}(\sin^2\theta\overline{\Lambda}_{11}+\cos^2\theta\overline{\Lambda}_{33}-\sin 2\theta\overline{\Lambda}_{13})}{\rho[\overline{\Lambda}_{11}\overline{\Lambda}_{33}-\Lambda_{13}^2]}\right) \quad \text{for } T_N<T_D, \tag{6}$$

$(k_z^2/\mathbf{k}^2\equiv\sin^2\theta,\quad \mathbf{k}^2\equiv k_x^2+k_z^2)$,

$\overline{\Lambda}_{ik}\equiv\Lambda_{ik}(k_x\equiv k\cos\theta,\quad k_z\equiv k\sin\theta)$

.

Analysis of the extremal points of the curves described by expressions (5) and (6) and a comparison of these points with the results of the foregoing analysis of the shape of the dispersion curves (1)–(4) show that the presence of a local maximum on the dispersion curve of the waveguide magnon under study is due to the formation of a segment with maximum negative curvature on the corresponding section of the diffraction surface of the normal spin wave of the same polarization [(5), (6)] in the infinite crystal. The position of this segment on the curve (5), (6) in $\mathbf{k}$ space is determined by the condition $\partial k/\partial\theta=0$ and is uniquely related to the frequency ω, mode index ν, film thickness $2d$, and wave number $k_\perp$ of the investigated waveguide magnon (1)–(4). If, on the other hand, the refraction surface (5) has a segment with a local maximum of the negative curvature (for $\partial k/\partial\theta=0$), then an analysis shows that this will lead to the formation of a local minimum for the corresponding ω, ν, d, and $k_\perp$ on the dispersion curve of the bulk electric-dipole-active spin wave (1)–(4).

If one considers the sections of the curve (5), (6) by straight lines $k_x=\text{const}$ or $k_z=\text{const}$, then an analysis of the common points of such a straight line and the diffraction surface (5), (6) can yield additional information about the structure of the spectrum of the corresponding waveguide magnon for a specified wave number $k_\perp$, frequency ω, and mode index ν (in this case, for curves (1)–(4)). In particular, if the direction of the normal $\mathbf{n}$ to the surface of the film in the plane of the wave vectors k_x, k_z corresponds to the easy axis ($\mathbf{n}\|0z$), then the number of common points of the straight line $k_x=k_\perp$ and the curve (5), (6) determines the mode index ν of the spectrum of bulk spin-wave oscillations of the electric dipole type that can propagate along the $0x$ axis of the investigated magnetoelectric film of thickness d with identical wave number $k_\perp$ and frequency ω (i.e., crossover points). In this same geometry the presence of common points of the curve (5), (6) and the straight line $k_z=\kappa_\nu$ enables one to determine the possible wave numbers $k_\perp$ with which the given type of waveguide magnon of fixed mode index ν and frequency ω can propagate along a thin film of thickness $2d$ for the magnetoelectric under study. Since the outer normal to the diffraction surface coincides with the direction of the group velocity of the wave,[2] a study of the local geometry of the section of the isofrequency surface (5), (6), as follows from a joint analysis of Eqs. (1)–(6), can establish the type of wave (forward or backward) that is associated with the corresponding segment (determined from (1)–(4) by the specified ω, κ_ν, and $k_\perp$) of the dispersion curve of the waveguide magnon. In the case under study, $\mathbf{k}\in xz$ a bulk spin wave (1)–(4) propagating along the film ($\mathbf{n}\|0z$) will be a wave of the backward type if the projection of the outer normal to the diffraction surface on the $0x$ axis at the crossing point of this surface with the straight line $k_z=\kappa_\nu$ is of negative sign. If this projection is positive, then the corresponding wave for specified $k_\perp$, ω, and κ_ν will be a forward wave; at a certain $k_\perp\neq 0$ this projection on the $0x$ axis can be equal to zero. Such a situation is observed when the dispersion curve of the mode ν of bulk oscillations traveling along the surface of a film of thickness $2d$ has an extremum at a frequency ω for this value of the wave number $k_\perp$. This point will be a maximum or minimum, depending on the sign of the local curvature of the curve (5), (6) at this point.

3. EFFECTS DUE TO A CHANGE OF THE ELECTRODYNAMIC BOUNDARY CONDITIONS

Up till now we have assumed that the electrostatic potential φ obeys the condition $\varphi=0$ or $\partial\varphi/\partial\zeta=0$ (1.15) on both surfaces of the investigated magnetoelectric film, depending on the relative orientation of the equilibrium antiferromagnetism vector $\mathbf{l}$ and the normal $\mathbf{n}$ to the surface of the film at $\zeta=\pm d$. This assumption allowed us to write the corresponding dispersion relation for the propagating bulk electric-dipole-active magnons (1)–(4) in explicit form in the case when not only the conditions of pinning of the magnetic

moments (1.11) but also the conditions of completely incoherent mating (1.14) hold on both boundaries of the film. If these electrodynamic conditions do not hold for a specified geometry of the film (relative orientation of the vectors **l**, **n**, and $\mathbf{k}_\perp$), e.g.,

$$\varphi+\alpha_*\partial\varphi/\partial\zeta=0; \quad \zeta=\pm d \tag{7}$$

(but, as before, the boundary conditions (1.11) and (1.14) hold at $\zeta=\pm d$), then for calculating the spectrum of bulk magnons one can use an approach developed previously in Refs. 3 and 4 in an analysis of the influence of the magnetic dipole interaction on the spectrum of bulk exchange magnons in a thin ferromagnetic film. For this purpose, in the case $\mathbf{k}\in xz$ ($\mathbf{n}\|0z$), with the aid of the Green's function

$$G(\zeta,t)=\begin{cases}\sinh(ak_\perp(t-d))\sinh(ak_\perp(\zeta+d))/\Delta, & -d\leqslant\zeta\leqslant t,\\ \sinh(ak_\perp(t+d))\sinh(ak_\perp(\zeta-d))/\Delta, & t\leqslant\zeta\leqslant d,\end{cases} \tag{8}$$

$$\Delta\equiv ak_\perp\sinh(2ak_\perp d), \quad a^2\equiv(1+\varepsilon_\perp)/\varepsilon$$

we can use the equations of electrostatics ($\omega/c\to0$) with the boundary condition (7) to obtain a relation between the amplitude of the electrostatic potential φ and the amplitude of the oscillation of the x component of the antiferromagnetism vector **l**, treating the spatial distribution of the latter along the normal to the surface of the film as a specified function. This makes it possible, using (8), to eliminate the variables associated with the electrostatic interaction from consideration in (1.7) and (1.8) ($\omega/c\to0$). Thus it is necessary to solve the corresponding boundary-value problem only with the exchange and elastic boundary conditions, which we, as before, assume to be specified by relations (1.11) and (1.14). Following the procedure developed in Refs. 3 and 4, we seek the solution of the given boundary condition-value problem in the form of a series in eigenfunctions of the exchange boundary-value problem. In the case (1.14) we have

$$l_x(r,t)=\sum_\nu A_\nu\sin(\kappa_\nu z)\exp(i\omega t-ik_\perp x). \tag{9}$$

As a result, the corresponding dispersion relation describing in the electro- and elastostatic approximations the spectrum of bulk magnons in the investigated film of an antiferromagnet with a center of antisymmetry in the case $\mathbf{k}\in xz$, $\mathbf{n}\|0z$ and with the boundary conditions (1.11), (1.14), and (7) can be written in the form of an infinite system of linear algebraic equations for the unknown amplitudes A_ν:

$$(W_{\nu\nu}(k_\perp)-\omega^2)A_\nu-W_{\nu\rho}(k_\perp)A_\rho=0; \tag{10}$$

$$\nu\neq\rho, \quad \nu, \quad \rho=1,2,\ldots,$$

$$T_N>T_D,$$

$$W_{\nu\nu}(k_\perp)=[R+s^2(k_\perp^2+\kappa_\nu^2)]\left(1-\xi^2+\frac{\xi^2}{\varepsilon}P_{\nu\nu}\right); \tag{11}$$

$$W_{\nu\rho}(k_\perp)=[R+s^2(k_\perp^2+\kappa_\nu^2)]\frac{\xi^2}{\varepsilon}P_{\theta\nu\rho};$$

$$T_N<T_D,$$

$$W_{\nu\nu}(k_\perp)=[R_\nu(k_\perp)+s^2(k_\perp^2+\kappa_\nu^2)]\left(1-\xi^2+\frac{\xi^2}{\varepsilon}P_{\nu\nu}\right); \tag{12}$$

$$W_{\nu\rho}(k_\perp)=[R_\nu(k_\perp)+s^2(k_\perp^2+\kappa_\nu^2)]\frac{\xi^2}{\varepsilon}P_{\nu\rho};$$

$$P_{\nu\nu}=k_\perp^2\int_{-d}^{d_{11}}dz\sin(\kappa_\nu z)\int_{-d}^{d_{11}}dtG(z,t)\sin(\kappa_\nu t);$$

$$P_{\nu\rho}=k_\perp^2\int_{-d}^{d_{11}}dz\sin(\kappa_\rho z)\int_{-d}^{d_{11}}dtG(z,t)\sin(\kappa_\nu t).$$

Analysis shows that if we set $\alpha_*=0$ in (7), then it follows from (10) that $W_{\nu\rho}(k_\perp)=0$, while $W_{\nu\nu}(k_\perp)=\Omega_\nu^2(k_\perp)$, where $\Omega_\nu^2(k_\perp)$ is given by Eq. (1) or (3), depending on the relationship between the Néel and Debye temperatures. Thus the off-diagonal elements of the infinite matrix $W_{\nu\rho}(k_\perp)$ (10) can be treated as a perturbation with respect to the zeroth approximation, which is governed by the diagonal elements of the infinite matrix $W_{\nu\rho}(k_\perp)$:

$$\omega^2=W_{\nu\nu}(k_\perp). \tag{13}$$

A comparison of relations (11), (12) and (1), (3) shows that in this zeroth approximation the structure of the spectrum of bulk magnetic oscillations does not differ qualitatively from that which was determined earlier by formulas (1) and (3) when, in addition to the boundary conditions (1.11) and (1.14), the condition of two-sided metallic coating (1.15) also holds for the magnetoelectric film under study. Then, however, for modes with indices ν and ρ ($\nu\neq\rho$) the spectrum will have no crossover points $W_{\nu\nu}=W_{\rho\rho}$, since $W_{\nu\rho}\neq0$ in (10). Carrying out the degenerate-level perturbation theory and taking relations (11) and (12) into account, we write the structure of the spectrum in the neighborhood of a specific crossover point to second order of perturbation theory as

$$(W_{\nu\nu}(k_\perp)-\omega^2)(W_{\rho\rho}(k_\perp)-\omega^2)-W_{\nu\rho}^2(k_\perp)\cong0,$$

$$\nu\neq\rho. \tag{14}$$

A joint analysis of (11), (12), and (14) allows us to assume, in particular, that if the dispersion curves for a forward ($\partial\Omega_\nu/\partial k_\perp>0$) and a backward ($\partial\Omega_\nu/\partial k_\perp<0$) intersect at the crossover point, then on account of (14) this degeneracy is lifted, the dispersion curves move away from each other, and instead of a crossover point there will be an extremum ($\partial\Omega_\nu/\partial k_\perp=0$) on each of the curves at (14); one of these extrema will correspond to a local maximum [for the forward wave ($\partial\Omega_\nu/\partial k_\perp>0$) for $W_{\nu\rho}=0$ in (14)] and the other to a local minimum of the dispersion curve [for the backward wave ($\partial\Omega_\nu/\partial k_\perp<0$) for $W_{\nu\rho}=0$ in (14)].

It is straightforward to show that everything that we said about the case $\mathbf{n}\|\mathbf{l}$ is also valid for $\mathbf{n}\perp\mathbf{l}\|\mathbf{k}_\perp$ ($\mathbf{k}_\perp\in xz$), but in the latter case, in order to have the spectrum $W_{\nu\rho}=0$ and $W_{\nu\nu}(k_\perp)=\Omega_\nu^2(k_\perp)$ for $\alpha_*\to\infty$ (here $\Omega_\nu^2(k_\perp)$ is determined by relation (2) for $T_N>T_D$ or by (4) for $T_N<T_D$), it is necessary that the Green's function used in the calculations have the following form instead of (8):

$$G(\zeta,t) = \begin{cases} \cosh(ak_\perp(t-d))\cosh(ak_\perp(\zeta+d))/\Delta, & -d\leqslant\zeta\leqslant t, \\ \cosh(ak_\perp(t+d))\cosh(ak_\perp(\zeta-d))/\Delta, & t\leqslant\zeta\leqslant d, \end{cases} \tag{15}$$

$$\Delta\equiv ak_\perp \sinh(2ak_\perp d), \quad a\equiv\varepsilon/(1+\varepsilon_\perp).$$

4. INCLUSION OF ACOUSTIC RETARDATION EFFECTS

Up till now the dynamics of the thin-film magnetoelectric antiferromagnet under study has been analyzed with the interaction of the spin and elastic subsystems of the low-temperature antiferromagnetic crystal taken into account only in the elastostatic approximation, i.e., for $\omega/c_{\rm ph}k_\perp\to 0$, while those of the high-temperature antiferromagnet are taken into account in the frozen lattice approximation, $\omega/c_{\rm ph}k_\perp\to\infty$. Meanwhile, the dispersion relations (1.16), which simultaneously take into account the electric-dipole, magnetoelastic, and inhomogeneous exchange interactions, were obtained for arbitrary values of $\omega/c_{\rm ph}$. This gives us an opportunity to analyze the role of acoustic retardation effects in the formation of the structure of the spectrum of bulk normal oscillations of a thin film of an antiferromagnet with a center of antisymmetry.

If we formally neglect the magnetoelastic interaction [this corresponds to taking the limit $\hat{B}\to 0$ in (1.16)], the resulting dispersion relation for both $\mathbf{n}\|\mathbf{l}$ and $\mathbf{n}\perp\mathbf{l}\|\mathbf{k}_\perp$ factorizes into two sets of noninteracting bulk modes corresponding to the following:

1) exchange–electric-dipole oscillations, the dispersion relation of which in this limit ($\hat{B}\to 0$) is given by equations (1) for $\mathbf{n}\|\mathbf{l}$ or (2) for $\mathbf{n}\perp\mathbf{l}$ ($\mathbf{k}\in xz$), regardless of the relationship between the Néel and Debye temperatures;

2) purely phononic oscillations, the spectrum of which for the chosen type of boudary conditions (1.15) can be written in the form

$$\Omega^2_{{\rm ph}\nu}(k_\perp) = \frac{N_1}{2} \pm \left(\left(\frac{N_1}{2}\right)^2 - N_2 \right)^{1/2}, \quad \nu = 1,2,\ldots, \tag{16}$$

$$N_1(k_\perp) = \Lambda^*_{11} + \Lambda^*_{33}, \quad N_2(k_\perp) = \Lambda^*_{11}\Lambda^*_{33} - \Lambda^{*2}_{13}.$$

From a comparison of Eqs. (16) and (1), (2) it follows that for $\nu\neq\rho$ the corresponding dispersion curves for the modes of the spectrum of phonon and dipole–exchange excitations $\Omega_{{\rm ph}\nu}(k_\perp)$ and $\Omega_\rho(k_\perp)$ both for $T_N>T_D$ and for $T_N<T_D$ can have crossing points for $k_\perp\neq 0$. If we go to an analysis of the more general case $\hat{B}\neq 0$ ($\omega/c\neq 0$) then, according to (1.16), independently of the relationship between the Néel and Debye temperatures for the investigated model of a thin magnetoelectric film, both for $\mathbf{n}\|\mathbf{l}$ and for $\mathbf{n}\perp\mathbf{l}\|\mathbf{k}_\perp$ ($\mathbf{k}\in xz$) in the electrostatic limit ($\omega/c\to 0$) the spectrum of bulk magnetoelastic oscillations for which $\tilde{l}_x\neq 0$ and the lattice displacement vector u lies in the sagittal plane (xz) can be written in the above notation as

$$\omega^2 \equiv \left(1 - \xi^2 + \frac{\xi^2\varepsilon_\perp k_x^2}{\varepsilon k_z^2 + k_x^2(1+\varepsilon_\perp)}\right) \times \left[\omega_0^2 + s^2(k_x^2+k_z^2) + \omega_{me}^2 \times \left(1 - \frac{c_{44}[k_x^2(\Lambda^*_{11}-\omega^2) + k_z^2(\Lambda^*_{33}-\omega^2) - 2\Lambda^*_{13}k_xk_z]}{\rho[(\Lambda^*_{11}-\omega^2)(\Lambda^*_{33}-\omega^2) - \Lambda^{*2}_{13}]}\right)\right] \tag{17}$$

($k_z\equiv\kappa_\nu$ for $\mathbf{n}\|0z$ and $k_x\equiv\kappa_\nu$ for $\mathbf{n}\|0x$, $\nu=1,2,\ldots$).

Thus, by taking into account the nonzero dynamic magnetoelastic interaction ($\hat{B}\neq 0$) leads to the situation that in a low-temperature antiferromagnet ($c_{\rm ph}>s$, $k_\perp>\omega/c_{\rm ph}$) the spectrum of bulk phonon oscillations with $\mathbf{u}\in xz$ is practically unchanged in comparison with (16), whereas the spectrum of dipole–exchange modes is not qualitatively different from that which was found above in the elastostatic limit (3) and (4).

The situation for $T_N>T_D$ ($c_{\rm ph}<s$) is different.[2)] In that case, as follows from (17), the dispersion relation for spin-wave excitations hardly changes (in comparison with the case $\hat{B}=0$). As before, they are qualitatively similar to (1), (2), while the structure of the spectrum of bulk phononic oscillations polarized in the sagittal plane (xz) of the crystal, in contrast to (16), takes the following form:

$$\omega^4 + N_1\omega^2 + N_2 = 0 \quad (\mathbf{k}\cdot\mathbf{n}\equiv\kappa_\nu); \tag{18}$$

$$N_1 = \tilde{\Lambda}_{11} + \tilde{\Lambda}_{33}; \quad N_2 = \tilde{\Lambda}_{11}\tilde{\Lambda}_{33} - \tilde{\Lambda}^2_{13};$$

$\tilde{\Lambda}_{ik}\equiv\tilde{c}_{iklm}k_{\perp k}k_{\perp m}/\rho$, $\tilde{c}_{iklm}\equiv c_{iklm}$ for $i\neq k$ and $i=k=1,2,3,6$; $\tilde{c}_{44}=c_{44}(1-\omega^2_{me}/\Omega^2_\nu(k_\perp))$. Here $\Omega^2_\nu(k_\perp)$ is given by relation (1) for $\mathbf{n}\|\mathbf{l}$ or by (2) for $\mathbf{n}\perp\mathbf{l}\|\mathbf{k}_\perp$.

Analysis of Eq. (18) shows that in this approximation the elastic dynamics of a film of a high-temperature antiferromagnet with a center of antisymmetry can be studied using the concept of effective elastic constants, which is widely used in the study of the spectrum of phononic oscillations in infinite magnets or the dynamics of dislocations in magnetically ordered crystals.[5,6] However, in contrast to the previously investigated model of an infinite medium, in a thin magnetoelectric film the spatial nonlocality of the elastic constants can be due not only to the inhomogeneous exchange interaction but to the electric-dipole interaction, i.e., it exists even in the zero-exchange limit ($\alpha\to 0$).

Furthermore, by analyzing relation (17) we arrive at the conclusion that for $\hat{B}\neq 0$, regardless of the relationship between the Néel and Debye temperatures, the degeneracy that existed between the spectra of purely phononic and dipole–exchange magnon excitations for $\hat{B}=0$ is lifted. Here the lifting of the degeneracy on account of the chosen boundary conditions (1.11), (1.14), and (1.15) occurs only in those modes of the spectrum of bulk magnetoelastic oscillations which for $\hat{B}=0$ had the same mode index ν. At the same time, the crossover points present on the dispersion curves of the magnon and phonon bulk oscillations for $\hat{B}=0$ and $k_\perp\neq 0$ and which correspond to modes with $\nu\neq\rho$ remain present for $\hat{B}\neq 0$.

If, as in Sec. 3, we consider a situation involving a change in the character of the electrodynamic boundary conditions from (1.11) to (7), then for $\mathbf{k}\in xz$, $\mathbf{n}\|0z$ it can be shown with the aid of (8) that the corresponding dispersion relation that generalizes (17) to the case of a finite propagation velocity of acoustic oscillations (both for $T_N>T_D$ and for $T_N<T_D$) can be put in the form (14), in which now $\nu=1,2,\ldots$:

$$W_{\nu\nu}(k_\perp)=\left(1-\xi^2+\frac{\xi^2}{\varepsilon}P_{\nu\nu}\right)\left[\omega_0^2+s^2(k_\perp^2+\kappa_\nu^2)+\omega_{me}^2\left(1-\frac{c_{44}[k_\perp^2(\Lambda_{11}^*-\omega^2)+\kappa_\nu^2(\Lambda_{33}^*-\omega^2)-2\Lambda_{13}k_\perp\kappa_\nu]}{\rho[(\Lambda_{11}^*-\omega^2)(\Lambda_{33}^*-\omega^2)-\Lambda_{13}^{*2}]}\right)\right]; \tag{19}$$

$$W_{\nu\rho}(k_\perp)=\frac{\xi^2}{\varepsilon}P_{\nu\rho}\left[\omega_0^2+s^2(k_\perp^2+\kappa_\nu^2)+\omega_{me}^2\left(1-\frac{c_{44}k_\perp^2(\Lambda_{11}^*-\omega^2)+\kappa_\nu^2(\Lambda_{33}^*-\omega^2)-2\Lambda_{13}k_\perp\kappa_\nu}{\rho[(\Lambda_{11}^*-\omega^2)(\Lambda_{33}^*-\omega^2)-\Lambda_{13}^{*2}]}\right)\right],\quad \nu\neq\rho.$$

If we set $\alpha_*=0$ in (7), then it follows from (19) that $W_{\nu\rho}=0$, while $W_{\nu\nu}(k_\perp)$ is determined by the right-hand side of (17). Thus even in this case the off-diagonal elements $W_{\nu\rho}$ of the infinite determinant (19) can be treated as a perturbation with respect to the zeroth approximation that determines the diagonal elements of the infinite matrix.

It should be noted that in all of the above cases of lifting of the degeneracy at the crossing points of the dispersion curves of bulk normal oscillations it is undoubtedly necessary to take the damping of the modes into account as well. The inclusion of this damping in the framework of the phenomenological theory used does not present any technical difficulties. A calculation shows that the corresponding physical picture here is qualitatively the same as that which was analyzed previously in an investigation of coupled bulk magnetoelastic and exchange–magnetic-dipole oscillations in a thin ferromagnetic film.[7] We shall therefore only list the main points that bear on the influence of damping [$\Delta\Omega_\nu$ is the linewidth of the bulk normal mode $\Omega_\nu(k_\perp)$] on the behavior of the dispersion curves of the bulk normal oscillations in the neighborhood of a crossover point. In rather thick films with $T_N>T_D$ ($c\gg s$) the bulk magnons will have a finite linewidth due to single-phonon processes, whereas for $T_N<T_D$ and $c\ll s$ the bulk phonons will have a finite linewidth due to single-magnon processes. As the thickness d of the film decreases, the dependence of the spectrum of normal bulk oscillations on the excitation frequency ω becomes discrete, but as before there is degeneracy of certain modes of the spectrum of bulk normal oscillations with indices ν and ρ. Then, as d decreases further, the investigated spectrum of bulk oscillations of the magnetoelectric film begins to exhibit fine structure: first, for the mode with fixed index ν, as the wave number $k_\perp$ approaches the crossover point of the dispersion curve of this mode with that of the mode with index ρ, there will be a substantial increase in the linewidth. If there are several such crossover points for the mode ν, then its linewidth will oscillate as the wave number changes. As the film thickness d is decreased further, the degeneracy of the spectra of the modes of bulk normal oscillations with indices ν and ρ is lifted, and at the positions of these $k_\perp$ a region of forbidden frequencies arises, within which the propagation of bulk normal oscillations with such values of $k_\perp$ becomes impossible. Analogous forbidden frequency regions brought about by the exchange–dipole interaction have been described previously in the physics of MSWs and are called dipole gaps (see, e.g., Ref. 3).

CONCLUSION

In summary, for films of an antiferromagnet with a center of antisymmetry we have determined the necessary conditions under which a consistent allowance for the linear magnetoelectric effect will give rise to previously unknown anomalies in the spectrum of bulk magnons. For their existence it is fundamentally important to simultaneously take into account not only the finite dimensions of the real sample but also the relationship between the Néel and Debye temperatures. The present study has revealed the following features of the bulk magnon spectrum which are due to hybridization of the magnetoelectric and inhomogeneous exchange interactions:

1) the possibility that additional points with $\partial\Omega_\nu/\partial k_\perp=0$ at $k_\perp\neq 0$ will appear on the dispersion curve $\Omega_\nu(k_\perp)$ when the inhomogeneous exchange interaction is taken into account. These points can correspond to a local maximum or a local minimum of the dispersion curve;

2) the possibility that for a thin magnetoelectric film, as a result of hybridization of the elastostatic, electrostatic, and Heisenberg mechanisms of spin–spin interaction, crossover points of the dispersion curves corresponding to modes with indices ν and ρ in the spectrum of bulk normal oscillations $\Omega_\nu(k_\perp)$ can exist for $k_\perp\neq 0$;

3) the presence of an interrelationship between the local geometry of the diffraction surface of the normal spin-wave oscillations of an infinite crystal and the structure of the spectrum of this type of waveguide oscillations in a thin film of the same material. The indicated correlation between the shape of the diffraction surface of a normal wave, the structure of the spectrum of waveguide oscillations and their type (forward or backward waves) is undoubtedly realized for other types of normal oscillations (phonons, excitons, etc.) of an infinite crystal as well.

As we know, the existence of points in the dispersion relation of the normal oscillations $\Omega_\nu(k_\perp)$ at which one or more components of the group velocity ($\partial\Omega_\nu/\partial k_\perp$) equal zero gives rise to features in the density of states of the corresponding type of quasiparticles (in this case magnons). Such points are called critical points, and they are associated with the presence of features of the thermodynamic, kinetic,

and optical properties of a crystal. The appearance of critical points is due to the symmetry properties of the crystal (symmetry critical points).[8] Furthermore, there can also exist critical points whose presence has nothing to do with the symmetry of the crystal. They are called dynamical critical points.[8] An analysis of the existence conditions for critical points in the magnon spectrum was presented in Refs. 9 and 10, but up till now it has been carried out only for an infinite crystal model. We have shown for the first time that the consistent allowance for the influence of the nonlocal interactions on the spin dynamics of a bounded magnet enables one to determine the mechanisms of formation and the existence conditions of a number of new (absent in the infinite crystal model) dynamical critical points in the magnon spectrum of an antiferromagnet with a center of antisymmetry.

It must be said that, although the calculation of the present paper was done for a concrete form of the exchange and elastic boundary conditions, the domain of applicability of the results obtained is actually wider, since, according to Ref. 11, the character of the spectrum of bulk oscillations which are nonuniform over the thickness of the sample is relatively insensitive to the type of boundary conditions. Analysis shows that for modes with $\nu \geqslant 1$, changing the type of the exchange and elastic boundary conditions does not materially affect the character of the observed anomalies of the spectrum of normal bulk oscillations in a thin magnetoelectric film. An exception may be the existence conditions for crossover points of the dispersion curves calculated on the basis of the boundary conditions (1.11), (1.14), and (1.15).

*E-mail: tarasen@host.dipt.donetsk.ua

[1)]From now on in citing the equations taken from Ref. 1 we shall use a dual numbering system; e.g., we shall refer to Eq. (3) of Ref. 1 as Eq. (1.3).

[2)]Or for a low-temperature antiferromagnet ($c_{\mathrm{ph}} > s$, $k_{\perp} < \omega/c_{\mathrm{ph}}$).

[1] S. V. Tarasenko, Fiz. Nizk. Temp. **27**, 52 (2001) [Low Temp. Phys. **27**, 40 (2001)].
[2] Yu. I. Sirotin and M. P. Shaskol'skaya, *Principles of Crystal Physics* [in Russian], Nauka, Moscow (1979).
[3] B. A. Kalinikos, Izv. Vyssh. Uchebn. Zaved. Fiz. **24**, 42 (1981).
[4] B. A. Kalinikos and A. N. Slavin, J. Appl. Phys. C **19**, 7013 (1986).
[5] E. A. Turov and V. G. Shavrov, Usp. Fiz. Nauk **130**, 429 (1983) [Sov. Phys. Usp. **26**, 593 (1983)].
[6] V. G. Bar'yakhtar and V. V. Tarasenko, Fiz. Tverd. Tela (Leningrad) **22**, 431 (1980) [Sov. Phys. Solid State **22**, 252 (1980)].
[7] Yu. V. Gulyaev, I. E. Dikshteĭn, and V. G. Shavrov, Usp. Fiz. Nauk **167**, 735 (1997).
[8] J. L. Birman, *Space Symmetry and Optical Properties of Solids*, Mir, Moscow (1978), Vol. 1.
[9] V. G. Bar'yakhtar, A. G. Kvirikadze, and V. A. Popov, Zh. Éksp. Teor. Fiz. **59**, 898 (1970) [Sov. Phys. JETP **32**, 488 (1971)].
[10] V. V. Eremenko, S. A. Zvyagin, Yu. G. Pashkevich, V. V. Pishko, V. L. Sobolev, and S. A. Fedorov, Zh. Éksp. Teor. Fiz. **93**, 2075 (1987) [Sov. Phys. JETP **66**, 1184 (1987)].
[11] L. M. Brekhovskikh, *Waves in Layered Media* [in Russian], Nauka, Moscow (1973).

Translated by Steve Torstveit

H–T phase diagram of a multilayered Gd/Si/Co film with ferrimagnetic ordering of the layers

D. N. Merenkov,* A. B. Chizhik, and S. L. Gnatchenko

B. Verkin Institute for Low Temperature Physics and Engineering, National Academy of Sciences of Ukraine, pr. Lenina 47, 61164 Kharkov, Ukraine

M. Baran and R. Szymczak

Institute of Physics, Polish Academy of Sciences, Al. Lotnikow 32/46, 02-668 Warsaw, Poland

V. O. Vas'kovskiy and A. V. Svalov

Urals State University, pr. Lenina 51, 620083 Ekaterinburg, Russia
(Submitted July 27, 2000)
Fiz. Nizk. Temp. **27**, 188–195 (February 2001)

The magnetization process of multilayered films $[Co(30\,Å)/Si(5\,Å)/Gd(75\,Å)/Si(5\,Å)]_{20}$ having a ferrimagnetic ordering of the magnetic moments of the cobalt and gadolinium layers and a compensation temperature $T_{comp} \approx 118$ K is studied by magnetometric and magnetooptical methods. A magnetic-field-induced spin-orientation transition from the collinear to the noncollinear state is observed. The transition field is determined and the $H-T$ magnetic phase diagram is constructed for the multilayered ferrimagnet Gd/Si/Co in the temperature interval 5–140 K. The phase diagram is also calculated in the framework of molecular field theory, and satisfactory agreement with the experimental results is obtained. The constant of the antiferromagnetic exchange interaction between the cobalt and gadolinium layers is established. [DOI: 10.1063/1.1353705]

INTRODUCTION

Among the various sorts of thin multilayered films that are intensively studied at the present time are structures consisting of alternating layers of two different types of metals: a rare-earth metal (REM) and a transition metal (TM). As a result of the exchange interaction at the interface, the magnetic moments of these layers are ordered antiparallel. These structures therefore have properties similar to those of classical ferrimagnets, in particular, compensation of the magnetic moments and spin-orientation transitions under the influence of an external magnetic field. Artificially prepared ferrimagnetic systems of this type have been studied for Gd/Fe (Ref. 1) and Gd/Co (Ref. 2) films; because of their layered structure, these objects also have specific properties that are not shared by ordinary ferrimagnets.

The magnetization reversal process for multilayered ferrimagnetic films was first described theoretically by Camley and Tilley.[3] According to their model, in the absence of magnetocrystalline anisotropy, an ideal REM/TM superlattice in an external field can have three main phases: 1) a phase in which the spins of the REM layers are parallel and the spins of the TM layers antiparallel to the field H (this phase is observed below the compensation temperature T_{comp}); 2) the spins of the TM layers are parallel and those of the REM layers antiparallel to H (above T_{comp}); 3) a noncollinear phase, in which the spins of each atomic row in the metal layers are at different angles to the direction of the external field. This last situation arises when H is sufficient to overcome the antiferromagnetic interaction between layers. Calculations show that the fields H_t of the transition of the layered structures to the noncollinear phase increase with distance from T_{comp} (as in two-sublattice ferrimagnets), but they are lower than the phase transition fields of ferrimagnetic alloys of similar composition. In addition, the process by which the noncollinear phase arises in a finite REM/TM layered structure depends on the type of the surface layer (REM or TM).[4] In such a structure one can observe a surface phase transition in fields at which the main part of the film is still found in the collinear phase. The penetration depth of the surface phase into the film can reach several periods of the structure (several hundred angstroms).

The properties of ferrimagnetic multilayered films turn out to be extremely sensitive to changes in their parameters, which on the whole are amenable to control. For example, varying the ratio of the thicknesses of the REM and TM layers,[3] changing the period of the structure,[5] and the intercalation of a nonmagnetic spacer between the magnetic layers[6] lead to both a shift of T_{comp} and a change in H_t.

In this paper we present the results of research on the magnetization reversal of a film of the Gd/Si/Co type. The presence of the silicon spacer, on the one hand, weakens the interlayer exchange interaction at the interface and thereby makes it possible for a noncollinear phase to exist over a wide interval of fields and temperatures accessible for study, and, on the other hand, prevents the formation of GdCo compounds, which have specific magnetic properties.[2] The main goal of this study was to investigate the field-induced transitions to the noncollinear phase and to construct the $H-T$ magnetic phase diagram. The experimental data were obtained in magnetooptical studies, which are extremely sensitive to a change in the magnetic structure of the sample, and

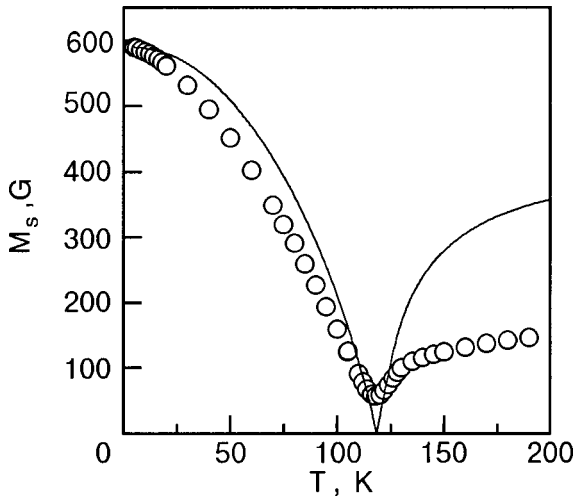

FIG. 1. Temperature dependence of the spontaneous magnetization of a $[Co(30\,Å)/Si(5\,Å)/Gd(75\,Å)/Si(5\,Å)]_{20}$ film, measured in an external field $H=500$ Oe. The circles are experimental data points, the continuous curve is the calculated dependence.

also by means of measurements of the magnetization on a SQUID magnetometer.

EXPERIMENT

A thin multilayer film of composition $[Co(30\,Å)/Si(5\,Å)/Gd(75\,Å)/Si(5Å)]_{20}$ was prepared by rf ion sputtering on a glass substrate at a base pressure of 10^{-6} torr and a working-gas (Ar) pressure of 10^{-4} torr. The deposition was carried out at a temperature not over 100 °C. The rates of deposition of Gd, Co, and Si, according to the results of a preliminary calibration, were 1, 0.4, and 0.3 Å/s, respectively. The upper layer of the film was gadolinium. The film had a silicon buffer layer and a silicon protective surface layer, each 200 Å thick.

Magnetooptical studies were done using the longitudinal Kerr effect. The magnetic field was oriented in the plane of incidence of a He–Ne laser beam (wavelength 633 nm) parallel to the film. The angle of rotation Φ of the plane of polarization of the reflected light was measured as a function of the strength of the external field. In the given geometry the Kerr rotation of the plane of polarization is proportional to the component of the magnetization M lying in the plane of the film and parallel to the plane of incidence of the light. The sample was placed on a cold stage in vacuum inside a superconducting solenoid.

The magnetization measurements were done on a Quantum Design MPMS-5 SQUID magnetometer.

Figure 1 shows the temperature dependence of the spontaneous magnetization M_s measured on the SQUID magnetometer in an external field $H=500$ Oe. The values of M_s correspond to the volume occupied by materials having an intrinsic magnetic moment (Co and Gd). The results of the measurements attest to the preservation of antiferromagnetic ordering of the magnetic moments of the Co and Gd layers at the given thickness of the silicon interlayer. The experimental curve has a clear minimum at 118 K, due to the compensation of the magnetic moments of the Gd and Co layers. The nonzero minimum value of the magnetization may be due to a slight inhomogeneity of the film or to the onset of a noncollinear phase at $T\approx T_{comp}$ in a field $H=500$ Oe. Increasing the temperature from 5 K to the compensation temperature leads to a rather rapid drop of the spontaneous magnetization. As the temperature is increased at $T>T_{comp}$ the magnetization increases rapidly at first and then more and more slowly, tending toward saturation.

The typical field dependence of the magnetization M and Kerr rotation Φ measured in the Gd/Si/Co film are shown in Fig. 2. In low fields both curves exhibit a clear hysteresis (see inset) due to the formation of domains of opposite magnetization and the motion of domain walls. When a certain value of the external field is reached the $M(H)$ and $\Phi(H)$ curves exhibit a kink (indicated by arrows and the dashed line in Figs. 2a and 2b, corresponding to a transition to a noncollinear state. At this point there is an increase in the

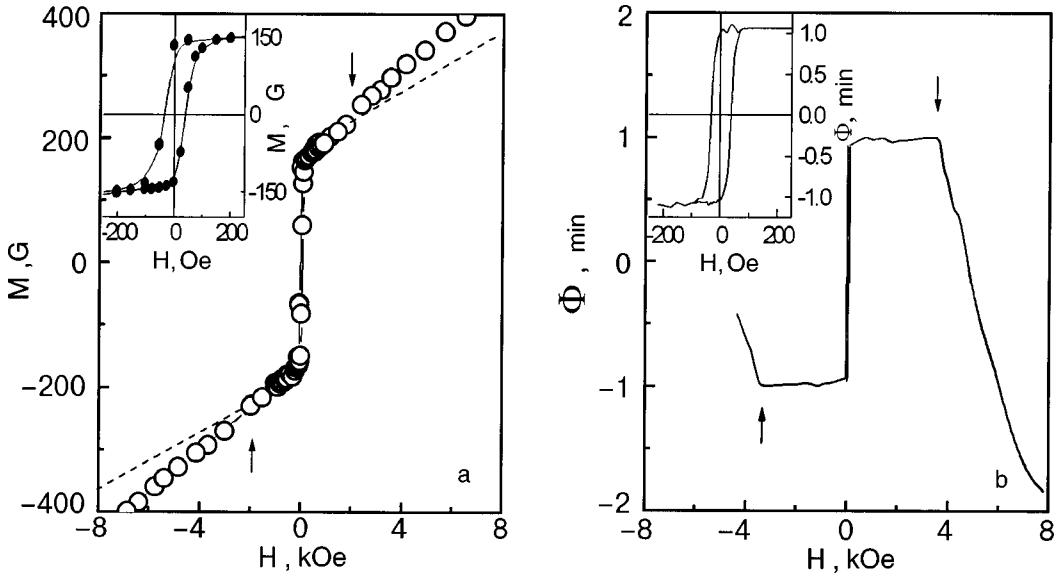

FIG. 2. Field dependence of the magnetization (a) and Kerr rotation (b) at $T=97$ K. The kink on the $M(H)$ and $\Phi(H)$ curves corresponds to the transition to the noncollinear state. The insets show the low-field $M(H)$ and $\Phi(H)$ curves on an expanded scale.

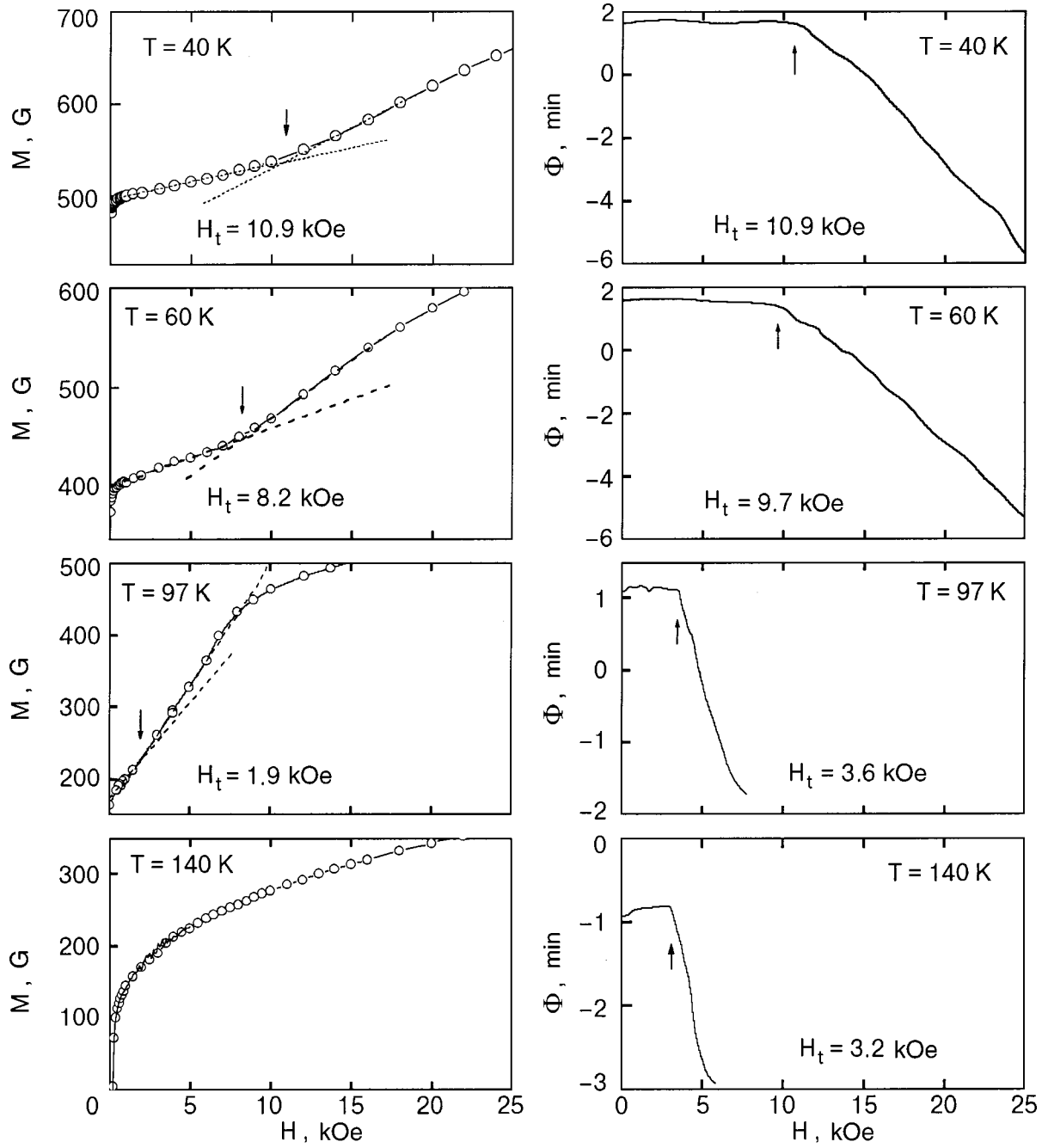

FIG. 3. Field dependence of the magnetization (left) and Kerr rotation (right) at different temperatures.

magnetic susceptibility dM/dH (Fig. 2a). As we see from Fig. 2, the transition to the noncollinear state is manifested significantly more clearly on the field dependence of the Kerr rotation than on the field dependence of the magnetization.

To construct the $H-T$ phase diagram of the film, we measured the field dependence of the magnetization and Kerr rotation at different temperatures. Figure 3 shows the measured $M(H)$ and $\Phi(H)$ curves. As the film is heated, the kink due to the transition to the noncollinear phase is more and more weakly manifested on the magnetization curve, and in the region above the compensation temperature it is no longer noticeable. With increasing temperature the values of the magnetic susceptibility in the collinear and noncollinear phases approach each other, making it difficult to determine the point of the phase transition on the $M(H)$ curves at temperatures $T \lesssim T_{\text{comp}}$ and $T > T_{\text{comp}}$. At the same time, on the field dependence of the Kerr rotation the transition is clearly identifiable all the way up to 140 K.

From the results of the experiments we constructed the $H-T$ phase diagram shown in Fig. 4. The data obtained from the magnetic and magnetooptical measurements are in satisfactory mutual agreement. In the interval $5\ \text{K} < T < T_{\text{comp}}$ the field of the phase transition to the noncollinear state decreases with increasing temperature, and for $T_{\text{comp}} < T < 140$ K the transition field remains practically constant. In the neighborhood of T_{comp} the determination of H_t is complicated by the proximity of the phase-transition and coercive fields. As $T \to T_{\text{comp}}$ the coercive field increases, while H_t decreases.

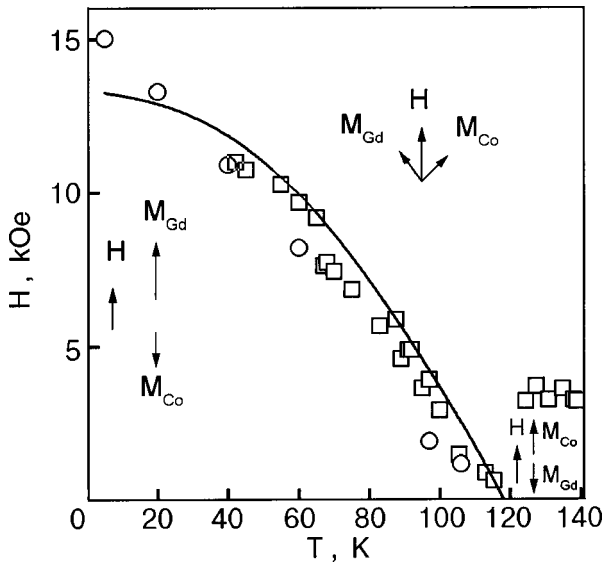

FIG. 4. The $H-T$ phase diagram of a [Co(30 Å)/Si(5 Å)/Gd(75 Å)/Si(5 Å)]$_{20}$ film; ○ — the data obtained from the magnetization measurements; □ — from magnetooptical measurements. The calculated dependence is shown by the continuous curve.

DISCUSSION

As we know, the spontaneous magnetization of a ferrimagnet is found as the difference of the partial magnetizations of its constituent subsystems. In a multilayered film the values and temperature dependence of these magnetizations depend on the thickness of the magnetic components of the structure and the intralayer and interlayer exchange interaction constants. The field of the spin-orientation transition to the noncollinear state in a multilayered film at a specified temperature is also a function of the magnetizations of the layers and these exchange constants. To construct the theoretical $H-T$ phase diagram we therefore calculated the temperature dependence of the magnetization of the film. A comparison of the calculated and experimental results for $M_s(T)$ yielded the parameters needed to calculate H_t. A determination of the interlayer exchange interaction is especially important for a film with a nonmagnetic spacer. The interaction suffers a considerable change that is hard to estimate analytically.

To calculate $M_s(T)$ we use the model proposed in Ref. 7. According to this model the temperature dependence of the spontaneous magnetization of a multilayered film of the Gd/Co type can be calculated using molecular field theory with allowance for the inhomogeneity of the interlayer exchange interaction over the thickness of the REM layers. It is assumed that the temperature dependence of the magnetization of the REM (Gd) layers is determined by both the intrinsic exchange interaction and by the outside influence of the TM (Co). At the same time, it is assumed that the Co layers are found only in their own molecular field (since the intralayer exchange in the Co layers is much greater than the interlayer exchange), which determines the temperature dependence of the magnetization of the cobalt subsystem. Thus we have

$$H_{\mathrm{Co}}=\lambda_{\mathrm{CoCo}}M_{\mathrm{Co}},$$

$$H_{\mathrm{Gd}}=\lambda_{\mathrm{GdGd}}M_{\mathrm{Gd}}+\lambda_{\mathrm{CoGd}}M_{\mathrm{Co}} \times\{\exp(-\gamma z)+\exp[-\gamma(l_{\mathrm{Gd}}-z)]\}, \quad (1)$$

where H_{Co} and H_{Gd} are the molecular fields acting on the Co and Gd layers, M_{Co} and M_{Gd} are the magnetizations of these layers, λ_{CoCo}, λ_{GdGd}, and λ_{CoGd} are the corresponding constants of the molecular fields, γ is the damping coefficient of the Co molecular field acting on the Gd, z is the coordinate along the normal to the surface of the Gd layer, and l_{Gd} is the thickness of the Gd layer. The spontaneous magnetization of the film is expressed in terms of the magnetizations of the subsystems, the temperature dependence of which is given by the Brillouin function $B_s(x)$. However, in the temperature interval of interest to us, the partial magnetization of the cobalt subsystem is practically constant, and so we can write

$$M_s(T)=|l_1M_{\mathrm{Gd}}(0)B_s(g_{\mathrm{Gd}}s_{\mathrm{Gd}}\mu_BH_{\mathrm{Gd}}/kT)-l_2M_{\mathrm{Co}}(0)|, \quad (2)$$

where g_{Gd} is the Landé factor, s_{Gd} is the spin number of gadolinium, μ_B is the Bohr magneton, k is Boltzmann's constant, and l_1 and l_2 are the reduced layer thicknesses, defined as $l_1=l_{\mathrm{Gd}}/(l_{\mathrm{Co}}+l_{\mathrm{Gd}})$ and $l_2=l_{\mathrm{Co}}/(l_{\mathrm{Co}}+l_{\mathrm{Gd}})$, where $l_{\mathrm{Co}}=30$ Å and $l_{\mathrm{Gd}}=75$ Å.

In the actual calculations of the magnetization of the gadolinium subsystem the exponential function in (1) was approximated by a step function. We assumed that each Gd layer consists of n atomic layers separated from each other by a distance d_{Gd}. In each of the atomic layers the molecular field is assumed constant, and as one goes from the interfaces into the interior of a gadolinium layer it was assumed to decrease exponentially. The value $z=0$ was assigned to the atomic layers bordering the silicon spacers. Thus the magnetization of the gadolinium layers was given by the expression

$$M_{\mathrm{Gd}}=\left[\sum_{k=1}^{n}M_k(z_k)\right]\frac{1}{n}, \quad (3)$$

where $n=l_{\mathrm{Gd}}/d_{\mathrm{Gd}}$.

In choosing the parameters in formulas (1)–(3) it is necessary to take the following considerations into account. It is known that the structural state of metals in nonepitaxial thin multilayered films can vary considerably. In particular, rare-earth metals such as gadolinium have a tendency toward amorphization. This leads to substantial changes in a number of the properties of such materials, including the density and the parameters of the magnetic ordering. The structural and magnetic properties of Gd/Si and Gd/Cu multilayered films with different layer thicknesses were studied in Ref. 8. The technology used to prepare those films was the same as that used for the films studied here. According to electron microscopy data, in Gd/Si films with $l_{\mathrm{Gd}}<100$ Å the gadolinium is found in a non-single-phase state consisting of a set of crystalline and amorphous phases with a substantial preponderance of the latter. The Curie temperature T_C of amorphous gadolinium lies in the range 130–160 K, which is considerably lower than T_C for bulk gadolinium. The Curie temperature of gadolinium in the crystalline phase is 240–290 K. We investigated a film with $l_{\mathrm{Gd}}=75$ Å. In light of the results of Ref. 8, it is natural to assume that in this multilay-

ered film the gadolinium is found predominantly in an amorphous state. This assumption will be confirmed below in a comparison of the calculated and experimental temperature dependence of the magnetization. The best agreement of the calculated and experimental temperature dependence is obtained for $T_C \approx 130$ K, which corresponds to the magnetic ordering temperature of amorphous gadolinium in thin films.[8]

To calculate the temperature dependence of the spontaneous magnetization $M_s(T)$ of our multilayered film, we need to know the mean interatomic distance d_{Gd}. We estimate it using the formula

$$M_s(0) = l_1 g_{\mathrm{Gd}} s_{\mathrm{Gd}} \mu_B N_{\mathrm{Gd}} - l_2 M_{\mathrm{Co}}(0), \tag{4}$$

where $N_{\mathrm{Gd}} = (1/d_{\mathrm{Gd}})^3$ is the number of gadolinium atoms in 1 cm^3. Substituting into (4) the values $g_{\mathrm{Gd}} = 2$, $s_{\mathrm{Gd}} = 7/2$, and $M_{\mathrm{Co}}(0) = 1400$ G along with the value $M_s(0) = 590$ G obtained experimentally for our film at $T = 5$ K, we find $d_{\mathrm{Gd}} \approx 3.6$ Å. In this case $M_{\mathrm{Gd}}(0) \approx 1400$ G.

The damping coefficient γ of the cobalt molecular field in the gadolinium was determined for a series of Gd/Co films ($l_{\mathrm{Gd}}/l_{\mathrm{Co}} = 2.5$) with different periods of the structure (fabricated by the same technology[7] as for the film under study) and was found to have the value 0.16 Å.

The procedure for calculating the temperature dependence of the spontaneous magnetization amounted to varying the parameters λ_{GdGd} and λ_{CoGd} in order to find the most satisfactory description of the experimental $M_s(T)$ curve by formulas (1)–(3). The continuous curve in Fig. 1 shows the results of the calculations for $\lambda_{\mathrm{GdGd}} = 440$ and $\lambda_{\mathrm{CoGd}} = 65$. For these parameters the calculated curve has the best agreement with the experimental dependence. We note that this value of λ_{GdGd} corresponds to a Curie temperature $T_C \approx 130$ K. The value obtained for the molecular field constant of the gadolinium λ_{GdGd} itself is in agreement with the data obtained for Gd/Co (Ref. 7) and Gd/Si (Ref. 8) films. At temperatures $T \lesssim T_{\mathrm{comp}}$ the calculated temperature dependence of the spontaneous magnetization M_s is in good agreement with the experimentally determined temperature dependence $M_s(T)$. At higher temperatures one observes a substantial difference between the experimental and calculated data, probably because the temperature dependence of the magnetization of the gadolinium subsystem is no longer described by the Brillouin function. According to Ref. 8, in layers less than 100 Å thick, gadolinium has an amorphous–crystalline structure with a substantial preponderance of the amorphous component. As we have said, in our multilayered film the gadolinium is found mainly in the amorphous state. At temperatures considerably below the Curie temperature of amorphous gadolinium ($T_C \approx 130$ K) the main contribution to the magnetization of the gadolinium subsystem is from the amorphous component, and the magnetization can be described by the corresponding Brillouin function. As the Curie temperature of amorphous gadolinium is approached, however, the contribution to the magnetization of the gadolinium subsystem from the crystalline component, which has a much higher T_C, becomes more and more noticeable. Apparently, even in the region of the compensation temperature (118 K) the contribution of the crystalline component to the magnetization causes the temperature dependence of the magnetization to deviate from the Brillouin function Eq. (2). This explains the appreciable difference of the experimental and calculated $M_s(T)$ curves at temperatures above the compensation temperature.

It should be noted that the influence of the nonmagnetic spacer on the properties of a Gd/Co multilayered film is manifested primarily in a weakening of the exchange interaction between the layers of different metals. According to the data obtained for Gd/Co films not containing such a spacer, the value of the antiferromagnetic exchange interaction constant λ_{CoGd} is around 1700.[7] Thus the intercalation of a silicon spacer 5 Å thick between the magnetic layers of the film leads to a decrease of this constant by more than an order of magnitude.

To calculate the $H-T$ phase diagram we used Motokawa's analytical method.[9] This method does not require complicated iterative calculations and enables one to determine the field of the transition to the noncollinear phase for ferrimagnetically ordered films with a broad spectrum of parameters. According to Motokawa, the value of the critical field H_t is equal to the intermediate root of the cubic equation

$$\begin{aligned}(N_i N_j \alpha_1 \alpha_2) h^3 - [N_i N_j(\alpha_1 - \alpha_2) + N_i \alpha_1 \beta_2 \\ - m N_j \alpha_2 \beta_1] h^2 - [N_i N_j - N_i(\alpha_1 - \beta_2) \\ - m N_j(\alpha_2 - \beta_1)] H + N_i - m N_j = 0.\end{aligned} \tag{5}$$

Here we have used the following notation: $N_i = l_i/2d_i$ is one-half the number of atomic layers of metal i (Co or Gd) in a layer of thickness l_i with a distance d_i between atomic layers;

$$m = M_j d_j / M_i d_i, \quad h = H_t d_j / \lambda_{ji}(d_i + d_j) M_i,$$

$$\alpha_1 = (N_i - 1)(N_i + 1)/6a_i, \quad \alpha_2 = (N_j - 1)(N_j + 1)/6a_j m,$$

$$\beta_1 = N_i(N_i - 1)/2a_i, \quad \beta_2 = N_j(N_j - 1)/2a_j m,$$

where $a_i = \lambda_{ii} d_j / \lambda_{ji}(d_i + d_j)$, and $a_j = \lambda_{jj} d_i / \lambda_{ji}(d_i + d_j)$. For $T < T_{\mathrm{comp}}$ the index i denotes Gd and j denotes Co. The values of M_{Gd}, M_{Co}, d_{Gd}, λ_{GdGd}, and λ_{GdCo} used were the same as in the calculation of $M_s(T)$. The constant of the internal molecule field of cobalt, λ_{CoCo}, was calculated from the Curie temperature of this metal ($T_C = 1394$ K) and was found to be 12000. The distance d_{Co} between layers of cobalt atoms was determined in accordance with the value of the parameter c of the unit cell of hcp cobalt ($d_{\mathrm{Co}} = 2.14$ Å $\approx 0.5c$).

The necessary conditions for correctness of the calculation by the Motokawa method,[9] viz., $H_t/\lambda_{ii} M_i \ll 1$, $H_t d_i / \lambda_{ii} M_j d_j \ll 1$, hold for our multilayered film in the entire temperature interval of interest to us here. Calculations show that the cubic term in Eq. (5) can be neglected.

The continuous curve in Fig. 4 shows the calculated temperature dependence of the fields of transition to the noncollinear state for $T < T_{\mathrm{comp}}$; the curve is in good agreement with the experimental values obtained from the magnetic and magnetooptical measurements. It should be noted that according to the Camley model, in this temperature interval the phase transition in the film with a gadolinium surface layer should occur at practically the same field at the surface and in the interior of the film, since the surface noncollinear phase arises in the film from the substrate side.

Using the parameters λ_{GdGd} and λ_{GdCo} determined from the calculation of $M_s(T)$, we obtained values of H_t in quantitative agreement with the experimental values. This confirms the applicability of the molecular field model for films of the Gd/Co type containing a nonmagnetic spacer between the magnetic layers.

Above T_{comp} the calculated values of H_t (not shown in Fig. 4) differ substantially from the experimental values; this is because, as in the case of the temperature dependence $M_s(T)$, we have not taken into account the influence of the crystalline component of the gadolinium in the calculations.

CONCLUSION

Our magnetic and magnetooptical studies of the magnetizing process for multilayered ferrimagnetically ordered Gd/Si/Co films have revealed a spin-orientation transition in them from the collinear to a noncollinear state and have enabled us to construct the $H-T$ phase diagram of our multilayered ferrimagnet. We have shown that molecular field theory describes the $H-T$ phase diagram satisfactorily (both quantitatively and qualitatively) for $T<T_{comp}$. We have determined the constant of the exchange interaction between Co and Gd layers across a silicon spacer ($l_{Si}=5$ Å): $\lambda_{GdCo}=65$, which turned out to be more than an order of magnitude lower than the constant $\lambda_{GdCo}\approx 1700$ for Gd/Co multilayered films not containing silicon layers. The lack of quantitative agreement between the calculated and experimental curves of $M_s(T)$ and $H_t(T)$ for $T>T_{comp}$ is due to the nonsingle-phase nature of the gadolinium in our multilayered film.

*E-mail: merenkov@ilt.kharkov.ua

[1] C. Dufour, Ph. Bauer, M. Sajeddine, K. Cherifi, G. Marshal, Ph. Mangin, and R. E. Camley, J. Magn. Magn. Mater. **121**, 300 (1993).
[2] D. J. Webb, R. G. Wamsley, K. Parvin, P. H. Dickinson, T. H. Geballe, and R. M. White, Phys. Rev. B **32**, 4667 (1985).
[3] R. E. Camley and D. R. Tilley, Phys. Rev. B **37**, 3413 (1988).
[4] L. G. Le Page and R. E. Camley, Phys. Rev. Lett. **65**, 1150 (1990).
[5] K. Takanashi, Y. Kamiguchi, H. Fujimori, and M. Motokawa, J. Phys. Soc. Jpn. **61**, 3721 (1992).
[6] K. Takanashi, H. Fujimori, and H. Kurokawa, J. Magn. Magn. Mater. **126**, 242 (1993).
[7] V. O. Vas'kovskiy, D. Garcia, A. V. Svalov, M. Vásquez, G. V. Kurlyandskaya, and A. V. Gorbunov, Fiz. Met. Metalloved. **86**, 140 (1998).
[8] V. O. Vas'kovskiy, A. V. Svalov, A. V. Gorbunov, N. N. Shchegoleva, and S. M. Zadvorkin, Fiz. Tverd. Tela (St. Petersburg) **73**, No. 4 (2001).
[9] M. Motokawa, Suppl. Prog. Theor. Phys. **101**, 537 (1990).

Translated by Steve Torstveit

Antiferromagnetic impurity states in a semi-infinite ferromagnet for various orientations of the surface relative to the crystal axes

T. G. Petrova*

B. Verkin Institute for Low Temperature Physics and Engineering, National Academy of Sciences of Ukraine, pr. Lenina 47, 61164 Kharkov, Ukraine

(Submitted August 30, 2000)
Fiz. Nizk. Temp. **27**, 196–202 (February 2001)

A study is made of spin states localized on an antiferromagnetic impurity found on the surface or in one of subsurface layers of a semi-infinite Heisenberg ferromagnet. Different orientations of the surface relative to the axes of the crystal are considered. The energies and eigenfunctions of the localized impurity states are found as functions of the parameters of the problem. It is found that in the system considered there always exists a definite subsurface layer in which it is energetically most favorable for the impurity to locate. The distance of this layer from the surface is completely determined by the direction of the surface plane relative to the axes of the magnetic lattice. © *2001 American Institute of Physics.*
[DOI: 10.1063/1.1353706]

1. INTRODUCTION

The properties of magnetically ordered crystals containing magnetic impurities are among the most interesting subjects in the theory of magnetism.[1–9] Of particular interest is the case of a ferromagnet with an antiferromagnetic (AFM) impurity, since the question of the ground state of such a system requires a separate analysis. A considerably number of papers have been devoted to solving this problem in an infinite ferromagnet.[1–7] As a result, it has been established that the ground state in question is localized on an impurity and has an energy lying below the continuous spectrum of excitations of the system.

In a semi-infinite lattice the characteristics of the near-surface impurity states are governed by the properties of the surface and can differ substantially from the case of an impurity found in the interior of the crystal. This circumstance leads, in particular, to dependence of the ground state energy of a semi-infinite ferromagnet with an AFM impurity on the position of the latter relative to the surface. An attempt to analyze this dependence for the simplest case, that of a (001) surface in a simple cubic lattice, was undertaken in Ref. 9. However, the relations between the energies of the impurity levels in that paper and the conclusions based on them correctly describe the physics of the problem only in a certain part of the investigated range of values of the exchange parameters.

A natural property that can appreciably influence the features of the impurity states in a semi-infinite system is the orientation of the surface plane relative to the crystal axes. In this paper we investigate how the surface orientation affects antiferromagnetic impurity states in a semi-infinite ferromagnet. We analyze the impurity levels in the energy spectrum of the system for arbitrary values of the exchange interaction parameters. We pay particular attention to the question of the energetically most favorable position of the impurity relative to the surface. We determine the dependence of this position on the direction of the surface plane in the magnetic lattice.

The energies and eigenfunctions of localized impurity states are found using the computational method of Jacobian matrices, which has been elaborated in detail in the field of lattice dynamics[10–13] and which has been applied numerous times to magnetically ordered systems.[6–9,14,15] This method allows one to avoid the spin-wave approximation, which is unsuitable in the given case, and to solve the stated quantum-mechanical problem in terms of spin deviation operators.

2. DESCRIPTION OF THE MODEL AND THE HAMILTONIAN OF THE SYSTEM

Let us consider a semi-infinite Heisenberg ferromagnet whose magnetic atoms have spin $S=1/2$ and form a simple cubic lattice with a nearest-neighbor interaction. We assume that the system has a free surface of the type $(n-10)$ with different possible orientations of the surface plane relative to the crystal axes, $n=0,2,3,\ldots$ (see Fig. 1). Such a model of the surface can give clear results that can be straightforwardly generalized to the case of arbitrary (not only integer) values of n.

In one of the sites of the magnetic lattice we place an AFM impurity, which differs from the regular atoms in that it has a negative exchange interaction with the neighboring spins. We note (see Fig. 1) that in the chosen model all of the surface planes with different values of n intersect along the z axis, and the pth subsurface layers parallel to them intersect along the axis $(0pz)$, where p is the number of the layer relative to the surface. Therefore, for further study it is convenient to place the impurity at a site with coordinates $(0p0)$, where it will be found in layer number p, which is the same for the whole group of surfaces $n=0,1,2,\ldots$.

With allowance for the arguments made above, the Heisenberg Hamiltonian for the system under study has the form

$$H=-I\sum_{\mathbf{m}(m_y\geqslant nm_x)}\mathbf{S}_{\mathbf{m}}[\mathbf{S}_{\mathbf{m}+(001)}+\mathbf{S}_{\mathbf{m}+(010)}+\mathbf{S}_{\mathbf{m}+(-100)}]$$
$$+(I-I')\mathbf{S}_{(0p0)}[\mathbf{S}_{(0p1)}+\mathbf{S}_{(0p-1)}+\mathbf{S}_{(0p+10)}+\mathbf{S}_{(-1po)}$$
$$+(1-\delta_{p0})\mathbf{S}_{(0p-10)}+\Theta(p-n)\mathbf{S}_{(1p0)}]. \quad (1)$$

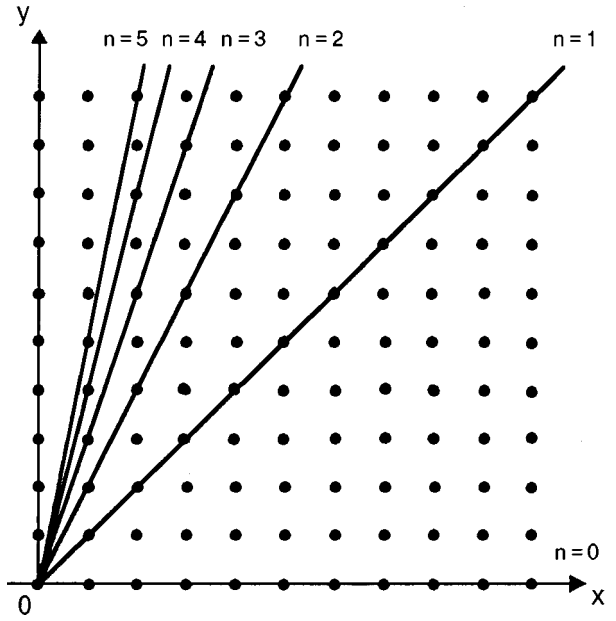

FIG. 1. Surface of the type $(n-10)$ in a simple cubic lattice ($n=0,1,2,\ldots$; the z axis is directed perpendicular to the plane of the figure).

Here $\mathbf{S_m}$ is the spin operator of a magnetic atom found in the **m**th lattice site (the magnetic moment of the system is directed along the z axis); $I>0$ and $I'<0$ are the integrals of the exchange interactions between the spins of the regular atoms and between the spin of the impurity and its neighbors; $n=0,1,2,\ldots$ denotes the different directions of the surface plane, and the index $p=0,1,2,\ldots$ numbers the layers parallel to the surface, including the surface; δ_{p0} is the Kronecker delta; $\Theta(p-n)$ is the step function, defined as

$$\Theta(x)=\begin{cases}1, & x\geqslant 0,\\ 0, & x<0.\end{cases} \tag{2}$$

Since the Hamiltonian (1) commutes with the z projection operator of the total spin of the system, the space of eigenfunctions of the operator H can be divided into subspaces characterized by definite values S_H^z of this z projection. The eigenstate of the operator H in which all of the atomic spins are parallel to one another belongs to the subspace with the maximum value of $S_H^z=NS$ and has the energy

$$E_0=-IS^2\{3N-(\eta+1)[5-\delta_{p0}+\Theta(p-n)]\}, \tag{3}$$

where $\eta=-I'/I$, N is the number of atoms in the lattice. Below the eigenvector describing this state will be denoted by the symbol $|0\rangle$, and the energy E_0 will be chosen as the zero of energy for the system.

In the absence of impurities ($I'=I$) or in the presence of a ferromagnetic defect ($I'>0$) the vector $|0\rangle$ corresponds to the ground state of the ferromagnet (see, e.g., Ref. 1). In the case of an AFM impurity with spin $S=1/2$ the ground state belongs to the subspace of single-particle excitations of the system with values $S_H^z=NS-1$ (Refs. 1–4). In this state the spin deviations localized on the impurity and on the neighboring atoms are large, and so the spin-wave approximation is unsuitable, and for solving the problem of the ground state of the system (1) it is convenient to use the above-described method of Jacobian matrices.

3. METHOD OF FINDING THE ENERGIES AND EIGENFUNCTIONS OF THE LOCALIZED STATES

Since the method of Jacobian matrices has been set forth in detail in a number of papers,[7,8,10–15] in this Section it will suffice to give a brief summary of the computational procedure. The method used here is based on choosing, in one of the subspaces of the operator H describing the system under study, a certain vector $\mathbf{g}_0$ of a definite form. This vector is used to construct a special cyclic subspace invariant with respect to the operator H:

$$\mathbf{g}_0,\ H\mathbf{g}_0,\ H^2\mathbf{g}_0,\ldots \tag{4}$$

and $\mathbf{g}_0$ is called the generating vector of the given cyclic subspace. The method of successive orthogonalization of the vectors (4) an orthonormalized basis $\{\mathbf{g}_l\}$ is constructed in the cyclic subspace ($l=0,1,2,\ldots$). The matrix operator H in this basis takes the Jacobian form:

$$H_{ll'}=\begin{pmatrix} a_0 & b_0 & 0 & 0 & 0 & \ldots\\ b_0 & a_1 & b_1 & 0 & 0 & \ldots\\ 0 & b_1 & a_2 & b_2 & 0 & \ldots\\ 0 & 0 & b_2 & a_3 & b_3 & \ldots\\ \ldots & \ldots & \ldots & \ldots & \ldots & \ldots \end{pmatrix}. \tag{5}$$

The energy spectrum of the operator H in the chosen basis is simple (nondegenerate), i.e., to each energy eigenvalue ε there corresponds a single eigenfunction $\Psi(\varepsilon)$, which can be represented in the form of an expansion in the basis $\{\mathbf{g}_l\}$:

$$\Psi(\varepsilon)=\mu(\varepsilon)\sum_{l=0}^{\infty}P_l(\varepsilon)\mathbf{g}_l. \tag{6}$$

Here $\mu(\varepsilon)$ is a normalizing factor, and $P_l(\varepsilon)$ is an lth-degree polynomial in ε which satisfies the recurrence relation

$$b_lP_{l+1}(\varepsilon)=(\varepsilon-a_l)P_l(\varepsilon)-b_{l-1}P_{l-1}(\varepsilon) \tag{7}$$

with the initial conditions $P_{-1}(\varepsilon)=0$, $P_0(\varepsilon)=1$.

If there are localized states in the system which lie outside the continuous spectrum of eigenvalues of the operator H, then their energy is found from the equation

$$P_l(\varepsilon)=0. \tag{8}$$

The rate of convergence of the local solutions of equation (8) to the true values of the energies for $l\to\infty$ depends on the degree of localization of the state in question. Expressions (6) and (8) are conveniently applied to states with a high degree of localization, since for them one can obtain results to good accuracy without going beyond small (single-digit) values of l. It is just such a situation that arises in the problem of states localized at an AFM impurity with spin $S=1/2$ in a ferromagnetic crystal. In that case the spin deviations are well localized even in the first coordination sphere of the impurity.[1,5]

It should also be noted that the described procedure for obtaining the energies and eigenfunctions of localized states is based on the correct choice of the generating vector $\mathbf{g}_0$. It is best to use for $\mathbf{g}_0$ the vector that appears with the highest weight in the eigenfunction (6) of the desired localized state. For the problem solved in this paper, the natural role of this

vector is played by the state with the spin of the impurity atom antiparallel to the direction of the magnetic moment of the rest of the lattice.

4. AFM IMPURITY STATES IN THE ENERGY SPECTRUM OF THE SYSTEM

Using the computational method described in the previous Section, we shall find the characteristics of localized impurity states in the subspace of single-particle excitations of system (1). To do this, we construct the first two orthonormalized basis vectors in the cyclic subspace of the operator $H-E_0$ generated by the vector $\mathbf{g}_0$ [the energy E_0 is determined by expression (3)]:

$$\begin{aligned}\mathbf{g}_0&=S^-_{(0p0)}|0\rangle,\\ \mathbf{g}_1&=[5-\delta_{p0}+\Theta(p-n)]^{-1/2}[S^-_{(0p1)}+S^-_{(0p-1)}\\ &\quad+S^-_{(-1p0)}+S^-_{(0p+10)}+(1-\delta_{p0})S^-_{(0p-10)}\\ &\quad+\Theta(p-n)S^-_{(1p0)}]|0\rangle,\end{aligned}\tag{9}$$

where the operator $S^-=S^x-iS^y$.

With the aid of vectors (9), we obtain the first three matrix elements of the Jacobian matrix (5):

$$a_0=-\frac{I}{2}\eta\alpha_{pn},\quad b_0=\frac{I}{2}\eta\sqrt{\alpha_{pn}},\tag{10}$$

$$\begin{aligned}a_1&=-\frac{I}{2}\left(\eta-5+\frac{\gamma_{pn}}{\alpha_{pn}}\right),\\ \alpha_{pn}&=5-\delta_{p0}+\Theta(p-N),\\ \gamma_{pn}&=4+\delta_{p0}(1+\delta_{n0})+\delta_{p1}-\Theta(p-n+1)\\ &\quad-2\Theta(p-n-1)-\Theta(p-2n).\end{aligned}\tag{11}$$

From the matrix elements (10) and (11), we construct the polynomials $P_l(\varepsilon)$ to $l=2$ inclusive using the recurrence relation (7). The smallest root of the equation $P_2(\varepsilon)=0$ gives the energy of the local impurity level lying below the energy E_0 and corresponding to the ground state of the system (1):

$$\varepsilon_{pn}=-\frac{I}{4}\left\{\eta(1+\alpha_{pn})-5+\frac{\gamma_{pn}}{\alpha_{pn}}+\sqrt{[\eta(\alpha_{pn}-1)+5-\gamma_{pn}/\alpha_{pn}]^2+4\eta^2\alpha_{pn}}\right\}.\tag{12}$$

The eigenfunction of this state is determined from formula (6) by substituting vectors (9) and the energy $\varepsilon=\varepsilon_{pn}$ into it.

In each region of values of the parameter $\eta\ll 1$ or $\eta\gg 1$ the energies ε_{pn} can be written in a convenient form for study by expanding expression (12) in powers of η or $1/\eta$:

$$\varepsilon_{pn}\approx-\frac{I\eta}{2}\begin{cases}\alpha_{pn}\left(1+\dfrac{\eta}{5-\gamma_{pn}\alpha_{pn}^{-1}}\right), & \eta\ll 1,\\ (1+\alpha_{pn})\left[1-\dfrac{5-\gamma_{pn}\alpha_{pn}^{-1}}{\eta(1+\alpha_{pn})^2}\right], & \eta\gg 1.\end{cases}\tag{13}$$

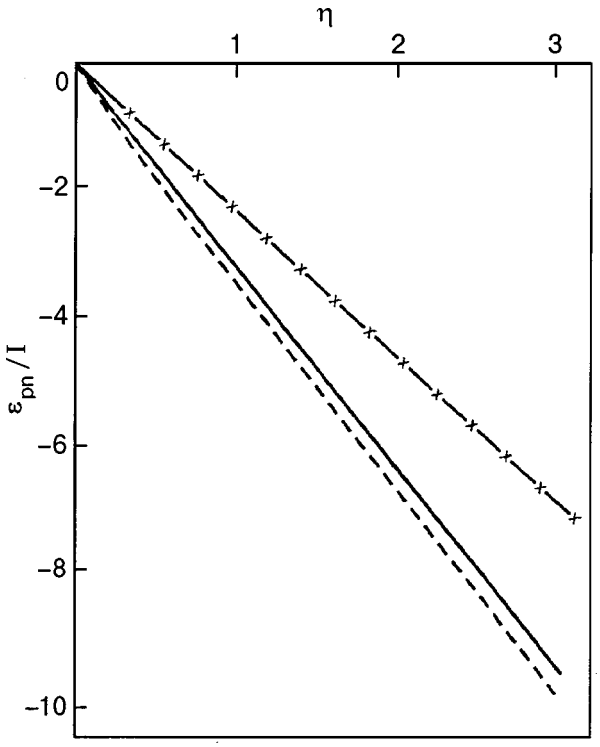

FIG. 2. Ground-state energy of the system (1) as a function of the parameter $\eta=-I'/I$ for positions of the AFM impurity in the interior of the crystal ($p\gg n$) (———), in the plane of the surface ($p=0$) (–×–×–), and in a subsurface layer with index $p=n+\delta_{n0}$ (– – –).

We note that the leading terms of the expansion (13) will be minimum at the maximum value of α_{pn}, while the higher-order terms will be minimum at the maximum value of γ_{pn}. For each fixed number n both these conditions hold simultaneously in the case $p=n+\delta_{n0}$ [see formula (11)]. Here the impurity level has the lowest energy $\varepsilon_{n+\delta_{n0},n}$ determined by expression (13) with $\alpha_{pn}=6$ and $\gamma_{pn}=3+\delta_{n1}-2\delta_{n0}$.

It also follows from relations (11) and (13) that the highest energy ε_{0n} belongs to the state in which the defect is found in the plane of the surface ($p=0$, $\alpha_{0n}=4+\delta_{n0}$, $\gamma_{0n}=5-\delta_{n0}-\delta_{n1}$). If the impurity is located in the interior of the crystal ($p\gg n$), then the energy ε_v of the local level ($\alpha_{pn}=6$, $\gamma_{pn}=0$) occupies an intermediate position $\varepsilon_{n+\delta_{n0},n}<\varepsilon_v<\varepsilon_{0n}$. In the solutions (13) obtained above, the impurity will already become insensitive to the surface for $p\geqslant 2(n+\delta_{n0})$, where the equality $\varepsilon_{pn}=\varepsilon_v$ holds. The same relation between the energies of the impurity states is obtained directly from expression (12) at any value η considered.

The relative position of the impurity levels ε_{0n}, ε_v, and $\varepsilon_{n+\delta_{n0},n}$ in the energy spectrum of the system (1) as a function of the parameter η is shown schematically in Fig. 2 (states with other indices p lie between the levels shown). As we see from Fig. 2 and formulas (12) and (13), all of the energies ε_{pn} behave in a similar way as η varies: they tend toward the lower boundary of the continuous spectrum as $\eta\to 0$ and split off ever farther from it as $\eta\to\infty$. However, the distances in the spectrum of the system between the level ε_v and different near-surface levels do not all have the same dependence on the parameter η. Using expressions (11) and (13), we easily find this distance in the case $p=n+\delta_{n0}$:

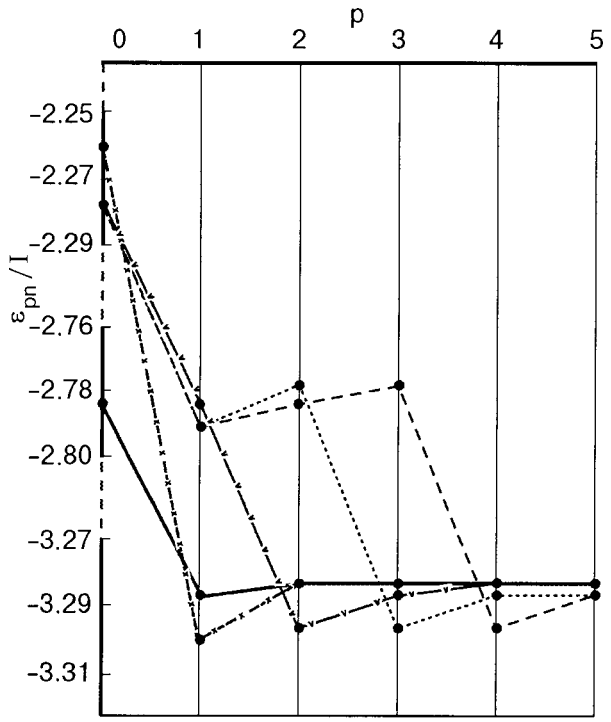

FIG. 3. Energies of AFM impurity states in a semi-infinite ferromagnet for different directions of the surface plane ($\eta=1$): $n=0$ (———); 1 (–×–×–); 2 (–\/–\/–); 3 (· · · ·); 4 (– – –).

$$\varepsilon_v-\varepsilon_{n+\delta_{n0},n}=I\begin{cases}\dfrac{3}{5}\,\eta^2\dfrac{3+\delta_{n1}-2\delta_{n0}}{27-\delta_{n1}+2\delta_{n0}}, & \eta\ll 1,\\[2ex] \dfrac{1}{84}(3+\delta_{n1}-2\delta_{n0}), & \eta\gg 1.\end{cases} \tag{14}$$

We see from (14) that for $\eta\to\infty$ this distance tends toward a certain positive value that does not depend on η. Here the levels ε_v and $\varepsilon_{n+\delta_{n0},n}$ in Fig. 2 run parallel to each other, maintaining their relative position for $\eta\ll 1$. At the same time, as follows from (11) and (13), the difference $\varepsilon_{0n}-\varepsilon_v$ increases with increasing η in proportion to the value of this parameter.

The behavior of the energy ε_v in Fig. 2 is in complete agreement with the results obtained previously in Refs. 6 and 7 for an AFM impurity in an infinite ferromagnet. However the relative position of the levels ε_{0n} and ε_v in the region $\eta\leqslant 1$ in this figure is fundamentally different from the analogous relations presented in Ref. 9 for the particular case of the surface, $n=0$. Apparently this difference is due to the insufficiently well thought-out choice of the zero of energy in the spectrum of the semi-infinite system in Ref. 9.

The influence of the orientation of the surface on AFM impurity states in a semi-infinite ferromagnet can be traced particularly clearly in Fig. 3, which shows the numerical dependence of the energy (12) on the position of the impurity in the lattice for different values of the number n. We see from Fig. 3 that for each fixed value of n the maximum and minimum energies ε_{pn} are reached for the same cases $p=0$ and $p=n+\delta_{n0}$ as in the approximate expressions (13). As the index p increases, the energies ε_{pn} grow, tending toward the limiting value ε_v and coinciding with it for $p\geqslant 2(n+\delta_{n0})$.

5. DISCUSSION OF THE RESULTS

The results obtained in Sec. 4 have a simple physical interpretation. It is clear that the state with the flipped spin of the AFM impurity [the vector $\mathbf{g}_0$ in expressions (9)] has the lowest energy when the defect has the maximum possible number of nearest neighbors. In turn, a flip of the spin of an atom in the first coordination sphere of the impurity [the vector $\mathbf{g}_1$ in (9)] becomes energetically more favorable when this atom is located on the surface of the system. Since the eigenfunction (6) of a localized impurity state contains a superposition of the vectors $\mathbf{g}_0$ and $\mathbf{g}_1$, the energy corresponding to it will be minimum when both of the conditions stated above are satisfied simultaneously. In the investigated model of the system such a situation can arise for each specified direction of the surface in a single case, which is realized when the impurity is located in the subsurface layer with index $p=n+\delta_{n0}$ (see Fig. 1). Thus the position of the minimum of the energies ε_{pn} shown in Fig. 3 is determined by the geometry of the semi-infinite magnetic lattice.

The relative depth of the minimum found, $(\varepsilon_v-\varepsilon_{n+\delta_{n0},n})/|\varepsilon_v|$ is small [see Fig. 3 and expressions (13) and (14)]. This is explained by the fact that the state $\mathbf{g}_1$ responsible for its appearance enters into the function (6) with a lower weight than does the vector $\mathbf{g}_0$ and carriers a comparatively smaller contribution to the energy of the local levels. It is expected that as the ferromagnetic exchange in the near-surface region of the system is weakened, the depth of the minimum obtained here increases, since flips of the spins of the nearest neighbors of the impurity are easier in that region. Otherwise the relationship between the energies ε_{pn} could change, and at a large enough value of the exchange in the surface region the energetically most favorable position for the impurity becomes one in the interior of the crystal. Taking the next coordination spheres of the defect into account gives a negligible contribution to the energies ε_{pn} and cannot appreciably affect their relative position in Figs. 2 and 3.

The above analysis is easily generalized to the case of fractional values of n. Since all of the feature of the system are concentrated in the (x,y) plane, it is sufficient to consider only the two-dimensional situation specified. Then the distance from the surface, which is specified by the relation $m_y=cm_x$ ($c=n_y/n_x\geqslant 1$ is an irreducible fraction, $n_x,n_y\geqslant 1$ are integers), to the impurity, which has coordinates $m_y'\geqslant cm_x'$, can be written as

$$r=a(m_y'-cm_x')(1+c^2)^{-1/2}, \tag{15}$$

where a is the lattice constant. According to the physical arguments presented above and in accordance with the geometry of the system, the energetically most favorable position for the impurity is reached at $m_y'=m_y$, $m_x'=m_x-1$ (see also Fig. 1). It follows from (15) that here the impurity is found in a layer that lies at a distance from the surface $r_{\min}=ac(1+c^2)^{-1/2}$. The distance between adjacent layers is obtained from expression (15) for $m_y'n_x-m_x'n_y=1$ and is equal to $r_0=an_x^{-1}(1+c^2)^{-1/2}$. Hence the index of the layer corresponding to the impurity level with the minimum energy is found as $p=r_{\min}/r_0=n_y$ and agrees, for $n_x=1$, $n_y=n$ with the result obtained in Sec. 4 for integer values

($c=n$). It is clear that for surfaces $m_x=m_y/c$ lying between the planes $n=0$ and $n=1$ in Fig. 1, the desired index will have the value $p=n_x$.

Thus the ground-state energy of a semi-infinite ferromagnet containing an AFM impurity depends substantially not only on the exchange interactions and the positions of the defect relative to the surface but also on the direction of the surface plane in the magnetic crystal. A particularly interesting circumstance is that for any of the values considered for the parameters of the system, there is a preferred subsurface layer which is the energetically most favorable location for the impurity. The distance from the layer to the surface is different for different directions of the surface plane and is determined completely by its orientation relative to the crystallographic axes of the lattice.

In closing the author thanks E. S. Syrkin for numerous discussions of the results of this study.

*E-mail: petrova@ilt.kharkov.ua

[1] Yu. A. Izyumov and M. V. Medvedev, *Theory of Magnetically Ordered Crystals with Impurities* [in Russian], Nauka, Moscow (1970).
[2] H. Ishii, J. Kanamori, and T. Nakamura, Prog. Theor. Phys. **33**, 795 (1965).
[3] Yu. A. Izyumov and M. V. Medvedev, Zh. Éksp. Teor. Fiz. **51**, 517 (1966) [Sov. Phys. JETP **24**, 347 (1967)].
[4] Y. I. Wang and H. Callen, Phys. Rev. **160**, 358 (1967).
[5] B. Ya. Balagurov and V. G. Vaks, Zh. Éksp. Teor. Fiz. **66**, 1135 (1974) [Sov. Phys. JETP **39**, 554 (1974)].
[6] V. I. Peresada, V. N. Afanasyev, and V. S. Borovikov, Solid State Commun. **17**, 867 (1975).
[7] V. I. Peresada, V. N. Afanas'ev, and V. S. Borovikov, Fiz. Nizk. Temp. **4**, 111 (1978) [Sov. J. Low Temp. Phys. **4**, 56 (1978)].
[8] T. G. Petrova, Fiz. Nizk. Temp. **4**, 1453 (1978) [Sov. J. Low Temp. Phys. **4**, 684 (1978)].
[9] V. S. Borovikov, Fiz. Tverd. Tela (Leningrad) **23**, 2530 (1981) [Sov. Phys. Solid State **23**, 1486 (1981)].
[10] V. I. Peresada, Zh. Éksp. Teor. Fiz. **53**, 605 (1967) [Sov. Phys. JETP **26**, 389 (1968)].
[11] V. I. Peresada, FKS (FTINT AN UkrSSR, Kharkov), No. 2, 172 (1968).
[12] V. I. Peresada and E. S. Syrkin, Fiz. Tverd. Tela (Leningrad) **16**, 687 (1974) [Sov. Phys. Solid State **16**, 452 (1974)].
[13] V. I. Peresada and E. S. Syrkin, Fiz. Nizk. Temp. **3**, 229 (1977) [Sov. J. Low Temp. Phys. **3**, 110 (1977)].
[14] T. G. Petrova, Fiz. Nizk. Temp. **6**, 627 (1980) [Sov. J. Low Temp. Phys. **6**, 302 (1980)].
[15] T. G. Petrova and E. C. Syrkin, Phys. Status Solidi B **116**, 475 (1983).

Translated by Steve Torstveit

LATTICE DYNAMICS

Raman scattering in the vicinity of the ferroelastic phase transition to the monoclinic phase in $KSc(MoO_4)_2$

N. M. Nesterenko,* A. V. Peschanskiĭ, and V. I. Fomin

B. Verkin Institute for Low Temperature Physics and Engineering, National Academy of Sciences of Ukraine, pr. Lenina 47, 61164 Kharkov, Ukraine
(Submitted July 27, 2000)
Fiz. Nizk. Temp. **27**, 203–209 (February 2001)

The low-energy lattice modes are investigated above and below the temperature of the phase transition from the trigonal to the monoclinic phase in $KSc(MoO_4)_2$ by the Raman scattering method. The Raman spectra exhibit anomalies at temperatures above the phase transition to the monoclinic phase ($T\sim 260$ K) in the region of external oscillations of the tetrahedral anion. Anomalous behavior of the damping A_g of the soft mode is observed in the temperature region 240–260 K. A model of the phase transition is discussed. © *2001 American Institute of Physics.* [DOI: 10.1063/1.1353710]

INTRODUCTION

Experiments done on the trigonal crystals $KSc(MoO_4)_2$ and $KFe(MoO_4)_2$ have made it possible to propose a model for their ferroelastic phase transitions, which has been extended to the family of isostructural trigonal double molybdates and tungstates.[1] Second-order phase transitions to the ferroelastic phases in these crystals are induced by the two-dimensional irreducible representations τ_5 (τ_6) of the point $\mathbf{k}=(1/2)\mathbf{b}_3$ of the Brillouin zone of the trigonal phase $P\bar{3}m1$ ($z=1$).[2] Later experimental studies have yielded additional data on the phase diagram of a number of crystals of this family. The results of x-ray structural studies[3] of the $KSc(MoO_4)_2$ crystal at a temperature above $T_1\sim 260$ K (where T_1 is the temperature at which the C_3 axis vanishes in the crystal) suggest another possible choice of initial space group, viz., $P\bar{3}c1$ ($z=2$). This is indicated by the nonzero intensity of a number of reflections corresponding to the doubled value of the crystallographic cell parameter c in comparison with $P\bar{3}m1$ ($z=1$) and by the lower divergence factor. Studies of the ESR spectra of a number of crystals containing impurity Cr^{3+} have revealed features that were attributed to the observation of incommensurate phases at the phase transition from the trigonal to the monoclinic phase;[4,5] these features have also been observed in $KSc(MoO_4)_2$. Finally, at temperatures near $T_2\sim 240$ K, according to the data of optical studies,[3,6] $KSc(MoO_4)_2$ has a first-order phase transition, the nature of which has not been investigated. It is assumed[3] that the phase transition at $T_2\sim 240$ K is due to a ''switching'' between the $C2/c$ and $C2/m$ monoclinic phases with preservation of the preferred axis C_2.

The vibrational spectrum of the $KSc(MoO_4)_2$ crystal has been investigated over a wide range of temperatures in a number of studies.[7–9] In the present study, with the goal of elucidating the phase diagram of $KSc(MoO_4)_2$, we have done additional research on the Raman scattering spectra, with an analysis of the behavior of the low-energy phonon modes over a wide range of temperatures. Particular attention has been devoted to temperatures near the ferroelastic phase transition from the trigonal to the monoclinic phase ($T_1\sim 260$ K) and the temperature region 260–240 K.

MEASUREMENT TECHNIQUE

The studies were done on $KSc(MoO_4)_2$ single crystals of good optical quality. The samples were cut out in the shape of rectangular slabs with typical dimensions of $5\times 10\times 1.5$ mm, the edges of which were parallel to the X, Y, and Z axes, where $Z\|C_3$, $X\|C_2$, and $Y\perp Z,X$.

The Raman spectra were excited by argon laser radiation at a wavelength of 488.0 nm with a power of 150 mW. The light scattered by the sample at an angle of 90° was analyzed by a Jobin Yvon U-1000 double monochromator and was recorded by means of a cooled photomultiplier and a photon counting circuit. The samples were placed in an optical cryostat permitting measurement over a wide temperature interval. The temperature was determined by a copper–Constantan thermocouple, the junction of which was placed on the surface of the sample. The error in the determination of the absolute value of the temperature was not over 1 K.

The spectra are represented in the standard notation $k(ij)q$, where k and q are the directions of propagation of the incident and scattered light, with the electric vector **e** along i and j, respectively. The symbols YZ, ZZ, etc. refer to components of the Raman scattering tensor.

EXPERIMENTAL RESULTS

The Raman spectra of the trigonal phase of $KSc(MoO_4)_2$ at room temperature contains eight intense lines, the frequency position and polarization of which are similar to those given in Ref. 9. In accordance with a group-theoretic analysis[9] for the trigonal cell with symmetry $P\bar{3}m1$ ($z=1$), all of the predicted modes $A_{1g}+2E_g$ in the frequency region corresponding to the external vibrations are observed: the

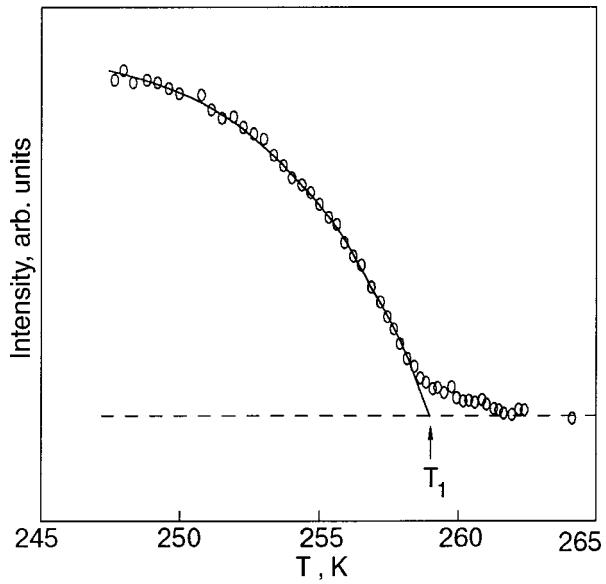

FIG. 1. Temperature dependence of the light-scattering intensity in the experimental geometry $X(YZ)Y$ at a frequency of 4 cm^{-1}.

translational vibrations A_{1g} (161 cm^{-1}) and E_g (154 cm^{-1}) and the librational vibration E_g (62 cm^{-1}) of the tetrahedral anions MoO_4^{2-}.

To determine the temperature of the second-order phase transition from the trigonal phase, we made observations of the light-scattering intensities near the excitation line as the temperature was lowered. A temperature $T_1 = 259$ K was obtained by extrapolating the smooth curve and is identified as the temperature of the second-order phase transition to the low-symmetry phase (Fig. 1). The weak increase in the scattering intensity in the temperature region 259–261 K may be due to a fluctuational contribution.

As we see in Fig. 2, in the spectrum with the ZZ component of the scattering tensor (the A_g modes), in which only one A_{1g} mode (161 cm^{-1}) should be observed, two additional low-intensity lines with frequencies of 62 and 120 cm^{-1} are observed above T_1. The line with the lower frequency coincides, within the measurement error, with an intense line in the YZ spectrum, which corresponds to the E_g modes, and may appear in the ZZ spectra on account of depolarization. The line at 120 cm^{-1} is not a consequence of depolarization, since there are no lines in this frequency region in the other polarizations. Its temperature behavior (Fig. 2) shows that it is not due to two-particle processes either: it is an ''extra'' line for the high-temperature phase of $KSc(MoO_4)_2$ described by the space group $P\bar{3}m1$ ($z=1$).

Below $T_1 = 259$ K some new lines appear, two of which exhibit soft-mode behavior. Figures 2 and 3 show the evolution of the spectra of the two soft modes, which are observed in the range 5–45 cm^{-1}, and also ''hard'' lattice modes (frequency range 55–165 cm^{-1}) over a wide interval of temperatures including T_1 and T_2.

For a more precise determination of the parameters of the lines corresponding to the soft modes, we recorded the Raman spectra at frequencies below 45 cm^{-1} (Fig. 4) with a spectral resolution of 1 cm^{-1}. This made it possible to reduce the elastic-scattering contribution at low frequencies and to decrease the error of determination of the parameters

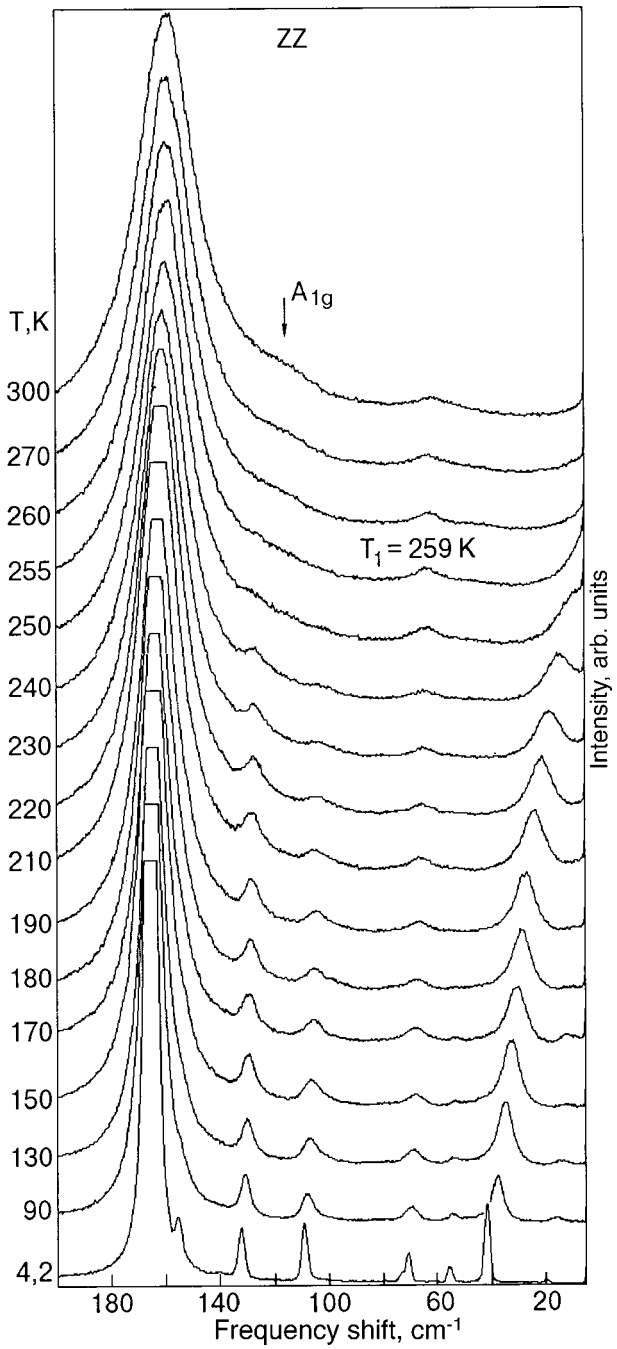

FIG. 2. Temperature evolution of the Raman spectrum (experimental geometry $X(ZZ)Y$) in the temperature region 4.2–300 K. The spectral resolution is 2 cm^{-1}.

of the lines by observing them all the way to the phase transition temperature T_1. The temperature dependence of the parameters A_g (the ZZ component of the scattering tensor) and B_g (YZ) of the soft modes in the monoclinic phase was determined in a damped-oscillator model; the results are shown in Fig. 5. The mode B_g has an approximately linear trend of the broadening with increasing temperature, whereas the A_g mode suffers substantial broadening above $T_2 \sim 240$ K (Fig. 5b). Above 240 K there is a large uncertainty in the determination of the parameters of the B_g mode.

Thus the observation of two soft modes indicates that an oscillation which is twofold degenerate in the high-temperature phase softens at T_1, attesting to a lowering of

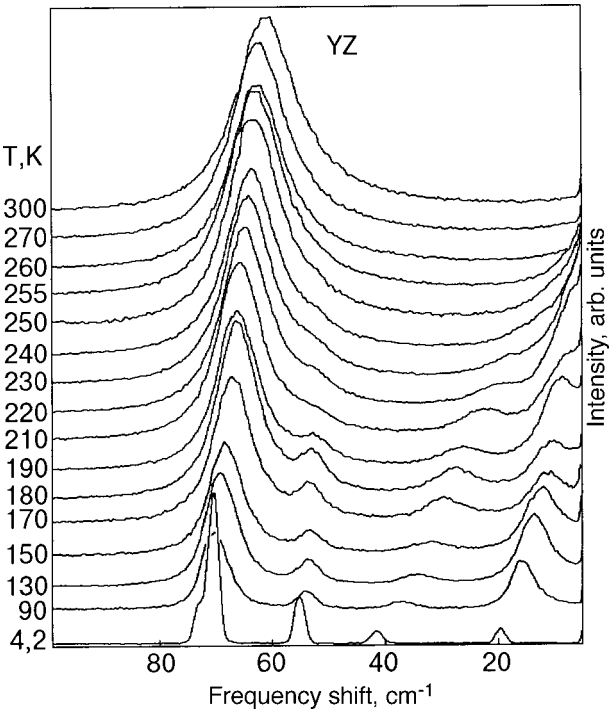

FIG. 3. Temperature evolution of the Raman spectrum (experimental geometry $X(YZ)Y$) in the temperature region 4.2–300 K. The spectral resolution is 2 cm^{-1}.

the symmetry from trigonal to monoclinic $C2/c$ $(z=2)$ or $C2/m$ $(z=2)$. Near $T_2 \sim 240$ K anomalous broadening of the soft mode A_g is observed, with no noticeable jumps in the position of the line or the appearance of new lines. Weak additional lines are observed in the Raman spectrum near T_1 at frequencies in the region corresponding to the external vibrations.

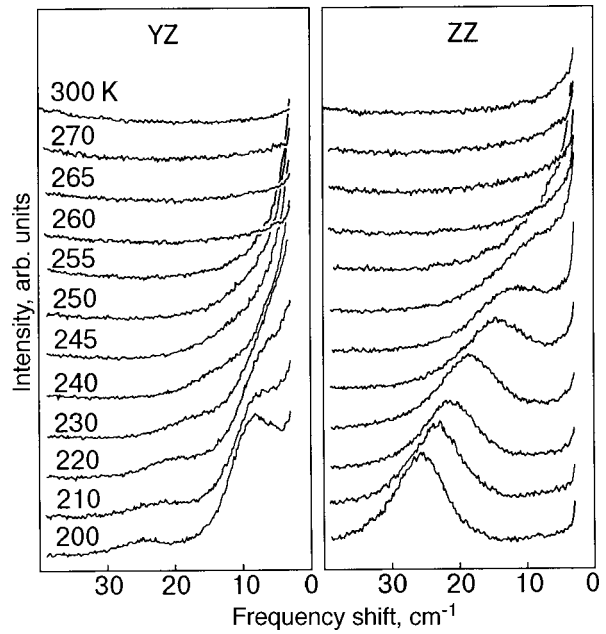

FIG. 4. Temperature behavior of the Raman spectra of the soft modes. The experimental geometries $X(YZ)Y$ and $X(ZZ)Y$. The spectral resolution is 1 cm^{-1}.

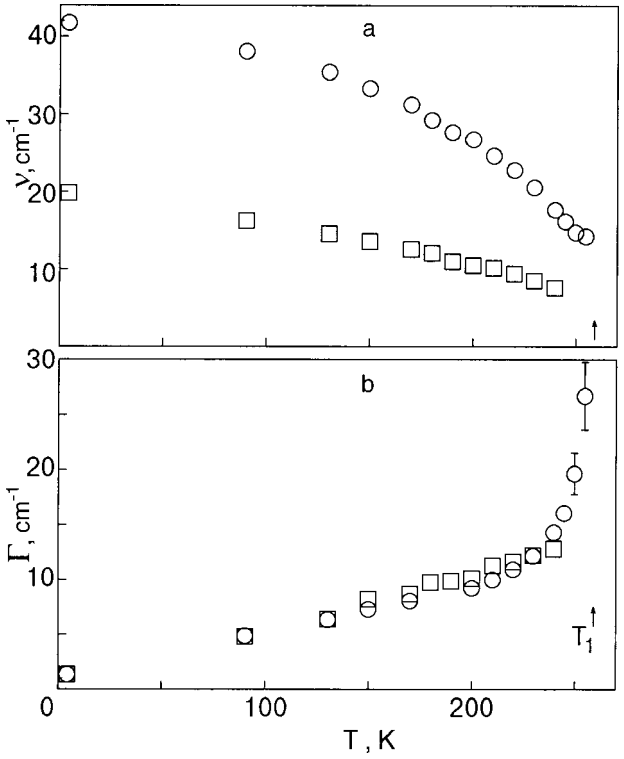

FIG. 5. Temperature behavior of the frequency ν (a) and half-width Γ (b) of the lines corresponding to the soft modes: the A_g mode (○); the B_g mode (□).

DISCUSSION

We assume that for $T>300$ K there is a phase transition between two trigonal phases, $P\bar{3}m1 \leftrightarrow P\bar{3}c1$, which is attested to by the additional weak lines in the Raman spectrum at temperatures above T_1. A second-order phase transition between these phases can occur at the point $\mathbf{k}=(1/2)\mathbf{b}_3$ of the Brillouin zone of $P\bar{3}m1$ according to the one-dimensional representations $\tau_2[R_z(A_1)+R_z(A_2)]$ and $\tau_3[R_z(A_1)-R_z(A_2)]$ (A_1 and A_2 are two types of MoO_4^{2-} tetrahedral complexes, and R_z describes the rotation about the C_3 axis).[9] The domains arising at this phase transition are optically indistinguishable. For further discussion let us consider the possible changes in the Raman spectra in the case of a phase transition $P\bar{3}m1 \leftrightarrow P\bar{3}c1$.

A phase transition is accompanied by the displacement of individual atoms from their equilibrium positions. If symmetry coordinates are constructed which transform according to the parameters τ_2 (τ_3) of the point $\mathbf{k}=(1/2)\mathbf{b}_3$ of the Brillouin zone of the trigonal phase $P\bar{3}m1$, then, as was shown in Ref. 9, the distortion in the $P\bar{3}c1$ phase is a static rotation of the tetrahedral anions MoO_4^{2-} about the C_3 axis. The correlated antiphase (in-phase) rotations of the anions in adjacent $\{K^+MoO_4^{2-}\}$ layers leads to a doubling of the volume of the trigonal cell and a lowering of the positional symmetry of the K^+ and Sc^{3+} ions.

Such a phase transition can also be realized as an order–disorder transition. In that case the appearance of reflections is brought about by the quasistatic distortions due to periodic jumps of the anions between different equilibrium positions, which should be accessible in the initial phase. In the case of

TABLE I. Symmetry of the vibrational modes in different phases of the $KSc(MoO_4)_2$ crystal.

Symmetry of the phase	Point of the Brillouin Zone	Symmetry of the external vibrations						Active representaion
$P\bar{3}m1$	$\mathbf{k} = \frac{1}{2}\mathbf{b}_3$	$2\tau_1$	τ_2	τ_3	$2\tau_4$	$3\tau_5$	$3\tau_6$	
$P\bar{3}c1$	$\mathbf{k} = 0$	$2A_{1u}$ $2A_{2g}$	A_{1g} A_{2u}	A_{2u} A_{1g}	$2A_{2g}$ $2A_{1u}$	$3E_u$ $3E_g$	$3E_g$ $3E_u$	τ_2 τ_3
$C2/m$	$\mathbf{k} = 0$	$2A_g$ $2B_u$	A_u B_g	B_g A_u	$2B_u$ $2A_g$	$3(A_g + B_g)$ $3(A_u + B_u)$	$3(A_u + B_u)$ $3(A_g + B_g)$	τ_5 τ_6
$C2/c$	$\mathbf{k} = 0$	$2B_g$ $2A_u$	B_u A_g	A_g B_u	$2A_u$ $2B_g$	$3(A_g + B_g)$ $3(A_u + B_u)$	$3(A_u + B_u)$ $3(A_g + B_g)$	τ_5 τ_6

Note: The Raman-active modes are A_{1g}, E_g, A_g, and B_g.

rapid processes a relaxational mode should appear in the scattering spectrum, but this has not been observed experimentally.

When the Brillouin zone is turned, the spectrum of optical vibrational excitations should acquire additional modes. An analysis shows that, as can be seen from Table I, regardless of which of the representations τ_2 or τ_3 induces the phase transition $P\bar{3}m1$ $(z=1) \leftrightarrow P\bar{3}c1$ $(z=2)$, the same number of additional Raman-active vibrational modes with symmetry $A_{1g}+3E_g$ can be observed in the spectrum of the external vibrations. The difference between the two cases is that in one case the antisymmetric $\tau_2+3\tau_6$ excitations from the Brillouin zone boundary lie at the center of the new band, while in the other it is the symmetric $\tau_3+3\tau_5$ excitations. Thus in the case that the $P\bar{3}c1$ phase is realized, an additional line should be observed in the Raman spectra with the ZZ component of the scattering tensor (A_{1g} mode).

A study of the temperature dependence of the Raman spectra with the YZ component of the scattering tensor established that, in contrast to the conclusions of Ref. 9, the splitting of the E_g rotational vibration of the MoO_4^{2-} tetrahedron is 2.5 cm^{-1} (the frequencies of the corresponding lines are 70.5 and 73 cm^{-1} at $T=4.2$ K; Fig. 3). As the temperature is increased and approaches T_1, the intensity of the line at frequency 55 cm^{-1} (which includes A_g and B_g modes which are close in frequency) decreases. Such a change in intensity indicates that this line is associated with the Brillouin zone boundary of the $P\bar{3}m1$ phase. This same line can also be observed in the high-temperature phase $P\bar{3}c1$. Because of its low intensity and its frequency position, it is masked by an intense line (Fig. 3) belonging to the $P\bar{3}m1$ $(z=1)$ and $P\bar{3}c1$ $(z=2)$ phases. Apparently an analogous situation is observed for the other additional E_g modes of the crystal described by the symmetry $P\bar{3}m1$. If the additional A_{1g} mode (120 cm^{-1}) that is the parameter of the transition $P\bar{3}m1 \leftrightarrow P\bar{3}c1$ has a very low intensity, then one would expect that the three additional E_g modes arising at such a transition will have low intensity.

If, however, the parameter c doubles for $T>T_1$, then the phase transition to the monoclinic phase near T_1 occurs without a change in the volume of the primitive cell. In other words, it is induced by the irreducible representation E_g of the point $\mathbf{k}=0$ of the $P\bar{3}c1$ phase. We note, first, that the second-order ferroelastic phase transition from the trigonal to the monoclinic phase at the Brillouin zone center should be accompanied only by splitting of the degenerate E_g modes and should not lead to the appearance of new vibrational modes (including soft modes) in the Raman spectra. Second, the second-order phase transition $\bar{3}m \rightarrow 2/m_x$ at $\mathbf{k}=0$ is strictly forbidden, since the thermodynamic potential constructed for the two-dimensional representation E_g contains a cubic invariant (a continuous phase transition is possible only at an isolated point on the $P-T$ diagram at which the coefficient of the cubic invariant passes through zero).

Our present study of the Raman spectra of the dissymmetric phases of the $KSc(MoO_4)_2$ crystal with a high spectral resolution (~ 1 cm^{-1}) shows that for 4.2 K$<T<T_1$ the number of lines observed in the region of the external and internal vibrations is satisfactorily described by a primitive cell containing two formula units, in agreement with the results of Ref. 9. Consequently, there are no grounds for assuming that the primitive cell of the monoclinic phase contains four formula units.

Thus the phase $P\bar{3}m1$ $(z=1)$ should represent the ''prototype phase'' for the phase transition from the trigonal $P\bar{3}c1$ $(z=2)$ to the monoclinic $C2/c$ $(z=2)$ or $C2/m$ $(z=2)$ phase.

It has been proposed[1] that the second-order phase transition to the monoclinic phase is accompanied by a doubling of the cell parameter. The appearance of two soft modes of different symmetry below the critical temperature T_1 indicates that in the course of the second-order phase transition a twofold degenerate vibration at the Brillouin boundary loses stability.[7] In other words, the active representations are the two-dimensional representations τ_5 and τ_6 (Ref. 10), which are associated with the point $\mathbf{k}=(1/2)\mathbf{b}_3$ at the Brillouin boundary of the trigonal phase $P\bar{3}m1$ $(z=1)$.

The phase transition induced by the τ_5 (τ_6) representations to the same monoclinic phases $C2/c$ or $C2/m$ is accompanied by the displacement of the K (Sc) ions and correlated rotations of the MoO_4^{2-} tetrahedra.[9] The spectrum of external vibrations should contain $3A_g+3B_g$ modes, which are ''in-

herited'' from the trigonal phase $P\bar{3}m1$: $A_{1g}\rightarrow A_g$, $A_{2g}\rightarrow B_g$, $2E_{2g}\rightarrow 2(A_g+B_g)$. In addition, one expects the appearance of additional modes that have come in from the Brillouin zone boundary. As we see from Table I, in the transition to the $C2/c$ or $C2/m$ phase, different numerical relationships of the A_g and B_g modes can be realized in the Raman spectra. At the transition to different monoclinic phases one also expects a different frequency position of the additional lines in the Raman spectrum, including those of the soft modes, since they originate from different vibrational branches at the Brillouin zone boundary (see Table I).

As we see in Figs. 2 and 3, at temperatures $T_1>T>T_2$ the additional lines of the spectrum have low intensity and an appreciable half-width and are masked by the wings of the intense lines of the trigonal phase. Therefore, at $T_2=240$ K we were unable to observe the change in the frequency position of the modes that have come in from the Brillouin boundary. However, an anomalous broadening of the soft mode A_g (Figs. 4 and 5) is observed in this region, and in our view this reflects a change in state of the crystal in the vicinity of 240 K and may be due to a phase transition between two monoclinic modifications. Let us discuss the possible nature of this broadening.

Optical studies of $KSc(MoO_4)_2$ in polarized light[7] have shown that at temperatures below $T_1\sim 260$ K, bulk samples are nonuniformly darkened, and only below a temperature $T_2\sim 240$ K can one positively observe orientational twins in them. The kinetics of formation of the domain structures in perfect thin slabs, as was shown in Ref. 3, also singles out the temperature region $T_2<T<T_1$ as being one in which nonuniform states are observed in the form of polysynthetic twins with a predominant type of domain walls W' and with the size of the twins equal to 3–10 μm. When the temperature is lowered to T_2 a spontaneous switching of the domain structures occurs, leading to the appearance of polysynthetic structures with domain wall of the W type and with twins 50 μm in size. A jump Δn in the refractive index has also been observed at this same temperature.[3] This jump is due not to a change in the orientational state in the bulk of the sample or to a lowering of the point symmetry of the crystal but to a phase transition between monoclinic phases. The conservation of the point group agrees with the conoscopic figures in the single-domain parts of the samples, which indicate a monoclinic group in the temperature interval $T_3<T<T_1$ and a triclinic group for $T<T_3$ ($T_3=183$ K).[11]

The cause of the jump Δn is as follows. The phase transition to each of the monoclinic phases $C2/c$ ($C2/m$) is accompanied by the onset of spontaneous strains due to the nonlinear coupling of the corresponding soft optical modes with the various components of the elastic strain tensor.[1] The temperature dependence of the spontaneous strain is proportional to the square of the order parameter, and far from T_1 these quantities are different in the different monoclinic phases. Therefore, the phase transition $C2/c\leftrightarrow C2/m$ should be accompanied by a jump in the strain.

As the temperature is lowered to T_2, one of the phases becomes unfavorable. In this case the broadening of the line corresponding to the soft mode A_g may be due to the presence of energetically different soft modes corresponding to the two phases, both $C2/c$ and $C2/m$.

CONCLUSION

We have proposed a phase diagram in which the $P\bar{3}m1$ phase is regarded as the paraphase, and the thermodynamic path for the transition to the monoclinic phase is $P\bar{3}c1$ $(z=2)\leftrightarrow P\bar{3}m1$ $(z=1)\leftrightarrow C2/c$ or $C2/m$ $(z=2)$. The phase that was observed in Refs. 4 and 5 from the ESR spectra near 260 K may arises as a result of the interaction of the different order parameters, which transform according to irreducible representations of the point $\mathbf{k}=(1/2)\mathbf{b}_3$ of the Brillouin of the ''prototype phase'' (space group $P\bar{3}m1$) — the one-dimensional τ_2 (or τ_3) and the two-dimensional τ_5 (or τ_6). It is assumed that near 240 K the crystals go from an inhomogeneous phase to one of the monoclinic phases.

In closing the authors thank N. F. Kharchenko for interest in this study and for a helpful discussion of the results.

*E-mail: nesterenko@ilt.kharkov.ua

[1] A. I. Otko, N. M. Nesterenko, and L. V. Povstyaniy, Phys. Status Solidi A **46**, 577 (1978).
[2] R. F. Klevtsova and P. V. Klevtsov, Kristallografiya **15**, 953 (1970) [Sov. Phys. Crystallogr. **15**, 829 (1970)].
[3] I. A. Kislov, V. V. Mitkevich, N. M. Nesterenko, and S. M. Tret'yak, Kristallografiya **36**, 1298 (1991) [Sov. Phys. Crystallogr. **36**, 735 (1991)].
[4] W. A. Zapart and M. B. Zapart, Phys. Status Solidi A **121**, K43 (1990).
[5] M. B. Zapart, Ferroelectrics **141**, 67 (1993).
[6] A. I. Otko, W. Zapart, M. B. Zapart, V. B. Kapustianik, and O. Kosznir, Ferroelectrics **141**, 43 (1993).
[7] N. M. Nesterenko, V. I. Fomin, Yu. A. Popkov, and A. I. Otko, Fiz. Nizk. Temp. **8**, 87 (1982) [Sov. J. Low Temp. Phys. **8**, 43 (1982)].
[8] N. M. Nesterenko and V. I. Fomin, Phys. Status Solidi A **51**, K101 (1979).
[9] N. M. Nesterenko, V. I. Fomin, and V. I. Kut'ko, Fiz. Nizk. Temp. **8**, 862 (1982) [Sov. J. Low Temp. Phys. **8**, 434 (1982)].
[10] O. V. Kovalev, *Irreducible Representations of Space Groups* [in Russian], Izd. Akad. Nauk Ukr. SSR, Kiev (1961).
[11] V. I. Fomin and N. M. Nesterenko, Kristallografiya **31**, 818 (1986) [Sov. Phys. Crystallogr. **31**, 485 (1986)].

Translated by Steve Torstveit

Optical constants of indium bromide

M. I. Kolin'ko* and O. V. Bovgyra

Ivan Franko National University of Lviv, vul Universytetskaya 1, 79602 Lviv, Ukraine

M. Piasecki

Pedagogical University at Czestochowa, Al. Armii Krajowej 13/15, 42-0200 Czestochowa, Poland
(Submitted August 8, 2000)
Fiz. Nizk. Temp. **27**, 210–215 (February 2001)

The optical functions of layered indium bromide single crystals are determined by the Kramers–Kronig technique using the polarized reflection spectra measured in the 2–30 eV region at liquid helium temperature. The spectra and the corresponding optical functions are found to exhibit strong anisotropy due to features of the group-theoretic selection rules and the crystal structure of indium bromide. The results are interpreted in comparison with the known optical properties and energy-band parameters of isoelectronic and isostructural (in relation to InBr) semiconductors. The origin of the principal structures of the spectra which are important for determining the quantitative parameters of the energy-band structure of InBr is identified. [DOI: 10.1063/1.1353711]

INTRODUCTION

The comparatively recently synthesized layered crystals of indium monobromide, like other members of the group-III metal halides, are promising materials for optoelectronics, particularly for the infrared region, and this has motivated intensive research on these materials in recent years. Although the reflection, absorption, and emission spectra are usually studied in a comparatively narrow energy interval near the fundamental absorption edge,[1–4] the results attest to a strong dichroism due to the anisotropic crystalline ordering. The spectra of this compound, like the spectra of alkali-halide crystals, have a pronounced excitonic character. It has been found, however, that the principal structures of the spectra are markedly different in structure, character, and temperature behavior from the spectra of the isostructural and isoelectronic single crystals α-TlI and InI.

Since no results of calculations of the energy-band diagram of indium bromide have yet been published, it is reasonable to use an alternative way of studying the electronic structure of this compound, viz., to determine the spectral distribution of the optical constants employing radiation in the energy range under study and using different polarizations of the probe radiation over a wide temperature interval.

The goal of the present study was to determine the mechanism and character of the optical transitions in indium bromide single crystals. For this it was necessary to obtain reliable energy curves of the optical functions, working from the experimental reflection spectra and using the Kramers–Kronig technique. The use of the known data on the optical properties and band diagrams of the isostructural III–VII compounds makes it possible to do an initial identification of the principal structures of the spectra both from a topological and from polarization and crystal-chemical points of view. Once the energy-band diagram of indium bromide is established, it will become possible to make a rigorous comparison of the oscillators of the optical transitions with the calculated matrix elements for various irreducible representations and with allowance for the polarization configuration.

1. PROCEDURES FOR THE CALCULATIONS AND EXPERIMENT

The complex of fundamental optical constants (functions) calculated from the experimental reflection spectra $R(E)$ includes the following: the real ε_1 and imaginary ε_2 parts of the dielectric function; the effective number of valence electrons $N_{\text{eff}}(E)$ involved in the transitions up to a definite value of the energy; the effective dielectric function ε_{eff}; the characteristic loss for bulk plasmons — $\operatorname{Im}\varepsilon^{-1}$; the absorption coefficient κ and refractive index n; the function $\varepsilon_2 E^2$, which is proportional to the reduced density of states under the condition that the oscillator strengths are equal to unity.

Among the optical constants, the real ε_1 and imaginary ε_2 parts of the dielectric function have a special status. This is because their spectra, like those of the reflectivity, can be measured over a wider energy interval than can the other optical functions, such as, e.g, the refractive index n or the absorption coefficient κ. In addition, the energies of the reflection peaks and of the imaginary part of the dielectric function are commonly associated with the energies of the interband or excitonic transitions.

For finding the optical functions we used a proven technique based on well-known formulas.[5,6] Extrapolation to the unmeasurable region in a calculation of the phase integral (the details are set forth in Refs. 7 and 8) was done using power-law functions, the parameters of which were obtained from the solutions of the determinant boundary conditions in the transparency region, where the phase $\theta(E) \equiv 0$.

The initial material was synthesized at a temperature of $\approx 340\,^{\circ}\text{C}$ in the reaction of metallic indium of certified quality and liquid bromine, with an excess of metal to prevent the formation of tribromide. Single crystals were grown from the melt by the Bridgman method after repeated purification; they were easily cleaved in one definite direction, and the

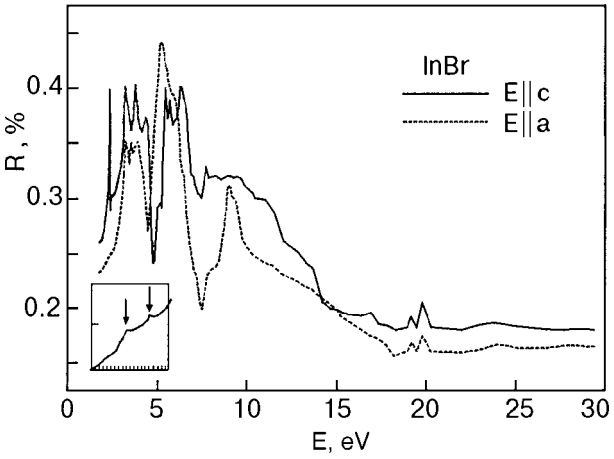

FIG. 1. Polarized reflection spectra of InBr single crystals at liquid helium temperature.

mirror surfaces of the samples did not require additional treatment. X-ray monitoring, which confirmed the space group of the InBr crystals (D_{2h}^{17}), showed that the cleavage plane was perpendicular to the **b** axis.

In the range 2.5–30 eV the spectra were measured on a Seya Numioka spectrometer for three angles of incidence, 8°, 12°, and 16°, and the data obtained were averaged using a special algorithm. The energy of the synchrotron radiation was 600 MeV, and the degree of polarization was 87%. In the 2–6 eV region the values of the reflection coefficient were also measured on the apparatus based on an SF-4 spectrophotometer. The spectra were recorded at liquid-helium and room temperatures.

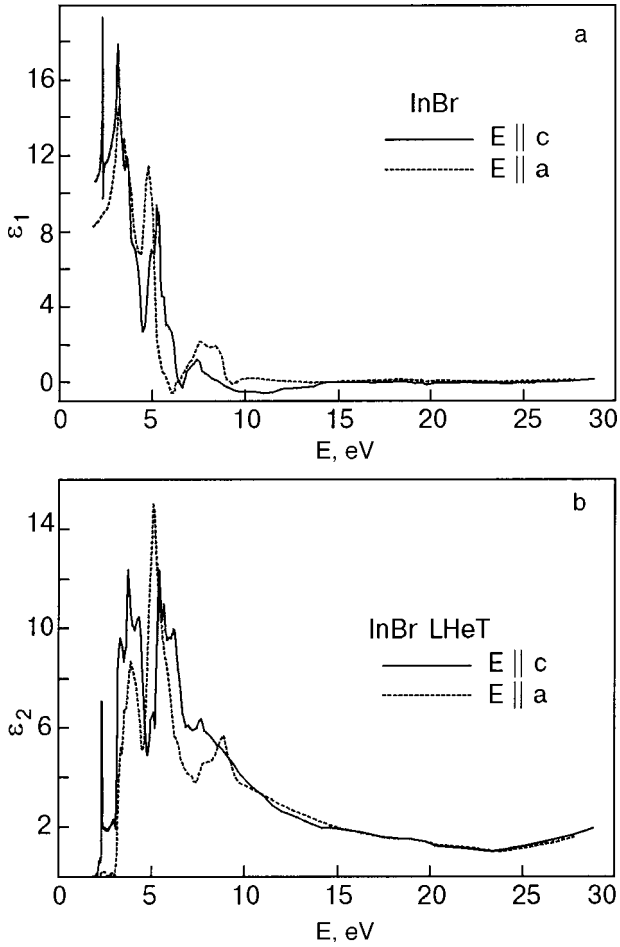

FIG. 2. Polarized spectra of the real ε_1 (a) and imaginary ε_2 (b) parts of the dielectric function of InBr single crystals.

2. RESULTS AND DISCUSSION FOR THE CALCULATIONS

The initial data used to calculate the fundamental optical functions were the low-temperature polarized reflection spectra of InBr illustrated in Fig. 1.

The plastic properties of this compound make it difficult to obtain high-quality surfaces and samples on the whole for investigation of the $\mathbf{E}\|\mathbf{b}$ geometry. The absolute values of the reflectivity were obtained with the use of a germanium single crystal.

On the whole, both spectra display a complex, dense structure consisting of a large number of peaks, especially in the region below 15 eV, after which the reflectivity tends to decrease. The trend of the $R(E)$ curve in this range is disrupted by two minima, near 4.6 and 7.5 eV.

In the long-wavelength region one observes a rather good analogy with the spectra obtained in other studies.[9] The first excitonic peak for the polarization $\mathbf{E}\|\mathbf{c}$, observed near 2.33 eV, is accompanied by a rather weak repetition at 2.34 eV ($n=2$).[3] At this energy mark for the polarization $\mathbf{E}\|\mathbf{a}$ one observes a rather weak shape. A rather weak peak is also observed in this polarization at $E=2.48$ eV, while for $\mathbf{E}\|\mathbf{c}$ no feature of any kind is seen. The next significant maximum in the spectra for both polarizations is at 3.22 eV. Outside this region excitonic transitions do not play an important role, except for the region near 19.7 eV, where the $4d$ excitation of the cation core is manifested.

When the sample is warmed to room temperature one observes a strong change in the shape of the $R(E)$ spectra, accompanied by a thermal decomposition of excitons; this attests to the influence of the phonon subsystem on the interband electronic transitions, and the presence of excitons in the high-energy region is a criterion of a strong electron–phonon interaction.

To determine the correspondence between the measured spectrum and the interband energy intervals, we calculated the real ε_1 and imaginary ε_2 parts of the dielectric function, which are shown in Fig. 2; they establish a direct connection between the microscopic and macroscopic characteristics of the crystals. The extrema of ε_2 correlate with the maxima of the reflectivity without any noticeable shift. However, between the spectra of the functions obtained for different polarizations of the radiation a pronounced dichroism is observed across nearly the entire energy interval of the radiation, and not only near the fundamental absorption edge. In addition, we note that for both polarizations one can discern more than ten oscillators in the region below 15 eV, whereas in the high-energy region the peaks in the spectra of the dielectric function are very weakly manifested.

The change in sign of ε_1 in the region 6.3–6.7 eV is indicative of possible collective effects. The excitation of plasma oscillations in this region is confirmed by the presence of maxima in the characteristic energy loss spectra ($-\mathrm{Im}\{1/\varepsilon\}$) near 7 eV in Fig. 3. The weakly manifestated structure associated with the main plasmons in the region 13–14 eV is masked by interband transitions of the $4s$ va-

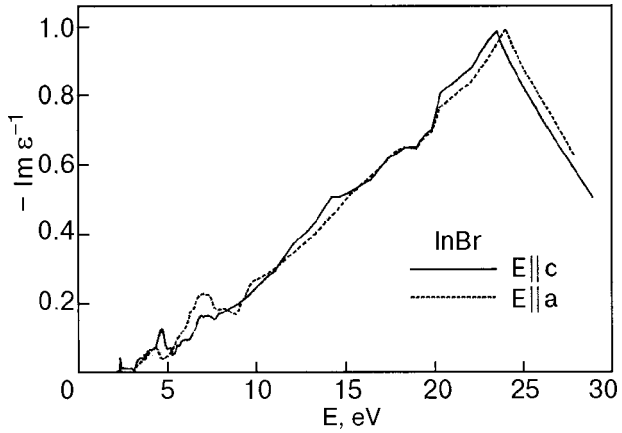

FIG. 3. Characteristic energy loss spectrum of indium bromide single crystals.

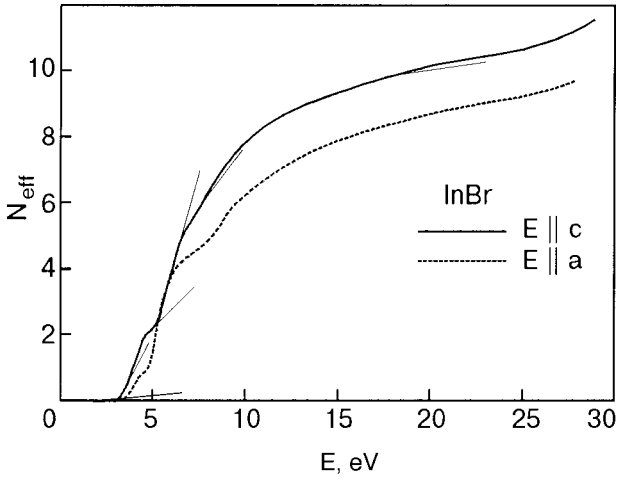

FIG. 4. Spectra of the effective number of valence electrons of InBr.

lence electrons of the halogen and the $4d$ electrons of the metal core, and no structure of any kind is seen in this region on the $R(E)$ spectra. The level of these excitations, according to the photoelectron spectroscopy data,[10] are localized (relative to the top of the valence band) near 14 and 17 eV, respectively, and merge into a single wide ($\approx$8 eV) band, unlike the case of single-crystal indium iodide, in which the the corresponding maxima are energetically localized.[11] The doublet structure of an excitonic character in the 20 eV region (Fig. 1), which is due to transitions of the $4d$ electrons of the indium core, makes for further broadening[12] of the plasmon peak. The existence of two types of plasmons is explained by the division of the valence electrons into two groups, formed separately by the π and σ electrons; the degree of this division is determined by the anisotropy of the crystal lattice. Two types of energetically divided plasmons have been observed previously for layered compounds, in the spectra of the optical functions of graphite[13] and molybdenum dichalcogenides.[14]

Of course, measurement of the characteristic energy losses in transmission would be preferable in this situation and would allow one, on the one hand, to divorce them from the conditions of the surface of this somewhat hygroscopic compound and, on the other hand, to determine more precisely the excitations with energies exceeding 15 eV.

We note that, although for solids with a large dielectric constant one often observes a change in the sequence of peaks of the characteristic electron energy loss function (e.g., for thallium iondide[15]), across the entire energy region here the maxima of ε_1, ε_2, and $-\mathrm{Im}\{1/\varepsilon\}$ are arranged in the same sequence as in alkali-halide compounds. The shift between the maxima of the characteristic energy loss peaks and the maxima of the imaginary part of the dielectric function ε_2, which determine the value of the longitudinal–transverse splitting of the transitions, amounts to 0.1–0.4 eV.

The dynamics of the involvement of valence electrons in phototransitions is illustrated in Fig. 4 by the energy dependence of the effective number of valence electrons N_{eff}, the values of which were obtained from a calculation for one formula unit. Analysis of the curve for the polarization $\mathbf{E}\|\mathbf{c}$ indicates the existence of six steps in the spectrum. On the basis of the results of a photoelectron spectroscopy study[10,11,16] and energy-band calculations[17,18] of the isostructural and isoelectronic compounds indium iodide and thallium iodide and in view of the fact that the valence complex of indium bromide consists of ten bands rather than five, as was stated in Ref. 10, we can give the following explanation for the observed features. The first three steps are due to transitions from the two highest valence bands, which are formed by the p_y and p_z orbitals of the halogen and the s orbitals of indium. We note that the absence of the first step in the spectrum of N_{eff} for the polarization $\mathbf{E}\|\mathbf{a}$ is evidence that the lowest direct transition is forbidden for it. The step that extends from $\approx$5 eV to $\approx$6.5 eV reflects the contribution of the next four bands of anionic character, formed by the p_x, p_y, and p_z orbitals of bromine. The participation of the cation states in them is insignificant, and it is in the region of these bands of the spectrum of indium bromide that the largest structural difference from the spectra of indium iodide should be exhibited. Unfortunately, at present it is impossible to verify this, since no studies of the reflection spectra of InI in such a wide energy interval has yet been reported. Strictly speaking, it is these electrons, which create π bonds and which are present in the region of the first plasmon in numbers of from 4 to 5.5, depending on the polarization, that are involved in the creation of the long-wavelength plasmons. The fifth step, which starts at $\approx$7.3 eV, is formed by two bands originating from the p_x and p_y orbitals of bromine and the s orbitals of indium. The last step near the 15 eV mark reflects the start of the transitions of the s electrons of the halogen, which form a quasi-core dispersionless band in orthorhombic crystals of group-III metal halides. The values of N_{eff} in the region of the plasmons of the second type in indium bromide crystals indicates that only the valence electrons participate in their excitation.

In the case of polarization $\mathbf{E}\|\mathbf{a}$ a smaller number of steps is observed, and their energy positions are different; this is because the selection rules for optical transitions give a smaller number of oscillators.

The curves in Fig. 5, like the N_{eff} curves, were obtained in a calculation of the spectral dependence of the effective value of the static dielectric function $\varepsilon_{\mathrm{eff}}$ characterizing the polarization of the electron shells. The spectrum $\varepsilon_{\mathrm{eff}}(E)$ can be divided somewhat arbitrarily into two parts. The first, extending to 9 eV, is characterized by a rapid growth of the

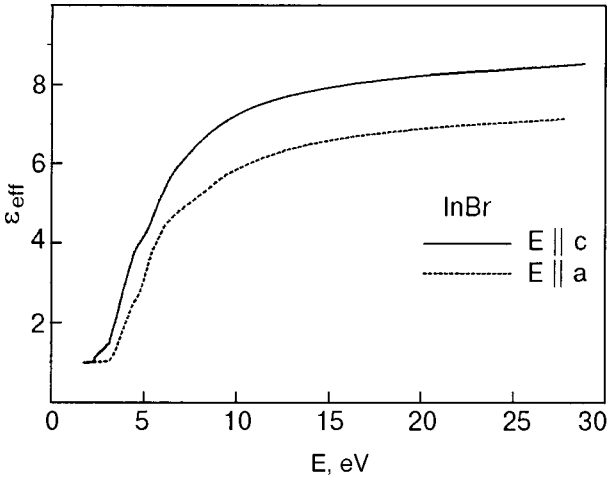

FIG. 5. Polarized spectra of the effective dielectric function of indium bromide.

function. The second part, from 9 eV to the end of the measurement region is much flatter. This behavior of the curve suggests that the main contribution to the distribution $\varepsilon_{\text{eff}}(E)$ is from interband transitions with energies below 9 eV, i.e., transitions involving the filling of all of the valence electron states except for the most tightly bound $4s$ electrons of bromine. We note that the valence electrons are exhausted only toward the end of the measurement range, where the $N_{\text{eff}}(E)$ curve reaches saturation.

According to the definition, the value of the dielectric function at large wavelengths, ε_0, should be equal to its value at high energies. For our case the value of ε_{eff} in the high-energy region is typically smaller than in the dispersionless transparency region; this reflects the substantial contribution of the long-wavelength IR oscillators for a predominantly ionic type of bonding. The peaks of the indirect excitonic transition ($E_i = 2.129$ eV), which are due to momentum-conserving phonons, have been observed in a study of the absorption spectra of indium bromide.[9] On the other hand, the integral parameter ε_{eff} for the polarization $\mathbf{E}\|\mathbf{c}$ has a value of 6.91, while that for $\mathbf{E}\|\mathbf{a}$ is 5.89. The difference between them is due to the difference, dictated by the selection rules, in the total number of oscillators and oscillator strengths. We note that the refractive indices n for these polarizations are ≈ 2.9 and ≈ 2.5, respectively.[2] The good correlation between the values $\sqrt{\varepsilon_{\text{eff}}}$ and n is evidence that the covalent contribution to the chemical bonding is still significant.

The strong anisotropy of the crystal structure is reflected in the dichroic spectra of the absorption coefficient κ and the refractive index n in Figs. 6a and 6b. The peaks in the spectra of κ tend to be shifted to higher frequencies in comparison with the corresponding peaks in the spectra of the imaginary part of the dielectric function, and this tendency becomes increasingly pronounced as the wavelength decreases.

The refractive index takes on its maximum values in the energy interval from 3 to 5 eV. We note that in two regions of the spectrum (near 6.5 eV and in the wide region 9–14 eV) the values of n are smaller than the values of the absorption coefficient; this is accompanied by a change in the sign

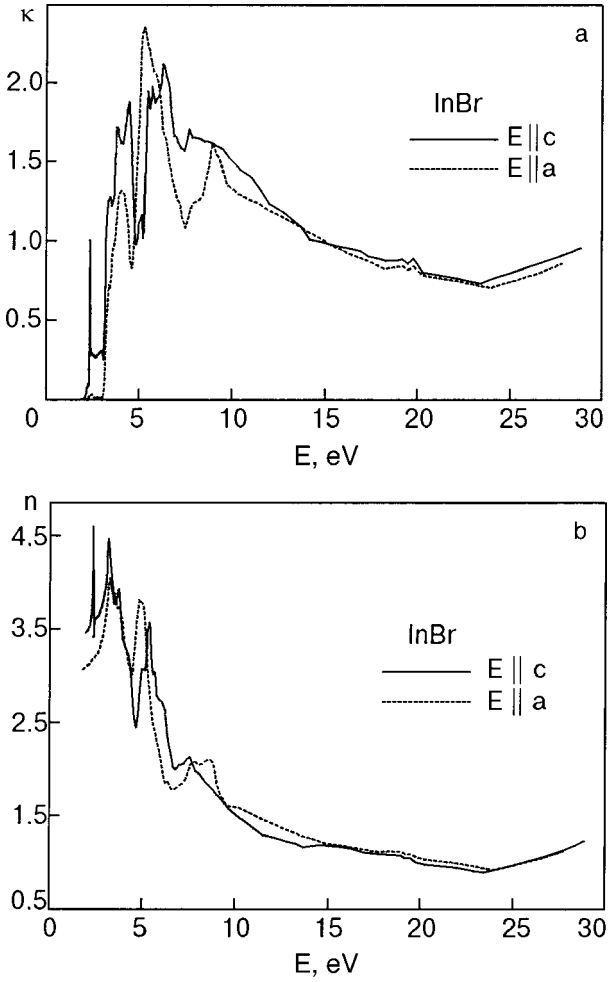

FIG. 6. Polarized energy curves of the absorption coefficient of InBr single crystals (a) and their refractive index (b) at liquid helium temperature.

of the real part of the dielectric function ε_1 (see Fig. 2) at these energies.

Although the positions of the maxima in the spectra of the refractive index and of the imaginary part of the dielectric function are approximately the same, the maxima of $n(E)$ are shifted to longer wavelengths in comparison with the corresponding maxima in the reflection spectrum $R(E)$; this shift increases with increasing energy and can reach 0.5 eV.

The data on the energy distribution of the interband combined density of states $\varepsilon_2 E^2$ in Fig. 7 can serve as a touchstone for evaluating the results of future calculations of the band diagram of InBr. With the energy eigenvalues $E(\mathbf{k})$ obtained from such a calculation one can solve the inverse problem, and after the corresponding integration in reciprocal space, find the distribution of the reduced density of states $\mathbf{J}(E)$ (which is equivalent to calculating ε_2 with a constant matrix element), comparison of which with the spectrum of $\varepsilon_2 E^2$ determined by the Kramers–Kronig method will be a rather rigorous test of the correctness of the calculation of the dispersion of the energy bands.

CONCLUSION

As a result of a calculation by the Kramers–Kronig technique we have determined the optical functions of layered

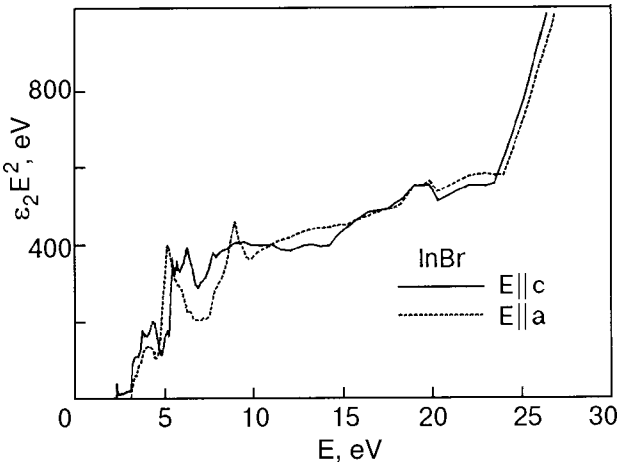

FIG. 7. Polarized spectra of the interband combined density of states $\varepsilon_2 E^2$ of indium bromide crystals.

single crystals of indium bromide over a wide energy range (2–30 eV) for different polarizations of the light.

A general interpretation of the principal structures of the spectra is offered on the basis of the known calculations of the energy-band spectra of isostructural and isoelectronic group-III metal halides.

The data obtained here provide a new information base for calculation and a deeper understanding of the electronic structure of indium bromide.

*E-mail: kolinko@franko.lviv.ua

[1] F. Lévy and E. Mooser, Helv. Phys. Acta **45**, 69 (1972).
[2] M. I. Gelten and P. Hoenderdos, J. Phys. Chem. Solids **35**, 653 (1974).
[3] M. Yoshida, N. Ohno, H. Watanabe, K. Nakamura, and Y. Nakai, J. Phys. Soc. Jpn. **53**, 408 (1984).
[4] A. Borghesi, G. Guizzetti, L. Nosenzo, E. Reguzzoni, A. Stella, and F. Lévy, Solid State Commun. **48**, 345 (1983).
[5] V. V. Sobolev, S. A. Alekseeva, and V. I. Donetskikh, *Calculations of Optical Functions of Semiconductors from the Kramers–Kronig Relations* [in Russian], Shtiintsa, Kishinev (1976).
[6] K. Jezierski, J. Phys. C: Solid State Phys. **19**, 2103 (1986).
[7] R. Klucker and U. Nielsen, Computer Phys. Commun. **6** 187 (1973).
[8] D. M. Roessler, Br. J. Appl. Phys. **16** 1119 (1965).
[9] M. Yoshida, N. Ohno, K. Nakamura, and Y. Nakai, Phys. Status Solidi B **109**, 503 (1982).
[10] L. Porte, Solid State Commun. **42**, 85 (1982).
[11] M. I. Kolinko, Phys. Rev. B **55**, 4007 (1997).
[12] W. Hanke and L. J. Sham, Phys. Rev. B **21**, 4656 (1980).
[13] E. A. Taft and H. P. Philipp, Phys. Rev. A **138**, 197 (1965).
[14] A. N. Timoshkin, V. Val. Sobolev, and V. V. Sobolev, Fiz. Tverd. Tela (St. Petersburg) **42**, 37 (2000) [Phys. Solid State **42**, 37 (2000)].
[15] J. Frandon and B. Lahaye, J. Phys. (France) **33**, 229 (1972).
[16] M. I. Kolinko and R. Y. Bibikov, Z. Phys. **95**, 167 (1994).
[17] M. I. Kolinko, J. Phys.: Condens. Matter **6**, 183 (1994).
[18] M. I. Kolinko, I. V. Kityk, and A. S. Krochuk, J. Phys. Chem. Solids **53**, 1315 (1992).

Translated by Steve Torstveit

SHORT NOTES

On the appearance of an orthogonal component of the spontaneous polarization in linear pyroelectrics in the low-temperature region

V. K. Novik* and N. D. Gavrilova

M. V. Lomonosov Moscow State University, Physics Department, Vorob'evy gory, 119899 Moscow, Russia
(Submitted July 14, 2000; revised September 19, 2000)
Fiz. Nizk. Temp. **27**, 216–219 (February 2001)

The appearance of an orthogonal component of the spontaneous polarization in the absence of signs of ferroelectricity does not violate the Curie–Neumann principle. These components are formed during the growth of a linear pyroelectric and are inherent to it always, but their values are several orders of magnitude smaller than the spontaneous polarization along the preferred polar axis. The low-temperature appearance of the components is due solely to a feature of the mechanism of their pyroelectricity — disordering of the charged structural units in asymmetric potential wells. © *2001 American Institute of Physics.* [DOI: 10.1063/1.1353712]

INTRODUCTION

The Curie–Neumann principle — the generalized principle of mutual correspondence of the crystalline forms (symmetry), the properties of the crystal, and its reaction to an action — is obeyed in crystals with a preferred polar axis (linear pyroelectrics) on account of the obvious hemimorphism (difference of crystalline forms) at the ''+'' and ''−'' ends of this axis (the Neumann principle). In certain nonpolar crystals upon a change in temperature (a scalar action) a spontaneous polarization (ferroelectric phase transition) arises in the unit cell of the crystal, but owing to the antiparallel electrical twinning (domain structure) the crystal remains macroscopically nonpolar (the Curie principle), maintaining its previous crystalline form (the Neumann principle). When an electric field is imposed (vector action), orienting the elementary dipoles in a single direction, the crystal become macroscopically polar (the Curie principle), demonstrating appreciable hemimorphism (the Neumann principle).[1] The appearance of a polar component on changing temperature (ferroelectricity) in a previously nonpolar matrix or orthogonal to an existing polarization corresponds precisely to the Curie–Neumann principle. A number of experimental facts have now been accumulated concerning the appearance of an orthogonal component of the spontaneous polarization $\overline{\mathbf{P}}_{si}(T)$ in the polar matrix of linear pyroelectrics at low temperatures. This phenomenon, which has been observed in oxygen-free crystals Ag_3AsS_3 (Ref. 2), sulfates $LiKSO_4$ (Refs. 3 and 4), selenates NH_4HSeO_4 (Ref. 5), and crystal hydrates $Li_2SO_4 \cdot H_2O$ (Ref. 6), is apparently quite general, which would justify its repeated discussion.

The studies listed above detected the onset both of a ferroelectric orthogonal component[2–5] and of a component that does not manifest the typical signs of ferroelectricity:[6] a distinct phase transition, peaks of the dielectric and pyroelectric anomalies, domain structure, etc. Thus, while the results of the experiments of Refs. 2–5 can be explained by proceeding from the arguments of Ref. 1, in the case of the $Li_2SO_4 \cdot H_2O$ (LSM) single crystal[6] its adherence to the Curie–Neumann principle must be based on some other arguments.

EXPERIMENTAL RESULTS AND DISCUSSION

It is commonly assumed that the LSM single crystal belongs to the point group 2 at room temperature; the crystallographic axis Y is associated with the polar axis and the orthogonal axes X and Z are assigned in a left-handed arrangement.[7] In this notation we shall analyze the data of Ref. 6, which have been refined somewhat from the original experimental material. Figure 1a, b, and c shows the results of the measurements of the pyrocoefficients $\gamma_i^\sigma(T) = \partial \mathbf{P}_{si}/\partial T$ of high-quality samples of the left enantiomorph of the LSM single crystal along the three crystallographic axes.[6] It is easy to see that the pyrocoefficient $\gamma_y^\sigma(T)$ is two or three orders of magnitude greater than the pyrocoefficients along the X and Z axes. For this reason the procedure of determining the temperature dependence of $\gamma_x^\sigma(T)$ and $\gamma_z^\sigma(T)$ involves the subtraction from the experimentally determined functions $[\gamma_x^\sigma(T)]_{\text{meas}}$ and $[\gamma_z^\sigma(T)]_{\text{meas}}$ the projections of $\gamma_y^\sigma(T)$ on the X and Z axes due to the error in the cut of the samples. The projection has an order of magnitude $\sim 10^{-2}\gamma_y^\sigma(T)$, and its exact value is determined from the ratios $[\gamma_x^\sigma(T)]_{\text{meas}}/\gamma_y^\sigma(T)$ and $[\gamma_z^\sigma(T)]_{\text{meas}}/\gamma_y^\sigma(T)$ at $T \geqslant 180$ K, where the proper contributions of $\gamma_x^\sigma(T)$ and $\gamma_z^\sigma(T)$ to $[\gamma_x^\sigma(T)]_{\text{meas}}$ and $[\gamma_z^\sigma(T)]_{\text{meas}}$, respectively, are vanishingly small in comparison with the projection of $\gamma_y^\sigma(T)$. This forced procedure allows one to determine $\gamma_x^\sigma(T)$ and $\gamma_z^\sigma(T)$ with acceptable error only for $T \leqslant 150$ K.

At $T = 1.5$ K the value of the spontaneous polarization along the Y axis is $|\overline{P}_{sy}| \cong 4.4 \times 10^{-6}$ C/cm^2 (Ref. 8). The values $|\overline{\mathbf{P}}_{sx}| \cong 3 \times 10^{-10}$ C/cm^2 and $|\overline{\mathbf{P}}_{sz}| \cong 2 \times 10^{-10}$ C/cm^2 calculated for $T = 1.5$ K by integrating the functions $\gamma_x^\sigma(T)$ and $\gamma_z^\sigma(T)$ over temperature are four orders of magnitude smaller than $|\overline{\mathbf{P}}_{sy}|$. The components $\overline{\mathbf{P}}_{sx}$ and $\overline{\mathbf{P}}_{sz}$ do not exhibit any signs of electrical twinning (ferroelectric domains),

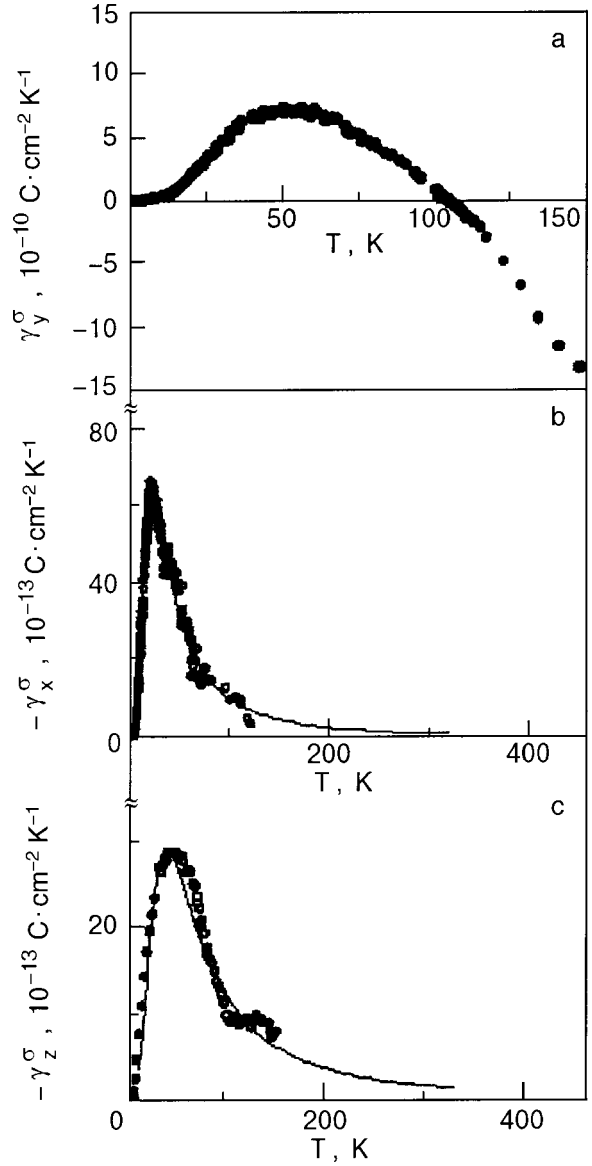

FIG. 1. Temperature dependence of the pyrocoefficients of a $Li_2SO_4 \cdot H_2O$ single crystal along the crystallographic axes *Y* (a), *X* (b), and *Z* (c): experimental points (●), approximation according to Eq. (1) (———).

and the temperature region where they begin to be manifested in experiment ($T \approx 150$ K) does not show traces of any singularity of the dielectric constant. The experimental fact that macroscopic polarization components arise in response to a scalar action without the imposition of an electric field and without any distinguishable hemimorphism with respect to the *X* and *Y* axes appears to be a paradox — a ''violation'' of the Curie–Neumann principle. The resolution of this paradox must come from a theory that faithfully describes the temperature dependence of the pyrocoefficients $\gamma_x^\sigma(T)$ and $\gamma_z^\sigma(T)$. As was shown in Ref. 9, the temperature-induced changes of the spontaneous polarization (pyroeffect) outside of phase transition regions are brought about by two mechanisms: a) anharmonicity of acoustic and optical modes; b) ordering of charged structural units in asymmetric potential wells. It was also shown that the experimentally determined pyrocoefficient $\gamma^\sigma(T)$ should be proportional to the primary pyrocoefficient $\gamma^\varepsilon(T)$.

To describe the effects of the second mechanism we used the Ising model in the mean field approximation.[10] In this approximation we calculated the dependence of the primary pyrocoefficient $\gamma^\varepsilon(T)$ for the structural elements that order in a double-well potential with an energy gap $\delta(T)$ (difference in the well depths), the elements having a dipole moment *p* that makes an angle of ξ_1 or ξ_2 to the direction of the spontaneous polarization of the matrix P_s in minimum 1 or 2, respectively, and a difference *S* between their binding energies with the crystalline skeleton in positions 1 and 2:

$$\gamma^\sigma(T) \cong \gamma^\varepsilon(T) = Np(\cos\xi_1 - \cos\xi_2) \times \frac{\ln^2[(1-w)/w]}{b\ln[(1-w)/w] + [(bw-a)/w(1-w)]}, \quad (1)$$

where

$$a = \frac{1}{k_B}\left[\frac{8\pi}{3}p(\cos\xi_1 - \cos\xi_2)[Np\cos\xi_2 \pm P_S(T=0\text{ K})] + S\right],$$

$$b = \frac{8\pi}{3k_B}Np^2(\cos\xi_1 - \cos\xi_2)^2,$$

$$T = (bw-a)/\ln[(bw-a)/w],$$

$$w(T) = [1+\exp(-\delta(t)/k_BT)]^{-1},$$

$$\delta(T) = k_B[a - bw(t)],$$

k_B is Boltzmann's constant, $w(T)$ is the probability of occupation of position 1: $w=1$ at $T=0$ and $w=0.5$ at $T\to\infty$; *N* is the number of ordering elements per unit volume. If it were possible to determine the values of *a* and *b* from the microscopic quantities δ, *N*, *p*, ξ_1, ξ_2, *S*, and P_s, then one could obtain the temperature dependence $\gamma^\varepsilon(T) \cong \gamma^\sigma(T)$ in explicit form. Unfortunately, the experimental determination of the values of this set of quantities is extremely difficult. Therefore, for a comparison of the theory with experiment we assumed that $A = Np(\cos\xi_1 - \cos\xi_2) = \text{const}$ and treated *a* and *b* as adjustable parameters. It is easy to conclude from an examination of Fig. 1b that for the values $A = 8\times10^{-10}$ C/cm^2, $a = 62$ K, and $b = 12$ K the theory of Ref. 10 (the continuous curve) gives a completely successful fit to the results obtained for $\gamma_x^\sigma(T)$: the curve lies beautifully on the rising edge and on the falling part of the experimental plot, and it describes the peak and its position on the temperature scale. The fundamental conclusion from this analysis for the theme of this article is that the pyrocoefficient $\gamma_x^\sigma(T)$ should have small but finite values all the way to the temperature ($\cong 350$ K) at which the crystal is destroyed as a result of loss of the water of crystallization.

In other words, the polarization $\overline{\mathbf{P}}_{sx}$ is *always* present in the LSM structure, but its value $|\overline{\mathbf{P}}_{sx}|$ in the room-temperature region is approximately five orders of magnitude smaller than the polarization $|\overline{\mathbf{P}}_{sy}|$ along the *Y* axis, which is recognized as the only polar axis. With the same precepts the theory of Ref. 10 also gives a good description of the experimental data on $\gamma_z^\sigma(T)$ (Fig. 1c), but with different values of the parameters: $A = 6.5\times10^{-10}$ C/cm^2, $a = 108$ K, $b = 15$ K. The conclusion is the same: the polarization $\overline{\mathbf{P}}_{sz}$ is *always* present in the LSM structure, although the value of $|\overline{\mathbf{P}}_{sz}|$ is even smaller than $|\overline{\mathbf{P}}_{sx}|$.

The answer to the paradox is obvious. The LSM crystal belongs to the point group 1 with a very small difference in a complex of properties from those characteristic for point group 2, which, strictly speaking, was incorrectly established[7] only from x-ray structural data and the morphology of the crystal at room temperature.

The ratios of the moduli of the polar components $|\overline{\mathbf{P}}_{sy}|$, $|\overline{\mathbf{P}}_{sx}|$, and $|\overline{\mathbf{P}}_{sz}|$ indicate an extremely small hemimorphism with respect to the X and Z axes, although for fundamental reasons it would be very desirable to obtain an experimental estimate of it. It would be extremely interesting to track the temperature-induced change in the crystalline forms in these directions as has been done for Rochelle salt.[1] Moreover, such an experiment would be of the most general significance for linear pyroelectrics having numerous anomalies of $\gamma^{\sigma}(T)$ (see, e.g., the case of the crystal $Ba(NO_2)_2 \cdot H_2O$; Ref. 11), in which it is possible to have the same special polar state.

The microscopic picture of the formation of the polar components along the X and Z axes and, accordingly, an explanation for the difference in the values of the adjustable parameters of the fit can be obtained from the data of Ref. 8. There it was shown that in the temperature interval 20–298 K there is a change in the dipole moment in the YZ plane and an angular displacement of the water molecules, and a change in the dipole moment in the XZ plane and an angular displacement of the dipole of the sulfate ion SO_4^{2-}.

The successful application of the theory of Ref. 10 proves that the contribution of these displacements to the temperature dependence $\gamma_x^{\sigma}(T)$ and $\gamma_z^{\sigma}(T)$ is due namely to the temperature-induced disordering of the ensemble of these dipoles, i.e., to a change in their statistically averaged position. For these reasons it appears justified to link the formation of the $\overline{\mathbf{P}}_{sx}$ component to the sulfate ion SO_4^{2-} and the $\overline{\mathbf{P}}_{sz}$ component predominantly to the change in state of the water molecules, although a partial contribution from the sulfate ion is not ruled out. That might possibly explain the more complicated form of the $\gamma_z^{\sigma}(T)$ curve and its somewhat worse approximation by the theory of Ref. 10.

The participation of the various elements of the lattice in the formation of $\overline{\mathbf{P}}_{sx}$ and $\overline{\mathbf{P}}_{sz}$ also gives a consistent explanation for the difference in the values of the adjustable parameters a and b (see Eq. (1)), since the values of δ, N, p, ξ_1, ξ_2, and S are different for the H_2O molecules and the SO_4^{2-} ions.

CONCLUSION

1. The Curie–Neumann principle for the formation of nonferroelectric orthogonal components is preserved by the proposed mechanism, which should be quite general (if not unique) for linear pyroelectrics, since only this mechanism is characterized by a monotonic *decline* of the $\gamma^{\sigma}(T)$ curve with increasing temperature.

2. The reliability of determining the symmetry (and the corresponding forms and components of the tensors) of linear pyroelectrics at room temperature must be monitored by an investigation of the polar properties in all crystallographic directions and in the entire temperature range in which these properties are manifested, starting at liquid helium temperatures. Only then will the level of phenomena neglected on account of the assertion of a particular symmetry be known in each particular case.

*E-mail: novikmp@orc.ru

[1] H. Mueller, Phys. Rev. **57**, 829 (1940).
[2] N. D. Gavrilova, V. A. Koptsik, V. K. Novik, and T. V. Popova, Ferroelectrics **20**, 199 (1978).
[3] R. Cach, P. Tomaszewski, P. Bastie, and J. Bornarel, Ferroelectrics **53**, 337 (1984).
[4] R. C. de Sousa, J. A. C. de Paiva, J. M. Filho, and A. S. B. Sombra, Solid State Commun. **87**, 959 (1993).
[5] R. Poprawski, J. Dziedzic, and J. V. Shaldin, Solid State Commun. **55**, 39 (1985).
[6] A. B. Esengaliev, V. K. Novik, V. N. Novikov, and N. D. Gavrilova, Fiz. Nizk. Temp. **18**, 395 (1992) [Sov. J. Low Temp. Phys. **18**, 268 (1992)].
[7] A. Bechmann, Proc. Phys. Soc. London, Sect. B **65**, 375 (1952).
[8] M. Karppinen, R. Liminga, A. Kvick, and S. C. Abrahams, J. Chem. Phys. **88**, 351 (1988).
[9] V. K. Novik and N. D. Gavrilova, Fiz. Tverd. Tela (St. Petersburg) **42**, 961 (2000) [Phys. Solid State **42**, 991 (2000)].
[10] V. Yu. Galitskiĭ, Fiz. Tverd. Tela (Leningrad) **23**, 815 (1981) [Sov. Phys. Solid State **23**, 463 (1981)].
[11] R. Poprawski and Yu. V. Shaldin, Solid State Commun. **68**, 487 (1988).

Translated by Steve Torstveit

PERSONALIA

Sergeĭ Vladimirovich Peletminskiĭ (on his 70th birthday)

Fiz. Nizk. Temp. **27**, 220 (February 2001)
[DOI: 10.1063/1.1353707]

February 14, 2001 marked the 70th birthday of the theoretical physicist Sergeĭ Vladimirovich Peletminskiĭ, Member of the National Academy of Sciences of Ukraine, Distinguished Scientist and Engineer, Department Head of the Institute of Theoretical Physics at the Kharkov Physicotechnical Institute National Science Center, and Professor of the Kharkov National University. The rare talent of Prof. Peletminskiĭ has been displayed in his solution of fundamental problems of statistical mechanics and the physics of condensed matter and magnetic phenomena. The awards he has received — he was awarded two State Prizes of the Ukraine, the N. M. Krylov Prize and the K. D. Sinel'nikov Prizes of the National Academy of Sciences of Ukraine, and a Certificate of Discovery for the magnetoacousic resonance effect — represent only the official recognition of the importance of his scientific results. The honor of having worked in Prof. Peletminskiĭ's scientific group is shared by scores of Candidates and Doctors of Science, for most of whom the path to science started at his brilliant lecture courses at Kharkov University.

We heartily congratulate Prof. Peletminskiĭ on his birthday and wish him robust health, creative inspiration, and new achievements in science.

V. G. Bar'yakhtar, B. V. Grinev, V. V. Eremenko, I. I. Zalyubovskiĭ, V. F. Zelenskiĭ, B. G. Lazarev, V. I. Lapshin, L. N. Litvinenko, V. G. Manzheliĭ, I. M. Neklyudov, V. P. Seminozhenko, A. G. Sitenko, V. V. Slezov, K. N. Stepanov, V. T. Tolok, Ya. B. Faĭnberg, P. I. Fomin, N. F. Shul'ga, V. M. Yakovenko, A. S. Bakaĭ, A. V. Volobuev, V. N. Grigor'ev, A. N. Dovbnya, A. M. Egorov, I. M. Karnaukhov, V. F. Klepikov, M. Yu. Kovalevskiĭ, A. P. Rekalo, É. Ya. Rudavskiĭ, Yu. V. Slyusarenko, and A. A. Yatsenko

Yuriĭ Andreevich Osip'yan (on his 70th birthday)

Fiz. Nizk. Temp. **27**, 221–222 (February 2001)
[DOI: 10.1063/1.1353708]

February 15, 2001 marked the 70th birthday of Academician Yuriĭ Andreevich Osip'yan, the Director of the Institute of Solid State Physics of the Russian Academy of Sciences, an outstanding scientist and scientific organizer.

Prof. Osip'yan made an important contribution to the development of the physics of dislocations in crystals. His pioneering experimental research on the interaction of dislocations with the electronic system in semiconductors and metals was published in the mid-1960s. The first result of this research was the discovery of a new physical phenomenon — the photoplastic effect in semiconductors. His later work in the development of the spectroscopy of defect structures in papers by Prof. Osip'yan and his co-workers and students led to the discovery of a number of new effects. Among them are the electroplastic effect and the presence of charge on dislocations in semiconductors, the observation of clusters of dangling valence bonds on the cores of dislocations in silicon, and inversion of the type of conductivity of semiconductors upon the introduction of dislocations. His elegant experiments on high-frequency conduction led to the discovery of quasi-one-dimensional electron bands associated with dislocations and the combination resonance of electrons on dislocations in silicon. The achievements of Prof. Osip'yan and his scientific group in this field have received international recognition. In 1984 Osip'yan was awarded one of the highest awards of the Academy of Sciences of the USSR in the field of physics — the P. N. Lebedev Gold Medal, and later the A. P. Karpinskiĭ International Prize and Gold Medal.

Since the discovery of high-temperature superconductivity, Prof. Osip'yan has actively persued research on the properties of this new class of materials. At the present time he is devoting much of his attention to studying the mechanical and physical properties of fullerites and carbon nanocomposite materials based on fullerene molecules and nanotubes. Prof. Osip'yan has taken part in the development of the technology for growing perfect fullerite crystals at his institute, in its basic research on the photoluminescence, absorption, and excitation spectra of C_{60} crystals, and in the experiments begun on the doping of fullerites by metal atoms.

The exceptional organizational skills of Prof. Osip'yan have been clearly demonstrated in the founding and growth of the Institute of Solid State Physics (ISSP). The fact that this institute operates in the best academic traditions, where a benevolent creative atmosphere is combined with a high level of research, is perhaps the main achievement of Prof. Osip'yan. The ISSP is now one of the largest institutes of the Russian Academy of Sciences, a recognized center of re-

search on condensed-matter physics and physical materials science. One of Prof. Osip'yan's main concerns is with the selection and training of junior staff members capable of carrying out independent research. For about 40 years Osip'yan has been Chairman of Solid State Physics at the Moscow Physicotechnical Institute, and in recent years he has also been the Director of the City Branch of Moscow State University. At the ISSP is an affiliate of one of the departments of the Moscow Institute of Steel and Alloys. Every year groups of gifted students take instruction and scientific training at the ISSP. Prof. Osip'yan's activities in science and society are on an impressive scale. He is a member of the Presidium of the Russian Academy of Sciences, Chairman of the Scientific Council on Condensed-Matter Physics, of the National Committee of Russian Crystallographers, of the Committee of Russian Scientists for Disarmament, of the Space Technology and Materials Science Section of the Space Council of the Russian Academy of Sciences and Russian Aerospace Agency, a member of the Council of the European Physical Society, and has been elected to several foreign academies. Prof. Osip'yan is the Editor-in-Chief of the magazine *Kvant (Quantum)* and of the journals *Poverkhnost' (Surface)*, *Materialovedenie*, and *Physics of Low-Dimensional Structures*, and a member of the Editorial Board of the journal *Physica C*. Prof. Osip'yan is the Head of the Presidium of the Science Center of the Russian Academy of Sciences at Chernogolovka.

Yu. A. Osip'yan is a Hero of Socialist Labor and has been awarded numerous orders and medals.

His benevolence and kindly disposition toward others, his mildness of speech, democratic spirit, personal charm, and innate intelligence have attracted many people to him. He is full of energy and works intensely and productively. His friends, colleagues and students sincerely congratulate him on his birthday, and wish him good health, many happy days, and the successful fruition of his creative plans.

V. T. Dolgopolov, V. V. Eremenko,
V. V. Kveder, N. V. Klassen, A. M. Kosevich,
V. D. Kulakovskiĭ, A. A. Levchenko,
V. G. Manzheliĭ, A. P. Mezhov-Deglyn,
V. D. Natskik, E. G. Ponyatovskiĭ,
Yu. M. Romanov, É. V. Suvorov,
V. S. Tsoĭ, V. Sh. Shektman, and V. B. Shikin

ERRATA

Erratum: Medium effects on the spectroscopy and intramolecular energy redistribution of C_{60} in cryogenic matrices [Low Temp. Phys. 26, 632 (2000)]

M. Chergui
Fiz. Nizk. Temp. **27**, 223 (February 2001)

[DOI: 10.1063/1.1353709]

The corrected version of Fig. 5 is as follows:

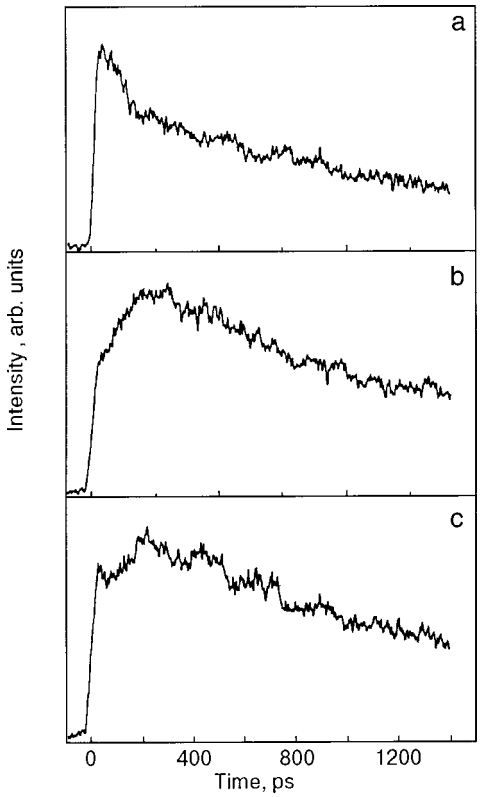

FIG. 5. Time-resolved fluorescence decay of the fluorescence bands of C_{60} in Ar matrices belonging to different emitting characters: $h_u(4)$, of the G_g character (a); $t_{1u}(4)$, of the T_{1g} character (b), and $h_u(1)$, of the T_{2g} character (c).

QUANTUM LIQUIDS AND QUANTUM CRYSTALS

Nonlinear phenomena in phonon–ripplon oscillations in a two-dimensional electron crystal over liquid helium

V. E. Sivokon', V. V. Dotsenko, and Yu. Z. Kovdrya*

B. Verkin Institute for Low Temperature Physics and Engineering, National Academy of Sciences of Ukraine, pr. Lenina 47, 61164 Kharkov, Ukraine

(Submitted July 26, 2000; revised September 1, 2000)
Fiz. Nizk. Temp. **27**, 115–120 (February 2001)

The characteristics of the spectra of phonon–ripplon oscillations of a two-dimensional electron crystal over liquid helium are investigated at temperatures of 70–500 mK, electron surface densities of $(3-12)\times 10^8$ cm^{-2}, and clamping electric fields of 500–2300 V/cm. Experiments are done in a frequency range of 1–20 MHz. It is shown that at a low level of the exciting signal the characteristics of the spectra are well described by the self-consistent theory of phonon–ripplon oscillations in a crystal. As the exciting signal is increased there is a decrease in the frequencies of the fundamental harmonics of the oscillations, apparently because of a nonlinearity in the electron displacements in the depressions on the liquid helium surface. As the level of the exciting signal is increased further, new modes of phonon–ripplon oscillations begin to be excited in the crystal. These modes are either the theoretically predicted division resonances arising at large electron displacements or the asymmetric modes caused by the coupling of the oscillations of different modes owing to nonlinear effects and by plastic deformation processes. [DOI: 10.1063/1.1353696]

Electrons localized above the surface of liquid helium present a unique two-dimensional system with a strong Coulomb interaction. Surface electrons moving above liquid helium interact with helium atoms in the vapor and with thermal excitations of the surface (ripplons).[1] At temperatures $T>0.9$ K the mobility of the electrons is governed mainly by their scattering on helium atoms in the vapor. At temperatures $T<0.9$ K it is limited by the interaction of the electrons with ripplons.

In a two-dimensional electron system over liquid helium the strong electron–electron interaction at sufficiently low temperatures and high electron densities leads to the formation of a two-dimensional electron crystal. The transition to the crystalline state in the two-dimensional electron layer has been detected from the observation of phonon–ripplon oscillations[2] and from the onset of features in the electron mobility at the transition temperature T_m.[3]

As we know, upon forming a crystal the surface electrons cause depressions on the surface of the liquid helium. This gives rise to coupled phonon–ripplon modes in the crystal.[4,5] Studying the characteristics of these modes yields information about the properties of the two-dimensional crystal and the surface of the quantum liquid.

The features of the propagation of phonon–ripplon oscillations in an electron crystal have been investigated in Refs. 6 and 7. It has been shown that in low driving electric fields the main properties of the phonon–ripplon spectrum can be described in the framework of a self-consistent theory,[5] although a number of effects are not completely explained in such an approach.

The behavior of a Wigner crystal under nonlinear conditions is an interesting problem. The nonlinear properties of an electron crystal in a magnetic field were investigated experimentally in Ref. 8. It was found that the behavior of the longitudinal magnetoconductance changes sharply beginning at a certain critical value of the driving electric field. The nonlinear properties of a Wigner crystal in zero magnetic field were investigated for large driving electric fields in Ref. 9, where a change in the spectrum of phonon–ripplon oscillations was detected.

The goal of the present study was to investigate in detail the features of the propagation of phonon–ripplon oscillations in an electron crystal on the surface of liquid helium, particularly at large driving fields, where nonlinear effects are observed.

EXPERIMENT

We studied the characteristics of the spectra of phonon–ripplon oscillations of a two-dimensional electron crystal over a wide range of temperatures, electron surface densities, and clamping electric fields. The measurements were made in a cell with a circular geometry, which is described in detail in Ref. 10. The construction of the cell permitted the measuring electrodes to be mounted parallel to the liquid helium surface to an accuracy of 10^{-3} rad. The measuring cell was in thermal contact with a dilution refrigerator with a cryogenic cycle of ^{3}He circulation.

The experiments were carried out in the frequency range 1–20 MHz at temperatures of 70–500 mK for crystals with electron surface densities $n_s=(3-12)\times 10^8$ cm^{-2} in clamping electric fields $E_\perp=600-2300$ V/cm. The exciting signal

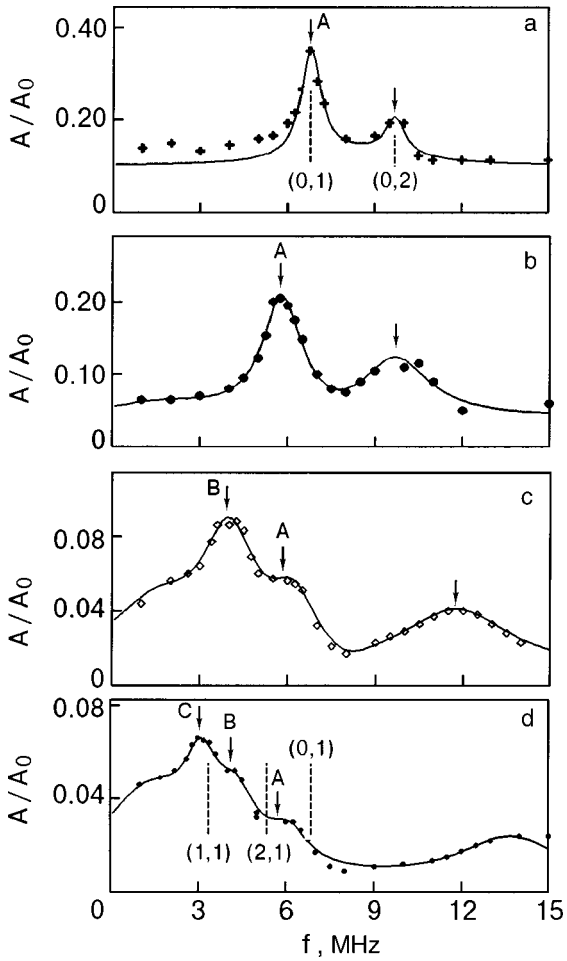

FIG. 1. Relative amplitude of the signal transmitted through the cell as a function of frequency for different values of the exciting signal A_0 [mV]: 0.3 (a), 3 (b), 5 (c), and 10 (d). $n_s = 5.9\times10^8$ cm^{-2}, $T = 70$ mK. The arrows indicate the experimentally determined positions of the resonances, and the dashed lines show the calculated values according to Ref. 5.

A_0 from the generator was varied in the range 0.3–10 mV. The amplitude A of the signal transmitted through the cell was measured.

RESULTS AND DISCUSSION

Figure 1 shows the relative amplitude A/A_0 of the signal transmitted through the cell as a function of frequency for different values of the exciting signal. The electron surface density n_s was 5.9×10^8 cm^{-2}. The points are the experimental data, and the solid curves are approximations by a sum of Lorentzian functions. This type of processing makes it possible to find both the frequencies and widths of the resonance peaks. The positions of the resonances obtained in this way are indicated by arrows in Fig. 1.

At low values of the exciting signal one can readily distinguish two peaks corresponding to the axisymmetric first (0,1) and second (0,2) harmonics of the phonon–ripplon resonances in the electron crystal (Figs. 1a and 1b).

For the case of low driving fields the spectra of the electron–phonon oscillations were investigated over a wide range of temperatures both at saturated electron energies, when the clamping electric field above the electron layer was completely compensated by the surface charge, and for the unsaturated case, when the densities are lower than the equilibrium value. Figure 2 shows the positions of the fundamental harmonic (0,1) of the resonance as a function of temperature. The data points are the experimental results, and the solid curves are the results of a calculation according to Ref. 5. The calculations were done using the temperature dependence of the surface of surface tension of a ^{3}He–^{4}He solution with an impurity concentration of 5.5×10^{-7} (Ref. 11; commercial-grade helium). The unfilled circlet near curve *1* pertains to the case of a vanishingly small amplitude of the exciting signal (0.3 mV). It corresponds to the resonance in Fig. 1a and agrees with the theoretical calculation. Unfortunately, as the temperature is raised the width of the resonance peak increases, making it much harder to isolate the signal from the background noise. The filled circlets in plot *1* were obtained at a signal amplitude $A_0 = 1$ mV. We see that at this value of A_0 the resonance frequency is lower than that obtained at a small signal amplitude; it follows from the theory[12] that this attests to nonlinear processes occurring in the electron crystal. Curves *2* and *3*, which pertain to different electron densities, were taken at the same value of the clamping voltage V and, hence, at the same clamping field. It is seen that the results obtained for the saturated case (curve *2*) and the data obtained under conditions of incomplete compensation of the clamping electric field above the electron layer (curve *3*) are well described by the theory.[5] We note that the nonlinear effects are suppressed by an increase in the clamping field. It has been established experimentally that the nonlinear behavior of curves *2* and *3* begins to be manifested at a value of the exciting signal $A_0 = 1.7$ mV.

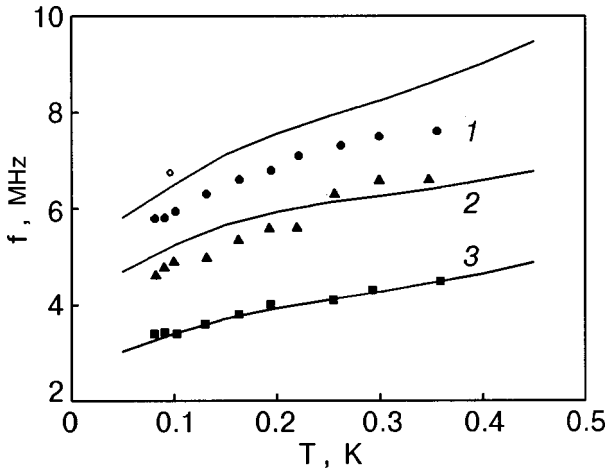

FIG. 2. Temperature dependence of the resonance frequency of the (0,1) mode of an electron crystal. $n_s = 5.9\times10^8$ cm^{-2}, $A_0 = 0.3$ mV (○), $A_0 = 1.0$ mV (●), $V_\perp = 119$ V (curve *1*); $n_s = 1.2\times10^8$ cm^{-2}, $A_0 = 1.0$ mV, $V_\perp = 222$ V (▲, curve *2*); $n_2 = 5.9\times10^8$ cm^{-2}, $A_0 = 1.0$ mV, $V_\perp = 222$ V (■, curve *3*).

A complete theoretical description of the character of the propagation of phonon–ripplon oscillations in an electron crystal over liquid helium in the absence of nonlinear effects has been given in Ref. 5. The dynamical properties of a Wigner crystal depend on the electron–ripplon coupling coefficient

$$C_n = \frac{3n_s V_g^2}{\alpha m \omega_n} \exp\left(-\frac{q_n^2 \langle u_f^2 \rangle}{2} \right). \quad (1)$$

Here m is the mass of an electron, α is the coefficient of surface tension of helium, and $\langle u_f^2 \rangle$ is the mean-square displacement of the electrons in the sites of the crystal lattice for a high-frequency optical mode. The frequency ω_n and wave vector q are connected by the dispersion relation:

$$\omega_n = \left(\frac{\alpha}{\rho}\right)^{1/2} g_n^{3/2}, \tag{2}$$

where ρ is the density of the helium, and n enumerates the wave vectors (and frequencies) corresponding to reciprocal lattice vectors of the crystal:

$$q_n = g_n = \frac{8\pi n_s}{\sqrt{3}n}, \quad n = 1, 2, 4, 7, 9 \ldots . \tag{3}$$

The quantity V_g characterizes the intensity of the electron–ripplon interaction. In the limit of high clamping fields it obeys $V_g \approx eE_\perp$, where e is the charge of an electron. If we take into account the coupling of the phonons of the crystal only with the lowest-frequency mode of oscillation of the surface of the liquid helium, with wave vector k $(C_1 \gg C_2)$, the dispersion relation of the phonon–ripplon oscillations can be written as

$$\omega_{s,p}^2(k) = \frac{\omega_1^2 \omega_p^2(k)}{C_1 \omega_1^2 + \omega_p^2(k)}, \quad p = l, t, \tag{4}$$

where $\omega_p(k)$ is the spectrum of oscillations of the electron crystal above an absolutely flat surface; p is the polarization of the oscillations (l for longitudinal and t for transverse). For the circular geometry used in the experiments the important oscillations are those with longitudinal polarization, the spectrum of which, with allowance for the screening effect of the electrons of the cell, has the form

$$\omega_l^2(k) = \frac{4\pi n_s e^2 k \sinh(kd)\sinh[k(H-d)]}{m \sinh(kH)}, \tag{5}$$

where H is the distance between the measuring and clamping electrodes, and d is the height of the layer of liquid helium. The wave vectors k_i corresponding to standing waves in the cell are determined from the condition

$$J_1(k_i R) = 0, \tag{6}$$

where R is the radius of the electron spot, and $J_1(x)$ is a first-order Bessel function. The theory of Monarkha and Shikin[5] gives a good description of the experimental results obtained at small values of the exciting signal in the region of linear behavior of the crystal over a wide range of temperatures, electron surface densities, and clamping electric fields. This is seen in Fig. 2, where the temperature dependence of the frequency of the main maximum is shown by the solid curves, and in Fig. 3, which shows the dependence of the same quantity on the electron density n_s. Interestingly, at a fixed value of n_s the frequency of the resonances decreases as the clamping electric field is increased. This agrees with the theory developed in Ref. 5.

It is seen from Fig. 1 that as the exciting signal A_0 and, accordingly, the driving field are increased, the character of the amplitude–frequency curves for the phonon–ripplon oscillations are altered in an essential way. First, as we have said, the manifestation of nonlinear behavior in the characteristics of the phonon–ripplon resonances of an electron crystal reduces to the circumstance that the frequency of the fundamental resonances decreases (see Figs. 1a and 1b). It has been established experimentally that for $A_0 = 1$ mV the dependence is like that presented in Fig. 1b. The observed decrease in frequency was predicted in Ref. 12, where a theoretical analysis was made for nonlinear effects in the conductivity of a Wigner crystal. In that paper the anharmonicities arising in the displacement of the electrons in the depressions at large driving fields was considered. Numerical calculations done according the Ref. 12 using the results of Ref. 10, which made it possible to determine the conductance of an electron layer for a specific geometry of the experimental cell, show that a lowering of the frequency of the resonances does in fact occur, starting at certain values of the exciting signal.

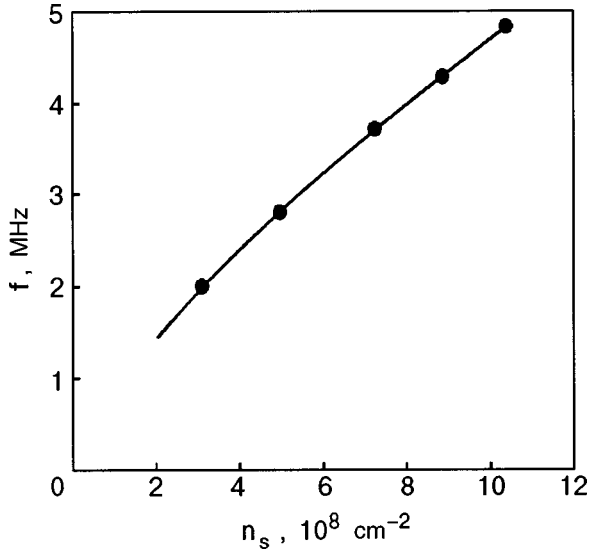

FIG. 3. Resonance frequency of the (0,1) mode of an electron crystal versus the electron density. $T = 76$ mK, $V_\perp = 222$ V.

As the nonlinear processes develop further, new resonances appear in the oscillation spectrum in addition to the fundamental resonance (0,1), which is labeled as *A*. For example, at an exciting signal of 5 mV (Fig. 1c) a resonance *B* appears at a frequency of 4.0 MHz, while the position and width of the fundamental peak remain practically the same as for $A_0 = 1-3$ mV. As A_0 is increased further to 10 mV, still another resonance appears in the spectrum, at a frequency of 3.1 MHz (resonance *C*), while the resonances existing at $A_0 = 5$ mV have practically the same position and width as before (see Fig. 1d).

It is seen in Fig. 1 that at large amplitudes of the exciting signal the $A(f)/A_0$ curve becomes rather complicated (Figs. 1c and 1d), with new low-frequency resonances appearing and with the maximum observed at $f = 10$ MHz broadening and shifting to higher frequencies. In addition, at large values of the exciting signal the relative amplitude of the response signal decreases. The width of the resonance peak roughly doubles as A_0 increases from 0.3 to 1 mV and then remains practically unchanged as A_0 increases further.

The appearance of new resonances can be explained by two alternative possibilities. The first derives from the fact

that, as was shown in Ref. 12, for large displacements of the electrons so-called division resonances arise at frequencies equal to f_{0n}/i (here f_{0n} is the frequency of the harmonic $(0,n)$, $i=1,2,3\ldots$). The most distinct additional resonance should correspond to $i=3$. In this picture the resonance B at 4 MHz might correspond to the division resonance $f_{03}/3$, where $f_{03}=12$ MHz is the frequency of the (0,3) mode, and resonance C at 3.1 MHz to the division resonance $f_{02}/3$, where $f_{02}=10$ MHz is the frequency of the harmonic (0,2).

The second alternative possibility for the appearance of new resonances is that the given resonances are additional, higher harmonics of the phonon–ripplon oscillations which arise at large values of the exciting signal. Thus the new resonances observed in the electron layer over liquid helium could be attributed to the excitation of asymmetric phonon–ripplon oscillations with an angle dependence.

The problem of the excitation of plasma oscillations in a two-dimensional charged system was solved in general form in Ref. 13. The wave vectors corresponding to resonances in a cell with a circular geometry are determined by the equation

$$jJ_j(k_iR)-k_iRJ_{j+1}(k_iR)=0, \tag{7}$$

which for $j=0$ goes over to Eq. (6), which corresponds to axisymmetric oscillations.

A calculation of the frequencies of the different harmonics of the oscillations excited in the crystal with the use of Eq. (7) shows that only two harmonics, (1,1) and (2,1), have a frequency lower than the frequency of the fundamental resonance. The corresponding frequencies are indicated by the dashed lines in Fig. 1d.

The temperature dependence of the frequency and width of the two new low-frequency resonances observed at $A_0=10$ mV is shown in Fig. 4. The width of the relaxation peaks increases with increasing temperature, making the results of the processing less accurate. It can be seen, however, that within the error limits for the determination of these quantities the frequency f and width Δf of the resonances increase with increasing temperature. Such behavior is also characteristic for the fundamental modes of coupled phonon–ripplon oscillations in the region of linear behavior observed both in a previous study[9] and in the present work, including under conditions of weak nonlinearity of the oscillations.

It was not possible to analyze the spectrum at frequencies above 8 MHz, because all sorts of combination harmonics arising as a result of nonlinearity in the system lie in this frequency range.

Unfortunately, the mechanism for the excitation of the angular modes in an electron crystal of circular geometry at large exciting signals is not completely clear at the present time. The most likely explanation for the excitation of angular modes by an axisymmetric exciting signal is the coupling of the various modes as a result of the anharmonicities arising in the phonon–ripplon oscillations at large signal amplitudes. This gives rise to a transfer of oscillation energy from some modes to others. Another possibility is the influence of plastic deformation of the crystal, which can occur differently in different directions, giving rise to anisotropy of the oscillations. The excitation of asymmetric modes may also be caused by a slight inclination of the electrodes with respect to the liquid helium surface and, accordingly, to asymmetry of the electron density in the experimental cell.

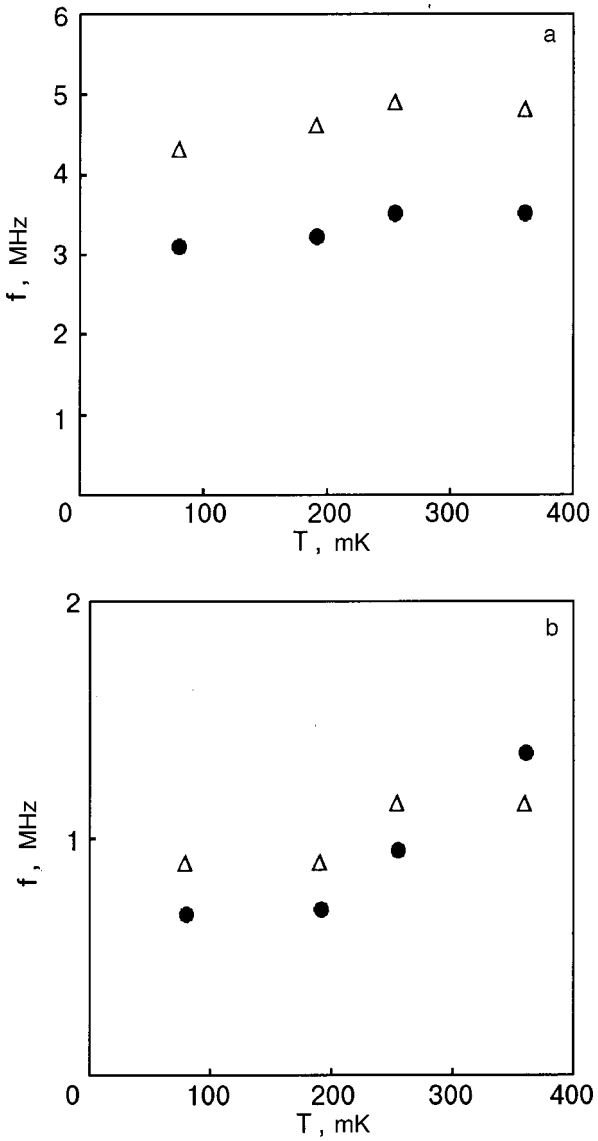

FIG. 4. Temperature dependence of the frequency (a) and half-width (b) of nonaxisymmetric angular resonances. $n_s=5.9\times10^8$ cm^{-2}, $A_0=10$ mV; the (1,1) mode (●); the (2,1) mode (△).

The effects of plastic deformation in an ionic crystal were studied in Ref. 14. Analysis of the data obtained in the present study shows that at large enough amplitudes of the exciting signal the (0,1) mode vanishes, while the angular modes are still observed. This may be evidence that the crystal is destroyed at frequencies corresponding to the (0,1) mode, whereas it still exists at frequencies corresponding to the angular modes.

CONCLUSION

In summary, we have done an experimental study of the features of the propagation of coupled phonon–ripplon oscillations of a Wigner crystal over a wide range of tempera-

tures, clamping electric fields, and exciting signals. We have shown that at a low signal level the axisymmetric phonon–ripplon oscillation modes corresponding to the fundamental frequencies (0,1) and (0,2) are excited. The characteristics of these modes are described well by the self-consistent theory developed in Ref. 5 over a wide range of temperatures, electron surface densities, and clamping electric fields, including the unsaturated case. Further increase in the driving field leads to the nonlinear excitation of new modes of phonon–ripplon oscillations in the crystal. These modes may be due to either the excitation of the predicted[12] division resonances in the crystal at large displacements of the electrons or to the nonlinear excitation of angular modes. When the new resonance modes appear the fundamental axisymmetric modes are suppressed. As to the excitation of angular modes, this effect may be due to coupling of the oscillations of different modes as a result of nonlinear effects and also to plastic deformation processes and the destruction of spatial symmetry in the electron crystal.

The authors thank V. N. Grigor'ev and Yu. P. Monarkha for their interest in this study and for a discussion of the results.

This study was supported in part by the project INTAS-97-1643.

*E-mail: kovdrya@ilt.kharkov.ua

[1] Yu. P. Monarkha and V. B. Shikin, Fiz. Nizk. Temp. **8**, 563 (1982) [Sov. J. Low Temp. Phys. **8**, 279 (1982)].
[2] C. C. Grimes and G. Adams, Phys. Rev. Lett. **42**, 795 (1979).
[3] A. S. Rybalko, B. N. Esel'son, and Yu. Z. Kovdrya, Fiz. Nizk. Temp. **5**, 947 (1979) [Sov. J. Low Temp. Phys. **5**, 450 (1979)].
[4] D. S. Fisher, B. I. Halperin, and P. M. Platzman, Phys. Rev. Lett. **42**, 798 (1979).
[5] Yu. P. Monarkha and V. B. Shikin, Fiz. Nizk. Temp. **9**, 913 (1983) [Sov. J. Low Temp. Phys. **9**, 409 (1983)].
[6] V. E. Sivokon', V. V. Dotsenko, Yu. Z. Kovdrya, and V. N. Grigor'ev, Fiz. Nizk. Temp. **22**, 1107 (1996) [Low Temp. Phys. **22**, 845 (1996)].
[7] V. V. Dotsenko, V. E. Sivokon', Yu. Z. Kovdrya, and V. N. Grigor'ev, Fiz. Nizk. Temp. **23**, 1028 (1997) [Low Temp. Phys. **23**, 772 (1997)].
[8] K. Shirihama and K. Kono, J. Low Temp. Phys. **104**, 237 (1998).
[9] V. E. Sivokon', V. V. Dotsenko, Yu. Z. Kovdrya, and V. N. Grigor'ev, Fiz. Nizk. Temp. **23**, 789 (1997) [Low Temp. Phys. **23**, 595 (1997)].
[10] V. E. Sivokon', V. V. Dotsenko, S. S. Sokolov, Yu. Z. Kovdrya, and V. N. Grigor'ev, Fiz. Nizk. Temp. **22**, 715 (1996) [Low Temp. Phys. **22**, 549 (1996)].
[11] G. Deville, J. Low Temp. Phys. **72**, 135 (1988).
[12] Yu. P. Monarkha, Fiz. Nizk. Temp. **6**, 685 (1980) [Sov. J. Low Temp. Phys. **6**, 331 (1980)].
[13] C. F. Barenghi, C. J. Mellor, J. Meredith, C. M. Muiruherd, P. K. H. Sommerfeld, and W. F. Vinen, Philos. Trans. R. Soc. London, Ser. A **334**, 139 (1991).
[14] P. L. Elliot, C. I. Pakes, L. Skrbek, and W. F. Vinen, Czech. J. Phys. **46**, Suppl. 1, 333 (1996).

Translated by Steve Torstveit

SUPERCONDUCTIVITY, INCLUDING HIGH-TEMPERATURE SUPERCONDUCTIVITY

Electrophysical properties of crystals containing small superconducting inclusions

V. I. Sugakov and O. N. Shevtsova*

Institute of Nuclear Research Science Center, National Academy of Sciences of Ukraine, pr. Nauki 47, 03680 Kiev, Ukraine

(Submitted January 31, 2000; revised September 18, 2000)
Fiz. Nizk. Temp. **27**, 121–126 (February 2001)

The influence of superconducting inclusions on the electrophysical properties of a semiconductor or insulator crystal is investigated. The critical magnetic field of an isolated spherical inclusion is calculated under the assumption that the radius of the inclusion is smaller than or of the order of the coherence length. The conductivity of a crystal containing a set of inclusions is calculated as a function of temperature and magnetic field. It is assumed in the conductivity calculations that the concentration of inclusions is insufficient for the appearance of superconductivity in the whole sample (i.e., it is below the percolation threshold). It is shown that the presence of superconducting inclusions leads to a sharp increase in the conductivity of the sample at low temperatures and to a strong dependence of the conductivity on magnetic field (magnetoresistance). The magnetoresistance is due to suppression of the superconductivity in the inclusions as the magnetic field is increased. The influence of a variance in the dimensions of the inclusions on the temperature and magnetic-field dependence of the conductivity is investigated.
[DOI: 10.1063/1.1353697]

1. INTRODUCTION

Research on materials containing superconducting inclusions is of interest both from a scientific standpoint, since it enables one to investigate the superconductivity and, hence, effects of interaction between quasiparticles in systems of small size, and from a practical standpoint, since such systems can manifest various physical effects that can be useful in applications. In addition, there may be superconducting inclusions of a technological origin which must be taken into account for a correct description of the properties of a system.

There is a vast literature devoted to the study of the superconducting properties of small particles (see the reviews in the monograph[1] and review article[2] and also the original papers[3–10]). For particles of very small sizes one observes a change in the critical parameters (phase transition temperature, critical magnetic fields). This is a result of modification of the phonon spectrum, quantization of the electron spectrum, surface effects, and structural imperfection. A quantitative description of these effects requires the use of microscopic equations, which is complicated, since knowledge of both the spectrum of the quasiparticles and the structure of the small samples is necessary. However, in a certain size region of the small particles, for which the radius is smaller than the coherence length, one may use the Ginzburg–Landau (GL) theory, which is considerably simpler than a microscopic treatment and is more general, since it makes use of phenomenological parameters. For example, for dirty superconductors with $l<R<\sqrt{\xi_0 l}(1-T/T_c)^{-1/2}$ (l is the mean free path of the electrons) the dependence of the critical magnetic field of a sphere on its radius in the framework of a microscopic model (see the book by de Gennes[11]) agrees with the dependence obtained by Ginzburg in the GL model.[12] Here the critical temperature in the absence of magnetic field is independent of the size, and the critical magnetic field is inversely proportional to the radius of the spherical inclusion. Similarly, starting at a certain value of the film thickness d (according to Ref. 8, for $d>10^{-6}$ cm) the dependence of the critical values of the magnetic field of a film on its thickness is the same whether calculated in the framework of the microscopic theory[11] or in the GL model, and the critical magnetic field is inversely proportional to the film thickness; here the film thickness remains small than the coherence length $\xi(T)$. In what follows we shall consider systems that can be described using the GL theory; in particular, we shall examine the electrophysical properties of a semiconductor crystal containing superconducting inclusions.

The formation of metallic regions in a nonsuperconducting material can be explained by various technological processes, in particular, in the decomposition of solid solutions of multicomponent systems.[13] If one of the components is a superconducting metal, its precipitation during technological processes will give rise to superconducting regions in the crystal. For example, the precipitation of a superconducting phase has been observed in the heat treatment of lead telluride–tin telluride[14,15] and in the irradiation of InAs by α particles.[16]

In this paper we shall show that small admixtures of superconducting inclusions in a material can have a significant effect on the electrophysical and magnetic properties of the material at low temperatures.

2. CRITICAL PARAMETERS OF A SPHERICAL NANOSIZE SUPERCONDUCTING INCLUSION EMBEDDED IN AN INSULATOR MATRIX

Before considering a medium containing many superconducting inclusions, let us analyze the superconducting transition in an individual inclusion of radius R in a medium with low conductivity (an insulator or semiconductor). Let us assume that the dimensions of the inclusion are such that it can be described by the GL equations. This imposes restrictions on the minimum size of an inclusion, below which a microscopic approach is required. For a spherical sample, Ginzburg found that in the GL approach the critical magnetic field is inversely proportional to the radius of the inclusion provided that this radius is much less than λ, ε. The lower limit of applicability of this solution is determined by the domain of applicability of the GL theory. To get an estimate of the upper limit, further investigation is necessary. The GL equation for a superconducting sample has the form

$$\left(-i\nabla - \frac{\mathbf{A}}{\sqrt{2}\kappa}\right)^2 \psi - \alpha\psi + |\psi|^2\psi = 0; \tag{1}$$

here ψ is the superconducting order parameter, κ is the GL parameter, and $\alpha = 1 - T/T_{c0}$, where T_{c0} is the critical temperature of a bulk superconductor.

If the matrix is a low-conducting medium, then the order parameter satisfies the boundary condition

$$\frac{\partial\psi}{\partial\rho} = 0 \quad \text{at } \rho = R. \tag{2}$$

Since we are considering the behavior of the system near the phase transition ($\psi \to 0$), the addition to the external magnetic field H caused by the inclusion can be assumed small (it is of the order of $|\psi|^2$), and we can neglect the magnetic field generated by the inclusion. The vector potential for the magnetic field is chosen in the form $\mathbf{A} = 1/2 \times [\mathbf{H} \times \mathbf{r}]$.

To determine the critical magnetic fields, let us consider the linearized version of the equation in (1), which in a spherical coordinate system takes the form

$$-\frac{1}{\rho^2}\left(\frac{\partial}{\partial\rho}\rho^2\frac{\partial}{\partial\rho} + \frac{1}{\sin\theta}\frac{\partial}{\partial\theta}\sin\theta\frac{\partial}{\partial\theta} + \frac{1}{\sin^2\theta}\frac{\partial^2}{\partial\varphi^2}\right)\psi$$

$$-\alpha\psi + i\frac{H}{\sqrt{2}\kappa}\frac{\partial\psi}{\partial\varphi} + \frac{1}{8\kappa^2}H^2\rho^2\sin^2\theta\psi = 0, \tag{3}$$

where $\rho = r/\xi_0$ is the dimensionless modulus of the radius vector from the origin to the center of the sphere; the angle θ is measured from the magnetic field direction; the magnetic field is given in units of the thermodynamic critical field H_{c0}; ξ_0 is the coherence length.

The general solution of this equation is found in the form of an expansion in orthogonal functions:

$$\psi = \sum_{i,l,m} A_{ilm}\phi_{ilm}, \tag{4}$$

where

$$\phi_{ilm} = j_l\left(\frac{\rho}{R}\sqrt{\alpha_{li}}\right)Y_{lm}(\theta,\varphi), \tag{5}$$

$j_l(z) = \sqrt{\pi/2z}\, J_{l+1/2}(z)$ is a spherical Bessel function of the first kind, $J_{l+1/2}(z)$ is a Bessel function of the first kind, $Y_{lm}(\theta,\varphi)$ are normalized spherical harmonics, and the coefficients α_{li} are roots of the equation $(\partial j_l(\rho)/\partial\rho)|_{\rho=R} = 0$.

Substituting relations (4) and (5) into Eq. (3) and integrating over coordinates, we obtain an infinite system of algebraic equations for the coefficients A_{jlm}:

$$\left(\alpha - \alpha_{lj} + \frac{mH}{\sqrt{2}\kappa}\right)A_{jlm} = \frac{H^2R^2}{8\kappa^2}\sum_{np} A_{npm}F(l,p,j,n,m), \tag{6}$$

where

$$F(l,p,j,n,m) = \int_0^R d\rho\rho^4 j_l\left(\frac{\rho}{R}\sqrt{\alpha_{lj}}\right)j_p\left(\frac{\rho}{R}\sqrt{\alpha_{pn}}\right)$$

$$\times \int_0^{2\pi} d\varphi \int_0^{\pi} d\theta \sin^3\theta Y_{lm}(\theta,\varphi)Y_{pm}(\theta,\varphi). \tag{7}$$

The solutions of Eqs. (6) are characterized by quantum numbers m, which correspond to the number of magnetic flux quanta trapped by the inclusion. Setting the determinant of equation (6) to zero (for fixed m) yields the eigenvalues α, which depend on R and H. The critical temperature $T_c(H,R)$ is determined from the minimum value of α for which a nontrivial solution of equation (6) exists. As the magnetic field changes, the value of m corresponding to this minimum value of α can change. This is caused by a change in the number of trapped magnetic flux quanta. The states with $m = 0$ are realized in the absence of magnetic field and in weak magnetic fields. In the absence of magnetic field the solution of system (6) with the smallest value of α is possible only for a nonzero coefficient A_{100} ($A_{jlm} = A\delta_{j,1}\delta_{l,0}\delta_{m,0}$). Here $\alpha_{10} = 0$ and, hence, $\alpha = 0$, $T = T_{c0}$.

In the presence of a magnetic field but for small values of R ($R < 1$), the coefficient A_{100} is dominant over the others, i.e., for $j \neq 1$, $l \neq 0$, $m \neq 0$ the condition $A_{100} \gg A_{jlm}$ holds. In this case the system of equations (6) can be solved by perturbation theory. If one keeps in (6) only the coefficients A_{jlm} with $j = 1,2$; $l = 0,1,2$, then the dependence of the critical temperature of the inclusions on the radius and magnetic field will turn out to be given by the expression

$$\frac{T_c}{T_{c0}} = 1 - 0.05R^2\left(\frac{H}{\kappa}\right)^2 + 0.000141R^6\left(\frac{H}{\kappa}\right)^4. \tag{8}$$

The series is decreasing for small R.

We see that in zero magnetic field the phase transition temperature is the same as the critical temperature for a bulk sample. It should be noted that for boundary conditions of a more general form than (2), as would apply at a superconductor–metal boundary, the phase transition temperature exhibits a dependence on the radius even in zero magnetic field. In addition, at very small sizes the critical temperature depends on the radius because of the change in the phonon and electron spectra, structural defects, and other factors. As was discussed in the Introduction, such small samples will not be considered in this paper.

Keeping only the first two terms on the right-hand side in (8), we obtain an expression relating the critical tempera-

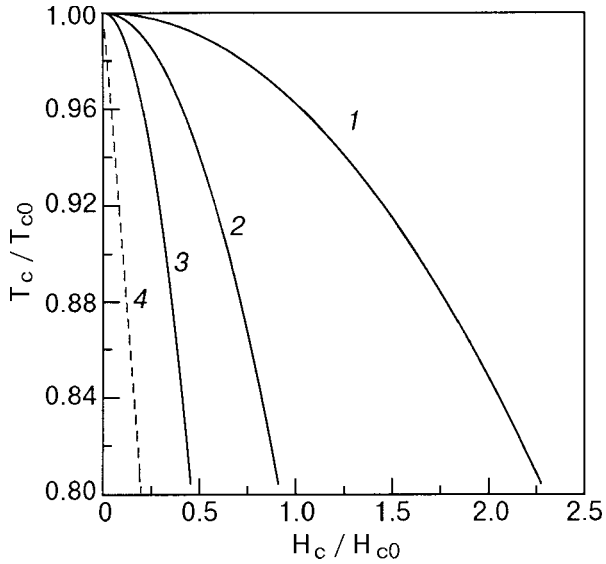

FIG. 1. Temperature–magnetic field diagram for different values of the radius of the inclusions, R/ξ_0: 0.2 (*1*), 0.5 (*2*), 1 (*3*) ($\kappa=0.23$). Curve *4* shows the dependence of the critical temperature on the magnetic field for a massive superconductor in the GL theory.

ture, critical magnetic field, and radius which is the same as the Ginzburg result.[12] Even in this case the state with $l=0$, $m=0$ is realized, and states with $m>0$ cannot be generated. Physically this means that the inclusion is too small to accomodate even one vortex when the inclusion is in the superconducting state. Such mesoscopic disks were studied in Ref. 17.

Figure 1 shows the dependence of the critical temperature on the magnetic field for various radii of the inclusions in a crystal with the parameters of Pb (for which $T_{c0}=7.2$ K, $\xi_0=830$ Å, $\kappa=0.23$).

A study of the solution of system (6) shows that perturbation theory does not apply for certain radii ($1<R<2$). In that case the solutions of the system of equations (6) are found by equating the determinant to zero for a limited number of nonzero coefficients A_{jlm}. As the magnetic field is increased, states with $m\neq 0$ will be realized starting at certain values of the fields; this corresponds to the trapping of a quantum of magnetic flux. In what follows we shall consider crystals with inclusions for which $R\leqslant 1$, and therefore results pertaining to states with $m>0$ will not be presented in this paper.

3. MACROSCOPIC PROPERTIES OF A CRYSTAL CONTAINING SUPERCONDUCTING INCLUSIONS

To determine the temperature and magnetic-field dependence of the conductivity of a sample containing inclusions, let us apply the results obtained for an individual superconducting inclusion.

We consider a crystal containing spherical inclusions that can have a superconducting phase. We suppose that there is dispersion in the radii of the inclusions. The conductivity of the matrix is assumed to be low, so that boundary conditions (2), which apply to a superconductor–insulator boundary, can be used in the calculations.

Let us calculate the conductivity of a system containing superconducting inclusions by the effective medium method. We assume that the total volume occupied by the inclusions is smaller than the volume necessary for the onset of percolation, and supercurrent does not flow through the entire sample. Therefore, in calculating the conductivity we can assume that, depending on the temperature and magnetic field, a spherical inclusion can be in one of two states: superconducting, with an infinite conductivity, or normal, with a resistance corresponding to that of the inclusion material at the given temperature. According to the formula for the conductivity in multicomponent systems[18,19]

$$\frac{\sigma_1-\sigma}{\sigma_1+2\sigma}P_s+\frac{\sigma_2-\sigma}{\sigma_2+2\sigma}P_n+\frac{\sigma_3-\sigma}{\sigma_3+2\sigma}P_3=0, \tag{9}$$

where in the present problem $\sigma_1=\infty$ is the conductivity of an inclusion in the superconducting state, σ_2 is the conductivity of an inclusion in the nonsuperconducting state, and σ_3 is the conductivity of the matrix ($\sigma_2>\sigma_3$); P_s and P_n are the relative volumes of the superconducting and normal inclusions, respectively:

$$P_s=P\frac{\int_0^{R_c(T,H)}R^3W(R)dR}{\int_0^{\infty}R^3W(R)dR},\quad P_n=P-P_s,\quad P_3=1-P, \tag{10}$$

where $W(R)$ is the probability that the system contains an inclusion with a radius R within a unit interval, and P is the inclusion part of the sample.

In general, the lower limit of integration over R in the formula for P_s should be determined by a certain value $R_{\min}$ below which the GL equations used are invalid. We shall assume that the size distribution of the inclusions is such that inclusions of that kind are few and their contribution to the conductivity is unimportant, so that we can set $R_{\min}=0$. Quantitative calculations were done for a normal distribution of inclusions over radius, $W(R)$, with a variance s^2 and a center R_0:

$$W(R)=Z\exp\left[-\frac{(R-R_0)^2}{2s^2}\right], \tag{11}$$

where Z is determined from the normalization condition $\int_0^{\infty}W(R)dR=1$.

The results of the calculations of the temperature dependence of the conductivity at various magnetic fields for inclusions with different variances of the size distribution are presented in Fig. 2. A jump in the conductivity is observed in the low-temperature region. For $H=0$ this jump is very sharp (curve *1*), since in the model used the critical temperature in zero magnetic field is independent of the radius, and all of the inclusions undergo a phase transition at the same temperature.

In the presence of a magnetic field ($H>0$) the critical temperature of the superconducting inclusions is dependent on the radius, and therefore at a given temperature T only those inclusions with $R\leqslant R_c(T,H)=2\kappa\sqrt{5(1-T/T_{c0})}/H$ are superconducting. Therefore, as the magnetic field is increased, the temperature region of increased conductivity becomes lower (curves *2* and *3*). The step becomes smoother as the variance of the size distribution increases.

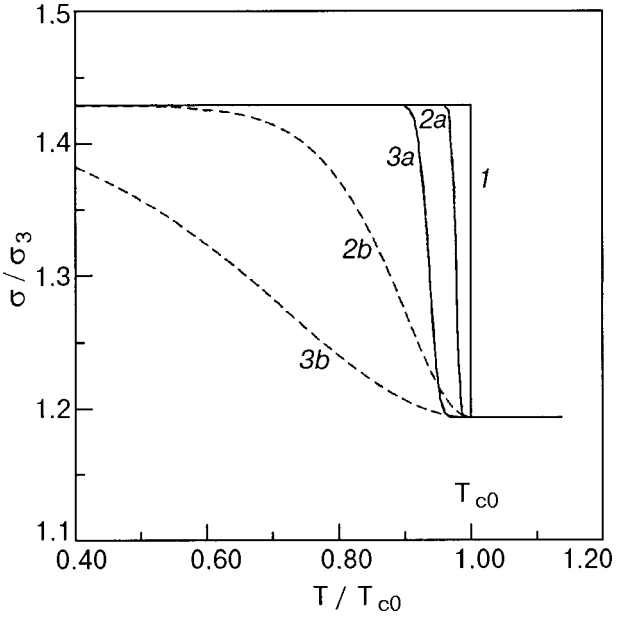

FIG. 2. Conductivity versus temperature ($P=0.1$, $\sigma_2/\sigma_3=5$, $\kappa=0.23$, $R_0=0.1$) for $H=0$ (*1*), 1.5 (*2*), 2.5 (*3*); $s=0.01$ (a), $s=0.1$ (b).

Figure 3 shows the dependence of the conductivity on the magnetic field. It is seen that the conductivity is high at low fields and falls off with increasing magnetic field, i.e., a strong dependence of the conductivity on magnetic field (magnetoresistance) is observed. In this case the magnetoresistance is due to suppression of superconductivity by the magnetic field: at first in the larger inclusions and then in progressively smaller inclusions as the magnetic field is increased. Figure 4 shows the dynamics of the change in the phase state of a crystal containing inclusions as the magnetic field is increased. The darkened circles denote inclusions in the superconducting state, the number of which decreases with increasing magnetic field. The region of magnetic fields in which the magnetoresistive drop in conductivity occurs

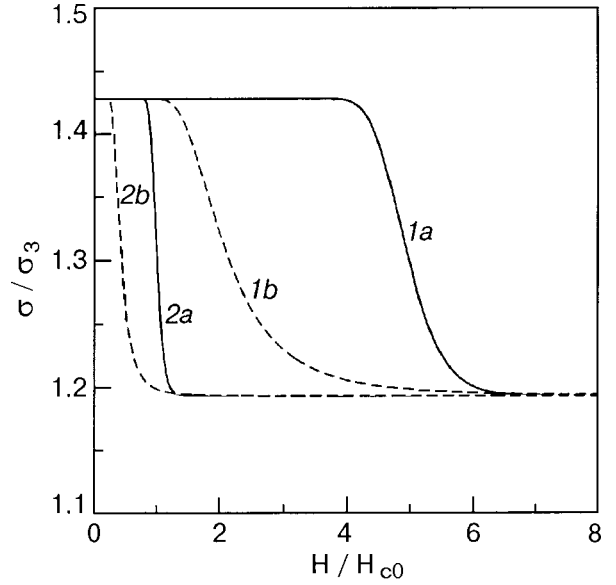

FIG. 3. Conductivity versus magnetic field ($P=0.1$, $\sigma_2/\sigma_3=5$, $\kappa=0.23$, $R_0=0.1$) for $T=0.75T_{c0}$ (*1*) and $0.99T_{c0}$ (*2*); $s=0.01$ (a), $s=0.1$ (b).

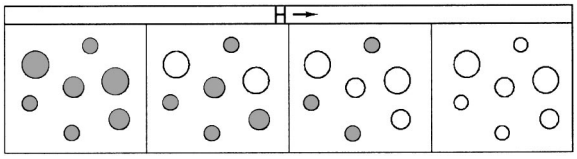

FIG. 4. Redistribution of the number of inclusions in the superconducting and normal states as the magnetic field is increased: $H_1<H_2<H_3<H_4$. The darkened circles indicate inclusions in the superconducting state, and the light circles those in the normal state.

depends on the mean radius of the inclusions, and the width of the drop region depends on the variance of the radius. Thus the low-temperature curves of the resistance versus field and temperature depend substantially on the size of the inclusions.

DISCUSSION OF THE RESULTS

In summary, the presence of superconducting inclusions has a substantial effect on the electrophysical properties of a crystal at low temperatures. The conductivity of the crystal increases, and one observes a strong dependence of the conductivity on magnetic field, which is due to phase transitions of the inclusions from the superconducting to the nonsuperconducting state as the magnetic field is increased. All of these effects are strongly dependent on radii of the inclusions and on the distribution of the inclusions with respect to their radii. Therefore, the study of the temperature and magnetic-field dependence in comparison with experiment provides an opportunity for determining the variance of the radius distribution of the inclusions.

The results can also be important for correct description of the electrical conductivity at low temperatures in binary and more-complex semiconductors, in which precipitation of a superconducting phase may take place during technological processing or under external influences. Such features of the conductivity and magnetic properties have been observed in InAs, PbTe, PbI_2, and GaAs, where the precipitation of metal-enriched phases (In in InAs, Pb in PbTe and PbI_2, and Ga in GaAs) can occur.

*E-mail: shevtsova@naverex.kiev.ua

[1] Yu. I. Petrov, *Physics of Small Particles* [in Russian], Moscow, Nauka (1982).
[2] Yu. F. Komnik, Fiz. Nizk. Temp. **8**, 115 (1982) [Sov. J. Low Temp. Phys. **8**, 57 (1982)].
[3] E. A. Shapoval, JETP Lett. **5**, 45 (1967).
[4] I. Giaever and H. R. Zeller, Phys. Rev. Lett. **20**, 1504 (1968).
[5] A. Rothwarf, Phys. Lett. A **30**, 55 (1969).
[6] J. H. P. Watson, Phys. Rev. B **2**, 1282 (1970).
[7] I. O. Kulik, JETP Lett. **14**, 228 (1971).
[8] V. M. Gvozdikov and I. I. Fal'ko, Ukr. Fiz. Zh. **21**, 859 (1976).
[9] V. M. Gvozdikov and É. Manninen, Fiz. Nizk. Temp. **6**, 1137 (1980) [Sov. J. Low Temp. Phys. **6**, 552 (1980)].
[10] F. Braun, Phys. Rev. Lett. **79**, 921 (1997).
[11] P. G. de Gennes, *Superconductivity of Metals and Alloys* [Benjamin, New York (1966); Mir, Moscow (1968)].
[12] V. L. Ginzburg, Zh. Éksp. Teor. Fiz. **34**, 113 (1958) [Sov. Phys. JETP **7**, 78 (1958)].
[13] M. G. Mil'vidskiĭ and V. B Osvenskiĭ, *Structural Defects in Semiconduc-*

tor Single Crystals [in Russian], Metallurgiya (1984).
[14] T. T. Dedegkaev, V. A. Moshnikov, D. B. Chesnokova, and D. A. Yas'kov, Pis'ma v ZhTF **6**, 1030 (1980) [Sov. Tech. Phys. Lett. **6**, 443 (1980)].
[15] S. D. Darchuk, T. Ditl, L. A. Korovina, S. Kolesnik, M. Savitskiĭ, and F. F. Sizov, Fiz. Tekh. Poluprovodn. **32**, 786 (1998) [Semiconductors **32**, 700 (1998)].
[16] G. A. Vikhliĭ, A. Ya. Karpenko, and P. G. Litovchenko, Ukr. Fiz. Zh. **43**, 103 (1998).
[17] A. K. Geim, I. V. Grigorieva, S. V. Dubonos, J. G. S. Lok, J. C. Maan, A. E. Filippov, and F. M. Peeters, Nature (London) **390**, 259 (1997).
[18] S. Kirpatrick, Rev. Mod. Phys. **45**, 574 (1973).
[19] B. E. Springett, Phys. Rev. Lett. **31**, 1483 (1973).

Translated by Steve Torstveit

Structural investigations of superconducting multilayers consisting of semiconducting materials

A. I. Erenburg and Yu. V. Bomze

B. Verkin Institute for Low Temperature Physics and Engineering, 47 Lenin Avenue, 61164 Kharkov, Ukraine

N. Ya. Fogel*

B. Verkin Institute for Low Temperature Physics and Engineering, 47 Lenin Avenue, 61164 Kharkov, Ukraine; Department of Applied Physics, Department of Environmental Inorganic Chemistry, and Department of Engineering Metals, Chalmers University of Technology, S-41296, Göteborg, Sweden

A. Yu. Sipatov and A. I. Fedorenko

Kharkov State Polytechnic University, 27 Frunze Street, 61002 Kharkov, Ukraine

V. Langer and M. Norell

Department of Applied Physics, Department of Environmental Inorganic Engineering Chemistry, and Department of Engineering Metals, Chalmers University of Technology, S-41296, Göteborg, Sweden

(Submitted July 14, 2000; revised September 14, 2000)
Fiz. Nizk. Temp. **27**, 127–130 (February 2001)

There are rather exotic semiconductor superlattices (SL) consisting of monochalcogenides of Pb, Sn, and rare-earth metals which exhibit superconductivity at temperature as high as 6 K. Here we report the results of precision x-ray diffractometry and TEM investigations as well as Auger spectroscopy data obtained on some of the epitaxially grown superconducting semiconductor SLs. It is established that the essential features of the SL structure determining the appearance of superconductivity are the perfect single-crystallinity of the samples and the presence of continuous dense grids of misfit dislocations on the interfaces between two semiconductors. The segregation of free Pb which was observed in some cases does not correlate, according to experimental data, with the appearance of superconductivity. [DOI: 10.1063/1.1353698]

INTRODUCTION

Among the wide variety of different kinds of artificial superconducting superlattices (SL), a special place belongs to the superconducting semiconductor SLs consisting of IV–VI semiconductors. Two SLs of this type—PbTe/PbS and PbTe /SnTe—have been known for a long time.[1] Recently, novel superconducting semiconducting SLs with transition temperatures T_c in the range 3–6 K have been discovered.[2] Superconductivity has been observed in a number of additional multilayered compositions: PbTe/PbSe; PbS/PbSe; PbTe/YbS; PbTe/EuS.[2] The appearance of superconductivity in all these SLs is rather fascinating because it is inherent only to the multilayered compositions, while the individual materials constituting the SLs are not superconductors (the only exception being SnTe, with $T_c = 0.22$ K). Single thin films (with thickness $d = 15–300$ nm) of the chalcogenides of Pb, Sn, and rare-earth metals do not exhibit superconductivity, either. The suggestions explaining the origin of this phenomenon in semiconductor SLs are rather controversial,[1–3] and none of them can be considered satisfactory to date, if all the known experimental data are taken into account.

In this situation, when the phenomenon of superconductivity itself demands a clear explanation, structural investigations of the SLs become of major importance. On the one hand, they can enable one to clarify the correlations between the structural features of SLs and the appearance of superconductivity. On the other hand, they may be helpful for explaining the processes which lead to the degradation of superconductivity with time in the structures considered.

EXPERIMENTAL RESULTS AND DISCUSSION

The SLs investigated were grown epitaxially on the cleaved (001) face of KCl single crystals. The details of the PbTe/PbS SLs preparation are described in Ref. 4. Other SLs were prepared in the same way. In some cases the (0001) face of mica was used as a substrate. The thicknesses of both constituent layers in the SLs were, as a rule, 100 nm. The number of bilayers N in the majority of the samples was equal to 10. For the electron microscopy investigations samples with $N = 1$ and $N = 1.5$ were used, because our technique permitted studying samples with thicknesses not exceeding 150 nm (in the case of monochalcogenides).

The transmission electron microscopy (TEM) and x-ray diffractometry (XRD) studies that are the main topics of this work show what essential features of the SL structure are important for the appearance of superconductivity in semiconductor SLs and for its degradation.

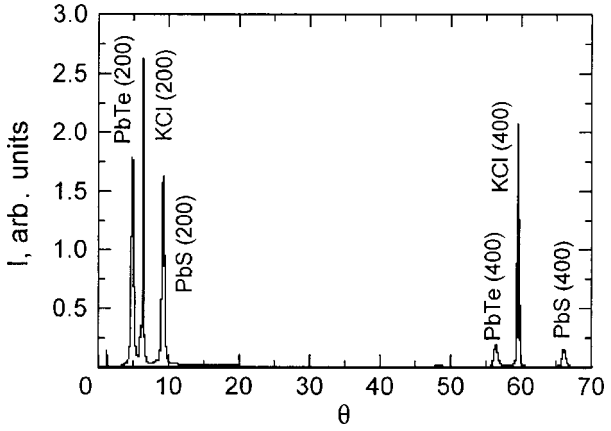

FIG. 1. Diffractogram of PbTe/PbS SL.

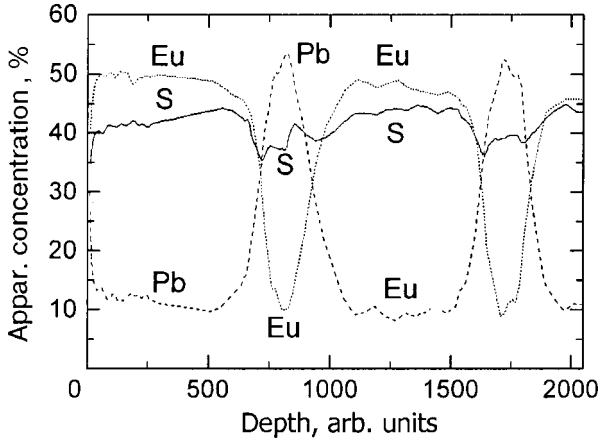

FIG. 2. Apparent concentrations of components in a EuS/PbS SL as a function of depth.

A typical diffractogram of a SL is shown in Fig. 1. According to XRD data, the most perfect single crystal heterostructures can be grown by the Frank-van der Merve method on the (001) face of KCl substrates both at small misfit parameters f and at large ones as well. The misfit f is determined by the difference in the lattice parameter a of the two compounds:

$$f = 2\frac{(a_1 - a_2)}{(a_1 + a_2)}.$$

The XRD data cover the whole range of parameters f from the lowest value 0.5% (for EuS/PbS) to the largest value 13% (for PbTe/YbS) for isomorphic monochalcogenides with the NaCl-type structure and may be summarized as follows.

i) All the data obtained may be regarded as evidence that SLs prepared on KCl substrates are perfect single-crystal multilayered structures with relatively small average stresses. In the measurements in the $\theta - 2\theta$ scanning mode with characteristic Cu radiation, only the reflections of ($h00$) type are present for all compounds in the SLs and for the substrate. The data of the other special scan modes that allow getting the reflections from crystal planes with different (hkl) values, not parallel to the layer planes, testify that all crystallographic directions in the substrate and in heterostructure components coincide.

ii) For PbTe and PbS in all SLs the values of the lattice parameters a hardly differ from the ones tabulated for the bulk compounds. Larger changes of a (up to 0.3%) are observed in YbS and EuS when they are in combination with PbTe.

iii) The areas of coherent x-ray scattering in different SL layers as a rule are about 100–200 nm (the only exception is YbS, where it is 30 nm). The microstresses in the layer planes (with the same exception) are rather small (the value of deformation is in the range 0.05–0.4%) and show a tendency to increase with increasing f. Both the blocks of coherent scattering and the microstress values were determined by an approximation method.

iv) In the case of the samples prepared on the mica substrate the SLs consist of blocks with two different orientations (with the axes [100] and [111] perpendicular to the layer planes).

The stability of the semiconductor SLs studied is rather low, and their lifetime, during which the samples stay continuous and conducting, is very limited. There are a number of factors leading to the destruction of multilayers. SLs appear to be destroyed due to the thermocycling connected with low-temperature measurements. The most stable composition is PbTe/PbS. These SLs may last for 10–20 temperature cycles without degradation of the structure and superconducting properties. Another reason for the degradation is mechanical destruction (the appearance of cracks penetrating through the entire depth of the sample) due to elastic stresses. In some cases a partial decomposition of the Pb-containing compounds occurs, and the reflections characteristic for polycrystalline Pb appear. They are always present on diffractograms of the freshly-prepared and aged EuS/PbS. In fresh PbTe/PbS SLs the Pb reflections are absent, but they appear as a result of aging after a month or two. This corresponds approximately to the superconductivity lifetime in these samples, but a rather large statistics would be needed in order to say whether this type of decomposition is directly associated with the destruction of superconductivity. The reflections corresponding to pure Pb have never been seen on PbTe/YbS samples (even after year-long aging). Finally, solid-state chemical reactions between different elements take place. As a result of the aging effect, additional reflections appear on the x-ray diffractograms. The majority of these reflections may be identified as belonging to the compounds of K and S with different valences. The location of these new compounds should be close to the interface between the substrate and the first semiconducting layer because, according to Auger electron spectroscopy (AES) analysis, no traces of K were observed in several upper layers of the EuS/PbS superlattice. Figure 2 shows the composition–depth profile obtained by means of ion etching and AES on a EuS/PbS sample (the depth is shown in arbitrary units because the calibration of the etching rates was not yet done on the single films). The difference in the crystal lattice parameters of these two chalcogenides is extremely small, and on the diffractograms of these samples the separate reflections belonging to the two compounds cannot be distinguished. The diffractogram appears to be similar to that which is characteristic for a mixture of the two compounds.

TABLE I. The misfits *f*, grid periods D_g, and transition temperatures T_c for the investigated systems.

System	*f*, %	D_g, nm		T_c, K
		Calc.	Exp.	
PbS/EuS	0.57	74.0	absent	no data
PbTe/SnTe	2.0	23.0	23-25	2.97
PbS/PbSe	3.16	13.5	13.5-14	4.29
PbTe/PbSe	4.8	8.6	8.6	6.02
PbTe/EuS	7.7	5.7	5.7	5.01
PbTe/PbS	8.3	5.2	5.2	6.03
PbTe/YbS	13.0	3.3	3.3	5.93

*T_c values for each multilayered system are the averages for several identical samples.

But the AES data in Fig. 2 show that there are the alternating layers of EuS and PbS. The apparent concentration of the elements Eu, Pb and S (Fig. 2) obtained in the different layers corresponds to the expected one for monochalcogenides, within the limits of the experimental uncertainty. The relatively large length over which the Eu and Pb concentrations vary substantially as the interfaces cannot be considered as a real scale of the transition region due to the specifics of the technique used (it is attributed to the loss in depth resolution caused by the ion etching).

According to TEM investigations which have been carried out on 2- and 3-layer samples (condensed on KCl substrates) with a total sample thickness <150 nm, for heterostructures with $f>2\%$ regular grids of misfit dislocations are observed. The grid periods obtained experimentally agree well with the ones calculated according to the formula[5]

$$D_g=\frac{|\mathbf{b}|_e}{f},$$

where $\mathbf{b}_e$ is the Burgers vector of the misfit dislocation. The misfits *f*, grid periods D_g, and transition temperatures T_c for the investigated systems are presented in Table I. It is seen that in the *f* range between 2% and 4.8%, decreasing the dislocation density leads to a noticeable lowering of the superconducting transition temperature. At $f>4.8\%$ the dependence of T_c on the dislocation density shows an approach to saturation at a level of about 6 K. Misfit dislocations have not been observed in EuS/PbS SLs with $f=0.5\%$. The quick mechanical destruction of the latter SLs (just after preparation) did not allow us to test these heterostructures for superconductivity. The PbTe/PbS SLs prepared on mica substrates have island-type dislocation grids covering only a small part of the interfaces. On these samples only partial superconducting transitions have been found, at temperatures which are close to those for the same SLs condensed on KCl. The resistance jumps are usually about 15–20% of the normal resistance.

SUMMARY

From a comparison of the structural and superconducting properties of all the SLs investigated, the following conclusions may be stated.

1. For the appearance of superconductivity it is essential to have perfect single-crystalline structure and regular grids of misfit dislocations on the interfaces. When the latter are of the island type, only a partial superconducting transition is seen against the background of a large normal resistivity, surviving until the lowest temperature of the measurements.

2. There is no correlation between the presence of pure Pb in the SLs and the appearance of superconductivity. In particular, pure Pb has never been observed in superconducting PbTe/YbS SLs. Thus the origin of superconductivity in semiconductor SLs can hardly be attributed to lead segregation on the interfaces between two compounds.

3. Evidence obtained from the measurements of the critical magnetic fields shows that the superconducting layers in the SLs considered are confined to all interfaces between two semiconductors.[4] On the basis of this fact and the conclusion formulated in item 1, one may suggest that in semiconductor SLs the superconductivity itself may result from the dislocation structures and specific interfacial electronic states.

*E-mail: fogel@ilt.kharkov.ua

[1] K. Murase, S. Ishida, S. Takaoka, and T. Okumara, Surf. Sci. **170**, 486 (1986).
[2] N. Ya. Fogel, V. G. Cherkasova, A. S. Pokhila, A. Yu. Sipatov, and A. I. Fedorenko, Czech J. Phys. Suppl. S2 **46**, 727 (1996).
[3] D. Agassi and T. K. Chu, Phys. Status Solidi B **160**, 601 (1990).
[4] I. M. Dmitrenko, N. Ya. Fogel, V. G. Cherkasova, A. I. Fedorenko, and A. Yu. Sipatov, Fiz. Nizk. Temp. **19**, 747 (1993) [Low Temp. Phys. **19**, 533 (1993)].
[5] V. M. Kosevich and L. S. Palatnik, *Electron Microscopic Images of Dislocations and Stacking Faults*, Nauka, Moscow (1986).

This article was published in English in the original Russian journal. Reproduced here with stylistic changes by AIP.

Temperature dependence of the critical current in high-T_c superconductors with low-angle boundaries between crystalline blocks

É. A. Pashitskiĭ,* V. I. Vakaryuk, S. M. Ryabchenko, and Yu. V. Fedotov

Institute of Physics, National Academy of Sciences of Ukraine, rp. Nauki 46, 03022 Kiev, Ukraine
(Submitted July 26, 2000)
Fiz. Nizk. Temp. **27**, 131–139 (February 2001)

A model for the limiting of the critical current in rather perfect high-T_c superconducting crystals and epitaxial films with a block structure with small angles of misorientation θ of the crystalline blocks is considered for the case when the distance d between edge dislocations along the boundary between blocks is greater than the coherence length $\xi(T)$. It is shown that under these conditions the transparency of low-angle boundaries for the superconducting current carriers near the critical temperature T_c is practically independent of θ and T. As a result, the only factor governing the temperature dependence of the critical current density $j_c(T)$ remains the depairing current $j_0(T) \propto (1-T/T_c)^{3/2}$. Near T_c, when $\xi(T) > d$, a transition from the dependence $j_c(T) \sim (1-T/T_c)^{3/2}$ to a dependence $j_c(T) \sim (1-T/T_c)^2$ occurs. This behavior of $j_c(T)$ is in good agreement with the results of experimental measurements of the critical currents in thin epitaxial films of $YBa_2Cu_3O_{7-\delta}$.
[DOI: 10.1063/1.1353699]

1. INTRODUCTION

Along with the critical temperature T_c, the critical current density j_c is one of the most important characteristics of a superconductor. It can be measured both by the experimental determination of the transport properties of samples (resistive methods) and by noncontact methods based, for example, on measurement of the magnetic susceptibility of samples in alternating magnetic fields. The value and temperature dependence of j_c are governed by various mechanisms that limit the supercurrent, decreasing j_c from its maximum possible value corresponding to the depairing current j_0.

One of the known mechanisms that limit the supercurrent is due to the depinning of Abrikosov quantum vortices in type-II superconductors and can be described in a model based on the collective pinning of isolated vortices on structural defects.[1] In the collective pinning model the character of $j_c(T)$ is intimately connected to the type of disorder that is responsible for the vortex pinning in the sample, and it is determined by the dependence of the corresponding disorder parameter δ. For pinning due to spatial variations of T_c (δT_c pinning) the dependence of the disorder parameter on T has the form $\delta_T \sim (1-T/T_c)^{-1/2}$, while the temperature dependence of the parameter δ_l characterizing the variation of the mean free paths of the current carriers (δl pinning) is given by the expression $\delta_l \sim (1-T/T_c)^{3/2}$.

For both types of disordering in the collective pinning of isolated vortices the critical current density is given by the expression[1]

$$j_c = j_0 (\delta/\varepsilon_m)^{2/3}, \tag{1}$$

where $j_0 = c\varphi_0/(12\sqrt{3}\pi^2\lambda_L^2\xi)$ is the depairing current density in the superconductor, $\varphi_0 = hc/2e$ is the magnetic flux quantum, λ_L is the London penetration depth of the magnetic field, ξ is the coherence length, and ε_m is the ratio of the anisotropic effective masses. For high-T_c superconductors (HTSCs) based on layered cuprate compounds one has $\varepsilon_m = m_c^*/m_{ab}^* \gg 1$, where m_{ab}^* and m_c^* are the effective masses of the current carriers in the plane of the layers (**ab**) and in the direction normal to the plane of the layers (along the c axis).

It follows from Eq. (1) that the dependence of the critical current density on T is determined by the temperature dependence of the depairing current j_0 and the disorder parameter δ. For temperatures sufficiently close to T_c the function $j_0(T)$ can be obtained using the expressions for ξ and λ_L in the BCS theory: $\xi(T) \propto \lambda_L(T) \propto (1-T/T_c)^{-1/2}$, which gives $j_0 \propto (1-T/T_c)^{3/2}$. Substitution of the temperature dependence of j_0, δ_T, and δ_l into (1) leads to a dependence of the form $j_c(T) \propto (1-T/T_c)^{7/6}$ in the case of δT_c pinning and to $j_c(T) \propto (1-T/T_c)^{5/2}$ in the case of δl pinning.

Another possible factor limiting $j_c(T)$ is the existence of different interfacial boundaries in granular and polycrystalline samples of HTSC materials. Then the dependence of $j_c(T)$ would be determined by the currents $j_m(T)$ flowing through the intergranular Josephson contacts. The temperature dependence of the Josephson current $j_m(T)$ has been calculated previously in the Ginzburg–Landau theory for different models of the contacts.[2,3] In particular, for contacts of the superconductor–insulator–superconductor (SIS) and superconductor–normal metal–superconductor (SNS) types the temperature dependence was found to be $j_m(T) \propto (T_c - T)$ and $j_m(T) \propto (T_c - T)^2$, respectively. We note that a quadratic temperature dependence of the critical current $j_c(T) \propto (T_c - T)^2$ has been observed in HTSC materials.[4–6] In addition, for a complex contact of the superconductor–normal metal–insulator–superconductor (SNIS) type a dependence $j_m(T) \propto (T_c - T)^{3/2}$, similar to the T dependence of the depairing current j_0, was observed in Ref. 3.

In an experimental study[7] of the temperature dependence $j_c(T)$ in thin (~500 Å thick) epitaxial films of

$YBa_2Cu_3O_{7-\delta}$ a relatively large value was obtained for the critical current ($\sim 10^6$ A/cm^2), and a dependence $j_c(T) \propto (1 - T/T_c)^{3/2}$ was found.

Irradiation of the films by fast electrons with an energy of 4 MeV at doses of $\sim 3 \times 10^{16}$ electrons/cm^2 led to a severalfold decrease in the absolute value of the critical current but did not alter the character of its temperature dependence. In discussing the results, the authors of Ref. 7 offered the conjecture that the dependence $j_c(T) \propto (1 - T/T_c)^{3/2}$ may be due to the presence of a granular structure in the film, with intergranular contacts of the SNIS type. However, this conjecture is in poor agreement with the high critical current density in those epitaxial films.

In Ref. 8 a non-Josephson mechanism was considered for the limiting of the critical current in rather perfect HTSC crystals and epitaxial films, which are generally characterized by a block structure and consist of slightly disoriented single-crystal blocks. The low-angle boundaries between these blocks are periodic chains of edge dislocations (EDs) separated by a distance that depends on the angle of mutual misorientation θ of the blocks and is determined by the well-known Frank formula $d(\theta) = b/2\sin(\theta/2) \approx b/\theta$, where b is the modulus of the Burgers vector, which is equal in order of magnitude to the lattice constant.

As was shown in Ref. 8, near a periodic chain of parallel EDs (a dislocation wall), in a region with a width of several times the coherence length $\xi(T)$, the proximity effect leads to suppression of the superconducting order parameter ψ and, as a consequence, a substantial weakening of the critical current through the boundary, even at angles of misorientation θ such that the nonsuperconducting regions around the cores of the EDs do not yet overlap and a continuous insulating or normal (metallic) Josephson barrier is not formed. The angle dependence of the critical current obtained in Ref. 8 is in good agreement with the quasiexponential dependence $j_c(\theta)$ observed experimentally in the absence of external magnetic field for HTSC bicrystals with different θ.

The temperature dependence of $j_c(T)$ through the boundary in Ref. 8 was not analyzed in detail, and it was only for the case of rather large misorientation angles θ, at which the strong inequality $d(\theta) \ll \xi(T)$ holds and a substantial role is played by the geometric effect of the narrowing of the superconducting channels between the insulating cores of the EDs, that a dependence $j_c(T) \propto (1 - T/T_c)^{5/2}$ was obtained, which formally coincides with the δl-pinning model but is realized in the absence of magnetic field. However, the case of low-angle boundaries, where the inequality $d(\theta) > \xi(T)$ holds over a wide temperature interval, was not analyzed in Ref. 8, even though this can be of interest for HTSC crystals in view of the anomalously small coherence length. In addition, the dependence $j_c(T) \propto (1 - T/T_c)^{5/2}$ given in Ref. 8 was obtained as the result of an assumption that the transparency of the system of superconducting channels at the boundary goes to zero as $T \to T_c$, whereas in actuality the transparency of the boundary at a fixed value of θ should increase as $T \to T_c$ and $\xi(T) \to \infty$ on account of the enhancement of the proximity effect between the superconducting channels.

In this paper we use a model analogous to that of Ref. 8 to consider the mechanism limiting the critical current through low-angle boundaries in rather perfect HTSC crystals and epitaxial films under the condition $d(\theta) > 2\xi(T)$. We show that in this case the transparency of the boundary for the superconducting current carriers, which is determined by the local suppression of the superconducting order parameter along the boundary, is practically independent of θ and T near T_c. If there is also a high transparency of the boundary due to the existence of rather wide superconducting channels between the cores of the EDs at small θ, then the only remaining factor governing the temperature dependence $j_c(T)$ is the depairing current. The dependence $j_c(T) \propto (1 - T/T_c)^{3/2}$ obtained in this model is in good agreement with the experimental results reported in Ref. 7 and in the present paper. On the other hand, if the ''geometric'' factor limiting the superconducting current in the channels is important (e.g., on account of a large radius of the nonsuperconducting cores of the EDs) and the transparency of the boundary does not go to zero as $T \to T_c$ but increases instead, then the temperature dependence of the critical current will have the form $j_c(T) \propto (1 - T/T_c)^{5/4}$, which is different from the dependence $j_c(T) \propto (1 - T/T_c)^{5/2}$ obtained in Ref. 8. However, as one approaches T_c, where the condition $d(\theta) > 2\xi(T)$ ceases to hold, in both cases one observes a transition to a quadratic dependence $j_c T \propto (1 - T/T_c)^2$, which is analogous to that for the critical current through an SNS contact. In the present paper we compare the theoretical results with the experimental data for a $YBa_2Cu_3O_{7-\delta}$ film before and after its irradiation.

2. EXPERIMENT

The parameters of the HTSC films were measured by the low-frequency magnetic susceptibility method at a frequency of 937 Hz in a temperature range 77–100 K in the magnetic field of the Earth. The amplitude of the alternating magnetic field perpendicular to the plane of the film was varied over the range 0.001–5 mT. The detection system consisted of an SR-830 lock-in amplifier connected to a computer through an RS-232 interface for storage and additional averaging of the data.

The contactless technique used to measure the critical current density was based on analysis of the imaginary part of the complex magnetic susceptibility χ'' of the samples as a function of the amplitude h of the alternating magnetic field.

As h is varied the measured value of χ'' reaches a maximum at a certain value h_m. In general the value of h_m has a rather complicated dependence on the critical current density and on the shape and dimensions of the sample. For samples in the form of thin films excited by an alternating field perpendicular to the film plane the dependence of χ'' on h has been examined in Ref. 9, for example. There it was found that for disk-shaped films the relation $j_c = 1.013 h_m / L$ is observed, where L is the thickness of the film. It has been shown[10] that this same expression also gives a good description of the results of experiments on films of other isometric shapes, including squares.

The value of T_c for the samples was determined on the same apparatus used to measure the magnetic susceptibility, from the start of the sharp rise of $\chi''(T)$ at the onset of

superconductivity. According to our estimates, the error in the measurements of T_c was ± 0.1 K.

We studied thin ($L=500$ Å) epitaxial films of the HTSC $YBa_2Cu_3O_{7-\delta}$ with $T_c=89.6$ K. The x axis of the $YBa_2Cu_3O_{7-\delta}$ epitaxial films, which were deposited on a $LaAlO_3$ substrate, were oriented perpendicular to the plane of the films. The samples had a nearly square shape in the plane, with dimensions of 0.5×0.5 cm.

The samples were irradiated at room temperature by 4-MeV electrons at the ÉLU-4 linear accelerator. The density of the electron beam was chosen so that the temperature of the sample did not exceed 70–80 °C during the irradiation.

The dependence of the relative values of χ'' on the amplitude h of the ac exciting field was measured prior to irradiation and after storage at room temperature for various time intervals. The relative error in the determination of h_m and, hence, of j_c, is not more than 5% of the measured value.

The main result of the studies of the temperature dependence of the critical current density in these films and how it is affected by electron irradiation (at a dose of 3×10^{16} electrons/cm^2) was given in Ref. 7. The experimental data can be approximated by the expression $j_c(T)=J_n(1-T/T_c)^s$, where the parameters J_n and s of the approximation were optimized by minimizing the mean-square deviation. For the initial film $J_n=(1.44\pm 0.19)\times 10^7$ A/cm^2, $s=1.48\pm 0.06$. For the irradiated film immediately after irradiation $J_n=(6.35\pm 0.62)\times 10^6$ A/cm^2, $s=1.51\pm 0.04$. Thus the exponent in the temperature dependence corresponds to a value $s=3/2$ and is not affected by irradiation, while the value of the critical current density, being initially rather high, decreases to less than half after irradiation. We did not observe any changes, outside the measurement error, in the critical temperature T_c of the films as a result of irradiation.

The first signs of the relaxation process began to appear during the first day after irradiation. However, these changes were observed more in the temperature dependence of $\chi''(T)$ and of the responses at high odd harmonics of the excitation frequency in experiments at given values of h but were hardly noticeable in the resulting temperature dependence of $j_c(T)$ obtained from the $\chi''(h)$ curves. Nevertheless, it turned out that that over a long period of time (several months) the relaxation after irradiation became noticeable in $j_c(T)$ as well. Here the exponent s remained constant (equal to 3/2 within the measurement error) the entire time, while J_n relaxed over time to the value observed prior to irradiation. Figure 1 shows the temperature dependence of $j_c(T)$ for a film prior to irradiation, immediately after irradiation, and 540 days after irradiation. It is seen that over the extended relaxation period the value of J_n, which had fallen to less than half immediately after irradiation, was almost completely restored to its original value.

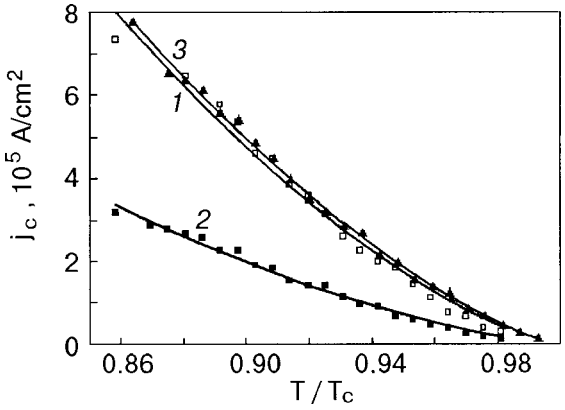

FIG. 1. Measured critical current density versus the reduced temperature T/T_c for an unirradiated film (□), immediately after irradiation of the film by a dose of 3×10^{16} electrons/cm^2 (■), and 540 days after irradiation (▲). Lines *1–3* are the approximating curves $j_c(T)=J_n(1-T/T_c)^s$ for these states of the film, with the values of the parameters J_n and s given in the text.

3. MODEL OF LOW-ANGLE BOUNDARIES AND THE TEMPERATURE DEPENDENCE OF THE CRITICAL CURRENT

To determine the temperature dependence of the critical current $j_c(T)$ through a low-angle boundary with allowance for the proximity effect under the condition $\tau\equiv(1-T/T_c)\ll 1$, we proceed from the Ginzburg–Landau (GL) equation for a spatially nonuniform superconducting order parameter $\psi(\mathbf{r})$ near the interfacial boundary, normalized to the uniform bulk value $\psi_\infty\sim\sqrt{\tau}$ (Ref. 8):

$$\xi^2(T)\Delta\psi+\psi-\psi^3-i^3/\psi^3=V(\mathbf{r})\psi. \tag{2}$$

Here Δ is the Laplacian operator, $i=j/j_0$ is the dimensionless uniform current density in the bulk of the superconductor, normalized to the depairing current $j_0(T)\sim\tau^{3/2}$, and V is the effective potential, which determines the measure of local suppression of $\psi(\mathbf{r})$ on account of the change in T_c and j near the interfacial boundary:

$$V(\mathbf{r})=\frac{\delta T_c(\mathbf{r})}{\tau T_c}-\frac{i_0^2(\mathbf{r})-i^2}{\psi^3(\mathbf{r})}, \tag{3}$$

where $i_0(\mathbf{r})$ is the local value of the superconducting current density near the boundary. We note that in Ref. 8 the denominator of the second term in (3) contained an additional factor of τ, which corresponds to the poorly grounded assumption that the ''geometric'' transparency of the boundary decreases as $T\to T_c$.

The change in the supercurrent density $i_0(\mathbf{r})$ flowing through the boundary is related to the spatial redistribution (filamentation) of the supercurrent in the superconducting channels between the nonsuperconducting cores of the EDs formed as a result of the plastic deformation of the crystal lattice and also on account of the accumulation of defects in the elastic stress fields around the EDs, primarily copper atoms and oxygen vacancies, the growth in the concentration of which leads to suppression of superconductivity in cuprate HTSC compounds. However, for low-angle boundaries the growth of the local supercurrent density is small, since the width of the superconducting channels $d_s(\theta)=d(\theta)-2r_i$ is significantly greater than the ''geometric shadow'' region created by the insulating cores of EDs of radius $r_i\ll d$.

The local variation of the critical temperature $\delta T_c(\mathbf{r})$ in (3) arises because the coupling constant $g_0(\mathbf{r})$ responsible for Cooper pairing varies near an ED on account of the elastic strain of the crystal lattice and the redistribution of the concentration of free current carriers (holes) in the electro-

static fields of charged defects (ions, oxygen vacancies) over distances of the order of the screening length l_D (Ref. 8).

As a result, in the neighborhood of an ED there arise regions with a depressed local value of $T_c(\mathbf{r})$, lower than T_c in the bulk of the sample. In these regions a transition to a normal metallic state can occur at sample temperatures in the interval $T_c(\mathbf{r})<T<T_c$, and that should lead to suppression of the superconducting order parameter on account of the proximity effect at scales comparable to the coherence length $\xi(T)=\xi_0/\sqrt{\tau}$.

The value of ξ_0 can be estimated from the slope of the temperature dependence of the second critical field $H_{c2}(T)$ of a type-II superconductor as $T\to T_c$:

$$\xi_0=\left[\frac{\varphi_0}{2\pi T_c H'_{c2}(T_c)}\right]^{1/2};\quad H'_{c2}=\frac{dH_{c2}}{dT}. \tag{4}$$

For $T_c\approx 90$ K and $H'_{c2}(T_c)\approx 2$ T/K, values typical for $YBa_2Cu_3O_{7-\delta}$, we obtain the estimate $\xi_0\approx 12$ Å.

Under the condition that $\xi(T)$ is much greater than l_D and greater than the distance $d(\theta)\approx b/\theta$ between EDs, the value of the potential $V(x,y)$ averaged over the spatial period along the boundary (i.e., along the y axis) can be written approximately as (see Ref. 8):

$$\langle V(x,y)\rangle\approx\frac{U_0}{\tau d(\theta)\xi(T)}\,\delta(\eta)\approx\frac{2\pi r_0^2\overline{u_0}\theta}{b\xi_0\sqrt{\tau}}\,\delta(\eta). \tag{5}$$

Here $\eta=x/\xi(T)$ is the dimensionless variable along the x axis, perpendicular to the plane of the boundary, $\delta(\eta)$ is a delta function, and U_0 is the zeroth Fourier component of the short-range (screened) potential of the nonsuperconducting core of the ED:

$$U_0=2\pi\int_0^\infty U(r)r\,dr=2\pi r_0^2\overline{u_0}, \tag{6}$$

where $\overline{u_0}$ is the dimensionless amplitude of the potential normalized to the energy k_BT_c (k_B is Boltzmann's constant), and r_0 is the effective radius of the normal (metallic) region around the ED and is equal in order of magnitude to the screening length l_D. We note that under the condition $d(\theta)\leqslant\xi(T)$, each ED in the xy plane is associated with a region of area $2d(\theta)\xi(T)$ in which suppression of the superconducting order parameter ψ on account of the proximity effect occurs.

However, at sufficiently large values of τ and small values of the misorientation angle θ, such that $d(\theta)\geqslant 2\xi(T)$, the regions with the suppressed value of ψ around the individual EDs are practically nonoverlapping, and their areas per ED are equal in order of magnitude to $\pi\xi^2(T)$. In this case we use the following expression instead of (5) for the y-averaged potential:

$$\langle V(x,y)\rangle\approx\frac{2\gamma U_0}{\tau\pi\xi^2(T)}\,\delta(\eta)=\gamma\frac{4r_0^2\overline{u_0}}{\xi_0^2}\,\delta(\eta), \tag{7}$$

where γ is a dimensionless coefficient that is determined by the spatial distribution of the nonuniform order parameter around the ED. We see that expression (7) is independent of both θ and τ.

Equating expressions (5) and (7), we find the τ-dependent value of the critical angle θ_c at which the averaged potential at the boundary begins to exhibit temperature and angle dependence:

$$\theta_c(\tau)=\frac{2\gamma}{\pi}\,\frac{b\sqrt{\tau}}{\xi_0}. \tag{8}$$

Assuming that $b\approx a\approx 4$ Å (a is the lattice constant in the plane of the layers) and taking a temperature interval corresponding to $\tau\approx 0.1$–0.25, we find from (8) that the critical angle has a value $\theta_c\approx(4\gamma/\pi)(1°$–$5°)$.

If we assume that the superconducting order parameter near the ED is suppressed inside a cylindrical region with a circular cross section of radius $\xi(T)$ and that the transition from dependence (5) to (7) occurs at $d(\theta)=2\xi(T)$, we obtain the coefficient $\gamma=\pi/4$. In general one has $\gamma\sim 1$.

As a result of the substitution of (5) and (7) into the GL equation (2), we obtain the following equation for the y-averaged order parameter $\psi(x,y)$:

$$\frac{d^2\psi}{d\eta^2}+\psi-\psi^3-\frac{i^2}{\psi^3}=\Gamma_1\psi\delta(\eta), \tag{9}$$

where

$$\Gamma_1(\theta)\approx 4\gamma\overline{u_0}\frac{r_0^2}{\xi_0^2}\begin{cases}1, & \theta<\theta_c(\tau);\\ \theta/\theta_c(\tau), & \theta>\theta_c(\tau).\end{cases} \tag{10}$$

The average (9) far from the boundary (for $\eta\neq 0$) is uniform and can be integrated with the use of the boundary conditions

$$\psi(0)=\psi_0;\quad \psi(\pm\infty)=\psi_\infty;\quad \psi'(\pm\infty)=0; \tag{11}$$

$$\psi'(+0)=-\psi'(-0)=\frac{1}{2}\Gamma_1\psi_0. \tag{12}$$

The first integral of equation (9) under conditions (11) and (12) is (see Ref. 8)

$$\frac{1}{2}\left(\frac{d\psi}{d\eta}\right)^2+U(\psi)=E, \tag{13}$$

where

$$U(\psi)=\frac{\psi^2}{2}+\frac{i^2}{2\psi^2}-\frac{\psi^4}{4};\quad E=U(\psi_\infty). \tag{14}$$

The equation for finding the value of the suppressed superconducting order parameter ψ_0 along the boundary is obtained by substituting (12) into (13) for $\psi=\psi_0$:

$$2E-\psi_0^2+\frac{\psi_0^4}{2}-\frac{i^2}{\psi_0^2}=\frac{\Gamma_1^2\psi_0^2}{4}. \tag{15}$$

At a low current density, when the condition $i^2\ll 1$ is satisfied, there is no appreciable change in the superconducting order parameter in the bulk of the superconductor, and so to good accuracy one can set $\psi_\infty\approx 1$. Then, according to Eq. (14), one has to leading terms $E\approx 1/4$. Assuming that the order parameter is strongly suppressed near the boundary, so that $\psi_0^2\ll 1$, we obtain in place of (15) the more general relation

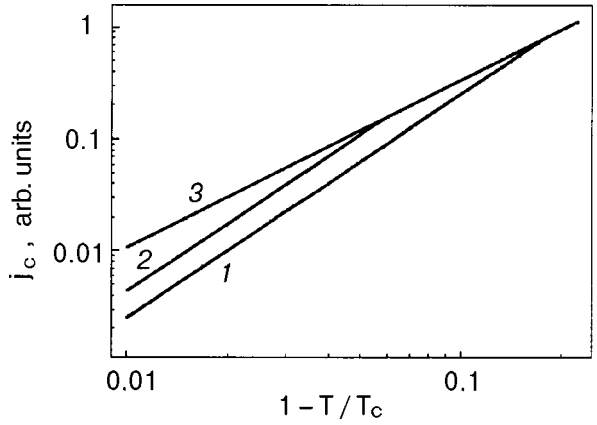

FIG. 2. Log–log plot of the calculated dependence of the critical current density j_c on $\tau = 1 - T/T_c$, obtained according to Eqs. (10) and (18) for the following angles of misorientation of the intercrystallite blocks: $\theta = 0.07$ (*1*), 0.04 (*2*), and 0.01 (*3*) radians ($\cong 4°$, 2.3°, and 0.57°). The curves were constructed for the parameters $b = 4$ Å, $\xi_0 = 12$ Å, and $\gamma = \pi/4$.

$$\frac{1}{2}(\Gamma_1^2+4)\psi_0^2 = 1 - \frac{2i^2}{\psi_0^2}, \tag{16}$$

which reduces to a biquadratic equation with respect to ψ_0. The roots of equation (16),

$$\psi_0^2 = \frac{1}{\Gamma_1^2+4}[1 \pm \sqrt{1-4i^2(\Gamma_1^2+4)}], \tag{17}$$

are real under the condition $i^2 \leqslant (1/4)(\Gamma_1^2+4)$, which implies the following expression for the maximum (critical) supercurrent density through the low-angle boundary:

$$j_c(\tau,\theta) = \frac{j_0(\tau)}{2[\Gamma_1^2(\theta,\tau)+4]^{1/2}}. \tag{18}$$

According to Eq. (10), for $\theta < \theta_c(\tau)$ the parameter Γ_1 is independent of τ and θ, so that the temperature dependence of the critical current (18) is the same as that for the depairing current, $j_c(\tau) \sim j_0(\tau) \sim \tau^{3/2}$.

On the other hand, according to Eqs. (8) and (10), for $\theta > \theta_c(\tau)$ the parameter $\Gamma_1 \sim \tau^{-1/2}$. In that case, under the condition $\Gamma_1 > 2$, Eq. (18) implies a quadratic dependence of the critical current on τ: $j_c(\tau) \sim \tau^2$. We note that then $\Gamma_1 \sim \theta$, so that the critical current j_c should fall off with increasing misorientation angle as θ^{-1}.

Figure 2 shows a log–log plot the critical current as a function of τ for different θ, according to a calculation using Eq. (18) together with (10). We see that in the region of small τ, where the critical angle $\theta_c(\tau)$ becomes smaller than the corresponding misorientation angle θ, one observes a transition from a dependence $j_c(\tau) \sim \tau^{3/2}$ to a dependence $j_c(\tau) \sim \tau^2$.

However, as θ increases and the distance between EDs decreases, it becomes necessary to take into account the aforementioned ''geometric'' factor connected with the decrease in the width of the superconducting channels between the insulating cores of the EDs. The the coefficient of the δ function on the right-hand side of Eq. (9) takes the form[8]

$$\Gamma(\psi,i) = \Gamma_1\psi + \Gamma_2 i^2/\psi^3, \tag{19}$$

where

$$\Gamma_2(\theta) = \frac{4r_i}{\xi(T)}\left[\frac{d^2}{(d-2r_i)^2} - 1\right] = \frac{4r_i\sqrt{\tau}}{\xi_0}\frac{\nu(2-\nu)}{(1-\nu)^2},$$
$$\nu = \frac{4r_i}{b}\sin(\theta/2). \tag{20}$$

We note that under the condition $\nu = 1$, which for $r_i \approx b$ holds at a misorientation angle $\theta \approx 30°$, the width $d_s = d - 2r$ of the superconducting channel goes to zero. Then a solid insulating barrier arises along the boundary, and the situation corresponds to a transition to the regime of a SIS Josephson contact with a linear dependence $j_c(\tau) \propto \tau$ (Ref. 2).

With allowance for relation (19) for $i^2 \ll 1$ we obtain in place of (16) the equation

$$\frac{1}{2}(\Gamma_1^2+4)\psi_0^2 = 1 - \frac{i^2}{\psi_0^2}(2+\Gamma_1\Gamma_2), \tag{21}$$

from which it follows that the critical current is

$$j_c(T) = \frac{j_0(T)}{[2(\Gamma_1^2+4)(2+\Gamma_1\Gamma_2)]^{1/2}}. \tag{22}$$

At small misorientation angles, when $\nu \ll 1$ and $\Gamma_2 \ll 1$, and for values of Γ_1 that are not too large, so that $\Gamma_1\Gamma_2 < 2$, expression (22) reduces to (18).

However, if the parameter Γ_1 assumes such a large value that, despite the smallness of Γ_2 for a low-angle boundary, the condition $\Gamma_1\Gamma_2 > 2$ holds, then for $\theta < \theta_c(\tau)$, when $\Gamma_1 = \text{const}$ [see Eq. (10)], the temperature dependence of the critical current (22) according to (20) has the form $j_c(\tau) \sim \tau^{5/4}$. At the same time, for $\theta > \theta_c(\tau)$, when $\Gamma_1\Gamma_2 = \text{const}$, in this case for $\Gamma_1 \gg 1$ a quadratic dependence $j_c(\tau) \sim \tau^2$ is also realized, which actually corresponds to the formation of an SNS contact along the boundary.

4. DISCUSSION

According to the above analysis, in rather perfect HTSC crystals and epitaxial films with a block structure and low-angle boundaries between blocks, there should be two regimes of limitation of $j_c(T)$. One of them, which was considered previously in Ref. 8, corresponds to small distances $d(\theta) < \xi(T)$ between EDs in the dislocation wall and can be realized at sufficiently large misorientation angles of the crystallites, whereas the second regime can occur only for small θ or for not-too-small τ, when $d(\theta) > 2\xi(T)$. These two cases are characterized by a different temperature dependence of the critical current density: $j_c(\tau) \sim \tau^2$ for $\theta > \theta_c(\tau)$, and $j_c(\tau) \sim \tau^{3/2}$ (for $\Gamma_1\Gamma_2 < 2$) or $j_c(\tau) \sim \tau^{5/4}$ (for $\Gamma_1\Gamma_2 > 2$) for small angles $\theta < \theta_c(\tau)$. Here it is assumed that the critical current for the depinning of Abrikosov vortices is much greater than the above-considered suppressed critical current for depairing across the boundary.

Since $\xi(T) \to \infty$ as $T \to T_c$, a transition to the case $\xi(T) > d$ should always occur in a certain region of temperatures near T_c. However, for HTSC materials, which are characterized by a small coherence length, this region can be too narrow for detection in experiments based on measure-

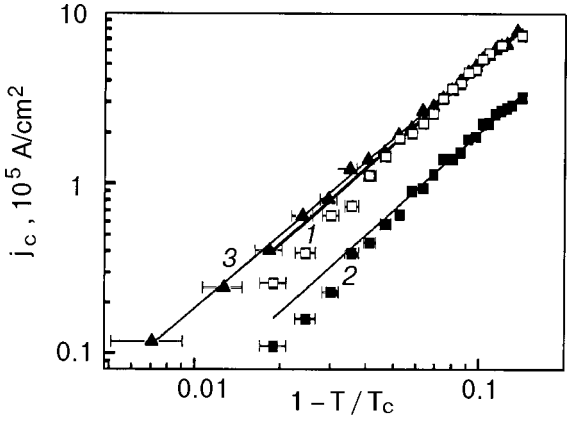

FIG. 3. Log–log plots of the measured critical current density versus $\tau = 1 - T/T_c$ for an unirradiated film (□), immediately after irradiation of the film with a dose of 3×10^{16} electrons/cm^2 (■), and 540 days after irradiation (▲). Lines *1–3* are the approximating curves $j_c(T) = J_n(1 - T/T_c)^s$ for these states of the film, with the parameters J_n and s given in the text. For the points at temperatures close to T_c the error bars (± 0.02) for the determination of τ are shown. For the other points the error is no bigger than the size of the symbols indicating the values of j_c.

ments of $j_c(T)$. Therefore, in the case of small misorientation angles not exceeding $\theta_c(\tau)$, for values of τ comparable to the experimental uncertainty in the measurement of T_c the dependence $j_c \sim \tau^{3/2}$ (or $j_c \sim \tau^{5/4}$) will be observed in practically the entire region of $j_c(T)$ measurements.

Apparently, it is this situation that is realized as a result of relaxation after irradiation in the epitaxial films investigated in the present study. When one considers the rather high initial value of j_c in the samples under discussion, this explanation is more natural than the conjecture of Ref. 7 that SINS Josephson contacts are formed in them.

Figure 3 shows a log–log plot of the experimental data of Fig. 1 on the temperature dependence of $j_c(T)$ in the initial and irradiated films. We see that at temperatures near T_c, both the unirradiated and the fast-electron irradiated (immediately after irradiation) films have a dependence of $j_c(T)$ that deviates from the dependence $j_c \propto \tau^{3/2}$ observed at lower T to the side of larger values of the exponent of τ, and within the experimental error limits approaches a quadratic law, $j_c \propto \tau^2$. These deviations were unnoticeable in Fig. 1.

Although these deviations are comparatively small, they nevertheless exceed the mean-square measurement error, which stems mainly from the inaccuracy in the determination of τ in the temperature interval where the deviations appear. The corresponding error bars are shown in Fig. 3. The errors in the measurement of j_c are no bigger than the size of the symbols representing the experimental data points in Fig. 3 and are therefore not given individually.

Such behavior of $j_c(T)$ is in qualitative agreement with the theoretical curves (Fig. 2) of the critical current through low-angle boundaries. From the point of transition of the experimental curves from $j_c \propto \tau^{3/2}$ to $j_c \propto \tau^2$ one can estimate the value of the characteristic angles of misorientationn of the single-crystal blocks in the film by taking into account that the critical angle $\theta_c(\tau)$ corresponds to the maximum angle of the boundary on the percolation paths of the supercurrent. As a result, for a critical value $\tau_c \approx 0.06$ (see Fig. 3), according to relation (7), for $b \approx a \approx 4$ Å, $\xi_0 \approx 12$ Å, and $\gamma = \pi/4$ we obtain the estimate $\theta \leqslant \theta_c(\tau_c) \approx 2.5°$, which corresponds to distance between EDs of $d(\theta_c) \cong 90$ Å $\ll \xi_0$.

Comparing the experimental values of the critical current in the region $\tau > \tau_c$ in the unirradiated film, $j_c(T) \approx 1.4 \times 10^7 \tau^{3/2}$ A/cm^2 with the depairing current, which for $\lambda_L(0) \approx 1500$ Å has the value $j_0(T) \approx 3.6\times10^8 \tau^{3/2}$ A/cm^2, we can estimate according to (18) the value of the transparency factor of the boundary in the region $\theta < \theta_c(\tau)$: $\Gamma_1 \approx \pi \bar{u}_0 r_0^2/\xi_0^2 \approx 12$. Clearly here $\Gamma_1\Gamma_2 < 2$.

As a result of irradiation by fast electrons the value of $j_c(T)$ decreases to less than half (see Fig. 1), and for $\tau > \tau_c$ it amounts to $j_c(T) \approx 6.4\times10^6 \tau^{3/2}$ A/cm^2. This corresponds to an increase in Γ_1 to a value $\Gamma_1 \approx 28$, which may be due to growth of the effective radius of the nonsuperconducting regions around the cores of the EDs on account of the accumulation of radiation defects. Here the quantity $\xi(T) + 2r_i$, as before, remains smaller than d, and in the corresponding region of τ values the dependence $j_c \propto \tau^{3/2}$ is preserved.

After a long relaxation of the film at room temperature, the value of the critical current is practically restored to its original value (cf. Figs. 1 and 3). In terms of the model considered here, this can be understood to be the result of recombination of the radiation-produced vacancies and interstitial oxygen atoms (with the restoration of the previous values of r_i and Γ_1). The possibility and rate of such a process will depend substantially on the specific types of radiation defects produced during the irradiation.

The effect of electron irradiation on the value of T_c and on the transport properties of HTSCs was investigated in Refs. 11–14. The maximum energy of the electrons in those experiments was not more than 350 keV. The authors of those studies concluded that the defects formed are due to displacements of the oxygen atoms. It was show in Ref. 14 that in the irradiation of thin films of $YBa_2Cu_3O_{7-x}$ by low-energy electrons ($E < 40$ keV) the oxygen defects are formed predominantly in the region of the CuO chains.

If it is assumed that, despite the much higher electron energy ($E = 4$ MeV) used for irradiation in the present study and in Ref. 7, oxygen vacancies remain the main type of defects, then the observed rate of their ''healing'' as a result of storage of the samples in air at room temperature would be about as expected.

However, the temperature dependence of $j_c(T)$ in the film after relaxation does not exhibit any deviation from $j_c \propto \tau^{3/2}$ outside the experimental error in the entire investigated interval of τ (see Fig. 3).

Of course, the initial state of the sample and its state after relaxation are not identical in respect to the parameters that influence the critical current, and one can make different assumptions about the causes of the possible differences of θ_c in them. For example, they may be due to a change in the block structure (polygonization) of the film during the long relaxation at $T \approx 300$ K, as a result of which the misorientation angles of the blocks decrease and, consequently, the number of EDs decreases and the average distance between them increases, so that the characteristic values of θ remain less than $\theta_c(\tau)$ all the way down to the lowest values of τ that can be measured.

However, we will not present a detailed analysis of the deviations of $j_c(T)$ from the dependence $j_c(T) \propto (1$

$-T/T_c)^{3/2}$ or of the possible causes of differences in the states prior to irradiation and after relaxation. Moreover, at temperatures near T_c the curves presented can also be affected by the systematic error due to the chosen method of determining T_c from the start of the sharp change in χ''.

5. CONCLUSION

In summary, our investigation of a particular mechanism limiting the critical supercurrent density in low-angle grain boundaries in HTSC crystals and epitaxial films has shown that in the typical case for a HTSC material, where the coherence length is smaller than the distance between EDs along a low-angle boundary, the dependence $j_c(T)$ is mainly determined by the temperature dependence of the depairing current under the condition that the critical current for depinning of vortices is greater than the given value of $j_c(T)$ at all temperatures T. In the region closest to T_c, where the inequality $d>2\xi$ is violated, the dependence $j_c \propto \tau^{3/2}$ (or $j_c \propto \tau^{5/4}$) gives way to a dependence $j_c \propto \tau^2$. This model can satisfactorily describe the experimental temperature dependence of the critical current observed in Ref. 7 and in the present study. It also makes it possible to understand qualitatively the main features of the changes in $j_c(T)$ brought about by fast-electron irradiation of the films and by relaxation of the radiation defects after a long storage of the sample.

This study was supported in part by the Grant CRDF UP1-306 under the auspices of a joint program of the USA and Ukraine.

*E-mail: pashitsk@iop.kiev.ua

[1] G. Blatter, M. V. Feigelman, V. G. Geshkenbein, A. I. Larkin, and V. M. Vinokur, Rev. Mod. Phys. **66**, 1125 (1994).
[2] P. De Genn, Rev. Mod. Phys. **36**, 225 (1964).
[3] N. L. Rowell and H. J. Smith, Can. J. Phys. **54**, 223 (1976).
[4] D. G. Steel, J. D. Hettinger, F. Yuan *et al.*, Appl. Phys. Lett. **68**, 120 (1996).
[5] Q.-H. Hu, L.-G. Johansson, V. Langer, Y. F. Chen, T. Claeson, Z. G. Ivanov, Yu. Kislinski, and E. A. Atepantsov, J. Low Temp. Phys. **105**, 1261 (1996).
[6] K. A. Delin and A. W. Kleinsasser, Supercond. Sci. Technol. **9**, 227 (1996).
[7] Yu. V. Fedotov, S. M. Ryabchenko, and A. P. Shakhov, Fiz. Nizk. Temp. **26**, 638 (2000) [Low Temp. Phys. **26**, 464 (2000)].
[8] A. Gurevich and E. A. Pashitskii, Phys. Rev. B **57**, 13878 (1998).
[9] J. R. Clem and A. Sánchez, Phys. Rev. B **50**, 9355 (1994).
[10] M. Wurlitzer, M. Lorenz, K. Zimmer, and P. Esquinazi, Phys. Rev. B **55**, 11816 (1995).
[11] S. K. Tolpygo, J.-Y. Lin, M. Gurvich, S. Y. Hou, and J. M. Phillips, Phys. Rev. B **53**, 12454 (1996).
[12] S. K. Tolpygo, J.-Y. Lin, and M. Gurvich, Phys. Rev. B **53**, 12462 (1996).
[13] S. K. Tolpygo, J.-Y. Lin, M. Gurvich, S. Y. Hou, and J. M. Phillips, Physica C **269**, 207 (1996).
[14] E. M. Jackson, B. D. Weaver, G. P. Summers, P. Shapiro, and E. A. Burke, Phys. Rev. Lett. **74**, 3033 (1995).

Translated by Steve Torstveit